UNIVERSITÄTSKLINIKUM HAMBURG-EPPENDORF

Hamburg 2025

Angenommen von der Medizinischen Fakultät der Universität Hamburg am: 16.09.2025

Veröffentlicht mit Genehmigung der Medizinischen Fakultät der Universität Hamburg.

Prüfungsausschuss, der/die Vorsitzende: Prof. Dr. Markus Glatzel

Prüfungsausschuss, zweite/r Gutachter/in: Prof. Dr. Thomas Oertner

[...] que cicatrice tu cuerpo, no cese tu canto, ni calle tu eco.

Edelma Zapata Pérez

To Lisa and Rubén

Table of Contents

1.	Introduction	7
1.1	Presenilin 1 (PS1) Physiology	8
1.2	PSEN1 E280A mutation and ADAD	9
1.3	Neuropathogenesis of Alzheimer's Disease	. 10
1.3	.1 Amyloid-beta precursor protein (APP) structure and processing	. 10
1.3	.2 Amyloid β and Tau protein-related neurodegeneration	. 13
1.4	Genetic Underpinnings of Alzheimer's Disease	. 14
1.4	.1 Apolipoprotein E (APOE)	. 14
1.4	.2 Genetic modifiers in neurodegeneration	. 16
1.4	.3 Beyond <i>APOE</i> as a genetic modifier	. 16
2.	Rationale and AIM of the Thesis.	. 18
3.	Key concepts and summary of the individual publications.	. 20
3.1	Summary Publication I: Distinct tau neuropathology and cellular profiles of	an
ΑP	OE3 Christchurch homozygote protected against autosomal dominant Alzheim	er's
der	nentia, Acta Neuropathol., 2022	. 20
3.2	Summary Publication II: Resilience to autosomal dominant Alzheimer's	
dis	ease in a Reelin-COLBOS heterozygous man, Nat Med., 2023	. 23
3.3	Summary Publication III: APOE3 Christchurch Heterozygosity and Autoson	nal
Do	minant Alzheimer's Disease, NEJM., 2024	. 27
3.4	Summary Publication IV: APOE3 Christchurch modulates β-catenin/Wnt	
sig	naling in iPS cell-derived cerebral organoids from Alzheimer's cases, Front Mol	
Ne	urosci., 2024	. 29
3.5	Summary Publication V: Single-nucleus RNA sequencing demonstrates an	
aut	osomal dominant Alzheimer's disease profile and possible mechanisms of dise	ase
pro	tection, Neuron, 2024	. 32
4.	Discussion	. 35
5.	Conclusions	. 42
6.	Bibliography	. 45
7.	Publication I	. 62
8.	Publication II	. 75
9.	Publication III	100
10.	Publication IV	109

11.	Publication V	123
12.	Abstract	148
13.	Zusammenfassung	149
14.	List of abbreviations	151
15.	List of figures and tables	156
16.	Declaration of own contribution to the publications	154
17.	Curriculum Vitae	155
18.	Acknowledgements	157
19.	Eidesstattliche Versicherung	158

1. Introduction

Alzheimer's disease (AD) is the most widespread neurodegenerative condition, causing adult-onset dementia, accounting for 60 to 80% of all cases. Worldwide, it is estimated that around 50 million persons are living with dementia, and the economic burden related to the health care of this population is approximately US\$1 trillion annually. Moreover, it has been projected that by 2030, the number of people with this condition will reach 74.7 million [1, 2]. In Germany, the current incidence of AD is over 300,000 cases per year, with an estimated prevalence of 1.6 million persons [3].

The primary cause of the disease remains unknown. Most likely, AD results from a complex interaction between environmental factors and individual genetic traits. [4, 5]. Several risk factors have been associated with AD, with advanced age as the most significant single risk factor [6-9]. Ninety percent of all AD patients are over 65 years old, and the prevalence doubles every five years [10]. Other risk factors include a family history of dementia, homozygosity for the apolipoprotein E gene type 4 allele (*APOE4*), traumatic brain injury, and modifiable risk factors like obesity, smoking, hypercholesterolemia, diabetes mellitus type 2, and hypertension [11-14].

Clinically, Alzheimer's disease constitutes a progressive continuum, beginning with a preclinical, asymptomatic stage, in which individuals show no evidence of cognitive or functional decline. However, biochemical signs of the associated pathology are already present, as evidenced by cerebrospinal fluid analysis or imaging tests [15]. At this early stage, the two underlying pathological hallmarks -the progressive extracellular deposition of amyloid-beta ($A\beta$) and the formation of intracellular neurofibrillary tangles (NFTs)- are evident. Next, there is a stage of mild cognitive impairment characterized by early clinical symptoms such as anterograde amnesia, apathy, and mood disturbances. As the disease advances, cognitive and affective symptoms may intensify, coupled with motor and language difficulties. Ultimately, AD dementia develops [11], with the worsening of motor and cognitive symptoms resulting in severe disability and eventually, death [1-3, 11-14, 16].

There are two primary variants of Alzheimer's disease: sporadic AD (SAD) and familial AD (FAD), also known as autosomal dominant AD (ADAD) [17]. SAD, or late-onset AD, occurs in individuals over 60 years old and lacks a clear inheritance pattern. ADAD is characterized by early onset (before age 60) and is an autosomal dominant condition caused by missense mutations in one of three genes: amyloid precursor protein (*APP*), presenilin 1 (*PSEN1*), or presenilin 2 (*PSEN2*). Mutations in *PSEN1* account for nearly 90% of all FAD cases [17, 18]. More than 300 distinct mutations in *PSEN1* have been identified [19]. These mutations show complete penetrance and lead to a dysfunctional presenilin 1 protein (PS1), which negatively affects the activity of the γ -secretase complex, resulting in A β overproduction, oligomerization, and deposition. According to the amyloid hypothesis, this process leads to neurodegeneration and, ultimately, Alzheimer's disease [20].

1.1 Presenilin 1 (PS1) Physiology

PS1 is a 467-residue-long multipass membrane protein encoded by *PSEN1*, located in the long arm of the 14th chromosome (locus 14q24.3). It has nine transmembrane domains (TM) and a large cytosolic hydrophilic loop segment between TM 6 and 7. It is primarily located in the membranes of organelles such as the endoplasmic reticulum and Golgi apparatus [46]. To a lesser extent, PS1 has also been identified in neurons' pre- and post-synaptic terminals [47]. Endoproteolytic cleavage of the PS1 holoprotein produces both an amino-terminal fragment (30 kDa NTF) and a carboxy-terminal fragment (20 kDa CTF); NTFs and CTFs form heterodimers that constitute the functionally active form of presenilin. PS1 and its homolog, Presenilin 2 (*PSEN2*, locus 1q42.13) [48], make up the catalytic unit -responsible for the γ -secretase activity- of a 1:1:1:1 heterotetrameric complex [49] that includes Nicastrin, Gamma-secretase subunit APH1 A or B (Anterior pharynx-defective 1), and PEN2 (Presenilin enhancer protein 2). Although *in vitro* assays have shown that PS1 and Presenilin 2 (PS2) possess catalytic activity independently [50], the presence of the other subunits of the complex is necessary to achieve optimal catalytic activity [51].

PS1 catalyzes the proteolysis of type I membrane proteins, notably APP and Notch receptors, through a process known as "regulated intramembrane proteolysis". A definitive function for PS1 has yet to be established; however, over 140 substrates

have been identified [143], along with its involvement in various roles such as modulation of intracellular calcium signaling, synaptogenesis, intracytosolic trafficking of proteins, and the susceptibility of neurons to death by apoptosis [46,52]. Another crucial physiological process associated with PS1 is the regulation of signal transduction during development. In murine models, the absence of the *PSEN1* gene, or its disruption, leads to embryonic or early perinatal death, outcomes most likely related to the interruption of Notch signaling pathways [53], in addition to severe developmental defects in somite and axial skeleton formation, and deficiencies in the differentiation of T and B lymphocytes [46, 47, 54, 52, 51]. While *PSEN1* haploinsufficiency is sufficient for the pathogenic effects to manifest, homozygosity for *PSEN1* E280A has been reported in adult humans with early-onset dementia [55].

1.2 PSEN1 E280A mutation and ADAD

The E280A Presenilin 1 mutation is the most common cause of ADAD [19]. It is a missense mutation (A \rightarrow C at codon 280), resulting in substituting glutamic acid for alanine at a residue in the intracellular loop of PSEN1 after its cleavage site [21, 22]. Worldwide, the largest group of individuals bearing the E280A mutation -often referred to as the "Paisa mutation"- belongs to a Colombian kindred from the "Paisa" region of the country (Antioquia, Colombia), with more than 6000 descendants spread among 25 families and over 1000 identified carriers of the mutation [22, 23].

Clinically, this population shows an early onset characterized by memory impairment followed by aphasia in 81% of cases. Additional clinical manifestations include headache (73%), gait difficulties (65%), seizures and myoclonus (45%), cerebellar signs (19%), and Parkinsonism (19%) [22, 24]. Although most patients develop the disease during the fourth decade of life, there is a broad range of onsets, spanning from 32 to 62 years, with a mean disease duration of 8 years [24, 23]. The variability in age of onset has been correlated with environmental factors, *APOE* allele status, and various loci mutations [25, 26], highlighting the role of the individual genetic imprint as a disease modifier. For instance, AD patients carrying the *PSEN1* E280A mutation and the *APOE2* allele experience a later onset than those without it [27]. In a Colombian carrier of the *PSEN1* E280A mutation, homozygous for a rare variant of *APOE*, specifically the R136S-Christchurch mutation, the onset of the disease was delayed until the age of 70, when he presented mild cognitive impairment [28]

Neuropathologically, the brains of subjects with E280A-related FAD exhibit pronounced brain atrophy, severe β-Amyloid pathology, and cerebellar damage [28].

1.3 Neuropathogenesis of Alzheimer's Disease

The brains of Alzheimer's patients exhibit several macroscopic and microscopic features that distinguish the disease from other dementias. Macroscopically, typical characteristics of dementia, such as cortical thinning and atrophy, are observed. Microscopically, the presence of senile plaques and neurofibrillary tangles (NFTs) constitutes the neuropathological signature of the disease [18]. Senile plaques consist of the extracellular deposition of A β peptides, a by-product of APP processing, whereas NFTs are intracellular aggregates of hyperphosphorylated tau, a main microtubule-associated protein [18, 29].

1.3.1 Amyloid-beta precursor protein (APP) structure and processing

APP belongs to a family of transmembrane proteins, including the amyloid precursor-like proteins 1 and 2 (APLP1 and APLP2), both present in mammals. It features a single transmembrane domain, a large N-terminal extracellular domain, and a short C-terminal cytosolic domain. Only the proteolytic processing of APP results in the production of amyloidogenic fragments [30].

The human Amyloid-beta precursor protein is encoded by a single gene (*APP*) that contains 19 exons on the long arm of chromosome 21, at locus 21q21.3. The alternative splicing of the *APP* transcript produces eight isoforms, with the 695, 751, and 770 amino acid residue forms being the most prevalent. The 695 amino acid form is primarily expressed in the central nervous system, while the latter two forms are ubiquitously expressed in the body [31]. Although our understanding of the physiological activity of APP remains incomplete, both *in vitro* and *in vivo* assays highlight the importance of its processing products in cellular functions such as cell growth and survival, motility, neurite outgrowth, increases in synaptic density, synaptic vesicle release, and zinc homeostasis, among others [30-33]. Furthermore, abnormalities in neuronal migration have been observed following the injection of APP RNAi into embryonic rodents [34].

The synthesis of APP, which is abundant in neurons, takes place in the endoplasmic reticulum and undergoes glycosylation in the Golgi apparatus before exiting via the trans-Golgi network. Subsequently, APP is transported to the axolemma and presynaptic terminal through the rapid component of anterograde axonal transport, where it may reach the plasma membrane directly or via endosomal compartments [32, 33]. Once at the cell membrane, APP may undergo sequential cleavage by α and γ -secretase complexes without producing A β fragments -following the *non-amyloidogenic pathway*- or it may be internalized through clathrin-coated pits and stored in endosomal compartments, where the proteases BACE1 and γ -secretase catalyze proteolytic activity resulting in the formation of A β fragments -following the *amyloidogenic pathway*- [4].

The α -secretase cleavage of APP is attributed to several disintegrin and metalloproteinase enzymes of the ADAM family of proteases, among which ADAM-9, -10, and -17 are the most likely candidates [35-36]. This α -cleavage, which occurs mainly on the cell surface, generates two fragments: the N-terminal fragment, also known as secreted APP alpha (sAPP α), and the C-terminal fragment CTF83, named for the number of amino acid residues that compose it. An additional small peptide fragment, p3, is produced upon cleavage of CTF83 by the γ -secretase complex [4, 35, 36].

BACE1 is a type I transmembrane aspartic protease, encoded by the *BACE1* gene, located on the long arm of chromosome 11 (locus 11q23.3). It is synthesized as a 501-residue pro-enzyme in the endoplasmic reticulum, where it undergoes glycosylation and acetylation. Unlike α -secretase, it interacts with APP primarily within cytosolic endosomes, where it cleaves at residues +1 and +11. BACE1's proteolytic activity results in the release of a soluble ectodomain known as sAPP β and the cytosolic APP C-terminal fragment CTF99. Subsequently, CTF99 is cleaved by the γ -Secretase complex to generate A β peptides and the amino-terminal APP intracellular domain (AICD). The cleavage of APP CTF99 may occur at several sites, varying from residue +40 to +44, with residues 1- 40 being the most common [30, 31].

 γ –Secretase is an aspartyl protease and a member of the intramembrane-cleaving proteases (i-Clips) [37]. Among its four components, PS1 or PS2 form the catalytic core, while APH-1, PEN2, and NCT contribute to the three-dimensional assembly of the protease and function as substrate recognition units [7]. However, the direct binding of the APP transmembrane (TM) domain to the PS1 proteolytic unit has been described [60]. Although cryogenic electron microscopy has allowed the modeling of γ -Secretase at an atomic scale [62], the recognition and interaction principles with various substrates remain to be discovered [63]. Understanding these principles is crucial for elucidating AD pathogenesis and could potentially lead to treatments to reverse the natural progression of this condition.

 γ –Secretase cleaves several integral membrane proteins, including ErbB-4, Ecadherin, LRP, Nectin-1 α , and δ , out of more than 149 described substrates, notably APP and Notch [38, 40, 41]. These substrates are involved in the regulation of a diverse range of cellular processes, including synaptogenesis, adhesion, cellular migration, neurite outgrowth, and axon guidance. Typically, the proteolytic activity of γ -Secretase releases both an extracellular and an intracellular domain. The APP intracellular domain (AICD), generated via APP proteolytic processing, and the NICD from the Notch signaling pathway interact with DNA-binding proteins, thereby regulating gene transcription [9]. The physiological functions of the extracellular fragments of APP and Notch -A β and N β , respectively- are not yet fully elucidated [42, 9]. Nonetheless, the production of the A β fragment has been linked to the pathogenesis of AD.

According to the amyloid hypothesis -discussed later- $A\beta$ fragment's production from APP and its subsequent aggregation are the first steps in a molecular cascade leading to cell death and neurodegeneration in AD [43]. As mentioned before, γ -Secretase cleavage of APP leads to peptide fragments with varying residue lengths. Differences in the number of residues and the proportion of the hydrophobic TM domain of APP retained in the $A\beta$ fragment determine its tendency to aggregate into plaques. For example, it has been described that $A\beta$ 42 peptides are more aggregation-prone than other fragments. Furthermore, a shift in the $A\beta$ 42: $A\beta$ 40 ratio by increasing the former

or decreasing the latter's production results in greater aggregation and, subsequently, more significant neurotoxicity [44].

1.3.2 Amyloid β and Tau protein-related neurodegeneration

The amyloid hypothesis posits that the accumulation of $A\beta$ peptides underlies a cascade of molecular events leading to neurotoxicity, neurofibrillary tangle formation, and cell death in AD. This buildup may result from excessive peptide production or a malfunction in its clearing mechanisms [43]. According to the hypothesis, missense mutations in the *APP*, *PSEN1*, or *PSEN2* genes lead to increased production or reduced clearance of $A\beta42$ peptides, which oligomerize and form extracellular deposits known as amyloid plaques. These oligomers can damage neurites, directly disrupt synaptic activity, or activate microglia and astrocytes. In addition to their harmful impact on synaptic transmission, oligomer deposition is associated with altered neuronal ionic homeostasis and disrupted kinase/phosphatase activity. This detrimental pleiotropic effect of $A\beta42$ peptides on neuronal metabolism ultimately results in cell death and dementia [20, 43].

Despite being a mainstream explanation for the pathogenesis of AD for nearly 30 years, there are several objections to the amyloid hypothesis as a sufficient explanation for the observed phenomena. For example, there is a lack of correlation between the burden of amyloid deposits in the brain and clinical disease features, such as age of onset and degree of cognitive impairment, as well as the notorious failure to develop a successful treatment based on the theory that A β 42 peptides metabolism should be the primary pharmacological target [1, 32].

In parallel with $A\beta$ extracellular deposition, intracellular aggregated tau proteins - neurofibrillary tangles- are a pivotal driver of neurodegeneration in AD. Tau is a microtubule-associated protein that binds tubulin through its microtubule-binding domains, with a single tau molecule cross-linking multiple tubulin dimers [56], thereby conferring stability to the microtubule and preventing sudden microtubule disintegration [57, 58]. In addition to its role in cytoskeleton stability, tau proteins are functionally related to axonal transport, long-term potentiation (LTP), synaptogenesis, and long-term depression in the hippocampus [59].

Tau pathology propagates in a prion-like manner, resulting in the spread of disease-related protein oligomers or aggregates across connected brain regions [60]. This likely occurs through a trans-synaptic mechanism, thereby expanding neurodegeneration [60, 150]. Unlike Aβ42/40 peptide levels in cerebrospinal fluid (CSF), CSF Tau levels more accurately correlate with cognitive decline as well as AD severity and duration. Furthermore, elevated phosphorylated tau levels in CSF may help estimate the risk of progression to AD in patients presenting with mild cognitive impairment [61]. In *PSEN1* E280A patients, the severity of hyperphosphorylated tau deposits correlates with age of onset; later-onset patients exhibit less tau pathology in the frontal, temporal, and parietal cortices [42].

1.4 Genetic Underpinnings of Alzheimer's Disease

The etiology of the vast majority of ADAD cases is linked to one of three genes: Amyloid Precursor Protein (*APP*), Presenilin-1 (*PSEN1*), and Presenilin-2 (*PSEN2*) [62-65]. Pathological mutations in these genes lead to increased levels or decreased clearance of Aβ-peptides, resulting in early deposition and plaque formation, as well as other pathophysiological mechanisms, such as dysregulation of calcium homeostasis [6], impaired autophagy and lysosomal function [66], endosomal trafficking defects [67, 68], and synaptic dysfunction [69]. Generally, these mutations are deterministic, and inheriting them yields a high probability of developing AD. However, differences exist in the clinical and pathological phenotype between affected genes, with *PSEN1* conveying almost complete penetrance and an earlier onset, while *PSEN2* shows a slightly later onset and incomplete penetrance [65].

1.4.1 Apolipoprotein E (APOE)

Apolipoprotein E (APOE) was first identified in the context of lipid transport and metabolism. Nevertheless, its importance goes beyond lipids, particularly in the brain, where it plays a crucial role in neuronal health, response to injury, and vulnerability to neurodegenerative diseases, especially AD [141, 142]. The human *APOE* gene is found on chromosome 19, *locus* q13.32, and encodes a glycoprotein featuring two primary domains: a C-terminal domain that facilitates lipid binding and an N-terminal domain, linked by a hinge, that includes the main receptor binding site. In the brain, APOE is predominantly produced by astrocytes, which release lipoprotein particles

containing APOE to transport lipids to neurons. Other glial cells, such as microglia, also express APOE, especially during stress, while oligodendrocytes use it to maintain the myelin sheath [141, 143].

Secreted APOE binds to cell surface receptors from the Low-Density Lipoprotein Receptor (LDLR) family. It can attach to all seven family members. Still, the primary receptors are LDLR, Very Low-Density Lipoprotein Receptor (VLDLR), LDLR-related protein 1 (LRP1, also called ApoER), and LDLR-related protein 8 (LRP8, also referred to as ApoER2) [144]. These receptors facilitate the endocytosis of APOE-lipoprotein particles into target cells, especially neurons. Significantly, LRP1 and LRP8 can also trigger intracellular signaling pathways that influence neuronal survival, synaptic plasticity, and cytoskeletal dynamics, among others [141, 143].

The binding efficiency of receptors differs among the APOE isoforms. In humans, APOE consists of three primary isoforms: APOE2, APOE3, and APOE4. The APOE $\varepsilon 4$ allele is the most significant genetic risk factor for SAD, elevating the likelihood of developing the condition by 12-15 times in individuals homozygous for the allele. Additionally, APOE $\varepsilon 4$ is linked to an earlier onset of the disease compared to those who are homozygous for APOE $\varepsilon 3$. Conversely, the APOE $\varepsilon 2$ allele is deemed protective, lowering the risk of developing AD and delaying its onset. Meanwhile, APOE $\varepsilon 3$ is viewed as neutral regarding Alzheimer's risk [142, 144]. APOE isoforms differentially affect the metabolism of $A\beta$. APOE $\varepsilon 4$ is associated with less efficient $A\beta$ clearance due to reduced interaction with the LRP1 receptor or impaired transport across the blood-brain barrier. It is also linked to the exacerbation of tau pathology [142].

Of increasing interest is the potential crosstalk between APOE and the Wnt/ β -catenin pathway, a cascade involved in embryonic development, neurogenesis, cell fate determination, synaptic regulation, and cellular homeostasis. In the canonical pathway, Wnt ligands bind to Frizzled (FZD) receptors and LRP5/LRP65 co-receptors at the cell surface, triggering a signaling cascade that prevents the degradation of β -catenin. The interaction of APOE with the Wnt co-receptors LRP5 and LRP6 modulates the Wnt signaling pathway in an isoform-dependent fashion. Non-APOE $\epsilon 4$ isoforms are

thought to enhance the pathway. In contrast, *APOE* ε4 impairs the signaling by competing with the Wnt ligands for their co-receptors, averting the formation of the Wnt-FZD-LRP signaling complex. Additionally, *APOE* ε4 may change the conformation of the Wnt co-receptors, making them less effective [142, 144].

1.4.2 Genetic modifiers in neurodegeneration.

AD shows significant clinical variability, even among subjects with similar genetic backgrounds, irrespective of the presence of risk factors such as $APOE\ \epsilon 4$ for SAD or causative mutations for ADAD [71]. This variability indicates that additional factors influence the disease phenotype, including genetic modifiers. Genetic modifiers are genes, loci, or allelic variants that are not themselves responsible for a disease but shape the clinical and pathological phenotype when a primary pathogenic cause -i.e., pathogenic mutations on APP, PSEN1, or PSEN2 in relation to ADAD- is present [70]. Regarding AD, genetic modifiers can change the age of onset, disease progression rate, brain pathology distribution (A β burden, neurofibrillary tangle density), or the singular clinical profile that a patient shows [74]. For instance, it has been reported in familial FAD and SAD patients that the rate of cognitive decline is modified by the presence of 172 and 227 gene variants, respectively [72]. Additionally, it has been documented that genetic variants might account for the paradoxical phenotypes of some APOE2 carriers burdened by AD and APOE4 carriers who remain disease-free [73].

1.4.3 Beyond APOE as a genetic modifier.

The *APOE* gene is the most notable and widely acknowledged example of a genetic modifier in Alzheimer's disease [75, 76]. A recent publication even suggests that the *APOE* $\varepsilon 4$ homozygosity effect is so strong that it can be considered a genetic form of Alzheimer's by its own [145]. Also, the *APOE* $\varepsilon 4$ allele not only increases the risk of suffering from the disease but also modifies the clinical phenotype, both in SAD and ADAD. In patients carrying pathogenic mutations of *APP*, *PSEN1*, or *PSEN2*, the presence of *APOE* $\varepsilon 4$ lowers the age of onset by several years when compared to *APOE* $\varepsilon 3/\varepsilon 3$ carriers within the same cohort. *APOE* $\varepsilon 2$ allelicity, on the other hand, appears to delay the age of onset in ADAD [73]. Aside from *APOE*, GWAS analysis has identified other genetic variants that act as risk factors or modifiers for disease

onset, progression, or clinical presentation; examples include *TREM2*, *ABCA7*, *CLU*, and *APP* gene variants.

TREM2 expression is required for microglia activation; some of its variants, such as R47H, have been found to increase the risk of SAD; *TREM2* variants are typically deemed to be a risk factor, albeit more recently variants like rs1582763 and rs6591561 have been described to have a protective effect [78, 79]. *ABCA7* transcript products are related to lipid transport and cholesterol metabolism. *ABCA7* loss-of-function variants are associated with an increased risk of AD, probably by impairing Aβ clearance by glial cells, mitochondrial metabolism, and neuron cholesterol homeostasis [80, 81]. Albeit typically associated as causative or increasing the risk for AD, protective variants of the *APP* gene have been described. The A673T mutation in the *APP* gene, also called the "Icelandic mutation," hampers BACE1 cleavage of APP, decreasing the production of Aβ peptides. Individuals with this mutation face a markedly reduced risk of developing AD and are more prone to maintain cognitive function in old age [82, 83].

The genes mentioned above and the influence of the polygenic background point to the importance of genetic modifiers in AD. Genetic factors beyond the primary causative of the disease can effectively change the baseline risk of suffering the disease, the age of onset, clinical presentation, and progression by modulating core molecular pathways involved in AD pathogenesis, like neuroinflammation, $A\beta$ metabolism, tauopathy, and cellular resilience.

2. Rationale and AIM of the Thesis.

PSEN1 E280A mutation has been identified in the world's largest ADAD kindred in the region of Antioquia (Colombia). Because of the near 100% penetrance of the mutation and the predictable age of onset of those affected (mild cognitive impairment typically presenting in the mid-40s, with dementia by the late 40s), this population is a unique model for the study of the disease, its preclinical stages, and the factors influencing disease trajectory. Despite this predictability, some individuals within the kindred have presented with an extreme phenotype of delayed age of onset for up to 30 years. These cases contest a fully deterministic view of ADAD and show that protection is possible even in the event of high genetic risk or significant Aβ pathology burden. However, the exact molecular mechanism and pathways by which protection is possible remain undefined.

From a genetic analysis point of view, two different approaches can be used to answer this question. Protective genes can be detected in population studies involving, ideally, large population samples [146]. The protective effects of genes identified by using this method are clear in the populations studied, but the size of the effect in every individual carrier might be small. This approach has also been used in the *PSEN1* E280A population, with moderate success [147, 25, 27, 148]. However, even though the E280A population is the largest population carrying an ADAD mutation, it still small for genomic analyses. This limitation creates uncertainty regarding the potential protective effects of the genetic variants discovered. The alternative approach focuses on identifying outstanding individuals with protective traits within this population. The rare genetic variants found in these protected ADAD carriers are more likely of being biologically relevant, as tested in cellular and animal models [28]. In-depth characterization of protected individuals can provide paramount insights into AD pathogenesis and open the possibility of developing new therapeutic targets replicating genetic modifiers' protective effects.

This thesis aims to make an in-depth characterization of the clinical, pathological, cellular, and molecular mechanisms underlying protection, as reflected by the significantly delayed age of onset, to ADAD conferred by the rare genetic variants of

APOE3 Christchurch (APOEch) and RELN-COLBOS within the context of the PSEN1 E280A mutation and to outline the molecular signature that differentiates PSEN1-ADAD from sporadic AD. Five publications are presented for this aim. The first two introduce a multidimensional description of the protected cases, including clinical, neuroimaging, and neuropathological profiles: "Distinct tau neuropathology and cellular profiles of an APOE3 Christchurch homozygote protected against autosomal dominant Alzheimer's dementia, Acta Neuropathol., 2022" and "Resilience to autosomal dominant Alzheimer's disease in a Reelin-COLBOS heterozygous man, Nat Med., 2023" for the latter I contributed as co-first author. A follow-up publication further investigates the effect of the APOEch variant in the age of onset between heterozygous carriers of this mutation within the PSEN1 E280A Colombian kindred, "APOE3 Christchurch Heterozygosity and Autosomal Dominant Alzheimer's Disease, NEJM., 2024". To assert the cellular and molecular mechanism related to protection in the context of APOEch mutation, iPS cells were used to produce organoids in which the β-catenin/Wnt signaling was evaluated as well as tau phosphorylation patterns "APOE3 Christchurch modulates β-catenin/Wnt signaling in iPS cell-derived cerebral organoids from Alzheimer's cases, Front Mol Neurosci., 2024". Finally, to explore the potential mechanism of disease protection associated with the APOEch variant and how its transcriptomics profile compares to SAD and typical PSEN1 E280A ADAD, snRNAseq was performed on prefrontal cortex samples "Single-nucleus RNA sequencing demonstrates an autosomal dominant Alzheimer's disease profile and possible mechanisms of disease protection, Neuron, 2024."

3. Key concepts and summary of the individual publications.

3.1 Summary Publication I: Distinct tau neuropathology and cellular profiles of an APOE3 Christchurch homozygote protected against autosomal dominant Alzheimer's dementia, Acta Neuropathol., 2022

Arboleda-Velasquez *et al.* [28] had previously reported a *PSEN1* E280A carrier from the described Colombian population with an extremely delayed age of onset (AOO). The subject, a female, developed mild cognitive impairment (MCI) in her seventies, almost three decades after the usual AOO for individuals of the same kindred. Whole-exome sequencing confirmed her *PSEN1* mutation and the presence of two copies of the rare Christchurch (*APOEch*) mutation [84], a missense mutation that results in an Arg → Ser substitution at residue 136 encompassing a receptor-binding domain known to interact with lipoprotein receptors (LDLR, LRP1) and heparan sulfate proteoglycans (HSPGs) [85, 86].

In this follow-up clinical background, *in vivo* imaging, postmortem assessment, and gene expression profiles of brain cell subpopulations were reported. The patient had a longitudinal follow-up with a standardized clinical rating and neuropsychological tests performed during life, as well as an MRI for structural assessment and functional imaging PET Scan 11C-Pitsburg Compound B (PiB) and 18F-Flortaucipir (FTP). Postmortem evaluation included conventional neuropathological assessment, electron microscopy examination of the cerebral cortex, and nuclei isolation from the hippocampal formation, frontal, and occipital cortex for snRNAseq.

The patient exhibited significant amyloid pathology, demonstrated by PiB PET scans and postmortem immunohistochemistry (Thal V, CERAD C). In terms of tau pathology, Flortaucipir PET revealed a relative preservation of the temporal and parietal cortices, while the occipital cortex showed an abnormally high Tau burden. Histopathological analysis indicated advanced disease (Braak VI) but showed only minimal Tau immunoreactivity in the frontal cortex, as noted in the functional imaging (Figs. 1 & 2).

The post-mortem analysis also revealed restricted cerebral amyloid angiopathy (CAA), favoring the posterior circulation with parenchymal CAA visible exclusively in the occipital cortex within the telencephalic structures and leptomeningeal involvement only in the cerebellum.

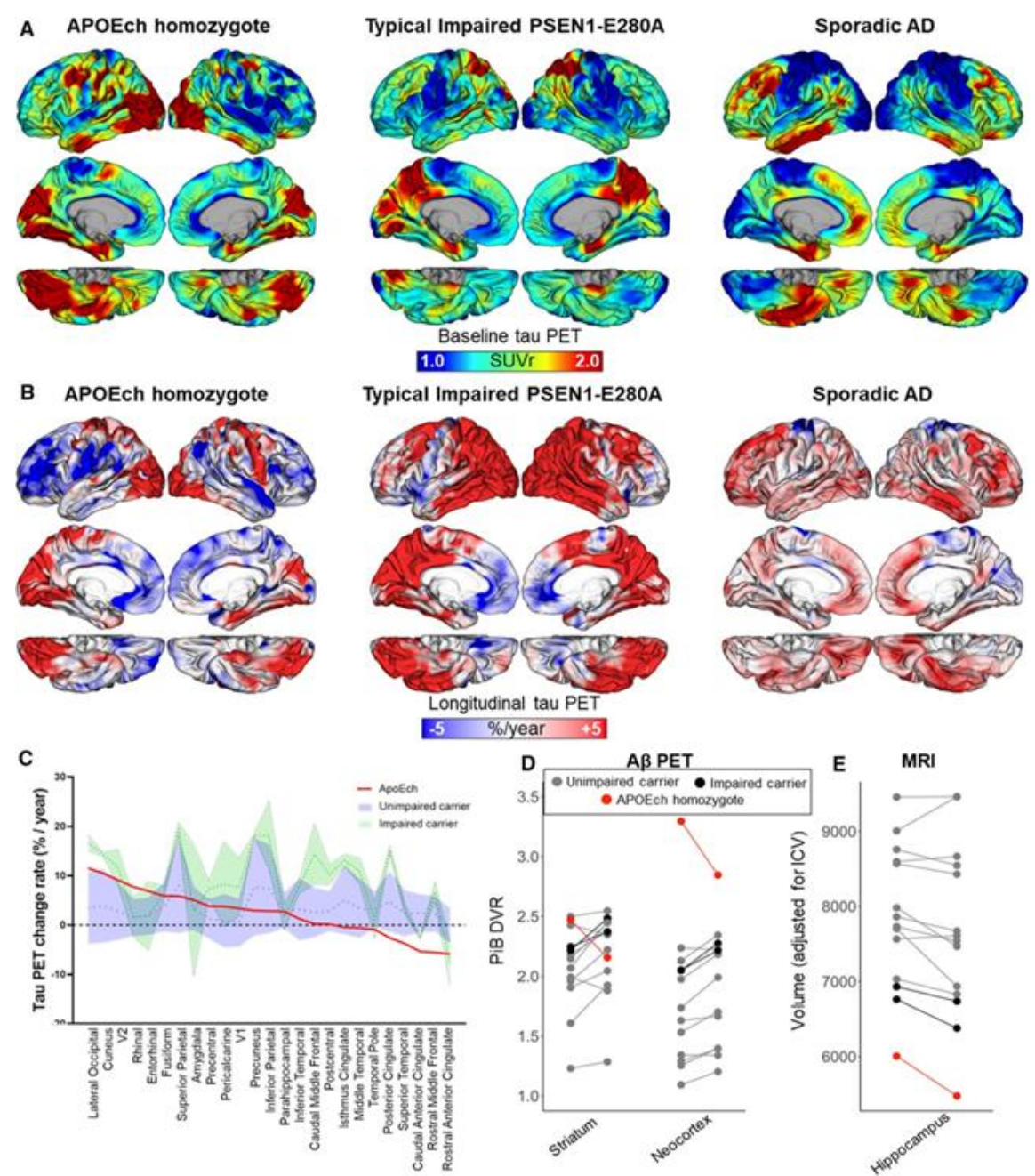


Figure 1| Longitudinal tau PET imaging measures in an *APOE3ch* homozygote. A. Surface rendering of tau PET (Flortaucipir) images (standardized uptake value ratio, SUVr), at baseline, 3-year follow-up (center), and $\bf B$. rate of change (expressed as %/year), in the APOE3ch homozygote, (left) a typical PSEN1-E280A impaired carrier (center) and a sporadic AD case (right). $\bf C$. Distribution area plot showing annualized percent change rates in tau PET for APOE3ch homozygote red line) relative to unimpaired (blue) and impaired (green) PSEN1-E280A carriers. Regions along the x-axis are ordered from highest to lowest change rate observed in the APOE3ch homozygote. $\bf D$. Spaghetti plots of Aβ PET (Pittsburgh Compound B, PiB) measurements at baseline and 2-year follow-up, E Structural MRI measurements at baseline and 2-year follow-up of hippocampal volume.

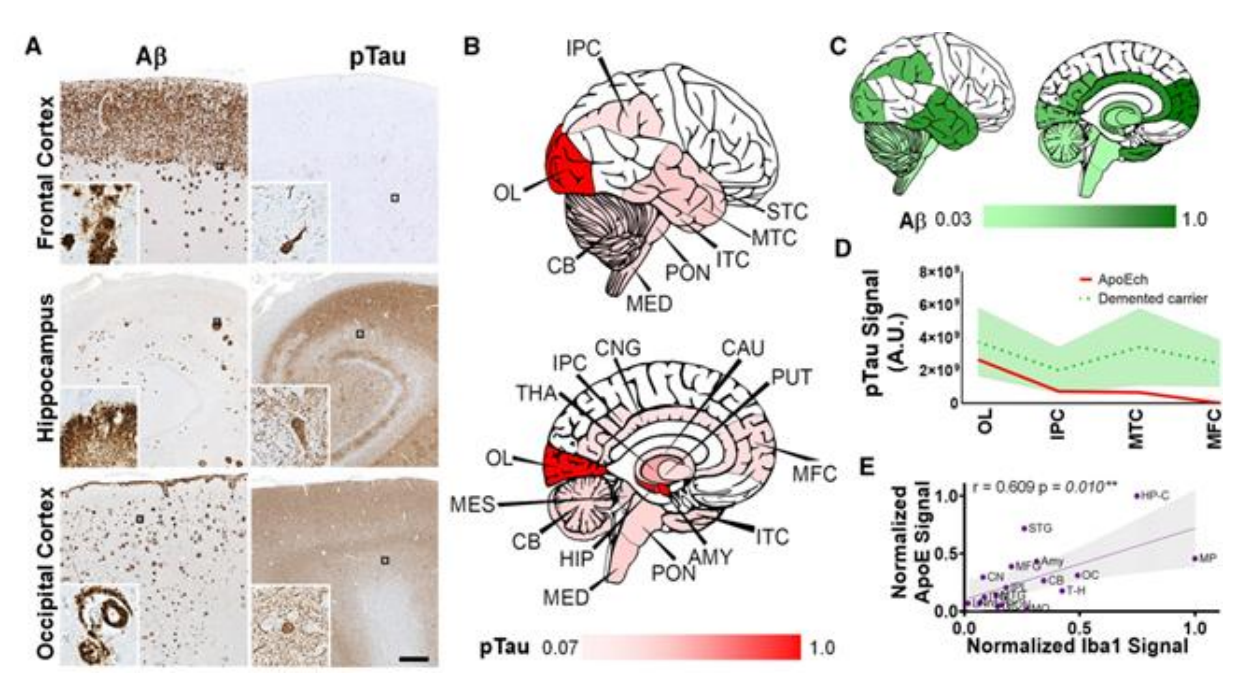


Figure 2| Neuropathological characterization of an ADAD *PSEN1* E280A mutation carrier with two copies of the APOE3ch variant. A. Representative panels for Tau and Aβ pathology in the frontal cortex, hippocampus, and occipital cortex. Insets show specific pathological features found in each brain area, such as NFT, dystrophic neurites, diffuse tau pathology, and diffuse core Aβ plaques and CAA. Bar = $500 \, \mu m$. B. Graphic representation of the general distribution and intensity of tau pathology signal with normalized lower and maximum values represented in red intensity. *MFC* medial frontal cortex, *STC* superior temporal cortex, *MTC* middle temporal cortex, *ITC* inferior temporal cortex, *HIP* hippocampus, *AMY* amygdala, *CNG* cingulate cortex, *PUT* putamen, *CAU* caudate, *THA* thalamus, *IPC* inferior parietal cortex, *OL* occipital lobe, *CB* cerebellum, *MES* mesencephalon, *PON* pons, *MED* medulla oblongata. C. Graphic representation of distribution and intensity of Aβ signal with normalized lower and maximum values represented in green intensity. D. Distribution area plot showing tau integrated density signal in cortical areas in APOE3ch homozygote (red line) relative to impaired (green) PSEN1-E280A carriers. Areas are ordered according to the highest to lowest tau integrated density in the APOE3ch homozygote. E. Correlation scatter plot for ApoE signal intensity against lba1 signal intensity in all areas studied in B.

Regarding the transcriptomic landscape, a subpopulation of excitatory neurons with high expression of *RORB* (Retinoid-Related Orphan Receptor B) was identified in the frontal cortex and hippocampus. These neurons exhibit a transcriptomic profile enriched in neurodevelopmental genes while demonstrating lower expression of synaptic-related genes. Concerning glial cells, there are regional differences in expression profiles between the frontal and occipital cortices for the same populations of glial cells, with *APOE* showing higher expression in astrocytes and microglia within the frontal cortex with a more homeostatic profile. Targeted gene expression analysis in microglia also reveals an acute immune response profile in the frontal cortex. Meanwhile, both cellular types show transcriptomic profiles commonly associated with neurodegeneration in the occipital cortex. The association between specific transcriptomic profiles, higher APOE levels in glial cells, and localized protection hints towards a dose-dependent effect of the *APOE3ch* variant.

In summary, the results highlight the *APOE3ch* variant as a significant genetic modifier in ADAD, delaying the onset age by several years and altering its clinical course. This protective effect seems to be linked to changes in Tau pathology, which affects its spatial distribution within the cerebral cortex. Conversely, the high amyloid burden strengthens the notion that tauopathy plays a pivotal role in driving neurodegeneration and cognitive decline in ADAD. From a cellular viewpoint, protection appears connected to maintained glial homeostasis and the resilience of specific neuronal populations, such as *RORB*+ in the frontal cortex. Different factors coalesce regarding the occipital cortex's vulnerability, including lower *APOE* expression levels, a persistent microglial inflammatory state, and concomitant CAA.

3.2 Summary Publication II: Resilience to autosomal dominant Alzheimer's disease in a Reelin-COLBOS heterozygous man, Nat Med., 2023.

This paper reports the clinical, *in vivo* neuroimaging, genetics, and neuropathological characterization of a second case of extreme protection against ADAD within the Colombian kindred carrying the "paisa" (*PSEN1* E280A) mutation. The subject, a male patient, developed MCI at the age of 67, twenty years later than the median for the same population, despite carrying the mutation. Unlike the previously reported case (female homozygote for the *APOE3Ch*), he was heterozygous for a rare variant in *RELN* (H3447R, hereinafter known as COLBOS after the Colombia-Boston biomarker research study), a missense mutation resulting in a Histidine → Arginine substitution in the C-terminal of RELN [87].

A multimodal approach was used to characterize the case, including *in vivo* and postmortem assessment, *in vitro* molecular and functional studies, and the development of a mouse model. Longitudinal cognitive and clinical evaluation was performed alongside structural (MRI) and functional imaging, PET Scan 11C-Pitsburg Compound B (PiB), 18F-Flortaucipir (FTP), and FDG to measure cerebral metabolic rate for glucose (CMRgI). Whole-exome (WES) and Whole-Genome (WGS) sequencing were used to identify potential protective variants. Post-mortem evaluation included conventional neuropathological assessment from 17 brain regions. *In vitro* studies included the review of the response of primary mouse cortical neurons treated with recombinant wild-type (WT) RELN or RELN-H3448R (mouse equivalent to human

RELN-COLBOS) to assess downstream signaling and binding assays (i.e., heparin affinity chromatography, surface plasmon resonance, biolayer interferometry, and isothermal titration calorimetry). A knock-in mouse carrying the *RELN-COLBOS* variant was generated. Mice brains from the WT strain, as well as homozygous and heterozygous *RELN-COLBOS* carriers, were analyzed for Dab1 immunoreactivity. Finally, the knock-in mice were crossed with a Tau P301L transgenic mouse model to evaluate the impact of the mutation on behavior (limb-clasping test) and tau pathology in the brain.

The male patient was diagnosed with MCI at the age of 70, and by the age of 73, he had progressed to moderate dementia. His sister, who also carried the *PSEN1*-E280A mutation, had severe dementia when first evaluated at the age of 64, progressing to end-stage dementia at the age of 72. The male carrier showed a higher amyloid burden as measured by PiB PET scan and an overall Tau burden comparable to that of younger carriers within the same kindred; however, he had limited Tau pathology in the entorhinal cortex, the posterior cingulate cortex, and the precuneus (Fig. 3).

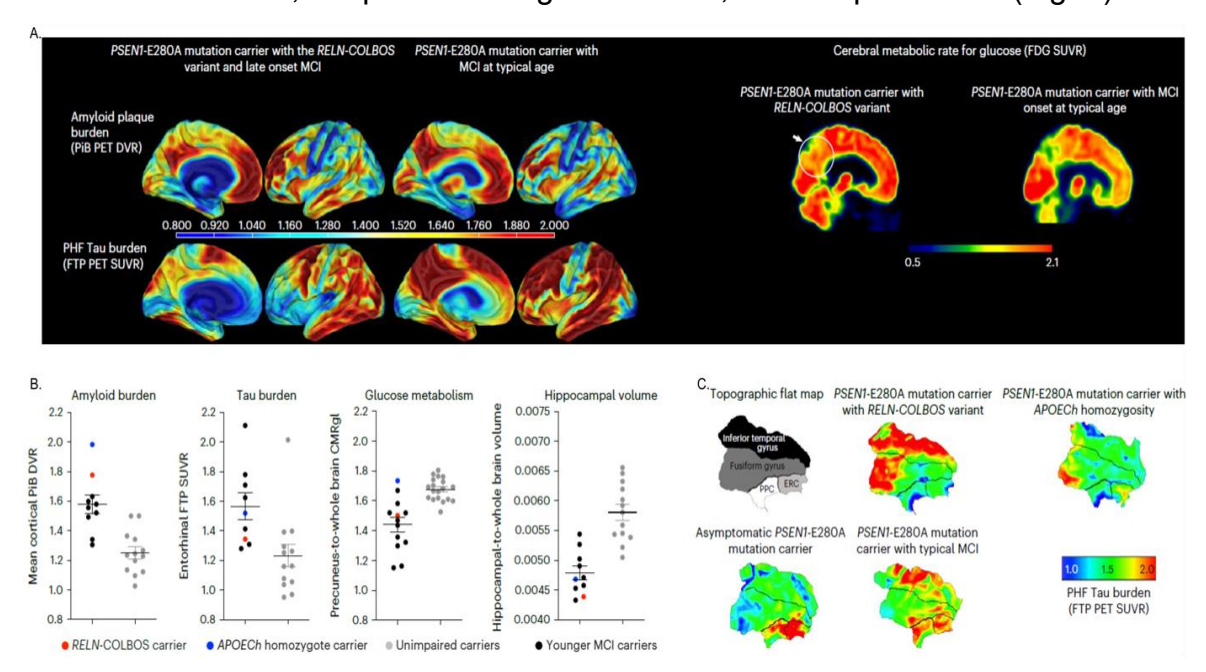


Figure 3| **PET imaging of the RELN-COLBOS (H3447R) carrier.** A. Representative PiB PET amyloid and FTP Tau PET imaging of the male case with *RELN-COLBOS* (left) compared to a *PSEN1*-E280A mutation carrier with MCI at a typical age (right). For both measurements, the specific binding of the tracer is represented using a color-coded scale, with blue being the lowest (DVR or SUVR = 0.8) and red being the highest (DVR or SUVR = 2.00) degree of binding. Right, representative FDG PET precuneus cerebral metabolic rate for glucose (CMRgI) of the male case with *RELN-COLBOS* (left) compared to a *PSEN1*-E280A carrier with MCI at a typical age (right). The binding affinity of the dye is represented using a color-coded scale, with blue being the lowest (SUVR = 0.5) and red being the highest (SUVR = 2.1) degree of binding. PHF: paired helical filament. B. Dot plot analysis of the imaging measurements shown in A. for amyloid and Tau burden, glucose metabolism, and hippocampal volume.

Brain imaging measurements of the male case with RELNCOLBOS (red dot) compared to the previously published APOEch homozygote female (blue dot), unimpaired PSEN1-E280A carriers (gray dots, n = 18 for the glucose metabolism panel, n = 13 for all other panels) and younger carriers of the MCI PSEN1-E280A mutation (black dots, n = 7 for the Tau burden plot, n = 8 for the amyloid burden and hippocampal volume plots, n = 11 for glucose metabolism)2. Some previously published data points are included in the figures because they are the only available data for comparison. Data are expressed as individual values with the mean \pm s.e.m. C. Anatomical details of Tau burden in the temporal cortex. Flat map representations of the right hemisphere temporal lobe cortex for regions of interest (ROIs) (top left, ERC), with Tau PET (FTP) overlay for four cases. The asymptomatic PSEN1-E280A carrier was 38 years old; the PSEN1-E280A carrier with typical MCI was 44 years old. The male carrier of RELN-COLBOS was notable for having a relatively lower tau burden in the medial temporal regions (ERC and PPC) compared to typical PSEN1-E280A mutation carriers.

WES/WGS analysis identified heterozygosity for the aforementioned *RELN* mutation (chromosome 7:g.103113302T>C, p.His3447Arg or H3447R); this mutation ranked in the top three candidate genes in the Genomizer priority score analysis, and its byproduct RELN is known to modulate tau phosphorylation [88, 89], as well as competing with APOE for binding to the Very Low-Density Lipoprotein Receptor (VLDLR) and the Low-Density Lipoprotein Receptor-related protein 8 (LRP8, also known as apolipoprotein E receptor 2) [90, 91]. In vitro analysis showed that after treatment with recombinant RELN-H3448R, primary mouse neurons in a monolayer culture increased the phosphorylation of Dab1 when compared to WT RELN treatment. Binding assays showed that the mutation does not directly affect the interaction with VLDLR or LRP8; instead, it increased the affinity of the CTR-RELN to heparin and NRP1. In vivo validation showed consistent findings; homozygous male knock-in mice showed increased Dab1 phosphorylation in the hippocampus and the cerebellum compared to the WT mice, confirming a gain-of-function effect. When crossed with the Tau P301L mice, the homozygous male mice showed a lower immunoreactivity for pTau T205 in the hippocampus and the medulla oblongata, as well as improved performance in the limb-clasping test.

Postmortem evaluation of the *RELN-COLBOS* case showed an advanced disease compatible with a Braak VI, Thal 5 stage. Despite widespread Tau pathology, the entorhinal cortex (ERC) proved to be relatively spared from Tau deposition, consistent with 18F-Flortaucipir PET findings. Another striking difference was a higher neuronal density in the ERC of the *RELN-COLBOS* case than in typical FAD E280A, sporadic AD cases, and the previously reported APOEch case (Fig. 4).

These results highlight the *RELN-COLBOS* (H3447R) variant as a significant genetic modifier in ADAD, delaying the onset age by several years and altering its clinical course. The resilience mechanisms seem to be related to the variant effect on Tau pathology in a spatially specific manner, given the relative sparing of the ERC and the higher neuronal density found in this area. *In vitro* and *in vivo studies* show the mutation to have a hypermorphic effect, enhancing Dab1 phosphorylation and increasing RELN affinity to extracellular matrix GAGs and potentially co-receptors like NRP1. Interestingly, both the disease course in the male carrier (later age of onset and milder disease) compared to his female sibling, and the results from the mouse model suggest that sex might be a driver of protection mediated by the *RELN-COLBOS* variant.

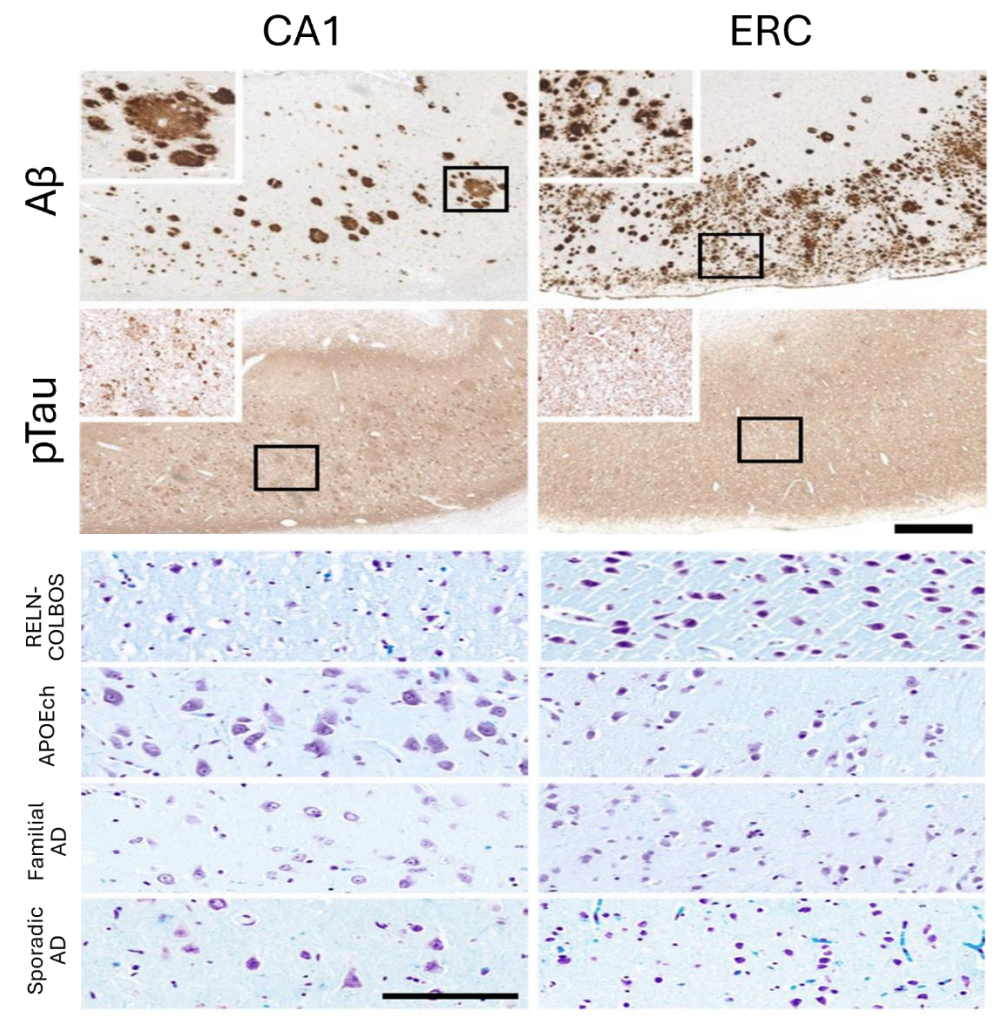


Figure 4| **Neuropathological characterization of the case with** *PSEN1* **E280A**; **RELN-H3447R.** A. Aβ and pTau pathologies in the CA1 and ERC. Both pathologies present a wide distribution and intensity. Aβ pathology shows diffuse plaques with varied distribution and size (panels and insets). pTau pathology shows varied density of neurofibrillary tangles and diffuse Tau pathology. Scale bar, 500 μm. B. Neurons stained with Kluver–Barrera stain in the CA1 and ERC of the case with *PSEN1*-E280A/*RELN-COLBOS*, the case with *PSEN1*-E280A/*APOEch*, a case with average-onset *PSEN1*-E280A familial AD, and a case with sporadic AD. Scale bar, 125 μm.

3.3 Summary Publication III: APOE3 Christchurch Heterozygosity and Autosomal Dominant Alzheimer's Disease, NEJM., 2024.

This follow-up paper further explores the role of the *APOE3ch* (R136S) genetic variant as a modifier of AD pathology. The previous publication reports a female carrier of the *PSEN1* E280A mutation who was also homozygous for the rare Christchurch variant in *APOE3*. Building on these findings, this publication examines whether heterozygosity for the *APOE3ch* variant could be a modifier for AD, delaying its age of onset and altering the clinical course or the neuropathological imprint.

Data from a cohort of 1077 descendants of a family carrying the *PSEN1* E280A mutation were retrospectively assessed. The information collected between 1995 and 2022 included clinical and neuropsychological evaluations and validated batteries for detecting AD-related cognitive impairment in this kindred (e.g., CERAD, Trail Making Test, Rey-Osterrieth complex figure, etc.). With this information, expert evaluators who were blind to the specific genetic background of the subjects classified them as having mild cognitive impairment or dementia. Within the cohort, 121 carriers of the *APOE3ch* variant were identified; of these, twenty-seven were simultaneously heterozygous for *APOE3ch* and the *PSEN1* E280A variant. In addition to the clinical follow-up, genotyping for *PSEN1* E280A and *APOE* variants was performed; two subjects underwent brain imaging, and four postmortem brain examinations.

Cumulative incidence function analysis of matched samples between *carriers* and *noncarriers* of the *APOE3ch* variant showed a clinically relevant delay in the onset of cognitive impairment for the Christchurch variant heterozygotes. Between carriers, there was a median age of 52 years (95% CI, 51 - 58) for the onset of MCI and 54 years (95% CI, 49 - 57) for the onset of dementia, whereas in the *noncarriers* group the median age for the onset of MCI was 47 years (95% CI, 47 - 49) and 50 years (95% CI, 48 to 51) for the onset of dementia (Fig. 5). Brain imaging in two living *carriers* showed an amyloid burden (PiB PET DVR) similar to a typical *PSEN1* E280A, meanwhile Tau imaging (18F-flortaucipir) was remarkable for limited Tau burden in relevant areas to AD including the ERC. Furthermore, FDG-PET for both *APOE3ch* heterozygous showed preserved glucose metabolism in certain areas (e.g., precuneus) compared to *noncarriers*, suggesting reduced neurodegeneration (Fig. 5).

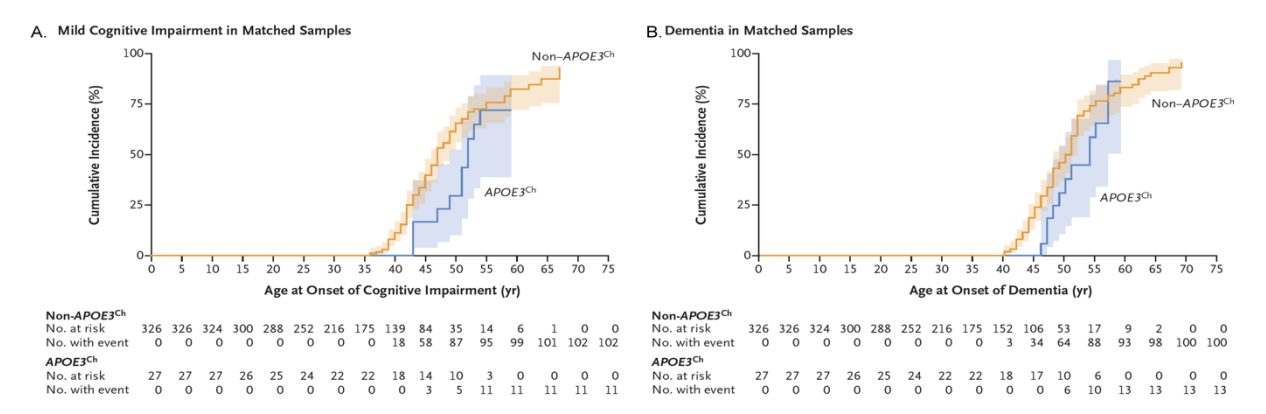


Figure 5 Cumulative incidence function for cognitive impairment and dementia among *PSEN1* **E280A carriers.** Shown are the cumulative incidence functions of mild cognitive impairment A. and dementia B. among persons with the *PSEN1* E280A variant, 27 of whom had the *APOE3*Ch variant and 326 without it. Participants were matched for sex, *APOE* genotype, and years of formal education. Death without a diagnosis of mild cognitive impairment or dementia was a competing risk. Shading indicates the 95% confidence interval.

Finally, the neuropathological assessment revealed similar amyloid and tau disease burden in *carriers* and *noncarriers*; however, *APOE3*ch heterozygous carriers showed less CAA in the frontal cortex and a lower percentage of vessel wall affected by CAA pathology (Fig. 6).

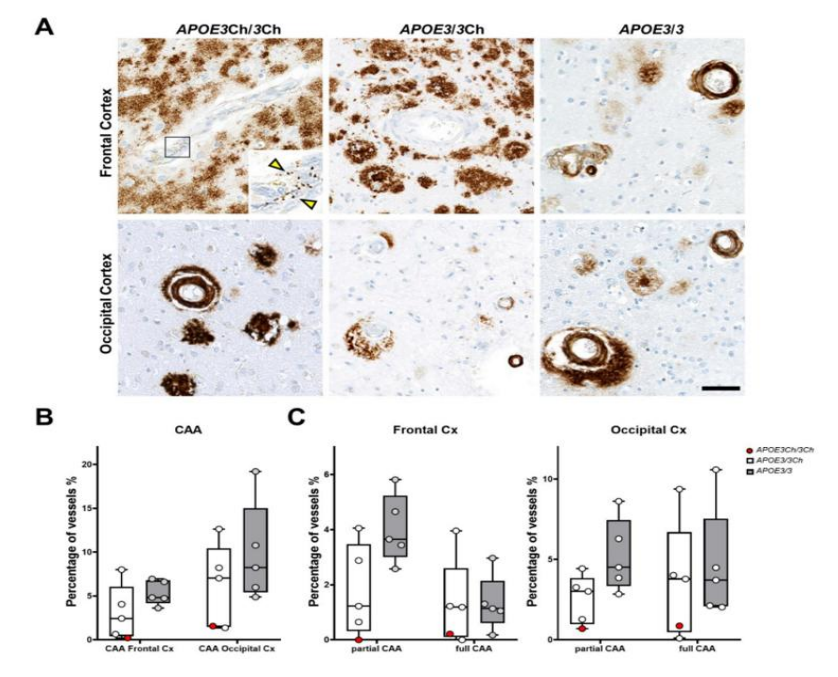


Figure 6| Decreased cerebral amyloid angiopathy in APOE3Ch PSEN1 E280A carriers

A. Representative microphotographs of amyloid beta (Aβ) immunostaining of the frontal cortex and occipital cortex of the homozygous *APOE3Ch PSEN1E280A* carrier (*APOE3Ch*), a heterozygous *APOE3Ch PSEN1E280A* carrier (*APOE3Ch*), and an *APOE3/3 PSEN1*E280A carrier (*APOE3/3*). **B.** Box and whiskers plot depicting the percentage of microvessels affected by CAA in *APOE3Ch PSEN1*E280A carriers (one *APOE3Ch/Ch* homozygote - red circles - and *APOE3Ch* heterozygotes n=4 **C.** Once CAA pathology is further discriminated into partial or total coverage of the wall perimeter of the vessel, it becomes evident that partially CAA-affected microvessels in *APOE3/3 PSEN1*E280A cases are more than their *APOE3ch* counterparts, or fully CAA affected microvessels in APOE3/3 cases, indicating a more varied CAA profile in APOE3/3 cases with higher impact in frontal cortices.

This comprehensive, longitudinal characterization of a large sample of *PSEN1* E280A carriers heterozygous for *APOE3ch* demonstrates that the Christchurch variant functions as a genetic modifier in ADAD, even for those carrying one allele. Although the observed delay in age of onset of 4 to 5 years is less dramatic than the decadeslong protection reported in the homozygous case, it remains clinically significant. Once again, protection is documented in the context of a high amyloid burden, yet with resistance to Tau pathology, as seen in PET scans and postmortem assessments. Modification of the CAA pathology also appears to be part of the variant characteristics. A possible reason for a less evident protective effect of *APOE3ch* in heterozygous carriers is the dose-dependent effect hinted by regional differences in the homozygous case.

3.4 Summary Publication IV: APOE3 Christchurch modulates β-catenin/Wnt signaling in iPS cell-derived cerebral organoids from Alzheimer's cases, Front Mol Neurosci., 2024.

Examining the role of the *APOE3ch* genetic variant as a disease modifier in the context of ADAD, an iPS system was developed to identify the biological pathways influenced by *APOE3* Christchurch. To this end, cells from a *protected* (*PSEN1* E280A + *APOE3ch* carrier) and *non-protected* patient (*PSEN1* E280A only carrier) were used to generate iPS cells; genomic editing was used to introduce or remove the *APOE3ch* or *PSEN1* E280A mutations, and organoids were produced. The Cadherin/Wnt/ β -catenin signaling pathway was identified as possibly regulated by the *APOE3ch* variant. Intracellularly, the Cadherin/ β -catenin complex plays a role in maintaining cell and tissue integrity through its binding to α -catenin [92]. On the other hand, in the canonical Wnt signaling pathway, β -catenin acts as a transcriptional co-activator; upon binding of Wnt ligands to Frizzled or Low-Density Lipoprotein Receptors (LRP5, LRP6), a signaling pathway is triggered that prevents the degradation of β -catenin in the cytoplasm [93]. APOE binds to the same Low-Density Lipoprotein Receptors and potentially modulates or competes with the Wnt ligand binding, thus modifying the downstream Wnt/ β -catenin signaling pathway [93, 94].

A multimodal approach was used to evaluate the molecular pathways involved in *APOE3ch* variant protection in ADAD. Two female subjects from the Colombian

PSEN1 E280A kindred, one homozygous for the *APOE3ch* variant (i.e., *PSEN1* E280A + *APOE3ch* homozygous or *Patient* α) and a typical -unprotected- *PSEN1* E280A carrier with a wild-type APOE3 (i.e., *PSEN1* E280A + *APOE3wt* homozygous or *Patient* ω). Peripheral blood mononuclear cells from *Patient* α and *Patient* ω were reprogrammed into iPS cells. CRISPR/Cas9 gene editing was performed on the iPS cell lines to correct the *PSEN1* E280A mutation to a WT genotype or introduce/remove the *APOE3ch* variant. Table 1 summarizes the genotype of the cell lines used in this study. The cell lines were further differentiated into cerebral organoids.

Table 1. Cell lines and their genotypes.

Reprogrammed cell line	Base genotype	CRISPR target	Mutation success	Final genotype
iPS patient α	E3Ch PS1mut	PS1mut → PS1WT	Successful	E3Ch PS1WT
		PS1mut → PS1WT	Unsuccessful	E3Ch PS1mut
iPS patient α	E3Ch PS1mut	E3Ch → E3WT	Successful	E3WT PS1mut
		E3Ch → E3WT	Unsuccessful	E3Ch PS1mut
iPS patient ω	E3WT PS1mut	PS1mut → PS1WT	Successful	E3WT PS1WT
		PS1mut → PS1WT	Unsuccessful	E3WT PS1mut
iPS patient ω	E3WT PS1mut	E3WT → E3Ch	Successful	E3Ch PS1mut
		E3WT → E3Ch	Unsuccessful	E3WT PS1mut

Six organoids were pulled from each line for single-cell isolation and transcriptomic analysis (scRNA-seq) using the 10X Genomics Chromium platform was performed. Immunostaining was used for the identification of key proteins on organoids as well as on formalin-fixed paraffin-embedded (FFPE) brain tissue samples from the frontal cortex, hippocampus, and occipital cortex of *Patient* α . Finally, the HEK293 cell line containing luciferase under a TCF/LEF reporter control was used to assess the effects of recombinant *APOE3* WT and *APOE3ch* variant on the Wnt signaling pathway.

Tau immunoreactivity was assessed using anti-pTau s396 (an early marker for pathological phosphorylation). In *PSEN1* WT organoids derived from the *Patient* ω (E3WT PS1WT), the pTau S396 signal was reduced; the same was observed when the *APOE3ch* variant was introduced to organoids derived from this patient. Conversely, removing the *APOE3ch* variant from organoids derived from the *Patient* ω (E3WT/PS1mut) led to a significant increase in pTau S396 immunoreactivity. scRNA-seq analysis identified that the *APOE3ch* variant modulated the Cadherin Wnt signaling pathways, both in neuronal and glial populations. In *APOE3ch* expressing

organoids, transcripts for several Wnt ligands (WNT2B, WNT4, WNT7B) were downregulated, primarily in glial cells, but β -catenin transcripts were not influenced. Organoids with the *APOE3ch* variant exhibited an increased immunoreactivity to β -catenin compared to controls, even with reduced levels of Wnt ligand transcripts. To assess the paradox of downregulated Wnt ligands but upregulated β -catenin immunoreactivity, a TCF/LEF luciferase reporter assay was used to examine whether APOE3ch could directly influence Wnt signaling. Neither APOE3 WT nor APOE3ch alone activated the Wnt signaling pathway. However, when tested alongside the Wnt ligand Wnt3a, APOE3 WT acts as an inhibitor, while APOE3ch acts as an activator in a dose-dependent manner. Immunostaining on FFPE samples from the homozygous *APOE3ch* carrier showed a higher colocalization between β -catenin and NeuN markers in the frontal cortex compared to the occipital cortex and hippocampus (Fig. 7).

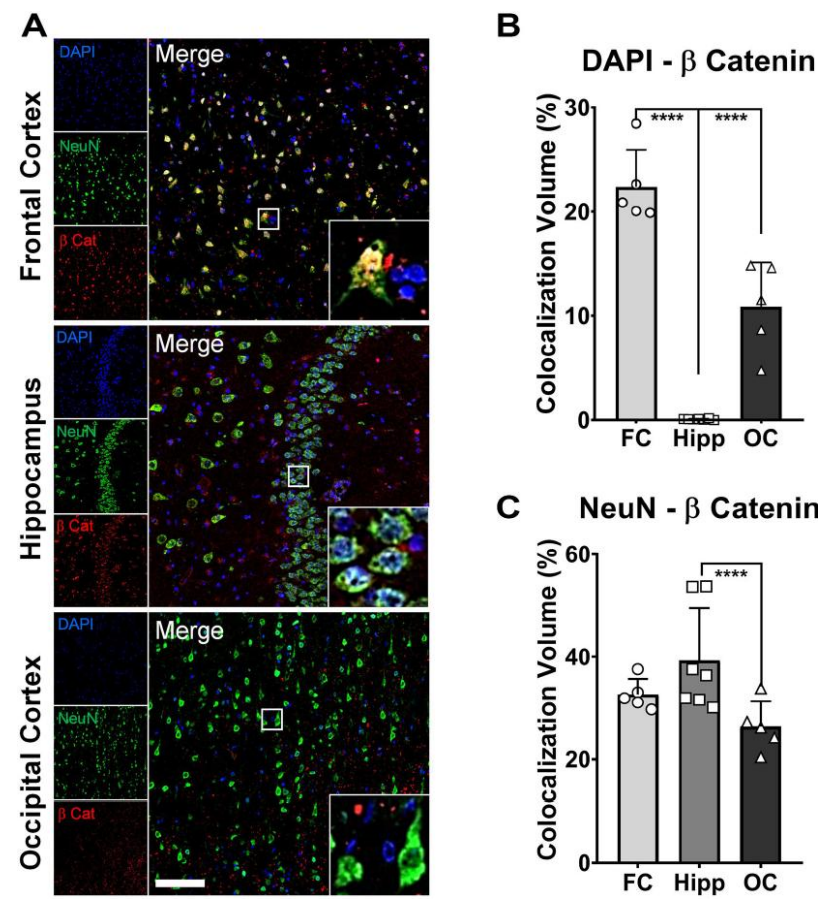


Figure 7| Increased nuclear β -catenin signal in frontal cortex neurons. Increased nuclear β -catenin in neurons of protected brain regions of *Patient* α . Representative immunofluorescence (IF) micrographs of the frontal cortex (FC), hippocampus (Hipp), and occipital cortex (OC) stained for β -catenin (red), NeuN (green), and cell nuclei (DAPI, blue). Insets present magnified images of neurons showing the degree of colocalization between the three markers. Scale bar = 100 μ m. A. Bar graphs for colocalization analysis depicting thresholded colocalization volumes (TCVs) between DAPI and β -catenin in FC, Hipp, and OC. The percentage of β -catenin colocalizing in nuclei is significantly higher in FC than in both

structures, Hipp and OC (one-way ANOVA, p < 0.0001 for both). B. Bar graphs for colocalization analysis depicting TCVs between DAPI and β -catenin in FC, Hipp, and OC. The percentage of β -catenin colocalizing with neurons is significantly higher only in Hipp when compared to OC (one-way ANOVA, p = 0.025) C.

3.5 Summary Publication V: Single-nucleus RNA sequencing demonstrates an autosomal dominant Alzheimer's disease profile and possible mechanisms of disease protection, Neuron, 2024.

ADAD often serves as a model for studying the pathogenesis of AD; the clear inheritance pattern and a more "uniform" genetic background among those affected by a single mutation within the same kindred facilitate the identification of causal and disease-modifying mutations [95]. Moreover, the ability to identify individuals impacted in a pre-clinical stage supports the decision to use these subjects for trials assessing prevention therapy. However, genetic vulnerabilities and the specific downstream cellular and molecular pathways behind ADAD and AD might differ, and identifying these differences is of the utmost relevance in the development of precision medicine. Here, the transcriptomic signature of ADAD and AD was identified by comparing the transcriptomes from postmortem frontal cortex tissue of non-AD controls, sporadic AD patients, and *PSEN1* E280A carriers, including the previously described case of a *PSEN1* E280A carrier who was homozygous for the protective *APOE3ch* variant.

A multimodal approach was used, including snRNA-seq, spatial transcriptomics to validate the findings of snRNA-seq *in situ*, and immunostaining on postmortem brain tissue for neuropathological characterization and validation of the transcriptomic results at the protein level. The sample included tissue from 27 donors: 8 non-AD control patients, 8 sporadic AD patients, 10 *PSEN1* E280A ADAD (including 3 heterozygous for the *APOE3ch* variant), and 1 ADAD protected patient *(PSEN1* E280A carrier homozygous for *APOE3ch*).

Astrocyte transcriptomic comparison between *PSEN1* E280A and SAD showed 186 upregulated and 53 downregulated genes in the ADAD group. According to GSEA, pathways related to autophagy, including macroautophagy, mitophagy, chaperone-mediated autophagy (CMA), and respiratory electron transport, were upregulated. CMA scores from the changes in mRNA levels revealed a significantly higher score in

PSEN1 E280A ADAD versus SAD cases. The overexpressed genes included HSP90AB1, HSPA9, EEF1A1, GABARAPL2, GABARAPL1, and mitochondrial-associated genes (VDAC1, TOMM20, TOMM7, ATP5F1A, ATP5F1B, and CHCHD2). Immunostaining confirmed a higher immunoreactivity to HSP90 and the chaperone PPIA in PSEN1 E280A astrocytes compared to SAD. Regarding neurons, inhibitory neurons expressing SST were reduced in both AD groups, whereas VIP/CALB2/PROX1 was reduced only in the SAD group, suggesting a selective vulnerability for the latter group. Excitatory and inhibitory neurons had significantly higher CMA scores in ADAD compared to SAD, and GSEA was significant for the upregulation of several molecular chaperones involved with protein folding, degradation, autophagy, cellular respiration, and MT3. Immunostaining confirmed a higher immunoreactivity to HSP90 and the chaperone PPIA in PSEN1 E280A neurons compared to SAD as well (Fig. 8).

When comparing the transcriptomic profile in the frontal cortex from the *APOE3ch* homozygous carrier versus typical *PSEN1* E280A astrocytes showed upregulation of genes involved in cholesterol and lipid synthesis (*CYP46A1*, *CYP2J2*, *CYP4V2*, *DEGS1*, *ACAA1*, and *PLCG1*), lipid metabolism (*ACAA1*, *ACAA2*, *ECHS1*, and *ELOVL2*), oxidoreductase-activity-related genes (*ERO1A*, *CYP2J2*, *DEGS1*, *CYP46A1*, and *CYP4V2*), and *LRP1*. Accordingly, immunostaining revealed a higher signal of LRP1 in astrocytes of the frontal cortex from *APOE3ch* homozygous carriers compared to typical *PSEN1* E280A. In neurons, an increased expression of *FKBP1B*, *PS35*, and downregulation of *PSEN1* and *FKBP5* were observed when comparing *APOE3ch* homozygous carriers to typical *PSEN1* E280A. Interestingly, the transcriptomic profile of astrocytes and neurons seen in the *APOC3ch* homozygotes didn't match the profile of the same brain cells in three heterozygotes for the *APOE3* Christchurch variant.

A distinctive transcriptomic signature for *PSEN1* E280A ADAD and sporadic AD was discovered, characterized by increased expression of autophagy and chaperone-related genes across different cell subpopulations, notably astrocytes and neurons. Further insights into the AD pathogenesis and genetic architecture came from the *APOE3ch* carrier transcriptome.

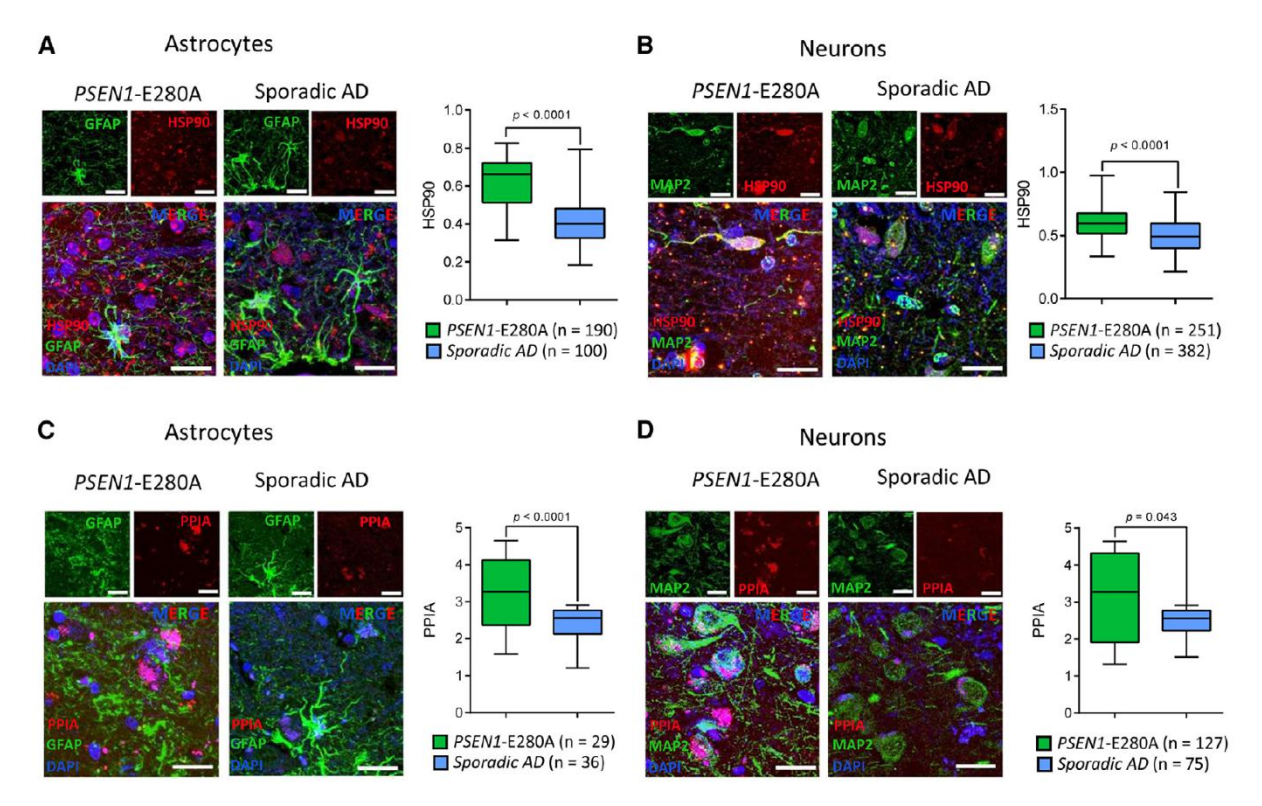


Figure 8| Protein immunoreactivity validates transcriptional alterations detected in the frontal cortex by snRNA-seq. A. Representative immunofluorescence micrographs of frontal cortex GFAP and HSP90 labeling from PSEN1-E280A and sporadic AD cases, as well as quantification of HSP90 expression in astrocytes. B. Representative immunofluorescence micrographs of frontal cortex MAP2 and HSP90 labeling from PSEN1-E280A and sporadic AD cases, as well as quantification of HSP90 expression in neurons. C. Representative immunofluorescence micrographs of frontal cortex GFAP and PPIA labeling from PSEN1-E280A and sporadic AD cases, as well as quantification of PPIA expression in astrocytes. D. Representative immunofluorescence micrographs of frontal cortex MAP2 and PPIA labeling from PSEN1-E280A and sporadic AD cases, as well as quantification of PPIA expression in astrocytes. Scale bars, 20 µm. n represents the number of cells analyzed in each group. The boxes represent the interquartile range, with the line inside indicating the median. Whiskers extend to the minimum and maximum values.

In this case, the frontal cortex showed a very low tau pathology burden, whereas the occipital cortex had a high burden. Accordingly, the expression of *LRP1*, a known mediator of tau pathology, was higher in the astrocytes of the frontal cortex when compared to the occipital, thus suggesting that active uptake of tau by astrocytes could alleviate the disease burden.

4. Discussion

The large kindred carrying the *PSEN1* E280A or "Paisa" mutation in Antioquia (Colombia) provides a unique opportunity to delve into all aspects of ADAD. With rare exceptions [28, 87, 96], Individuals within this kindred almost inexorably develop MCI in their forties (median age 44 years) and dementia by the end of the fifth decade (median age 49 years) [23]. This foreseeable trajectory and the aggressive clinical presentation give a priceless opportunity to determine early pathological changes (i.e., biomarker), systematically evaluate prevention strategies, and identify disease modifiers.

Two rare genetic modifiers granting protection to *PSEN1* E280A ADAD have been identified in this kindred: the *APOE3* R136S Christchurch variant (*APOE3ch*) and the *RELN* H3447R (*RELN-COLBOS*) variant. A female *PSEN1* E280A carrier, also homozygous for *APOE3ch*, remained asymptomatic until her 8th decade of life, nearly three decades later than other kindred members. The second case, a male *PSEN1* E280 carrier heterozygous for the *RELN-COLBOS* variant, also remained cognitively unimpaired until age 67, before developing dementia in his 8th decade of life [28, 87]. These instances of exceptional resilience highlight that AD is modifiable by genetic factors, even in the context of a strong autosomal dominant driver, and provide valuable insights into possible protective mechanisms against AD pathology.

As previously mentioned, both protected cases exhibited a significant delay in age of onset, with the *APOE3ch* homozygous carrier demonstrating the most outstanding resistance. In contrast, *APOE3ch* heterozygous carriers showed a less dramatic change in phenotype. While clinically relevant, the median delay for the onset of MCI increased only from 47 to 52 years, and the onset of dementia was postponed from 50 to 54 years, suggesting a possible dose-dependent effect of the hypermorphic *APOE3ch* mutation. Although direct comparison between the two described genetic modifiers is difficult in the absence of a larger sample, the resilience granted by the *RELN-COLBOS* variant heterozygosity appears to be a middle ground between the two *APOE3ch* zygosity status and to be driven by sex, as suggested by the less dramatic change of phenotype in the *RELN-COLBOS* carrier sister and the findings from the knock-in mouse model carrying the equivalent *RELN-COLBOS* variant. The

mouse model indicates a sexually dimorphic behavior of the mutation, a characteristic that has been described for *RELN* under physiological conditions [102, 103] and in the context of mental disease [104, 105], neurodevelopmental disorders [106], and neurodegeneration [107 - 109].

Interestingly, this protection exists despite a high amyloid burden in both protected cases, similar to or even more significant than that found in typical PSEN1 E280A cases, as determined by PiB-PET and confirmed through post-mortem assessments. This consistency among protected cases calls into question the amyloid hypothesis, challenges the notion of $A\beta$ as the primary driver of neurodegeneration in Alzheimer's disease, and suggests that molecular events downstream of amyloid deposition are pivotal for cognitive decline. It also raises concerns about the predominant focus on anti-amyloid therapy as the primary strategy for preventing and treating the disease [100, 101]. Instead, the protection of these individuals appears to be related to the modification in the spatial distribution of tau pathology, as evidenced by the sparing of tau deposition in the frontal cortex and the ERC of the APOE3ch carrier and the RELN-COLBOS carriers, respectively. Furthermore, the finding of lower tau pathology associated with a high neuronal density in the ERC of the RELN COLBOS compared to APOE3ch, ADAD, and SAD controls supports the idea that protection against tauopathy could translate into delayed neurodegeneration.

The difference in key protected areas across cases, alongside the significant tau burden in the occipital cortex of the *APOE3ch* homozygous, indicates that the mechanisms hindering tau accumulation are closely linked to regional variations within the cerebral cortex. These variations are recognized in the expressions of both *RELN* [110, 111] and *APOE* [112, 113], as well as in the activity of their protein products. Furthermore, additional factors, such as cerebral amyloid angiopathy (CAA), can shape the impact of genetic modifiers. CAA was less severe in the cerebral cortex of *APOE3ch* heterozygotes, particularly in the frontal cortex compared to non-carriers and restricted to the posterior circulation (occipital cortex, cerebellum) in the homozygous carrier of the same mutation. Both protected cases had age-related vascular comorbidities, suggesting that the genetic protection mechanisms effectively modify the disease even in the context of common age-related vascular changes.

The *APOE3ch* R136S variant is a rare missense mutation that involves the receptor-binding region of ApoE [85, 86], resulting in a reduced affinity for heparan sulfate proteoglycans (HSPGs) and APOE receptors compared to wild-type ApoE. HSPGs electrostatically interact with tau's microtubule-binding repeat (MTBR) regions and have a higher affinity for aggregated forms of the protein (i.e., oligomers and fibrils) [114-116]. This binding turns HSPGs into receptors/co-receptors that concentrate this pathological Tau species on the cell surface, facilitating their uptake by promoting endocytosis and mediating cell-to-cell spread [115, 117]. The reduced binding secondary to the *APOE3ch* variant could impair the HSPGs-mediated interaction with pathological Tau species, thus limiting the Tau pathology burden in carriers. On the other hand, *the APOE3ch*-encoded protein might be less efficient at binding to the vasculature, hence reducing the APOE-mediated sequestration of amyloid-β in the vessel wall, mitigating the microvascular damage and inflammation secondary to CAA. This would be consistent with the finding that *APOE3ch* carriers have a lower CAA pathology burden than non-carriers.

Besides modifying the binding site of the encoded protein, the APOE3ch variant modulates intracellular signaling pathways relevant in AD, notably the Wnt/β-catenin pathway [94, 118]. As previously discussed, isogenic organoid models showed that introducing the Christchurch variant elicits the upregulation of the Wnt/β-catenin and cadherin signaling pathways, suggesting an enhancement of pro-survival Wnt signaling [97]. APOE3ch seems to be a "gain of function" mutation, boosting Wnt3a signaling activity compared to wild-type *ApoEε3*. This hypermorphic mutation would sustain Wnt activity, providing a plausible mechanism for the documented increase in β-catenin levels in the frontal cortex of the *APOE3ch* homozygote carrier. Moreover, this novel property suggests that APOE3ch can promote pathways related to neuronal development, synaptic maintenance, and protection against tau pathology via GSK3β inhibition, a major kinase responsible for tau phosphorylation [119]. While it might appear contradictory, the simultaneous downregulation of specific Wnt ligand transcripts (Wnt2b, Wnt4, Wnt7b) observed in the organoids may indicate a compensatory feedback mechanism triggered by the sustained activation of the pathway by APOE3ch.

Another significant discovery is the upregulation of the Low-Density Lipoprotein Receptor-Related Protein 1 (LRP1) in regions shielded from Tau pathology, specifically the frontal cortex of the APOE3ch homozygote. LRP1 is a key APOE receptor facilitating tau uptake in neurons and astrocytes [120]. In the context of protection against ADAD pathology, higher levels of LRP1 in astrocytes, as documented by snRNAseq and immunofluorescence for the Christchurch homozygote carrier, could enhance the uptake and clearance of pathological tau by glial cells, thus averting its dissemination and accumulation in the neuronal compartment. This astrocyte-LRP1 protection mechanism would complement the activation of the Wnt pathway. While the activation of Wnt/ β -catenin signaling pathway promotes cellular resilience and regeneration, enhanced astrocytic clearance removes toxic proteins, leading to neuroprotection.

In summary, the *APOE3ch* variant protects against ADAD pathology through several mechanisms: Acting as an enhancer of the Wnt/ β -catenin signaling pathway, which might help resist degeneration, changing the affinity of the binding region of APOE, reducing APOE-mediated sequestration of amyloid- β in the vessel wall, and possibly facilitating astrocytic tau clearance. These mechanisms suggest that the mutation induces a shift toward a less permissive environment for AD pathology.

In addition to the *APOE3ch* variant, the *RELN-COLBOS* variant provides a new venue to explore Alzheimer's disease pathology and a possible protective mechanism. Reelin, encoded by the *RELN* gene located on chromosome 7q22 [121], is an extracellular matrix glycoprotein that participates in multiple biological functions [122], including neuronal migration, cortical layering, and the development of dendrites and spines in neurons [123, 124]. It interacts with the LDL receptor family members VLDLR and LRP8 (also called ApoER2) [125, 126], two key receptors in the APOE signaling pathway. When Reelin binds to its receptor, it initiates the phosphorylation and activation of the intracellular adaptor protein Dab1, which plays a crucial role in central cellular pathways that affect cytoskeletal stability and modification, synaptic plasticity, cell survival, neurite outgrowth, and neuronal migration [122 - 126]. The activation of Dab1 also inhibits Glycogen Synthase Kinase 3 beta (GSK3 β), which is particularly significant in the context of AD, as GSK3 β is one of the primary kinases that

phosphorylate Tau at various sites, including those associated with pathological hyperphosphorylation [127 - 129].

Findings from the mouse model indicate the RELN-COLBOS variant to be a hypermorphic mutation, increasing Reelin signaling and enhancing Dab1 activation, subsequently reducing Tau phosphorylation. This finding correlates with the extremely low density of Tau pathology found in the entorhinal cortex and dentate gyrus of RELN-COLBOS, given the high level of RELN expression in these areas [130, 131] as well as the markedly lower tau burden in other Reelin-rich areas. On the other hand, the extensive accumulation of amyloid throughout the brain indicates that the protective benefits of activating the Reelin pathway do not stop amyloid pathology. Instead, it may influence how amyloid interacts with tau. This is similar to what was observed with the APOE3ch variant and strengthens the idea that neurodegeneration driven by tau, not amyloid itself, serves as the mechanism through which these genetic factors modify Alzheimer's disease. Additionally, the RELN-COLBOS variant increases the affinity of Reelin for its co-receptor Neuropilin-1 (NRP1) as well as the affinity of the Reelin Cterminal domain for the glycosaminoglycan heparin. This increased affinity for heparin could increase the local concentration of Reelin in the vicinity of the cell membrane or facilitate its interaction with co-receptors like NRP1, enhancing Reelin's downstream signaling pathway. Interestingly, this would contrast with the observation of potential protection through reduced binding affinity to HSPGs seen in the APOE3ch variant.

Overall, the data suggest that Reelin and the Reelin/Dab1 cascade play key roles in moderating Alzheimer's disease pathology. By enhancing the activation of Reelin's signaling pathway, the *RELN-COLBOS* variant may protect synapses and neurons from the harmful effects associated with tauopathy. This finding aligns with previous research in animal models demonstrating that Reelin fosters dendritic spine development [135] and counters the toxic effects of phosphorylated tau [139]. Increased Reelin expression in neurons is associated with increased synaptic connections in the hippocampus [132, 133]. It can prevent the suppression of long-term potentiation caused by $A\beta$ and improve cognitive performance in long-term memory tasks [91]. On the other hand, decreased or dysfunctional Reelin expression has been linked to cognitive decline [134], synaptic loss, and greater impairments in

synaptic plasticity, learning, and memory in response to amyloid β accumulation [136, 137], as well as heightened tau hyperphosphorylation [88, 138].

The APOE3ch and RELN-COLBOS variants act as genetic modifiers, showing convergent phenotypes but divergent mechanisms. Their associated Aß burden resembles that seen in typical PSEN1 E280A carriers. Both variants offer cognitive protection by curbing tau-driven neurodegeneration and enhancing neuronal health. Additionally, APOE and Reelin signal via shared receptors (VLDL, LRP8). However, the intracellular mechanisms differ; APOE3ch features increased Wnt/β-catenin activity and decreased HSPG affinity, while RELN-COLBOS functions as a hypermorphic mutation, boosting Reelin signaling due to heightened affinity for GAGs and co-receptors. This indicates that disease modification can be achieved either by inhibiting a pathway, such as decreasing APOE-related buildup of harmful aggregates as suggested for the variations in CAA pathology, or by enhancing it, for example, through Dab1-mediated reduction of tau hyperphosphorylation. Investigating potential convergence points between these pathways, particularly involving tau kinases like GSK3β or Dab1-regulated phosphatases, remains a vital area for future research, opening the possibility for developing disease-modifying drugs. Irrespective of the specific molecular pathway involved, the finding in both cases highlights the importance of developing drugs that modify tau pathology as a strategy for preventing or treating AD. The prospect of severing the build-up of amyloid pathology from the spreading of pathological species of tau and neurodegeneration, as seen in both cases, either by targeting tau or enhancing mechanisms for its clearance, proffers an appealing therapeutic potential. It should be noted that APOE is widely expressed in the brain in relatively high amounts, while Reelin is expressed locally in specific brain structures during adulthood. This physiological difference can explain, at least partially, the protective phenotypes observed in the patients.

The revealed molecular pathways offer interesting targets for the development of treatment strategies. For example, based on the findings from the *APOE3ch* variant, therapeutic strategies could be developed to mimic the reduced binding affinity of HSPG to limit tau propagation, activate the Wnt/ β -catenin signaling pathway, or enhance tau uptake by astrocytes through the LRP1 receptor. From the *RELN*-

COLBOS, developing LRP8 or VLDL receptor agonist to enhance Dab1 activity could be promising. For instance, antisense oligonucleotides (ASO) therapy targeting ApoER2 has been shown to improve synaptic function, learning, and memory in an AD mouse model. Interestingly, the ASO treatment seemed to be more beneficial to males than females [140]. However, the variations in molecular signatures between *PSEN1* E280A ADAD cases and sporadic AD, especially concerning autophagy, chaperones, and microglial activation, must be considered to develop prevention or therapeutic strategies. The application of prevention or treatment methods from ADAD studies to the broader AD population may pose challenges if the differences in their molecular profiles are pronounced. Adopting a precision medicine strategy might necessitate a classification based on the etiology of AD (ADAD vs AD) or the use of biomedical markers to develop pathway-driven treatments.

Finally, while an in-depth characterization of large kindred, such as the Colombian, offers valuable context and additional information from heterozygous carriers of the *APOE3ch* variant, provides further support, drawing conclusions from single cases requires forethought. The validation of findings *in vitro* and *in vivo* also has limitations. iPSC-derived organoids mainly simulate early developmental processes and do not capture the complexities of an aging brain; mouse models may not accurately reflect the human-specific aspects of AD pathology. Furthermore, conducting post-mortem analyses on cases of end-stage disease presents challenges, as transcriptomic and proteomic changes may indicate secondary effects rather than primary mechanisms, and do not fully represent the dynamic process occurring early in the disease or the protective trajectory. In addition to the potential limitations of insights into AD pathology from the exceptional cases, we must consider whether the effects of lifelong genetic variants can be replicated by interventions initiated later in life. The *APOE3ch* and *RELN-COLBOS* mutations exist from conception, thereby affecting brain development, and the noted protective effect may stem from these developmental adaptations.

5. Conclusions

Characterizing the protected *APOE3ch* and *RELN-COLBOS* carrier cases and their genetic underpinnings has profound implications for our understanding of AD pathogenesis. They give compelling evidence that AD progression is not an immutable fate exclusively bound to amyloid β misfolding and deposition. Instead, progression results from highly dynamic crosstalk between starting factors (*PSEN1* mutation), downstream effectors (tau), modulatory pathways (APOE, Reelin), glial response, and vascular health. In the absence of a "theory of everything" to explain AD, it could be proposed that even if $A\beta$ "sets the fire", tau and other mediators are required to spread the flames. This highlights the possibility of genetic resilience in Alzheimer's disease.

A striking finding from the cases is the discrepancy between amyloid burden and clinical impairment, emphasizing the role of tau pathology in neurodegeneration and cognitive decline in the context of AD, and the relevance of targeted tau therapy, as well as combination strategies addressing both Aβ and tau. The multimodal approach used to characterize the cases, epidemiological studies, advanced structural and functional neuroimaging, neuropathological assessment, multiomics approaches (i.e., snRNAseq), and experimental models allowed a comprehensive insight into the genetic modifiers and their mechanisms. This collaborative model allows a feedback loop between human observational research and *in vivo/in vitro* mechanistic studies, offering a solid framework to address complex neurodegenerative diseases such as AD.

From a therapeutic perspective, identifying protective mechanisms linked to enhanced Wnt signaling (APOEch) and regulated Reelin pathways (RELN-COLBOS) indicates new, validated targets in humans. This encourages a reevaluation of therapeutic approaches to strengthen the brain's inherent protective systems against neurodegeneration beyond anti-amyloid therapy. Regarding clinical trials, these insights highlight the importance of considering the genetic background of the population to be treated. Unidentified protective variants may skew trial outcomes, obscuring actual treatment effectiveness. Individuals with unrecognized protective genotypes could bias the interpretation of the results, as a slowing decline in cognitive

impairment could be a mere reflection of inherently resilient participants. Consequently, future trial designs for ADAD, and potentially sporadic AD, should account for protective allele status as stratification criteria, conduct subgroup analyses based on pathway activations, or selectively include or exclude individuals with extreme phenotypes (resilience or rapid progression) to enhance understanding.

Regarding public health and genetic counseling for families carrying ADAD-related mutations, the formerly grim perspective linked to possessing a deterministic mutation is now more complex due to the emergence of potential resilience factors. Genetic counselors may soon include tests for known protective alleles, which could enhance prognosis accuracy, facilitate personalized monitoring, and inspire discussions about polygenic effects even in monogenic disorders. In basic science, these insights are set to foster further research into the complex relationships among vascular biology, lipid metabolism (with APOE at its core), developmental neuroscience (where Reelin plays a role), and neurodegeneration. The significant influence of *APOE* and *RELN* variants emphasizes that AD is not just about plaques and tangles; it is also profoundly influenced by systemic and developmental factors.

Critical limitations and important mechanistic questions should be addressed in future research. The limited number of subjects carrying protective variants requires careful consideration regarding the generalization of these findings. What is the exact mechanism by which the *APO3ch* mutation enhances Wnt3a signaling? What local factors explain the differences in protection or vulnerability observed across cortical regions between the *APOC3ch* and RELN-COLBOS carriers? How does increased affinity for GAG enhance Dab1 phosphorylation? Is there a downstream crosstalk between the ApoE and Reelin pathways?

Finally, linking the knowledge gained from ADAD protection to sporadic AD is crucial, as ADAD is still considered a model for AD in general. Future studies should emphasize comparative multi-omics research involving various ADAD-causing mutations and large sporadic AD cohorts. This effort is vital to identify shared pathogenic pathways, which can be targeted therapeutically, instead of mechanisms

unique to specific diseases. This comprehension is essential for creating more effective, biologically based, and potentially stratified clinical trials.

6. Bibliography

- 1. Levey, A. I. (2021). Progress with Treatments for Alzheimer's Disease. New England Journal of Medicine, 384(18), 1762–1763. https://doi.org/10.1056/NEJMe2103722.
- 2. 2020 Alzheimer's disease facts and figures. (2020). Alzheimer's & Dementia, 16(3),391–460.
- 3. Michalowsky, B., Flessa, S., Hertel, J., Goetz, O., Hoffmann, W., Teipel, S., & Kilimann, I. (2017). Cost of diagnosing dementia in a German memory clinic. Alzheimer's Research & Therapy, 9(1), 65.
- 4. Chow, V. W., Mattson, M. P., Wong, P. C., & Gleichmann, M. (2010). An Overview of APP Processing Enzymes and Products. Neuromolecular Medicine, 12(1), 1–12.
- 5. Alzheimer's Association. 2017 Alzheimer's Disease Facts and Figures. Alzheimer's Dement 2017;13:325-373.
- 6. Sepulveda-Falla, D., Barrera-Ocampo, A., Hagel, C., Korwitz, A., Vinueza-Veloz, M. F., Zhou, K., ... Glatzel, M. (2014). Familial Alzheimer's disease-associated presenilin-1 alters cerebellar activity and calcium homeostasis. The Journal of Clinical Investigation, 124(4), 1552–1567.
- 7. Zhang, X., Li, Y., Xu, H., & Zhang, Y. (2014). The γ-secretase complex: from structure to function. Frontiers in Cellular Neuroscience, 8, 427.
- 8. De Strooper, B., Iwatsubo, T., & Wolfe, M. S. (2012). Presenilins and γ-Secretase: Structure, Function, and Role in Alzheimer Disease. Cold Spring Harbor Perspectives in Medicine, 2(1), a006304.
- 9. Jurisch-Yaksi, N., Sannerud, R. and Annaert, W. (2013) A fast-growing spectrum of biological functions of gamma-secretase in development and disease. Biochim Biophys Acta, 1828, 2815-2827
- 10. Camandola, S. and Mattson, M.P. (2011) Aberrant subcellular neuronal calcium regulation in aging and Alzheimer's disease. Biochim Biophys Acta, 1813, 965-973.
- 11. Porsteinsson, A. P., Isaacson, R. S., Knox, S., Sabbagh, M. N., & Rubino, I. (2021). Diagnosis of Early Alzheimer's Disease: Clinical Practice in 2021. The Journal of Prevention of Alzheimer's Disease. https://doi.org/10.14283/jpad.2021.23.
- 12. Jack, C. R. J., Bennett, D. A., Blennow, K., Carrillo, M. C., Dunn, B., Haeberlein, S. B., Holtzman, D. M., Jagust, W., Jessen, F., Karlawish, J., Liu, E., Molinuevo, J. L., Montine, T., Phelps, C., Rankin, K. P., Rowe, C. C., Scheltens, P., Siemers, E., Snyder, H. M., & Sperling, R. (2018). NIA-AA Research Framework: Toward a biological definition

- of Alzheimer's disease. Alzheimer's & Dementia: The Journal of the Alzheimer's Association, 14(4), 535–562.
- 13. Corder, E. H., Saunders, A. M., Strittmatter, W. J., Schmechel, D. E., Gaskell, P. C., Small, G. W., Roses, A. D., Haines, J. L., & Pericak-Vance, M. A. (1993). Gene dose of apolipoprotein E type 4 allele and the risk of Alzheimer's disease in late onset families. Science (New York, N.Y.), 261(5123), 921–923. https://doi.org/10.1126/science.8346443.
- 14. Ballard, C., Gauthier, S., Corbett, A., Brayne, C., Aarsland, D., & Jones, E. (2011). Alzheimer's disease. The Lancet, 377(9770), 1019–1031.
- 15. Lilford, P., & Hughes, J. C. (2018). Biomarkers and the diagnosis of preclinical dementia. BJPsych Advances, 24(6), 422–430. https://doi.org/DOI: 10.1192/bja.2018.28.
- 16. Shah, H., Albanese, E., Duggan, C., Rudan, I., Langa, K. M., Carrillo, M. C., Chan, K. Y., Joanette, Y., Prince, M., Rossor, M., Saxena, S., Snyder, H. M., Sperling, R., Varghese, M., Wang, H., Wortmann, M., & Dua, T. (2016). Research priorities to reduce the global burden of dementia by 2025. The Lancet Neurology, 15(12), 1285–1294.
- 17. Robinson, M., Lee, B. Y., & Hane, F. T. (2017). Recent Progress in Alzheimer's Disease Research, Part 2: Genetics and Epidemiology. Journal of Alzheimer's Disease: JAD, 57(2), 317–330.
- 18. Hane, F. T., Lee, B. Y., & Leonenko, Z. (2017). Recent Progress in Alzheimer's Disease Research, Part 1: Pathology. Journal of Alzheimer's Disease: JAD, 57(1), 1–28.
- 19. https://www.alzforum.org/mutations/psen-1/. Consulted on April 2025.
- 20. Hardy, J., & Selkoe, D. J. (2002). The Amyloid Hypothesis of Alzheimer's Disease: Progress and Problems on the Road to Therapeutics. Science, 297(5580), 353 LP 356.
- 21. Clark, R. F., Hutton, M., Fuldner, M., Froelich, S., Karran, E., Talbot, C., Crook, R., Lendon, C., Prihar, G., He, C., Korenblat, K., Martinez, A., Wragg, M., Busfield, F., Behrens, M. I., Myers, A., Norton, J., Morris, J., Mehta, N., . . . Goate, A. (1995). The structure of the presenilin 1 (S182) gene and identification of six novel mutations in early onset AD families. Nature Genetics, 11(2), 219-222. https://doi.org/10.1038/ng1095-219
- 22. Sepulveda-Falla, D., Glatzel, M., & Lopera, F. (2012). Phenotypic profile of early-onset familial Alzheimer's disease caused by presenilin-1 E280A mutation. Journal of Alzheimer's Disease: JAD, 32(1), 1–12. https://doi.org/10.3233/JAD-2012-120907.
- 23. Acosta-Baena, N., Sepulveda-Falla, D., Lopera-Gómez, C. M., Jaramillo-Elorza, M. C., Moreno, S., Aguirre-Acevedo, D. C., Saldarriaga, A., & Lopera, F. (2011). Predementia clinical stages in presenilin 1 E280A familial early-onset Alzheimer's disease: a

- retrospective cohort study. The Lancet. Neurology, 10(3), 213–220. https://doi.org/10.1016/S1474-4422(10)70323-9.
- 24. Lopera, F., Ardilla, A., Martínez, A., Madrigal, L., Arango-Viana, J. C., Lemere, C. A., Arango-Lasprilla, J. C., Hincapíe, L., Arcos-Burgos, M., Ossa, J. E., Behrens, I. M., Norton, J., Lendon, C., Goate, A. M., Ruiz-Linares, A., Rosselli, M., & Kosik, K. S. (1997). Clinical features of early-onset Alzheimer disease in a large kindred with an E280A presenilin-1 mutation. JAMA, 277(10), 793–799.
- 25. Vélez, J. I., Chandrasekharappa, S. C., Henao, E., Martinez, A. F., Harper, U., Jones, M., Solomon, B. D., Lopez, L., Garcia, G., Aguirre-Acevedo, D. C., Acosta-Baena, N., Correa, J. C., Lopera-Gómez, C. M., Jaramillo-Elorza, M. C., Rivera, D., Kosik, K. S., Schork, N. J., Swanson, J. M., Lopera, F., & Arcos-Burgos, M. (2013). Pooling/bootstrap-based GWAS (pbGWAS) identifies new loci modifying the age of onset in PSEN1 p.Glu280Ala Alzheimer's disease. Molecular Psychiatry, 18(5), 568–575. https://doi.org/10.1038/mp.2012.81.
- 26. Vélez, J. I., Rivera, D., Mastronardi, C. A., Patel, H. R., Tobón, C., Villegas, A., Cai, Y., Easteal, S., Lopera, F., & Arcos-Burgos, M. (2016). A Mutation in DAOA Modifies the Age of Onset in PSEN1 E280A Alzheimer's Disease. Neural Plasticity, 2016, 9760314. https://doi.org/10.1155/2016/9760314.
- 27. Vélez, J. I., Lopera, F., Sepulveda-Falla, D., Patel, H. R., Johar, A. S., Chuah, A., Tobón, C., Rivera, D., Villegas, A., Cai, Y., Peng, K., Arkell, R., Castellanos, F. X., Andrews, S. J., Silva Lara, M. F., Creagh, P. K., Easteal, S., de Leon, J., Wong, M. L., ... Arcos-Burgos, M. (2016). APOE*E2 allele delays age of onset in PSEN1 E280A Alzheimer's disease. Molecular Psychiatry, 21(7), 916–924. https://doi.org/10.1038/mp.2015.177.
- 28. Arboleda-Velasquez, J. F., Lopera, F., O'Hare, M., Delgado-Tirado, S., Marino, C., Chmielewska, N., Saez-Torres, K. L., Amarnani, D., Schultz, A. P., Sperling, R. A., Leyton-Cifuentes, D., Chen, K., Baena, A., Aguillon, D., Rios-Romenets, S., Giraldo, M., Guzmán-Vélez, E., Norton, D. J., Pardilla-Delgado, E., ... Quiroz, Y. T. (2019). Resistance to autosomal dominant Alzheimer's disease in an APOE3 Christchurch homozygote: a case report. Nature Medicine, 25(11), 1680–1683. https://doi.org/10.1038/s41591-019-0611-3.
- 29. Oddo, S., Caccamo, A., Shepherd, J.D., Murphy, M.P., Golde, T.E., Kayed, R... and LaFerla, F.M. (2003) Triple-transgenic model of Alzheimer's disease with plaques and tangles: intracellular Abeta and synaptic dysfunction. Neuron, 39, 409-421.
- 30. O'Brien, R. J., & Wong, P. C. (2011). Amyloid precursor protein processing and Alzheimer's disease. Annual Review of Neuroscience, 34, 185–204. https://doi.org/10.1146/annurev-neuro-061010-113613.

- 31. Bayer, T. A., Cappai, R., Masters, C. L., Beyreuther, K., & Multhaup, G. (1999). It all sticks together--the APP-related family of proteins and Alzheimer's disease. Molecular Psychiatry, 4(6), 524–528. https://doi.org/10.1038/sj.mp.4000552
- 32. Koo, E. H., Sisodia, S. S., Archer, D. R., Martin, L. J., Weidemann, A., Beyreuther, K., Fischer, P., Masters, C. L., & Price, D. L. (1990). Precursor of amyloid protein in Alzheimer's disease undergoes fast anterograde axonal transport. Proceedings of the National Academy of Sciences of the United States of America, 87(4), 1561–1565. https://doi.org/10.1073/pnas.87.4.1561.
- 33. Koo, E. H., & Squazzo, S. L. (1994). Evidence that production and release of amyloid beta-protein involves the endocytic pathway. The Journal of Biological Chemistry, 269(26), 17386–17389.
- 34. Meziane, H., Dodart, J. C., Mathis, C., Little, S., Clemens, J., Paul, S. M., & Ungerer, A. (1998). Memory-enhancing effects of secreted forms of the beta-amyloid precursor protein in normal and amnestic mice. Proceedings of the National Academy of Sciences of the United States of America, 95(21), 12683–12688. https://doi.org/10.1073/pnas.95.21.12683
- 35. Jorissen, E., Prox, J., Bernreuther, C., Weber, S., Schwanbeck, R., Serneels, L., Snellinx, A., Craessaerts, K., Thathiah, A., Tesseur, I., Bartsch, U., Weskamp, G., Blobel, C. P., Glatzel, M., De Strooper, B., & Saftig, P. (2010). The disintegrin/metalloproteinase ADAM10 is essential for the establishment of the brain cortex. The Journal of Neuroscience: The Official Journal of the Society for Neuroscience, 30(14), 4833–4844. https://doi.org/10.1523/JNEUROSCI.5221-09.2010
- 36. Asai, M., Hattori, C., Szabó, B., Sasagawa, N., Maruyama, K., Tanuma, S., & Ishiura, S. (2003). Putative function of ADAM9, ADAM10, and ADAM17 as APP alphasecretase. Biochemical and Biophysical Research Communications, 301(1), 231–235. https://doi.org/10.1016/s0006-291x(02)02999-6
- 37. Wolfe, M. S. (2009). Intramembrane-cleaving proteases. The Journal of Biological Chemistry, 284(21), 13969–13973. https://doi.org/10.1074/jbc.R800039200.
- 38. Li, S., Zhang, W., & Han, W. (2017). Initial Substrate Binding of γ-Secretase: The Role of Substrate Flexibility. ACS Chemical Neuroscience, 8(6), 1279–1290. https://doi.org/10.1021/acschemneuro.6b00425.
- 39. Yan, Y., Xu, T.-H., Melcher, K., & Xu, H. E. (2017). Defining the minimum substrate and charge recognition model of gamma-secretase. Acta Pharmacologica Sinica, 38(10), 1412–1424. https://doi.org/10.1038/aps.2017.35.

- 40. Annaert, W., & De Strooper, B. (2002). A cell biological perspective on Alzheimer's disease. Annual Review of Cell and Developmental Biology, 18, 25–51. https://doi.org/10.1146/annurev.cellbio.18.020402.142302 Li, S., Zhang, W., & Han, W. (2017). Initial Substrate Binding of γ-Secretase: The Role of Substrate
- 41. Güner, G., & Lichtenthaler, S. F. (2020). The substrate repertoire of γ-secretase/presenilin. Seminars in Cell & Developmental Biology, 105, 27–42. https://doi.org/https://doi.org/10.1016/j.semcdb.2020.05.019
- 42. Okochi, M., Steiner, H., Fukumori, A., Tanii, H., Tomita, T., Tanaka, T., Iwatsubo, T., Kudo, T., Takeda, M., & Haass, C. (2002). Presenilins mediate a dual intramembranous gamma-secretase cleavage of Notch-1. The EMBO Journal, 21(20), 5408–5416. https://doi.org/10.1093/emboj/cdf541
- 43. Hardy, J. A., & Higgins, G. A. (1992). Alzheimer's disease: the amyloid cascade hypothesis. Science, 256(5054), 184 LP 185. https://doi.org/10.1126/science.1566067.
- 44. Phillips, J. C. (2019). Why A□42 Is Much More Toxic than A□40. ACS Chemical Neuroscience, 10(6), 2843–2847. https://doi.org/10.1021/acschemneuro.9b00068.
- 45. De Strooper, B., & Annaert, W. (2010). Novel research horizons for presenilins and γ-secretases in cell biology and disease. Annual Review of Cell and Developmental Biology, 26, 235–260. https://doi.org/10.1146/annurev-cellbio-100109-104117.
- 46. De Strooper, B., Beullens, M., Contreras, B., Levesque, L., Craessaerts, K., Cordell, B., Moechars, D., Bollen, M., Fraser, P., George-Hyslop, P. S., & Van Leuven, F. (1997). Phosphorylation, subcellular localization, and membrane orientation of the Alzheimer's disease-associated presenilins. The Journal of Biological Chemistry, 272(6), 3590–3598. https://doi.org/10.1074/jbc.272.6.3590.
- 47. Saura, C. A., Choi, S.-Y., Beglopoulos, V., Malkani, S., Zhang, D., Shankaranarayana Rao, B. S., Chattarji, S., Kelleher, R. J. 3rd, Kandel, E. R., Duff, K., Kirkwood, A., & Shen, J. (2004). Loss of presenilin function causes impairments of memory and synaptic plasticity followed by age-dependent neurodegeneration. Neuron, 42(1), 23–36. https://doi.org/10.1016/s0896-6273(04)00182-5.
- 48. Cai, Y., A An, S. S., & Kim, S. (2015). Mutations in presentilin 2 and its implications in Alzheimer's disease and other dementia-associated disorders. Clinical Interventions in Aging, 10, 1163-1172. https://doi.org/10.2147/CIA.S85808
- 49. Li Y, Lu SH, Tsai CJ, Bohm C, Qamar S, Dodd RB, Meadows W, Jeon A, McLeod A, Chen F, Arimon M, Berezovska O, Hyman BT, Tomita T, Iwatsubo T, Johnson CM, Farrer LA, Schmitt-Ulms G, Fraser PE, St George-Hyslop PH. Structural interactions between inhibitor and substrate docking sites give insight into mechanisms of human PS1

- complexes. Structure. 2014 Jan 7;22(1):125-35. doi: 10.1016/j.str.2013.09.018. Epub 2013 Nov 7. PMID: 24210759; PMCID: PMC3887256
- 50. Ahn, K., Shelton, C. C., Tian, Y., Zhang, X., Gilchrist, M. L., Sisodia, S. S., & Li, Y. (2010). Activation and intrinsic γ-secretase activity of presenilin 1. Proceedings of the National Academy of Sciences, 107(50), 21435-21440.https://doi.org/10.1073/pnas.1013246107
- 51. Edbauer, D., Winkler, E., Regula, J. T., Pesold, B., Steiner, H., & Haass, C. (2003). Reconstitution of gamma-secretase activity. Nature Cell Biology, 5(5), 486–488. https://doi.org/10.1038/ncb960.
- 52. Fraser, P. E., Yang, D. S., Yu, G., Lévesque, L., Nishimura, M., Arawaka, S., Serpell, L. C., Rogaeva, E., & St George-Hyslop, P. (2000). Presenilin structure, function and role in Alzheimer's disease. Biochimica et Biophysica Acta, 1502(1), 1–15. https://doi.org/10.1016/s0925-4439(00)00028-4
- 53. Ray, W. J., Yao, M., Nowotny, P., Mumm, J., Zhang, W., Wu, J. Y., Kopan, R., & Goate, A. M. (1999). Evidence for a physical interaction between presentlin and Notch. Proceedings of the National Academy of Sciences, 96(6), 3263-3268. https://doi.org/10.1073/pnas.96.6.3263.
- 54. De Strooper, B. (2003). Aph-1, Pen-2, and Nicastrin with Presenilin generate an active gamma-Secretase complex. Neuron, 38(1), 9–12. https://doi.org/10.1016/s0896-6273(03)00205-8.
- 55. Kosik, K. S., Muñoz, C., Lopez, L., Arcila, M. L., García, G., Madrigal, L., Moreno, S., Romenets, S. R., Lopez, H., Gutierrez, M., Langbaum, J. B., Cho, W., Suliman, S., Tariot, P. N., Ho, C., Reiman, E. M., & Lopera, F. (2014). Homozygosity of the autosomal dominant Alzheimer disease presenilin 1 E280A mutation. Neurology, 84(2), 206-208. https://doi.org/10.1212/WNL.0000000000001130
- 56. Lee, G., Neve, R. L., & Kosik, K. S. (1989). The microtubule binding domain of tau protein. Neuron, 2(6), 1615–1624. https://doi.org/10.1016/0896-6273(89)90050-0.
- 57. Drechsel, D. N., Hyman, A. A., Cobb, M. H., & Kirschner, M. W. (1992). Modulation of the dynamic instability of tubulin assembly by the microtubule-associated protein tau. Molecular Biology of the Cell, 3(10), 1141–1154. https://doi.org/10.1091/mbc.3.10.1141.
- 58. Amos, L. A. (2004). Microtubule structure and its stabilisation. Organic & Biomolecular Chemistry, 2(15), 2153–2160. https://doi.org/10.1039/b403634d.
- 59. Guo, T., Noble, W., & Hanger, D. P. (2017). Roles of tau protein in health and disease. Acta Neuropathologica, 133(5), 665–704. https://doi.org/10.1007/s00401-017-1707-9.

- 60. Clavaguera, F., Bolmont, T., Crowther, R. A., Abramowski, D., Frank, S., Probst, A., Fraser, G., Stalder, A. K., Beibel, M., Staufenbiel, M., Jucker, M., Goedert, M., & Tolnay, M. (2009). Transmission and spreading of tauopathy in transgenic mouse brain. Nature Cell Biology, 11(7), 909–913. https://doi.org/10.1038/ncb1901.
- 61. Shim, Y. S., & Morris, J. C. (2011). Biomarkers predicting Alzheimer's disease in cognitively normal aging. Journal of Clinical Neurology (Seoul, Korea), 7(2), 60–68. https://doi.org/10.3988/jcn.2011.7.2.60.
- 62. Goate A, Chartier-Harlin MC, Mullan M, Brown J, Crawford F, Fidani L, Giuffra L, Haynes A, Irving N, James L, et al. Segregation of a missense mutation in the amyloid precursor protein gene with familial Alzheimer's disease. Nature. 1991 Feb 21;349(6311):704-6. doi: 10.1038/349704a0. PMID: 1671712.
- 63. Sherrington R, Rogaev EI, Liang Y, Rogaeva EA, Levesque G, Ikeda M, Chi H, Lin C, Li G, Holman K, Tsuda T, Mar L, Foncin JF, Bruni AC, Montesi MP, Sorbi S, Rainero I, Pinessi L, Nee L, Chumakov I, Pollen D, Brookes A, Sanseau P, Polinsky RJ, Wasco W, Da Silva HA, Haines JL, Perkicak-Vance MA, Tanzi RE, Roses AD, Fraser PE, Rommens JM, St George-Hyslop PH. Cloning of a gene bearing missense mutations in early-onset familial Alzheimer's disease. Nature. 1995 Jun 29;375(6534):754-60. doi: 10.1038/375754a0. PMID: 7596406.
- 64. Levy-Lahad E, Wasco W, Poorkaj P, Romano DM, Oshima J, Pettingell WH, Yu CE, Jondro PD, Schmidt SD, Wang K, et al. Candidate gene for the chromosome 1 familial Alzheimer's disease locus. Science. 1995 Aug 18;269(5226):973-7. doi: 10.1126/science.7638622. PMID: 7638622.
- 65. Bateman RJ, Aisen PS, De Strooper B, Fox NC, Lemere CA, Ringman JM, Salloway S, Sperling RA, Windisch M, Xiong C. Autosomal-dominant Alzheimer's disease: a review and proposal for the prevention of Alzheimer's disease. Alzheimers Res Ther. 2011 Jan 6;3(1):1. doi: 10.1186/alzrt59. PMID: 21211070; PMCID: PMC3109410.
- Zhang W, Xu C, Sun J, Shen HM, Wang J, Yang C. Impairment of the autophagy-66. lysosomal pathway in Alzheimer's diseases: Pathogenic mechanisms and therapeutic potential. Acta Pharm Sin B. 2022 Mar;12(3):1019-1040. doi: PMCID: 10.1016/j.apsb.2022.01.008. Epub 2022 Jan 21. PMID: 35530153: PMC9069408.
- 67. Limone A, Veneruso I, D'Argenio V, Sarnataro D. Endosomal trafficking and related genetic underpinnings as a hub in Alzheimer's disease. J Cell Physiol. 2022 Oct;237(10):3803-3815. doi: 10.1002/jcp.30864. Epub 2022 Aug 22. PMID: 35994714; PMCID: PMC9804649.

- 68. Small SA, Simoes-Spassov S, Mayeux R, Petsko GA. Endosomal Traffic Jams Represent a Pathogenic Hub and Therapeutic Target in Alzheimer's Disease. Trends Neurosci. 2017 Oct;40(10):592-602. doi: 10.1016/j.tins.2017.08.003. PMID: 28962801; PMCID: PMC5654621.
- 69. Selkoe DJ. Alzheimer's disease is a synaptic failure. Science. 2002 Oct 25;298(5594):789-91. doi: 10.1126/science.1074069. PMID: 12399581.
- 70. Nadeau JH. Modifier genes in mice and humans. Nat Rev Genet. 2001 Mar;2(3):165-74. doi: 10.1038/35056009. PMID: 11256068.
- 71. Ryman DC, Acosta-Baena N, Aisen PS, Bird T, Danek A, Fox NC, Goate A, Frommelt P, Ghetti B, Langbaum JB, Lopera F, Martins R, Masters CL, Mayeux RP, McDade E, Moreno S, Reiman EM, Ringman JM, Salloway S, Schofield PR, Sperling R, Tariot PN, Xiong C, Morris JC, Bateman RJ; Dominantly Inherited Alzheimer Network. Symptom onset in autosomal dominant Alzheimer disease: a systematic review and meta-analysis. Neurology. 2014 Jul 15;83(3):253-60. doi: 10.1212/WNL.0000000000000596. Epub 2014 Jun 13. PMID: 24928124; PMCID: PMC4117367.
- 72. Sepulveda-Falla D, Vélez JI, Acosta-Baena N, Baena A, Moreno S, Krasemann S, Lopera F, Mastronardi CA, Arcos-Burgos M. Genetic modifiers of cognitive decline in PSEN1 E280A Alzheimer's disease. Alzheimers Dement. 2024 Apr;20(4):2873-2885. doi: 10.1002/alz.13754. Epub 2024 Mar 7. PMID: 38450831; PMCID: PMC11032577.
- 73. Kim YW, Al-Ramahi I, Koire A, Wilson SJ, Konecki DM, Mota S, Soleimani S, Botas J, Lichtarge O. Harnessing the paradoxical phenotypes of APOE ε2 and APOE ε4 to identify genetic modifiers in Alzheimer's disease. Alzheimers Dement. 2021 May;17(5):831-846. doi: 10.1002/alz.12240. Epub 2020 Dec 7. PMID: 33576571; PMCID: PMC8247413.
- 74. Jain N, Chen-Plotkin AS. Genetic Modifiers in Neurodegeneration. Curr Genet Med Rep. 2018 Mar;6(1):11-19. doi: 10.1007/s40142-018-0133-1. Epub 2018 Feb 5. PMID: 29977663; PMCID: PMC6028053.
- 75. Bellenguez C, Küçükali F, Jansen IE, Kleineidam L, Moreno-Grau, et al. New insights into the genetic etiology of Alzheimer's disease and related dementias. Nat Genet. 2022 Apr;54(4):412-436. doi: 10.1038/s41588-022-01024-z. Epub 2022 Apr 4. PMID: 35379992; PMCID: PMC9005347.
- 76. Serrano-Pozo A, Das S, Hyman BT. APOE and Alzheimer's disease: advances in genetics, pathophysiology, and therapeutic approaches. Lancet Neurol. 2021 Jan;20(1):68-80. doi: 10.1016/S1474-4422(20)30412-9. Erratum in: Lancet Neurol. 2021 Feb;20(2):e2. doi: 10.1016/S1474-4422(21)00004-1. PMID: 33340485; PMCID: PMC8096522.

- 77. Liu CC, Liu CC, Kanekiyo T, Xu H, Bu G. Apolipoprotein E and Alzheimer disease: risk, mechanisms and therapy. Nat Rev Neurol. 2013 Feb;9(2):106-18. doi: 10.1038/nrneurol.2012.263. Epub 2013 Jan 8. Erratum in: Nat Rev Neurol. 2013. doi: 10.1038/nmeurol.2013.32. Liu, Chia-Chan [corrected to Liu, Chia-Chen]. PMID: 23296339; PMCID: PMC3726719.
- 78. Colonna, M., Wang, Y. TREM2 variants: new keys to decipher Alzheimer disease pathogenesis. Nat Rev Neurosci 17, 201–207 (2016). https://doi.org/10.1038/nrn.2016.7
- 79. Winfree RL, Nolan E, Dumitrescu L, Blennow K, Zetterberg H, Gifford KA, Pechman KR, Seto M, Petyuk VA, Wang Y, Schneider J, Bennett DA, Jefferson AL, Hohman TJ; Alzheimer's Disease Neuroimaging Initiative*. Variants in the MS4A cluster interact with soluble TREM2 expression on biomarkers of neuropathology. Mol Neurodegener. 2024 May 18;19(1):41. doi: 10.1186/s13024-024-00727-7. PMID: 38760857; PMCID: PMC11101336.
- 80. Li H, Karl T, Garner B. Understanding the function of ABCA7 in Alzheimer's disease. Biochem Soc Trans. 2015 Oct;43(5):920-3. doi: 10.1042/BST20150105. PMID: 26517904.
- 81. Kawatani K, Holm ML, Starling SC, Martens YA, Zhao J, Lu W, Ren Y, Li Z, Jiang P, Jiang Y, Baker SK, Wang N, Roy B, Parsons TM, Perkerson RB 3rd, Bao H, Han X, Bu G, Kanekiyo T. ABCA7 deficiency causes neuronal dysregulation by altering mitochondrial lipid metabolism. Mol Psychiatry. 2024 Mar;29(3):809-819. doi: 10.1038/s41380-023-02372-w. Epub 2023 Dec 22. PMID: 38135757; PMCID: PMC11153016.
- 82. Jonsson T, Atwal JK, Steinberg S, Snaedal J, Jonsson PV, Bjornsson S, Stefansson H, Sulem P, Gudbjartsson D, Maloney J, Hoyte K, Gustafson A, Liu Y, Lu Y, Bhangale T, Graham RR, Huttenlocher J, Bjornsdottir G, Andreassen OA, Jönsson EG, Palotie A, Behrens TW, Magnusson OT, Kong A, Thorsteinsdottir U, Watts RJ, Stefansson K. A mutation in APP protects against Alzheimer's disease and age-related cognitive decline. Nature. 2012 Aug 2;488(7409):96-9. doi: 10.1038/nature11283. PMID: 22801501.
- 83. Shimohama S, Fujioka R, Mihira N, Sekiguchi M, Sartori L, Joho D, Saito T, Saido TC, Nakahara J, Hino T, Hoshino A, Sasaguri H. The Icelandic Mutation (APP-A673T) Is Protective against Amyloid Pathology In Vivo. J Neurosci. 2024 Nov 20;44(47):e0223242024. doi: 10.1523/JNEUROSCI.0223-24.2024. PMID: 39496485; PMCID: PMC11580785.
- 84. Wardell MR, Brennan SO, Janus ED, Fraser R, Carrell RW. Apolipoprotein E2-Christchurch (136 Arg----Ser). New variant of human apolipoprotein E in a patient with

- type III hyperlipoproteinemia. J Clin Invest. 1987 Aug;80(2):483-90. doi: 10.1172/JCI113096. PMID: 3038959; PMCID: PMC442261.
- 85. Mahley RW. Apolipoprotein E: cholesterol transport protein with expanding role in cell biology. Science. 1988 Apr 29;240(4852):622-30. doi: 10.1126/science.3283935. PMID: 3283935.
- 86. Ji ZS, Brecht WJ, Miranda RD, Hussain MM, Innerarity TL, Mahley RW. Role of heparan sulfate proteoglycans in the binding and uptake of apolipoprotein E-enriched remnant lipoproteins by cultured cells. J Biol Chem. 1993 May 15;268(14):10160-7. PMID: 7683668.
- 87. Lopera F, Marino C, Chandrahas AS, O'Hare M, Villalba-Moreno ND, Aguillon D, Baena A, Sanchez JS, Vila-Castelar C, Ramirez Gomez L, Chmielewska N, Oliveira GM, Littau JL, Hartmann K, Park K, Krasemann S, Glatzel M, Schoemaker D, Gonzalez-Buendia L, Delgado-Tirado S, Arevalo-Alquichire S, Saez-Torres KL, Amarnani D, Kim LA, Mazzarino RC, Gordon H, Bocanegra Y, Villegas A, Gai X, Bootwalla M, Ji J, Shen L, Kosik KS, Su Y, Chen Y, Schultz A, Sperling RA, Johnson K, Reiman EM, Sepulveda-Falla D, Arboleda-Velasquez JF, Quiroz YT. Resilience to autosomal dominant Alzheimer's disease in a Reelin-COLBOS heterozygous man. Nat Med. 2023 May;29(5):1243-1252. doi: 10.1038/s41591-023-02318-3. Epub 2023 May 15. PMID: 37188781; PMCID: PMC10202812.
- 88. Hiesberger T, Trommsdorff M, Howell BW, Goffinet A, Mumby MC, Cooper JA, Herz J. Direct binding of Reelin to VLDL receptor and ApoE receptor 2 induces tyrosine phosphorylation of disabled-1 and modulates tau phosphorylation. Neuron. 1999 Oct;24(2):481-9. doi: 10.1016/s0896-6273(00)80861-2. PMID: 10571241.
- 89. Hoe HS, Pocivavsek A, Chakraborty G, Fu Z, Vicini S, Ehlers MD, Rebeck GW. Apolipoprotein E receptor 2 interactions with the N-methyl-D-aspartate receptor. J Biol Chem. 2006 Feb 10;281(6):3425-31. doi: 10.1074/jbc.M509380200. Epub 2005 Dec 6. PMID: 16332682.
- 90. D'Arcangelo G, Homayouni R, Keshvara L, Rice DS, Sheldon M, Curran T. Reelin is a ligand for lipoprotein receptors. Neuron. 1999 Oct;24(2):471-9. doi: 10.1016/s0896-6273(00)80860-0. PMID: 10571240.
- 91. Durakoglugil MS, Chen Y, White CL, Kavalali ET, Herz J. Reelin signaling antagonizes beta-amyloid at the synapse. Proc Natl Acad Sci U S A. 2009 Sep 15;106(37):15938-43. doi: 10.1073/pnas.0908176106. Epub 2009 Sep 2. PMID: 19805234; PMCID: PMC2747222.
- 92. Nagafuchi A, Takeichi M. Transmembrane control of cadherin-mediated cell adhesion: a 94 kDa protein functionally associated with a specific region of the cytoplasmic

- domain of E-cadherin. Cell Regul. 1989 Nov;1(1):37-44. doi: 10.1091/mbc.1.1.37. PMID: 2519616; PMCID: PMC361423.
- 93. Clevers H, Nusse R. Wnt/β-catenin signaling and disease. Cell. 2012 Jun 8;149(6):1192-205. doi: 10.1016/j.cell.2012.05.012. PMID: 22682243.
- 94. Palomer E, Buechler J, Salinas PC. Wnt Signaling Deregulation in the Aging and Alzheimer's Brain. Front Cell Neurosci. 2019 May 22;13:227. doi: 10.3389/fncel.2019.00227. PMID: 31191253; PMCID: PMC6538920.
- 95. Neuner SM, Tcw J, Goate AM. Genetic architecture of Alzheimer's disease. Neurobiol Dis. 2020 Sep;143:104976. doi: 10.1016/j.nbd.2020.104976. Epub 2020 Jun 18. PMID: 32565066; PMCID: PMC7409822.
- 96. Quiroz YT, Aguillon D, Aguirre-Acevedo DC, Vasquez D, Zuluaga Y, Baena AY, Madrigal L, Hincapié L, Sanchez JS, Langella S, Posada-Duque R, Littau JL, Villalba-Moreno ND, Vila-Castelar C, Ramirez Gomez L, Garcia G, Kaplan E, Rassi Vargas S, Ossa JA, Valderrama-Carmona P, Perez-Corredor P, Krasemann S, Glatzel M, Kosik KS, Johnson K, Sperling RA, Reiman EM, Sepulveda-Falla D, Lopera F, Arboleda-Velasquez JF. APOE3 Christchurch Heterozygosity and Autosomal Dominant Alzheimer's Disease. N Engl J Med. 2024 Jun 20;390(23):2156-2164. doi: 10.1056/NEJMoa2308583. PMID: 38899694.
- 97. Perez-Corredor P, Vanderleest TE, Vacano GN, Sanchez JS, Villalba-Moreno ND, Marino C, Krasemann S, Mendivil-Perez MA, Aguillón D, Jiménez-Del-Río M, Baena A, Sepulveda-Falla D, Lopera F, Quiroz YT, Arboleda-Velasquez JF, Mazzarino RC. APOE3 Christchurch modulates β-catenin/Wnt signaling in iPS cell-derived cerebral organoids from Alzheimer's cases. Front Mol Neurosci. 2024 Mar 20;17:1373568. doi: 10.3389/fnmol.2024.1373568. PMID: 38571814; PMCID: PMC10987717.
- 98. Sepulveda-Falla D, Sanchez JS, Almeida MC, Boassa D, Acosta-Uribe J, Vila-Castelar C, Ramirez-Gomez L, Baena A, Aguillon D, Villalba-Moreno ND, Littau JL, Villegas A, Beach TG, White CL 3rd, Ellisman M, Krasemann S, Glatzel M, Johnson KA, Sperling RA, Reiman EM, Arboleda-Velasquez JF, Kosik KS, Lopera F, Quiroz YT. Distinct tau neuropathology and cellular profiles of an APOE3 Christchurch homozygote protected against autosomal dominant Alzheimer's dementia. Acta Neuropathol. 2022 Sep;144(3):589-601. doi: 10.1007/s00401-022-02467-8. Epub 2022 Jul 15. PMID: 35838824; PMCID: PMC9381462.
- 99. Almeida MC, Eger SJ, He C, Audouard M, Nikitina A, Glasauer SMK, Han D, Mejía-Cupajita B, Acosta-Uribe J, Villalba-Moreno ND, Littau JL, Elcheikhali M, Rivera EK, Carrettiero DC, Villegas-Lanau CA, Sepulveda-Falla D, Lopera F, Kosik KS. Single-nucleus RNA sequencing demonstrates an autosomal dominant Alzheimer's disease profile and possible mechanisms of disease protection. Neuron. 2024 Jun

- 5;112(11):1778-1794.e7. doi: 10.1016/j.neuron.2024.02.009. Epub 2024 Feb 27. PMID: 38417436; PMCID: PMC11156559.
- 100. van Bokhoven P, de Wilde A, Vermunt L, Leferink PS, Heetveld S, Cummings J, Scheltens P, Vijverberg EGB. The Alzheimer's disease drug development landscape. Alzheimers Res Ther. 2021 Nov 11;13(1):186. doi: 10.1186/s13195-021-00927-z. PMID: 34763720; PMCID: PMC8582156.
- 101. Weninger S, Irizarry MC, Fleisher AS, León T, Maruff P, Miller DS, Seleri S, Carrillo MC, Weber CJ. Alzheimer's disease drug development in an evolving therapeutic landscape. Alzheimers Dement (N Y). 2024 Nov 30;10(4):e70015. doi: 10.1002/trc2.70015. PMID: 39748838; PMCID: PMC11694530.
- 102. Absil P, Pinxten R, Balthazart J, Eens M. Effects of testosterone on Reelin expression in the brain of male European starlings. Cell Tissue Res. 2003 Apr;312(1):81-93. doi: 10.1007/s00441-003-0701-9. Epub 2003 Feb 26. PMID: 12712319.
- 103. Silva Hurtado TJ, Lassalle O, Ameloot A, Chavis P. Sex-specific trajectories of Reelin-dependent maturation of deep layer prefrontal neurons. bioRxiv [Preprint]. Posted 2021 Dec 24. doi: 10.1101/2021.12.23.473977.
- 104. Goes FS, Willour VL, Zandi PP, Belmonte PL, MacKinnon DF, Mondimore FM, Schweizer B; National Institute of Mental Health Genetics Initiative Bipolar Disorder Consortium; DePaulo JR Jr, Gershon ES, McMahon FJ, Potash JB. Sex-specific association of the Reelin gene with bipolar disorder. Am J Med Genet B Neuropsychiatr Genet. 2010 Mar 5;153B(2):549-553. doi: 10.1002/ajmg.b.31018. PMID: 19691043; PMCID: PMC3032172.
- 105. Shifman S, Johannesson M, Bronstein M, Chen SX, Collier DA, Craddock NJ, Kendler KS, Li T, O'Donovan M, O'Neill FA, Owen MJ, Walsh D, Weinberger DR, Sun C, Flint J, Darvasi A. Genome-wide association identifies a common variant in the reelin gene that increases the risk of schizophrenia only in women. PLoS Genet. 2008 Feb;4(2):e28. doi: 10.1371/journal.pgen.0040028. PMID: 18282107; PMCID: PMC2242812.
- 106. Kelemenova S, Ostatnikova D. Neuroendocrine pathways altered in autism. Special role of reelin. Neuro Endocrinol Lett. 2009;30(4):429-36. PMID: 20010491.
- 107. Fehér Á, Juhász A, Pákáski M, Kálmán J, Janka Z. Genetic analysis of the RELN gene: Gender specific association with Alzheimer's disease. Psychiatry Res. 2015 Dec 15;230(2):716-8. doi: 10.1016/j.psychres.2015.09.021. Epub 2015 Sep 13. PMID: 26384575.
- 108. Seripa D, Matera MG, Franceschi M, Daniele A, Bizzarro A, Rinaldi M, Panza F, Fazio VM, Gravina C, D'Onofrio G, Solfrizzi V, Masullo C, Pilotto A. The RELN locus in

- Alzheimer's disease. J Alzheimers Dis. 2008 Jul;14(3):335-44. doi: 10.3233/jad-2008-14308. PMID: 18599960.
- 109. Ober C, Loisel DA, Gilad Y. Sex-specific genetic architecture of human disease. Nat Rev Genet. 2008 Dec;9(12):911-22. doi: 10.1038/nrg2415. PMID: 19002143; PMCID: PMC2694620.
- 110. Alcántara S, Ruiz M, D'Arcangelo G, Ezan F, de Lecea L, Curran T, Sotelo C, Soriano E. Regional and cellular patterns of reelin mRNA expression in the forebrain of the developing and adult mouse. J Neurosci. 1998 Oct 1;18(19):7779-99. doi: 10.1523/JNEUROSCI.18-19-07779.1998. PMID: 9742148; PMCID: PMC6792998.
- 111. Valderrama-Mantilla AI, Martín-Cuevas C, Gómez-Garrido A, Morente-Montilla C, Crespo-Facorro B, García-Cerro S. Shared molecular signature in Alzheimer's disease and schizophrenia: A systematic review of the reelin signaling pathway. Neurosci Biobehav Rev. 2025 Feb;169:106032. doi: 10.1016/j.neubiorev.2025.106032. Epub 2025 Jan 31. PMID: 39894421.
- 112. Xu PT, Gilbert JR, Qiu HL, Ervin J, Rothrock-Christian TR, Hulette C, Schmechel DE. Specific regional transcription of apolipoprotein E in human brain neurons. Am J Pathol. 1999 Feb;154(2):601-11. doi: 10.1016/S0002-9440(10)65305-9. PMID: 10027417; PMCID: PMC1850012.
- 113. Sullivan PM, Mace BE, Maeda N, Schmechel DE. Marked regional differences of brain human apolipoprotein E expression in targeted replacement mice. Neuroscience. 2004;124(4):725-33. doi: 10.1016/j.neuroscience.2003.10.011. PMID: 15026113.
- 114. Su JH, Cummings BJ, Cotman CW. Localization of heparan sulfate glycosaminoglycan and proteoglycan core protein in aged brain and Alzheimer's disease. Neuroscience. 1992 Dec;51(4):801-13. doi: 10.1016/0306-4522(92)90521-3. PMID: 1488123.
- 115. Mah D, Zhao J, Liu X, Zhang F, Liu J, Wang L, Linhardt R, Wang C. The Sulfation Code of Tauopathies: Heparan Sulfate Proteoglycans in the Prion Like Spread of Tau Pathology. Front Mol Biosci. 2021 May 20;8:671458. doi: 10.3389/fmolb.2021.671458. PMID: 34095227; PMCID: PMC8173255.
- 116. Huynh MB, Ouidja MO, Chantepie S, Carpentier G, Maïza A, Zhang G, Vilares J, Raisman-Vozari R, Papy-Garcia D. Glycosaminoglycans from Alzheimer's disease hippocampus have altered capacities to bind and regulate growth factors activities and to bind tau. PLoS One. 2019 Jan 4;14(1):e0209573. doi: 10.1371/journal.pone.0209573. PMID: 30608949; PMCID: PMC6319808.

- 117. Zhu Y, Gandy L, Zhang F, Liu J, Wang C, Blair LJ, Linhardt RJ, Wang L. Heparan Sulfate Proteoglycans in Tauopathy. Biomolecules. 2022 Nov 30;12(12):1792. doi: 10.3390/biom12121792. PMID: 36551220; PMCID: PMC9776397.
- 118. Inestrosa NC, Toledo EM. The role of Wnt signaling in neuronal dysfunction in Alzheimer's Disease. Mol Neurodegener. 2008 Jul 24;3:9. doi: 10.1186/1750-1326-3-9. PMID: 18652670; PMCID: PMC2515306.
- 119. Hernandez F, Lucas JJ, Avila J. GSK3 and tau: two convergence points in Alzheimer's disease. J Alzheimers Dis. 2013;33 Suppl 1:S141-4. doi: 10.3233/JAD-2012-129025. PMID: 22710914.
- 120. Rauch JN, Luna G, Guzman E, Audouard M, Challis C, Sibih YE, Leshuk C, Hernandez I, Wegmann S, Hyman BT, Gradinaru V, Kampmann M, Kosik KS. LRP1 is a master regulator of tau uptake and spread. Nature. 2020 Apr;580(7803):381-385. doi: 10.1038/s41586-020-2156-5. Epub 2020 Apr 1. PMID: 32296178; PMCID: PMC7687380.
- 121. D'Arcangelo G, Miao GG, Chen SC, Soares HD, Morgan JI, Curran T. A protein related to extracellular matrix proteins deleted in the mouse mutant reeler. Nature. 1995 Apr 20;374(6524):719-23. doi: 10.1038/374719a0. PMID: 7715726.
- 122. Alexander A, Herz J, Calvier L. Reelin through the years: From brain development to inflammation. Cell Rep. 2023 Jun 27;42(6):112669. doi: 10.1016/j.celrep.2023.112669. Epub 2023 Jun 19. PMID: 37339050; PMCID: PMC10592530.
- 123. Lakatosova S, Ostatnikova D. Reelin and its complex involvement in brain development and function. Int J Biochem Cell Biol. 2012 Sep;44(9):1501-4. doi: 10.1016/j.biocel.2012.06.002. Epub 2012 Jun 15. PMID: 22705982.
- 124. Lee GH, D'Arcangelo G. New Insights into Reelin-Mediated Signaling Pathways. Front Cell Neurosci. 2016 May 9;10:122. doi: 10.3389/fncel.2016.00122. PMID: 27242434; PMCID: PMC4860420.
- 125. Ranaivoson FM, von Daake S, Comoletti D. Structural Insights into Reelin Function: Present and Future. Front Cell Neurosci. 2016 May 27;10:137. doi: 10.3389/fncel.2016.00137. PMID: 27303268; PMCID: PMC4882317.
- 126. Bock HH, May P. Canonical and Non-canonical Reelin Signaling. Front Cell Neurosci. 2016 Jun 30;10:166. doi: 10.3389/fncel.2016.00166. PMID: 27445693; PMCID: PMC4928174.
- 127. Hanger DP, Hughes K, Woodgett JR, Brion JP, Anderton BH. Glycogen synthase kinase-3 induces Alzheimer's disease-like phosphorylation of tau: generation of paired helical filament epitopes and neuronal localisation of the kinase. Neurosci Lett. 1992 Nov 23;147(1):58-62. doi: 10.1016/0304-3940(92)90774-2. PMID: 1336152.

- 128. Hooper C, Killick R, Lovestone S. The GSK3 hypothesis of Alzheimer's disease. J Neurochem. 2008 Mar;104(6):1433-9. doi: 10.1111/j.1471-4159.2007.05194.x. Epub 2007 Dec 18. PMID: 18088381; PMCID: PMC3073119.
- 129. Yu NN, Tan MS, Yu JT, Xie AM, Tan L. The Role of Reelin Signaling in Alzheimer's Disease. Mol Neurobiol. 2016 Oct;53(8):5692-700. doi: 10.1007/s12035-015-9459-9. Epub 2015 Oct 21. PMID: 26491027.
- 130. Abraham H, Meyer G. Reelin-expressing neurons in the postnatal and adult human hippocampal formation. Hippocampus. 2003;13(6):715-27. doi: 10.1002/hipo.10125. PMID: 12962316.
- 131. Kobro-Flatmoen A, Nagelhus A, Witter MP. Reelin-immunoreactive neurons in entorhinal cortex layer II selectively express intracellular amyloid in early Alzheimer's disease. Neurobiol Dis. 2016 Sep;93:172-83. doi: 10.1016/j.nbd.2016.05.012. Epub 2016 May 16. PMID: 27195475.
- 132. Pujadas L, Gruart A, Bosch C, Delgado L, Teixeira CM, Rossi D, de Lecea L, Martínez A, Delgado-García JM, Soriano E. Reelin regulates postnatal neurogenesis and enhances spine hypertrophy and long-term potentiation. J Neurosci. 2010 Mar 31;30(13):4636-49. doi: 10.1523/JNEUROSCI.5284-09.2010. PMID: 20357114; PMCID: PMC6632327.
- 133. Levenson JM, Qiu S, Weeber EJ. The role of reelin in adult synaptic function and the genetic and epigenetic regulation of the reelin gene. Biochim Biophys Acta. 2008 Aug;1779(8):422-31. doi: 10.1016/j.bbagrm.2008.01.001. Epub 2008 Jan 12. PMID: 18237558.
- 134. Stranahan AM, Haberman RP, Gallagher M. Cognitive decline is associated with reduced reelin expression in the entorhinal cortex of aged rats. Cereb Cortex. 2011 Feb;21(2):392-400. doi: 10.1093/cercor/bhq106. Epub 2010 Jun 10. PMID: 20538740; PMCID: PMC3020582.
- 135. Niu S, Yabut O, D'Arcangelo G. The Reelin signaling pathway promotes dendritic spine development in hippocampal neurons. J Neurosci. 2008 Oct 8;28(41):10339-48. doi: 10.1523/JNEUROSCI.1917-08.2008. PMID: 18842893; PMCID: PMC2572775.
- 136. Deutsch SI, Rosse RB, Deutsch LH. Faulty regulation of tau phosphorylation by the reelin signal transduction pathway is a potential mechanism of pathogenesis and therapeutic target in Alzheimer's disease. Eur Neuropsychopharmacol. 2006 Dec;16(8):547-51. doi: 10.1016/j.euroneuro.2006.01.006. Epub 2006 Feb 28. PMID: 16504486.

- 137. Lane-Donovan C, Philips GT, Wasser CR, Durakoglugil MS, Masiulis I, Upadhaya A, Pohlkamp T, Coskun C, Kotti T, Steller L, Hammer RE, Frotscher M, Bock HH, Herz J. Reelin protects against amyloid β toxicity in vivo. Sci Signal. 2015 Jul 7;8(384):ra67. doi: 10.1126/scisignal.aaa6674. PMID: 26152694; PMCID: PMC4652952.
- 138. Kocherhans S, Madhusudan A, Doehner J, Breu KS, Nitsch RM, Fritschy JM, Knuesel I. Reduced Reelin expression accelerates amyloid-beta plaque formation and tau pathology in transgenic Alzheimer's disease mice. J Neurosci. 2010 Jul 7;30(27):9228-40. doi: 10.1523/JNEUROSCI.0418-10.2010. PMID: 20610758; PMCID: PMC6632461.
- 139. Rossi D, Gruart A, Contreras-Murillo G, Muhaisen A, Ávila J, Delgado-García JM, Pujadas L, Soriano E. Reelin reverts biochemical, physiological and cognitive alterations in mouse models of Tauopathy. Prog Neurobiol. 2020 Mar;186:101743. doi: 10.1016/j.pneurobio.2019.101743. Epub 2019 Dec 20. PMID: 31870804.
- 140. Hinrich AJ, Jodelka FM, Chang JL, Brutman D, Bruno AM, Briggs CA, James BD, Stutzmann GE, Bennett DA, Miller SA, Rigo F, Marr RA, Hastings ML. Therapeutic correction of ApoER2 splicing in Alzheimer's disease mice using antisense oligonucleotides. EMBO Mol Med. 2016 Apr 1;8(4):328-45. doi: 10.15252/emmm.201505846. PMID: 26902204; PMCID: PMC4818756.
- 141. Mahley RW, Rall SC Jr. Apolipoprotein E: far more than a lipid transport protein. Annu Rev Genomics Hum Genet. 2000;1:507-37. doi: 10.1146/annurev.genom.1.1.507. PMID: 11701639.
- 142. Jackson RJ, Hyman BT, Serrano-Pozo A. Multifaceted roles of APOE in Alzheimer disease. Nat Rev Neurol. 2024 Aug;20(8):457-474. doi: 10.1038/s41582-024-00988-2. Epub 2024 Jun 21. PMID: 38906999.
- 143. Flowers SA, Rebeck GW. APOE in the normal brain. Neurobiol Dis. 2020 Mar;136:104724. doi: 10.1016/j.nbd.2019.104724. Epub 2020 Jan 3. PMID: 31911114; PMCID: PMC7002287.
- 144. Lane-Donovan C, Herz J. ApoE, ApoE Receptors, and the Synapse in Alzheimer's Disease. Trends Endocrinol Metab. 2017 Apr;28(4):273-284. doi: 10.1016/j.tem.2016.12.001. Epub 2017 Jan 2. PMID: 28057414; PMCID: PMC5366078.
- 145. Fortea J, Pegueroles J, Alcolea D, Belbin O, Dols-Icardo O, Vaqué-Alcázar L, Videla L, Gispert JD, Suárez-Calvet M, Johnson SC, Sperling R, Bejanin A, Lleó A, Montal V. APOE4 homozygozity represents a distinct genetic form of Alzheimer's disease. Nat Med. 2024 May;30(5):1284-1291. doi: 10.1038/s41591-024-02931-w. Epub 2024 May 6. Erratum in: Nat Med. 2024 Jul;30(7):2093. doi: 10.1038/s41591-024-03127-y. PMID: 38710950.

- 146. Zhou X, Cao H, Jiang Y, Chen Y, Zhong H, Fu WY, Lo RMN, Wong BWY, Cheng EYL, Mok KY, Kwok TCY, Mok VCT, Ip FCF; Alzheimer's Disease Neuroimaging Initiative; Miyashita A, Hara N, Ikeuchi T, Hardy J, Chen Y, Fu AKY, Ip NY. Transethnic analysis identifies SORL1 variants and haplotypes protective against Alzheimer's disease. Alzheimers Dement. 2025 Jan;21(1):e14214. doi: 10.1002/alz.14214. Epub 2024 Dec 10. PMID: 39655505; PMCID: PMC11772736.
- 147. Lalli MA, Bettcher BM, Arcila ML, Garcia G, Guzman C, Madrigal L, Ramirez L, Acosta-Uribe J, Baena A, Wojta KJ, Coppola G, Fitch R, de Both MD, Huentelman MJ, Reiman EM, Brunkow ME, Glusman G, Roach JC, Kao AW, Lopera F, Kosik KS. Wholegenome sequencing suggests a chemokine gene cluster that modifies age at onset in familial Alzheimer's disease. Mol Psychiatry. 2015 Nov;20(11):1294-300. doi: 10.1038/mp.2015.131. Epub 2015 Sep 1. PMID: 26324103; PMCID: PMC4759097.
- 148. Sepulveda-Falla D, Chavez-Gutierrez L, Portelius E, Vélez JI, Dujardin S, Barrera-Ocampo A, Dinkel F, Hagel C, Puig B, Mastronardi C, Lopera F, Hyman BT, Blennow K, Arcos-Burgos M, de Strooper B, Glatzel M. A multifactorial model of pathology for age of onset heterogeneity in familial Alzheimer's disease. Acta Neuropathol. 2021 Feb;141(2):217-233. doi: 10.1007/s00401-020-02249-0. Epub 2020 Dec 14. PMID: 33319314; PMCID: PMC7847436.
- 149. Güner, G., & Lichtenthaler, S. F. (2020). The substrate repertoire of γ -secretase/presenilin. Seminars in Cell & Developmental Biology, 105, 27-42. https://doi.org/10.1016/j.semcdb.2020.05.019.
- 150. de Calignon A, Polydoro M, Suárez-Calvet M, William C, Adamowicz DH, Kopeikina KJ, Pitstick R, Sahara N, Ashe KH, Carlson GA, Spires-Jones TL, Hyman BT. Propagation of tau pathology in a model of early Alzheimer's disease. Neuron. 2012 Feb 23;73(4):685-97. doi: 10.1016/j.neuron.2011.11.033. Erratum in: Neuron. 2012 Oct 18;76(2):461. PMID: 22365544; PMCID: PMC3292759.

7. Publication I

Acta Neuropathologica (2022) 144:589–601 https://doi.org/10.1007/s00401-022-02467-8

CASE REPORT



Distinct tau neuropathology and cellular profiles of an APOE3 Christchurch homozygote protected against autosomal dominant Alzheimer's dementia

Diego Sepulveda-Falla 10 · Justin S. Sanchez · Maria Camila Almeida 3.4 · Daniela Boassa 5.6 · Juliana Acosta-Uribe · Clara Vila-Castelar · Liliana Ramirez-Gomez · Ana Baena · David Aguillon · Nelson David Villalba-Moreno · Jessica Lisa Littau · Andres Villegas · Thomas G. Beach · Charles L. White III · Mark Ellisman · Solution · Susanne Krasemann · Markus Glatzel · Keith A. Johnson · Reisa A. Sperling · Eric M. Reiman · Solution · Solution · Charles · Charles A. Sperling · Eric M. Reiman · Solution · Solution · Solution · Solution · Charles · Charle

Received: 29 March 2022 / Revised: 21 June 2022 / Accepted: 1 July 2022 / Published online: 15 July 2022 © The Author(s) 2022

Abstract

We describe in vivo follow-up PET imaging and postmortem findings from an autosomal dominant Alzheimer's disease (ADAD) *PSEN1* E280A carrier who was also homozygous for the *APOE3* Christchurch (APOE3ch) variant and was protected against Alzheimer's symptoms for almost three decades beyond the expected age of onset. We identified a distinct anatomical pattern of tau pathology with atypical accumulation in vivo and unusual postmortem regional distribution characterized by sparing in the frontal cortex and severe pathology in the occipital cortex. The frontal cortex and the hippocampus, less affected than the occipital cortex by tau pathology, contained Related Orphan Receptor B (RORB) positive neurons, homeostatic astrocytes and higher APOE expression. The occipital cortex, the only cortical region showing cerebral amyloid angiopathy (CAA), exhibited a distinctive chronic inflammatory microglial profile and lower APOE expression. Thus, the Christchurch variant may impact the distribution of tau pathology, modulate age at onset, severity, progression, and clinical presentation of ADAD, suggesting possible therapeutic strategies.

 $\textbf{Keywords} \ \ Alzheimer's \ disease \cdot Dementia \cdot Tau \cdot PET \cdot Transcriptomics \cdot APOE$

Introduction

Familial Alzheimer's disease is characterized by its high pathological severity and early disease onset. Nevertheless, some cases belonging to a large kindred carrying the presenilin-1 (*PSENI*) E280A mutation have shown delayed onset, suggesting possible mechanisms of disease modulation [31,

Diego Sepulveda-Falla and Justin S. Sanchez contributed equally to this work

Kenneth S. Kosik, Francisco Lopera and Yakeel T. Quiroz are cosenior authors.

Extended author information available on the last page of the article

32]. Apolipoprotein E (APOE) haplotype variants such as APOE4 have been associated with increased risk of sporadic Alzheimer's disease [35]. APOE's possible role in Alzheimer's pathophysiology include cellular mechanisms involving neuronal and glial functions [34, 35], together with direct effects in amyloid- β (A β) aggregation and deposition [37]. We previously reported a PSEN1 E280A mutation carrier from the world's largest known autosomal dominant Alzheimer's disease (ADAD) kindred who was spared from Alzheimer's symptoms until her seventies, nearly three decades after the typical age of clinical onset among mutation carriers in this kindred [1]. At the time of first examination, she was found to carry two copies of the rare APOE3 Christchurch variant (APOE3ch) and had severely elevated brain Aβ with limited tau pathology and neurodegeneration, as measured by in vivo PET imaging.

In vitro experiments from that report suggested that the *APOE3ch* variant may have protective effects by reducing ApoE binding to heparan sulfate proteoglycans and



lipoprotein receptors involved in tau uptake and spread compared to other *APOE* variants. Since the original report, the availability of follow-up in vivo imaging and postmortem data has enabled us to further evaluate in greater detail the mechanisms of protection in this patient. In this study we aim to describe these longitudinal in vivo and postmortem findings, including an atypical regional distribution of tau pathology evident in both imaging and postmortem assessments, and gene expression profiles of neurons and neuroglia that correspond to regional vulnerability and protection against tau.

Materials and methods

Clinical assessments

This study was approved by the institutional review boards of the University of Antioquia, Massachusetts General Hospital, and the Schepens Eye Research Institute of Massachusetts Eye and Ear. All subjects provided informed written consent. Clinical ratings and neuropsychological tests were performed according to standard protocols as previously described [1].

MRI and **PET** imaging

Structural MRI, 11C-Pittsburgh Compound B (PiB) and 18F-Flortaucipir (FTP) PET data were acquired at Massachusetts General Hospital, as previously described [29]. Imaging data from the patient was compared with data from other, typical PSEN1 E280 carriers; as well as older (>65 years/old) sporadic AD patients described in a previous report [30]. T1-weighted structural MRI data were acquired using a Siemens 3 Tesla Tim Trio (Siemens, Erlangen, Germany; repetition time = 2300 ms; echo time = 2.95 ms; flip angle = 9° ; voxel size = $1.05 \times 1.05 \times 1.2$ mm). Images were processed with FreeSurfer (FS) version 6.0 (http://surfer. nmr.mgh.harvard.edu) to identify white and pial surfaces, standard regions-of-interest (ROI) from the Desikan atlas for PET sampling, and hippocampal volumes (HV) [5]. FS outputs were quality-checked and manually edited where necessary to ensure accurate segmentation and surface identification. Bilateral HV measures derived from FS were adjusted for intracranial volume (ICV) by regressing out the contribution of ICV on HV, using previously published parameters [26]. PiB and FTP PET were prepared and acquired according to previously published protocols [17]. All PET data were acquired on a Siemens ECAT HR + (3D mode; 63 image planes; 15.2 cm axial field of view; 5.6 mm transaxial resolution; 2.4 mm slice interval). PiB data were acquired using a 60-min dynamic protocol and analyzed by the Logan reference method with distribution volume ratio (DVR) as

outcome. FTP data were acquired from 80 to 100 min postinjection in 4×5-min frames with the standardized uptake value ratio (SUVr) as outcome. Cerebellar gray matter was used as reference for PiB and FTP. Partial volume correction (PVC) was applied to the PET frame data using geometric transfer matrix (GTM) method for ROI analyses and an extended Muller–Gartner method (implemented in FS) for surface-based analyses [11].

PET images were affine co-registered to each subject's contemporaneous T1 images (SPM8) and all PET data sets were sampled using FS-derived ROI. Aβ burden was represented using PiB DVR in a large, neocortical aggregate region, as well as striatum (volume-weighted average of bilateral caudate and putamen) [14]. Tau PET uptake was assessed in standard FS ROIs, as well as rhinal cortex [30] and visual cortex subregions (V1 and V2) from the FS Brodmann Area maps [8]. Change rates were expressed as annualized percent change (i.e., the difference in DVR or SUVr from baseline to follow-up, divided by the baseline value, divided by the elapsed time in years). For visualization purposes, FTP SUVr and PiB DVR images were normalized to standard (MNI) space and projected onto the fsaverage surface using FS methods (sampled at the midpoint of gray matter, surface-smoothed 8 mm).

Neuropathological and immunohistochemical analysis

The patient died from systemic failure secondary to malignant metastatic melanoma, stage III, at 77 years of age. Brain donation took place following informed consent signature and ethical approval from the bioethics committee from the School of Medicine from the University of Antioquia. The brain presented with severe atrophy, weighing 894.3 g, and with severe atherosclerosis in all major vessels. Weight of the content of the posterior fossae: 129.5 g. Weight of cerebellum: 107.6 g. During microscopic examination we confirmed moderate cortical atrophy and presence of AD pathological hallmarks by immunohistochemistry (IHC). We examined 17 brain areas including medial frontal gyrus, superior temporal gyrus, medial temporal gyrus, inferior temporal gyrus, hippocampus, amygdala, insula, gyrus cinguli, lenticular nucleus, caudate nucleus, thalamus, inferior parietal lobule, occipital lobule, cerebellum, mesencephalon, pons, and medulla oblongata. 4 µm thick sections were stained with haematoxylin and eosin (H&E) and further processed for immunohistochemical (IHC) staining for amyloid beta (Aβ, 1:100; mouse monoclonal BAM-10, Mob410; Zytomed Systems, Berlin, Germany), hyperphosphorylated tau Ser 202 and Thr 205 (tau, 1:1500; mouse monoclonal AT8, MN1020; ThermoFisher Scientific, Dreieich, Germany), Ionized calcium-binding adapter molecule 1 (Iba1, 1:500; rabbit polyclonal, 019-19741; FUJIFILM Wako



chemicals GmbH, Neuss, Germany), Transmembrane Protein 119 (TMEM119, 1:100; rabbit polyclonal, 400 102; Synaptic Systems, Göttingen, Germany), Cluster of Differentiation 68 (CD68, 1:100; rat monoclonal, HS-460 017; Synaptic Systems, Göttingen, Germany), Glial Fibrillary Acidic Protein (GFAP, 1:200; mouse monoclonal M0761, DAKO GmbH, Jena, Germany), Nuclear receptor RZR-β (RORB, 1:500; rabbit polyclonal, HPA008393; Merck Millipore, Darmstadt, Germany) and Apolipoprotein E (ApoE, 1:100; Goat polyclonal, AB947, Merck Millipore, Darmstadt, Germany). Automatic immunostaining was performed with a Ventana Benchmark XT system (Roche AG, Basel, Switzerland) according to manufacturer instructions. Briefly, after dewaxing and inactivation of endogenous peroxidases (PBS/3% hydrogen peroxide), antibody specific antigen retrieval was performed, sections were blocked and afterwards incubated with the primary antibody. For detection of specific binding, the Ultra View Universal 3,3'-Diaminobenzidine (DAB) Detection Kit (Ventana, Roche) was used which contains secondary antibodies, DAB stain and counter staining reagent. Sections were scanned using a Hamamatsu NanoZoomer automatic digital slide scanner (Hamamatsu Photonics, Hamamatsu, Japan) and obtained images of whole stained sections at a resolution of at least 1 pixel per µm. Signal of total area and signal integrated density were assessed using ImageJ Software (version 1.52p, NIH, Bethesda, MA, USA.) in the brown (DAB) color channel after performing color deconvolution and thresholding. Data was analyzed using GraphPad Prism 6 (GraphPad Software, Inc., La Jolla, CA, USA) and R statistical software (R Foundation for Statistical Computing, Vienna, Austria). Analyses, including distribution analysis and correlation analysis, were performed using Spearman's ρ test. Brain color maps were created using the cerebroViz package for R [3] for a general reference of the anatomical distribution of pathology and IHC signal. Statistical significance of all analyses was determined with $p \le 0.05$, $p \le 0.01$ and $p \le 0.001$.

Electron microscopy of human specimen

Surgically excised specimens were immediately placed in 4% paraformaldehyde and 2.5% glutaraldehyde in PBS pH 7.4 and kept in the fridge until shipment to UCSD. Upon arrival, specimens were transferred to a freshly prepared ice-cold solution of 4% paraformaldehyde and 2.5% glutaraldehyde in 0.15 M cacodylate buffer pH 7.4 containing 2 mM CaCl₂ and kept overnight in the fridge. The next day, the samples were sectioned using a vibratome (Leica) to 100 micron-thick sections and placed in the same fixative solution overnight in the fridge. Slices were then washed 3 times in 0.15 M cacodylate buffer pH 7.4 containing 2 mM CaCl₂, and post-fixed in 2% OsO₄/1.5% K₄Fe(CN)₆ (Sigma-Aldrich, St. Louis, MO) for 1 h at room temperature (RT) in

0.15 M cacodylate buffer. After 3 washes with double distilled water (ddH₂O), 5 min each at RT, slices were placed in filtered 1% thiocarbohydrazide solution for 30 min at RT, rinsed again in ddH₂O (3 times, 5 min each) and then placed in 2% OsO₄ for 1 h at RT. After this second osmium step, the sections were rinsed at RT in ddH₂O (3 times, 5 min each) and left in filtered 2% uranyl acetate aqueous solution overnight at 4 °C. The next day, after three washes in ddH₂O, 5 min each, at RT, en bloc Walton's lead aspartate staining was performed for 30 min at 60 °C. Following three washes for 5 min each in ddH₂O at RT, sections were dehydrated using a series of ice-cold graded ethanol solutions for 10 min each, and an additional 100% acetone step at RT for 10 min. Slices were infiltrated with a solution of 50% acetone: 50% Durcupan ACM epoxy resin (Electron Microscopy Sciences) overnight and then placed into fresh 100% Durcupan for three additional days. Lastly, the sections were embedded using two mold-release coated glass slides and kept at 60 °C for 72 h. X-ray microCT imaging was performed using Xradia 510 Versa (Carl Zeiss Microscopy) to evaluate tissue preservation and homogeneity before proceeding to EM imaging. Ultra-thin sections were cut using a diamond knife (Diatome) at a thickness of 70-90 nm. Thin sections were examined using a FEI Technai 12 Spirit (Thermo Fisher Scientific) transmission electron microscope operated at 80 kV. Micrographs were produced using a Tietz 2 k by 2 k CCD camera and collected using the SerialEM package. Images were then processed and analyzed using Fiji software (a bundled version of ImageJ, see above).

Single nuclei RNA sequencing

Nuclei isolation

Hippocampal formation (HIP), frontal cortex (middle frontal gyrus, Brodmann area 46; FC) or occipital cortex (Brodmann areas 19 and 18, OL) were dissociated, and nuclei isolation was performed separately for each of these regions using the Nuclei Isolation Kit: Nuclei EZ Prep (Sigma, #NUC101) as described by Habib et al. [13]. Briefly, tissue samples were Dounce homogenized in 2 ml of ice-cold EZ PREP and incubated on ice for 5 min. Following initial Dounce homogenization, an additional 2 ml of EZ PREP was added and the samples were incubated for 5 min. Nuclei suspension was centrifuged ($500 \times g$, 5 min and 4 °C) washed 1X in ice-cold EZ PREP buffer, and 1X in Nuclei Suspension Buffer (NSB; consisting of 1X PBS, 1% (w/v) BSA and 0.2 U/µl RNase inhibitor (Clontech, #2313A), resuspended in 1 ml of NSB and filtered through a 40 µm cell strainer. Nuclei were stained with SYTOX green (1:1000) and counted twice. A final concentration of 1000 nuclei per ul was used for loading onto the 10X Chromium (10X Genomics). Library construction was



performed using the Chromium Single Cell 3' Library and Gel Bead Kit v3.1 (10X Genomics) and sequencing on one high-output lane of the NextSeq 4000 (Illumina).

Mapping single nuclei reads to the genome

Using the Grch38 (1.2.0) reference from 10×Genomics, we made a pre-mRNA reference according to the steps detailed by 10X Genomics (https://support.10xgenomics.com/single-cell-gene512expression/software/pipelines/latest/advanced/references). Sequencing reads were aligned to the human pre-mRNA reference transcriptome using the 10×Genomics CellRanger pipeline (version 3.0.0; RRID: SCR_017344) with default parameters.

Quality control for expression matrix

Downstream analysis was performed using Seurat 4.0 in RStudio Version 4.1.0. An individual Seurat object was generated for each sample. Cells with fewer than 200 detected genes and with more than 5% of reads mapped to mitochondrial genes were filtered out. Doublets were identified using the DoubletFinder package [24] and removed assuming a doublet rate formation of 3%.

Data processing, analyses, visualization, and differential expression testing

The samples were then merged into a single Seurat object and SAVER (version 1.1.2) was used for missing data imputation [15]. Data were then normalized and scaled by using the Sctransform function in Seurat using the default parameters. Anchor-based sample Integration was performed on the normalized counts, with the number of features in the anchor finding process set to 3000. Nonlinear dimensionality reduction was performed by running UMAP on the first 20 PCs. Clustering was performed on the top 20 PCs as input in the FindNeighbors function, and a resolution of 0.2 in the FindClusters function, which resulted in 12 clusters and was in good agreement with the expression of known marker genes for cell types found in human brain. To enable an unbiased verification of the cluster identities, the top marker genes per cluster were computationally determined with the FindAllMarkers function, using the Wilcoxon rank sum test with a FDRcorrected p value ≤ 0.01 . Only positive marker genes were considered, and these markers were used with known celltype markers from the literature [12, 19, 20, 23] to carefully assign cluster identities.

Identification of differentially expressed genes in cell-type subpopulations

After cell-type annotation, for differential gene expression analysis across regions, each cell type was subseted, re-clustered and differential gene expression analysis was performed. To identify genes differentially expressed by a cell-type subpopulation across different regions (i.e., FC, HIP or OL), we performed differential expression based on the non-parametric Wilcoxon rank sum test accessed through the FindMarkers function in Seurat. We compared the differences between OL vs HIP, OL vs FC and HIP vs FC for each cell subtype. An FDR-corrected p value of ≤ 0.01 and a logFC threshold = 0.5 was used. For heatmaps of relative gene expression across cell-type subpopulations or across brain regions, SCT normalized counts of each gene were z-score transformed across all cells and then averaged across cells in each cluster to enhance visualization of differences among clusters. Thus, genes with high relative expression had above-average expression (positive z-scores) and genes with low relative expression had below-average expression (negative z-scores).

Correlation analysis

For all three regions we ran a correlation analysis between average expression of SCT normalized values of APOE and all other genes expressed in microglia and astrocytes, which were the two cell types that showed expression of APOE. We performed Gene ontology enrichment analysis on the list of genes with a statistically significant ($p \le 0.05$) r correlation coefficient $\ge \pm 0.5$ using PANTHER Gene List Analysis tools and Clusterprofiler [38].

Targeted analysis of microglia

Differentially expressed genes (DEG) identified in FC, HIP and OL were contrasted with gene signatures identified for acute (using LPS), and neurodegenerative chronic responses in a transgenic AD murine model as described by Krasemann et al. [18].

Results

Neuroimaging findings

The patient's cognitive profile at age 72 showed deficits in memory recall, with relatively preserved verbal learning and recognition, naming, verbal fluency, and visuospatial skills. She was then diagnosed with mild cognitive impairment, hypertension, and mixed dyslipidemia, and received statin treatment. A 24-months follow-up assessment showed

relatively stable cognitive function, but increased need for assistance in all instrumental activities of daily living (ADLs) and some basic ADLs mostly due to limited mobility. Her neurological examination was significant for frontal release signs. She was diagnosed with mild dementia at age 75, and her last assessment, completed at age 76, revealed further decline in cognition across all domains and ADLs (Supp. Table 1, online resource). Her cognitive profile then was indicative of global deficits, consistent with the atrophy noted in the postmortem neuropathological findings. Nine months before her death, she developed multiple hyperpigmented nodular lesions on her face and abdomen, associated with neck, torso, and inguinal soft tissue lesions. She was diagnosed with metastatic melanoma with multiorgan involvement. The family opted for palliative measures, and she died at home at age 77.

As part of the COLBOS longitudinal biomarker study [31], she underwent in vivo MRI and positron emission tomography (PET) measurements at age 73 and 75. At baseline, she had very high PET measurements of Aß plaque burden, particularly in neocortex, consistent with the overproduction of Aβ previously observed in PSEN1 E280A carriers, drawn out over nearly four decades [9, 31]. Aβ plaque burden appeared to decrease during the three-year follow-up period (Fig. 1D) but remained at higher levels compared to the other PSEN1 E280A carriers. Tau PET revealed an anatomical pattern of accumulation that deviated from that seen in sporadic Alzheimer's disease (AD) as well as that observed in other impaired PSEN1 E280A carriers, both cross-sectionally and longitudinally (Fig. 1A, B). In particular, tau PET showed relative sparing of temporal and parietal neocortex with abnormally elevated tau burden in the occipital cortex. Marked increases in PET measurements of tau tangle burden were observed during the three-year follow-up period, including in medial temporal regions (entorhinal cortex: 6.9%/year, amygdala: 5.1%/year) and most prominently in occipital cortex (lateral occipital: 11.5%/year) (Fig. 1C) consistent with her cognitive and functional decline during this period. On structural MRI measurements, her brain showed greater global atrophy relative to younger impaired PSEN1 mutation carriers (see Fig. 1E, consistent with autopsy findings). All these findings indicated a distinctive disease progression pattern.

Neuropathological findings

The family donated her brain for research in accordance with ethical guidelines. The brain was collected with a postmortem delay of 200 min, it presented with global atrophy, weighing 894.3 g, and with severe atherosclerosis in all major vessels. Microscopic examination confirmed moderate thinning of the gray matter ribbon and presence of AD pathological hallmarks by immunohistochemistry

(IHC). We examined 17 brain regions to assess Aβ and tau pathology distribution. The case was classified as a Braak VI due to extensive pTau isocortical pathology, Thal V due to the severity and wide distribution of Aβ pathology, and as CERAD C given the age of the patient and the high frequency of Aβ neuritic plaques. Furthermore, the integration of these pathological assessments following the NIAA guidelines gives a classification of AD neuropathological changes of A3B3C3 [16], that can be interpreted as high, similar to other PSEN1E280A cases. Although the case was classified as Braak VI [4], the distribution was atypical, with the highest density of tau signal in the hippocampus, amygdala and occipital cortex (Brodmann areas 17 and 18) and an unusually low density of pathological tau in other typicallyinvolved structures, including negligible tau signal in the frontal cortex (Fig. 2A, B, Supp. Figure 1, online resource). In contrast, Aβ pathology distribution showed an expected [6, 32] fronto-temporal predominant pattern (Fig. 2A–C, Supp. Figure 2, online resource). These postmortem findings are therefore similar to our in vivo tau PET findings, confirming the presence of a distinctive anatomical pattern when compared with other ADAD cases (Fig. 2C). The case was screened for both, TDP-43 and alpha synuclein pathologies. There were some granular diffuse TDP-43 intraneuronal deposits in the hippocampus and the amygdala, while there was no evidence of synucleopathy in any of the regions studied (Supp. Figure 3, online resource).

Tau pathology presented across isocortical regions (including temporal, parietal, and occipital cortex) with neuropil threads (NPTs) as well as dystrophic neurites (DNs), evenly distributed between supra and infragranular layers. In somatosensory cortices, namely the superior temporal gyrus, inferior parietal lobule, and striate cortex, NPTs mostly compromised layer II, the upper part of layer III, and layer V. Neurofibrillary tangles (NFTs) in the cortex, including the insula, showed no particular layering pattern except for the cingulate gyrus, where they were restricted to layer V. Among subcortical structures (including hypothalamus, caudate, and lenticular nucleus), NPTs were homogenously distributed without visible NFT formation. In sections of the midbrain, pons, and medulla oblongata, tau immunoreactivity was low with a predominance of NPTs. In the midbrain, there was a cluster of mature NFTs restricted to the borders between the tectum and the tegmentum whereas in the medulla oblongata there was pre-tangle formation in the inferior olivary complex. Finally, in the hippocampus, NFTs were distributed across Amon's horn with lower density in the CA3 region, and abundant dystrophic neurites in CA1. Tau immunoreactivity in the subiculum comprised mainly NPT without NFT and was noticeably low in the pre-subiculum. Scarce tau deposits were seen in frontal cortex and no tau immunoreactivity was detected in the meninges or the cerebellum, neither perivascular nor



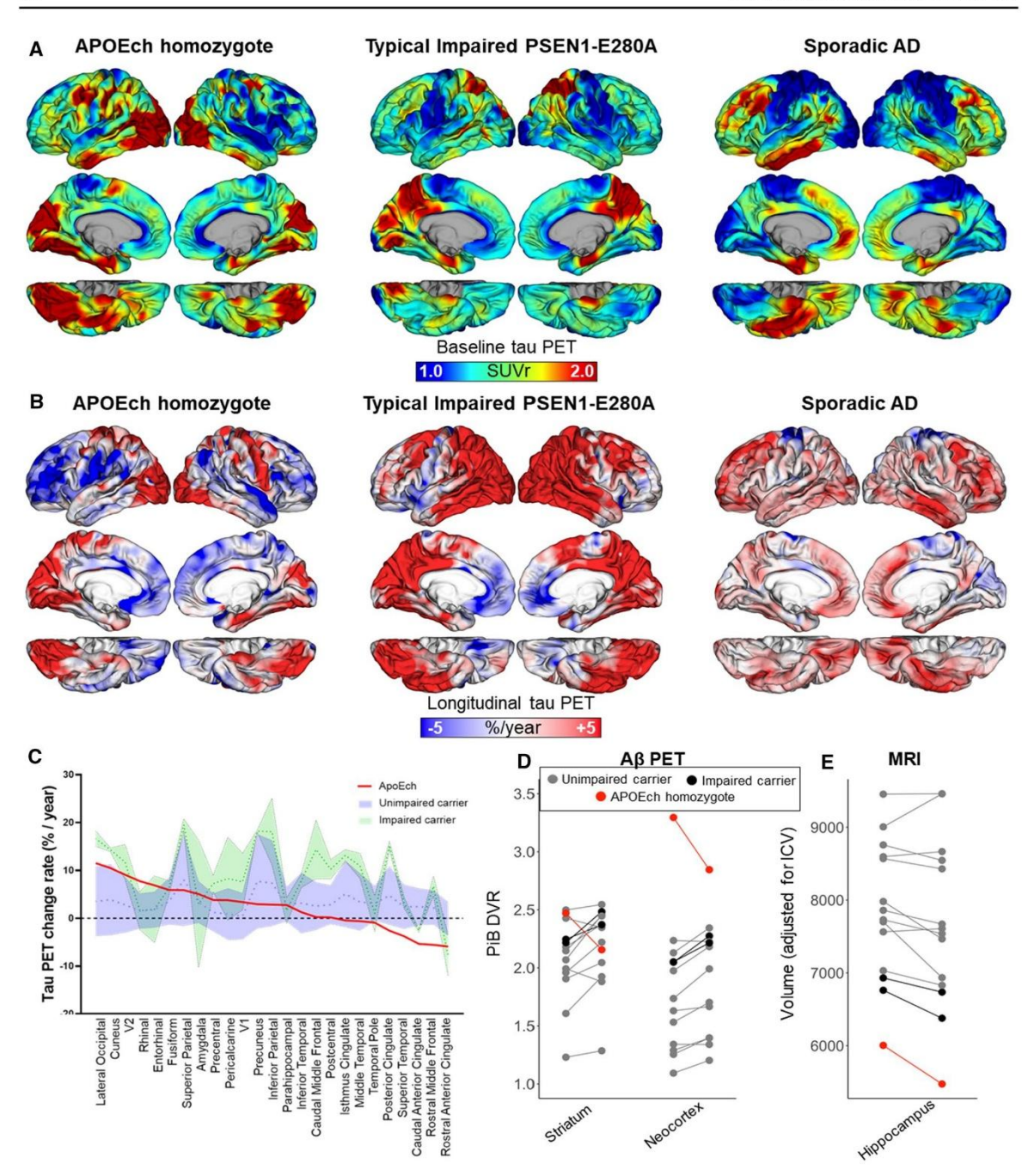


Fig. 1 Longitudinal tau PET imaging measures in an APOE3ch homozygote. A Surface rendering of tau PET (Flortaucipir) images (standardized uptake value ratio, SUVr), at baseline, 3-year follow-up (center), and B rate of change (expressed as %/year), in the APOE3ch homozygote, (left) a typical PSEN1-E280A impaired carrier (center) and a sporadic AD case (right). C Distribution area plot showing annualized percent change rates in tau PET for APOE3ch homozy-

gote (red line) relative to unimpaired (blue) and impaired (green) PSEN1-E280A carriers. Regions along the x-axis are ordered from highest to lowest change rate observed in the APOE3ch homozygote. **D** Spaghetti plots of A β PET (Pittsburgh Compound B, PiB) measurements at baseline and 2-year follow-up, **E** Structural MRI measurements at baseline and 2-year follow-up of hippocampal volume



subpial deposition (Fig. 2A, Supp. Table 1, and Supp. Figure 1, online resources). Cortical differences for tau deposits were confirmed by ultrastructural analysis (Supp. Figure 4, online resource). We did not see evidence of aging-related tau astrogliopathy or argyrophilic grain disease in the studied areas.

On the other hand, A\beta pathology was variable amongst studied areas, leading to a Thal phase 5 classification [33] (Supp. Figure 5A, online resource), with diverse severity and Aβ plaque subtypes. Cortical structures presented with varied subtypes and distribution of $A\beta$ plaques. The different hippocampal subfields varied in the type of plaques. In CA3, there were predominantly cored plaques with scant neuritic plaques, while CA2 lacked A\beta burden. Cored plaques as well as large diffuse plaques were observed in CA1, and mainly small diffuse plaques were visible in the subiculum. In the pre-subiculum, there was a profuse accumulation of Aβ in the form of diffuse plaque through the cerebral cortex without a particular layer distribution. In the entorhinal cortex, there were diffuse plaques in the subpial and layer I segments, whereas from layer II through VI, there were cored as well as neuritic plaques (Fig. 2C, Supp. Table 2, and Supp. Figure 2, online resources). Interestingly, the occipital cortex had mainly neuritic and cored plaques, and it was the only neocortical structure that showed Aß deposits in blood vessels (cerebral amyloid angiopathy, CAA) (Fig. 2C, Supp. Figure 5B, C, online resource), while the cerebellum was the only area with CAA in leptomeningeal vessels (Supp. Figure 5B, C, online resource), which contrasted to more generalized distribution of CAA in other PSEN1 E280A cases [7, 22]. Intraparenchymal CAA density correlated positively with tau IHC signal intensity, with amygdala and occipital cortex showing both CAA and high signal intensity for tau (Supp. Figure 5D, online resource). Notably, there was no correlation between A_β burden and CAA density (Supp. Figure 5E, online resource). We have recently reported mild to severe small vessel disease findings in the PSEN1 E280A population, together with enlargement of perivascular spaces and decreased perivascular astrocytic podocytes [22]. The APOE3ch case presented with some of these features, including cortical microinfarcts, arteriosclerosis and perivascular space enlargement. Some of these features were found to be above the average identified in this population, possibly related to the older age at the time of death (Supp. Figure 6, online resource).

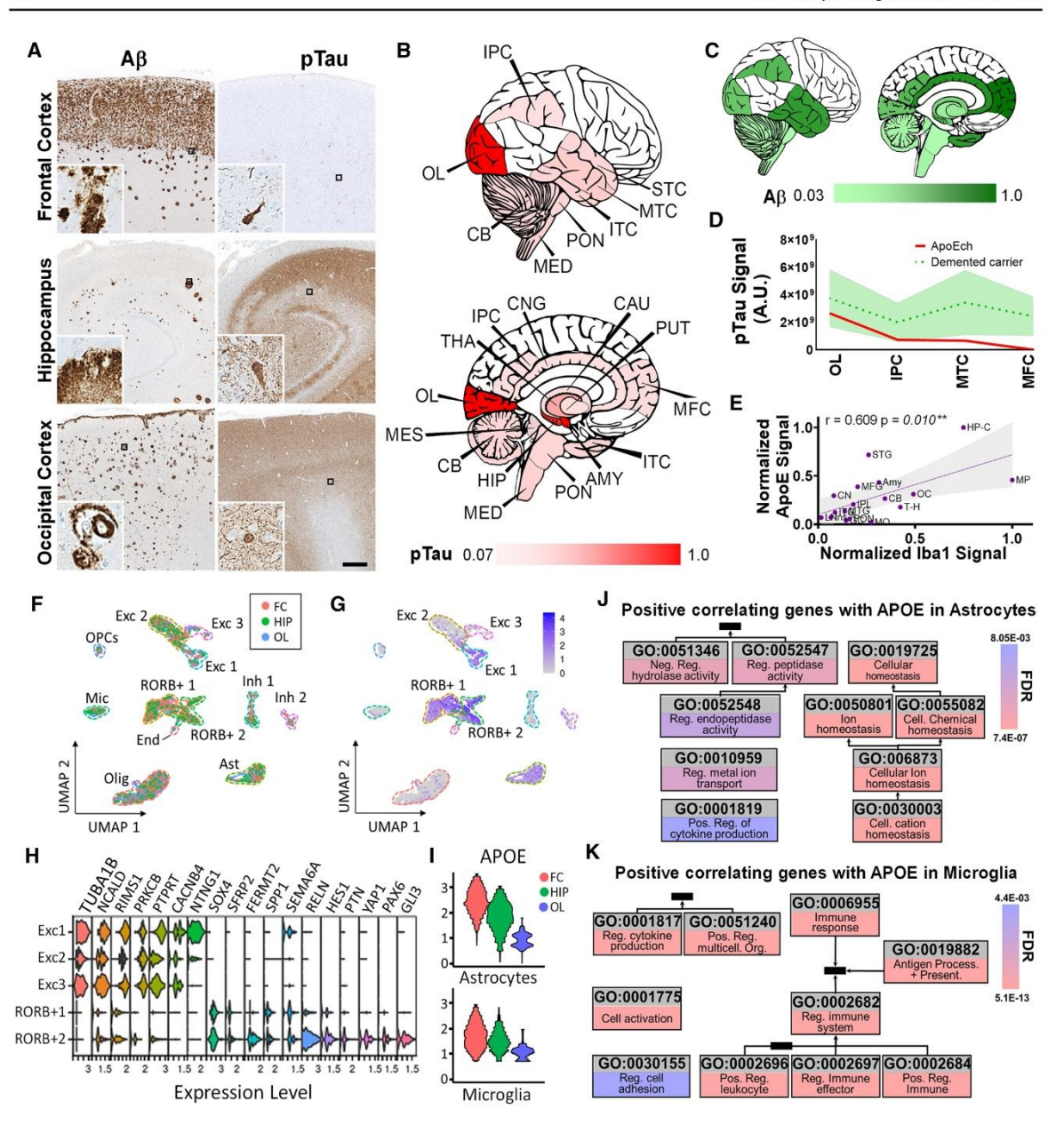
ApoE, Iba1 (microglia) and GFAP (astrocyte) signal and distribution were also evaluated in all regions to investigate any relationship between ApoE presence and glial reactivity to pathology (Supp. Figure 7A–C, online resource). ApoE signal showed a plaque-like pattern with stronger intensity in the areas more affected by tau pathology. Iba1 signal showed larger and more branched microglia in the hippocampal and occipital cortex, and ApoE and Iba1 immunoreactivity

were positively correlated (Fig. 2E). Regarding microglia profiles, cortical Iba1 signal was higher in occipital cortex when compared to frontal and temporal cortices, while TMEM119 signal was higher in frontal cortex and CD68 signal was higher in occipital cortex. CD68/TMEM119 signal ratio was higher in occipital cortex as well, indicating higher activation of microglia in this area (Supp. Figure 8, online resource). GFAP staining detected strong astrocytic immunoreactivity that was negatively correlated with the AB signal (Supp. Figures 7C, 9, online resource). Finally, the distribution pattern of pathological tau was not correlated with those of AB, ApoE, microglial marker Iba1 and the astrocytic marker GFAP (Supp. Figure 9, online resource). In summary, there were distinctive regional and local tau pathology and glial reactivity profiles suggestive of protection in most of the studied areas, except for areas also presenting with parenchymal CAA.

Single nuclei transcriptome findings

For a deeper understanding of regional pathological differences observed in this patient, we performed single nuclei RNA sequencing (snRNA seq) in frontal cortex, hippocampus and occipital cortex (Supp. Table 4, Supp. Figure 10, online resources). Clustering of these data revealed well-defined populations of both excitatory and inhibitory neuronal populations as well as glial populations (Supp. Tables 5, 6, online resource). Remarkably, a subset of excitatory neurons was clustered independently in frontal cortex and hippocampus, characterized by high expression of RORB (Fig. 2F, G, Supp. Figure 11A, B, online resource). Recently, RORB positive excitatory neurons were identified as being more abundant in the entorhinal cortex of non-demented cases unaffected by tau pathology in this region [21]. In our case, RORB positive neurons showed lower expression of synaptic-related genes while showing higher expression of genes associated with neurodevelopment (GO: 0030154, GO:0048699 and GO:0050767) (Fig. 2H, Supp. Figure 11C, online resource). By comparing expression levels and cluster distribution of RORB positive neurons in previously published datasets (Syn21788402, GSE97930) [20, 21], we identified that RORB showed higher expression and a more distinctive cluster distribution (Supp. Figure 12, online resource). Furthermore, we compared the expression profile of neurodevelopmental-associated genes between the RORB positive neurons identified in the APOE3ch case and previously published datasets. Even though neurodevelopmental genes or genes associated with neuronal morphogenesis are presented in RORB positive neurons in all datasets (ours and previously published controls), the specific set of genes were different (Supp. Figure 13, online resource). The identification of RORB





positive neurons in the areas less affected by tau, together with their distinctive expression profile, supports a selective response of vulnerable neuronal populations in this case. Regarding other cellular populations, we identified differential gene expression profiles in oligodendrocytes, astrocytes, and microglia, with specific subsets of genes highly expressed in the frontal cortex while being downregulated in the occipital cortex for the same cell types (Supp. Figures 14A–16 and 18, online resources). *APOE* was among the differentially expressed genes in astrocytes

and microglia with an expression gradient from high in frontal cortex down to low in occipital cortex (Fig. 2I, Supp. Figure 14B, C, online resource).

We explored which genes followed the same expression gradient as *APOE* by identifying gene expression correlates in astrocytes (Supp. Figure 17A, online resource) and microglia (Supp. Figure 18A, online resource). Our analyses revealed a positive correlation for a subset of homeostatic genes in astrocytes (Fig. 2J, Supp. Figure 17B, Supp. Table 7, online resources), with stronger correlations



√Fig. 2 Neuropathological and molecular characterization of an ADAD PSEN1E280A mutation carrier with two copies of the APOE3ch variant. A Representative panels for tau and AB pathology in frontal cortex, hippocampus, and occipital cortex. Insets show specific pathological features found in each brain area, such as NFT, dystrophic neurites and diffuse tau pathology, together with diffuse, core Aβ plaques and CAA. Bar=500 μm. B Graphic representation of general distribution and intensity of tau pathology signal with normalized lower and maximum values represented in red intensity. MFC medial frontal cortex, STC superior temporal cortex, MTC middle temporal cortex, ITC inferior temporal cortex, HIP hippocampus, AMY amygdala, CNG cingulate cortex, PUT putamen, CAU caudate, THA thalamus, IPC inferior parietal cortex, OL occipital lobe, CB cerebellum, MES mesencephalon, PON pons, MED medulla oblongata. C Graphic representation of distribution and intensity of Aß signal with normalized lower and maximum values represented in green intensity. D Distribution area plot showing tau integrated density signal in cortical areas in APOE3ch homozygote (red line) relative to impaired (green) PSEN1-E280A carriers. Areas are ordered according to the highest to lowest tau integrated density in the APOE3ch homozygote. E Correlation scatter plot for ApoE signal intensity against Iba1 signal intensity in all areas studied in B. A positive correlation was identified as statistically significant. (** $p \le 0.01$). F UMAP clustering plot of snRNA sequencing data from the frontal cortex (FC, red dots), hippocampus (HIP, green dots) and occipital cortex (OL, blue dots). Identified clusters include excitatory neurons (Exc 1, 2 and 3), oligodendrocyte precursor cells (OPCs), microglia (Mic), RORB positive neurons (RORB+1 and 2), inhibitory neurons (Inh 1 and 2), endothelial cells (End), oligodendrocytes (Olig) and astrocytes (Ast). G UMAP clustering plot of snRNA sequencing data from the analyzed areas depicting RORB expression levels in the different clusters. H Violin plots for differential expression of representative genes between excitatory neurons and RORB + neurons clusters. Excitatory clusters differentially express functional synaptic genes while RORB1 clusters express neuronal development genes. I Violin plots for APOE expression in FC, HIP and OL in astrocytes and microglia. J Top gene ontology terms from overrepresented genes positively correlating with APOE expression in astrocytes from frontal cortex, hippocampus and occipital cortex. K Top gene ontology terms from overrepresented genes positively correlating with APOE expression in microglia from frontal cortex, hippocampus and occipi-

in frontal cortex and hippocampus (Supp. Figure 18C, online resource). On the other hand, we determined a positive correlation for immune response regulation in microglia (Fig. 2K, Supp. Figure 19B, Supp. Table 8, online resources), with stronger correlations in occipital cortex (Supp. Figure 19C, online resource). Given the characteristic morphology of microglia found in the occipital cortex and increased correlation of immune response gene expression, we performed gene expression targeted analysis in microglia, taking as reference neurodegenerative microglia signatures for chronic (Supp. Figure 20A, online resource) and acute (Supp. Figure 21A, online resource) responses, according to Krasemann et al. [18]. We identified a subset of genes for cellular response in hippocampus and cellular locomotion in occipital cortex, indicating active inflammatory processes, while only some genes related to reactive oxygen species (ROS) response were found in frontal cortex (Supp. Figure 20B, online resource). In addition, only frontal cortex

showed a clear signature for acute immune response, with a subset of genes overrepresented for cellular energy regulation (Supp. Figure 21B, online resource). All these findings together suggest that astrocyte homeostasis is responsive to *APOE3ch* expression levels in more protected brain areas, while lower levels of *APOE3ch* expression can be associated with a more deleterious, chronic microglial response.

Discussion

Our current findings extend several observations suggested in the original report about this patient who was a carrier of the autosomal dominant Alzheimer's disease PSEN1 E280A variant and homozygote for the APOE3 Christchurch variant, and who only developed cognitive impairment thirty years after the typical age of clinical onset for her kindred [1]. For instance, amyloid and tau pathologies were differentially impacted in a pattern not observed in other forms of AD. Longitudinal follow-up measures of in vivo PET imaging and postmortem neuropathology analyses confirmed this observation. This discrepancy between Aβ and tau pathology indicates that putative APOE3ch protective molecular mechanisms may be modulated further by other pathological events during the course and progression of disease. We have recently reported a prominent role for tau pathophysiology in the modulation of age of onset in this ADAD population [32]. Similar to our current findings, AD protected cases showed decreased tau cortical pathology, with the exception of the occipital cortex which showed the same degree of tau pathology regardless of age of onset [32]. Another finding supporting the distinct features of AD pathology in this patient is the almost exclusive presence of CAA in the occipital cortex. This finding is consistent with previous reports in sporadic AD cases of increased CAA severity in this region [2], possibly related to A_β drainage and structural characteristics of the brain vascular system. Moreover, an association between parenchymal CAA pathology, perivascular tau pathology [36], and neuronal tau pathology severity has been described [27], consistent with this case's unique pattern of pathology in which the few regions affected with CAA showed also higher tau pathology. We suggest that, even though the homozygous APOE3ch variant likely rendered general protection for tau pathology in this patient, it could not render specific protection against CAA-related tau pathology in the occipital cortex, possibly due to the local effects of CAA pathology and associated tau deposition. Additionally, pathological tau has been reported in the occipital cortex of aged non-demented subjects [28]. Given the advanced age of the PSEN1 E280A APOE3ch case, the pathology pattern observed in this patient can be a cumulative result of different processes including senescence.



Of note, even though neuroimaging and neuropathological findings revealed severe pathology in the occipital cortex, a region affected in Posterior Cortical Atrophy (PCA) [5], this patient did not present clinical features consistent with a PCA syndrome, such as visual and/or spatial impairments. Further, in PCA the neurodegenerative process is known to follow an occipito-parietal to temporal lobe progression, and in the E280A APOE3ch case we observed a relative sparing of parietal and frontal cortices (Supp. Fig. 22, online resource), which may explain, at least in part, the preserved visuo-spatial functioning in this case.

The specific gene expression profile presented by RORB positive neurons in frontal cortex and hippocampus provides further evidence for complex mechanisms of protection in this patient. The expression of neurogenesis-related genes in these neurons can be contrasted to previous findings in control cases [20, 21] and decreased adult neurogenesis in AD patients [25]. We discarded the possibility that the expression of proliferative genes in these cells would indicate neural stem cell activity or that they could be related to the metastatic melanoma present in the patient (Supp. Figure 23, online resource), suggesting alternative functions of neurogenesis-related genes in this context. It is known that ApoE has a relevant role in AD pathophysiology in astrocytes and immune response to the disease [35, 36]. Depletion of astrocytic APOE4 reduces tau levels [35], while ApoE specific immunotherapy against human ApoE reduces CAA [37], both findings obtained in murine models. ApoE also functions as an activator of microglia response against Aβ plaque deposition [34]. In the APOE3ch case, a regional decreasing gradient of APOE expression levels from frontal cortex to occipital cortex was associated with astrocyte homeostasis and the presence of activated neurodegenerative microglia in occipital cortex, the most affected area with lower APOE expression levels, supporting the idea of a dose-dependent mechanism of protection with the participation of both cell types. It is intriguing that, in contrast to APOE expression levels, ApoE IHC signal intensity did not follow a gradient pattern but was more easily associated with AD pathology regional severity. This might be explained by pathological ApoE protein aggregation, together with or independent to other protein aggregates as it has been observed in demented cases [10]. It should be also noted that in general, gene expression does not necessarily represent actual protein levels and further studies would be necessary to confirm our findings regarding the pathways involved.

In summary, we described the in vivo follow-up and postmortem findings of an ADAD *PSENI* E280A carrier who also was found to be homozygous for the *APOE3* Christchurch variant, and who was protected against AD symptoms for almost three decades. We identified a distinct anatomical pattern of tau pathology, including atypical accumulation of in vivo tau pathology, as measured by

PET imaging, and an unusual regional distribution of tau aggregates and CAA pathology. Our findings suggest that APOE3ch may have a regionally specific role in modifying the effect of tau on the severity, progression, and clinical presentation of AD, and that its protective role is associated with its expression and resulting impact on astrocytic and microglia function. We previously reported the impact of tau pathology as a disease onset modifier [32] and disease progression marker in vivo [31] in this ADAD population. This study has some limitations, the most prominent being that the findings are based on the analyses of one case and the fact that mere associations cannot address causal connections by themselves. Nevertheless, the findings draw a remarkable picture on the relationship between ApoE function as a modulator of pathology in Alzheimer's disease. Further studies involving more protected patients would be ideal to compare and validate our findings, but locating another ADAD case homozygous for the ApoE3ch variant might be very challenging.

Our findings provide evidence supporting tau pathology as the main driver of cognitive decline in *PSEN* E280A ADAD, as suggested by other previous findings in this population [31, 32], and that the protection against this pathology should be clinically effective. The strong putative protective effect of homozygous *APOE3ch* in this patient suggests that ApoE may be one of the main modulators of tau pathology in AD, possibly via different mechanisms including aggregation by modifying ApoE heparin binding [1], and homeostatic regulation of glial cells. More studies are necessary to further examine the interactions between ApoE and tau, to clarify the role of adult neurogenesis in AD protection, and to advance possible therapies mimicking the effect of *APOE3ch* in AD pathophysiology.

Supplementary Information The online version contains supplementary material available at https://doi.org/10.1007/s00401-022-02467-8.

Acknowledgements We thank the Colombian families with autosomal dominant Alzheimer's Disease and participants in the AD Genetics Consortium for making this work possible. This study was supported by grants R01 AG054671 from National Institute of Aging (Y.T.Q), the Massachusetts General Hospital Executive Committee on Research (Y.T.Q), Alzheimer's Association Research Grant (Y.T.Q), the Deutsche Forschungsgemeinschaft (DFG) project CellNetFAD # 458854216 (D.S-F.), UH3 NS100121 and RF1 NS110048 from National Institute of Neurological Disorders and Stroke (J.F.A-V. and D.S-F)., Alzheimer's Association Research Fellowship (C.V.C), Comité para el Desarrollo de la Investigación (CODI) of Universidad de Antioquia (F.L.), Fapesp Grant 2019/22819-8 (M.C.A.), the Werner Otto Stiftung 14/97 (S.K.), and by the BMBF with the "Understanding disease modifiers and heterogeneity in Alzheimers disease - UndoAD" grant (D.S-F and M.G.).

Author contributions DS-F, FL, and YTQ conceived this work. DS-F, JS, KSK, FL, and YTQ drafted the manuscript. AB, CV-C, LR-G, DA, collected and analyzed clinical and phenotypic data. JS, RAS, KAJ,



and YTQ analyzed and interpreted imaging data. AV-L and DA collected brain donations. JA-U, AV and KSK analyzed genotypic data. DS-F, AV-L, TGB, CLWIII and MG performed neuropathological diagnoses. DS-F, NDV-M, JLL and SK performed neuropathological quantitative analyses. DB and ME performed ultrastructural studies and analyses. DS-F and MCA performed single nuclei sequencing analyses. All authors reviewed, discussed, and approved the manuscript before submission.

Funding Open Access funding enabled and organized by Projekt DEAL.

Declarations

Conflicts of interest RAS has received personal compensation from AC Immune, Eisai, Roche, and Takeda, and research grant support from Eli Lilly and Janssen. YTQ, JFAV, EMR, FL are listed as coinventors of a patent application for therapeutics modulating interactions between APOE and HSPG filed by MGB. All other authors have no competing interests.

Open Access This article is licensed under a Creative Commons Attribution 4.0 International License, which permits use, sharing, adaptation, distribution and reproduction in any medium or format, as long as you give appropriate credit to the original author(s) and the source, provide a link to the Creative Commons licence, and indicate if changes were made. The images or other third party material in this article are included in the article's Creative Commons licence, unless indicated otherwise in a credit line to the material. If material is not included in the article's Creative Commons licence and your intended use is not permitted by statutory regulation or exceeds the permitted use, you will need to obtain permission directly from the copyright holder. To view a copy of this licence, visit http://creativecommons.org/licenses/by/4.0/.

References

- Arboleda-Velasquez JF, Lopera F, O'Hare M, Delgado-Tirado S, Marino C, Chmielewska N et al (2019) Resistance to autosomal dominant Alzheimer's disease in an APOE3 Christchurch homozygote: a case report. Nat Med 25:1680–1683. https://doi. org/10.1038/s41591-019-0611-3
- Attems J, Jellinger KA, Lintner F (2005) Alzheimer's disease pathology influences severity and topographical distribution of cerebral amyloid angiopathy. Acta Neuropathol 110:222–231. https://doi.org/10.1007/s00401-005-1064-y
- Bahl E, Koomar T, Michaelson JJ (2017) cerebroViz: an R package for anatomical visualization of spatiotemporal brain data. Bioinformatics 33:762–763. https://doi.org/10.1093/bioinformatics/btw726
- Braak H, Braak E (1991) Neuropathological stageing of Alzheimer-related changes. Acta Neuropathol 82:239–259. https://doi. org/10.1007/bf00308809
- Crutch SJ, Schott JM, Rabinovici GD, Murray M, Snowden JS, van der Flier WM et al (2017) Consensus classification of posterior cortical atrophy. Alzheimers Dement 13:870–884. https://doi. org/10.1016/j.jalz.2017.01.014
- Desikan RS, Cabral HJ, Hess CP, Dillon WP, Glastonbury CM, Weiner MW et al (2009) Automated MRI measures identify individuals with mild cognitive impairment and Alzheimer's disease. Brain 132:2048–2057. https://doi.org/10.1093/brain/awp123

- Dinkel F, Trujillo-Rodriguez D, Villegas A, Streffer J, Mercken M, Lopera F et al (2020) Decreased deposition of beta-amyloid 1–38 and increased deposition of beta-amyloid 1–42 in brain tissue of presenilin-1 E280A familial Alzheimer's disease patients. Front Aging Neurosci 12:220. https://doi.org/10.3389/fnagi.2020. 00220
- Fischl B, Rajendran N, Busa E, Augustinack J, Hinds O, Yeo BTT et al (2008) Cortical folding patterns and predicting cytoarchitecture. Cereb Cortex 18:1973–1980. https://doi.org/10.1093/cercor/ htm225
- Fleisher AS, Chen K, Quiroz YT, Jakimovich LJ, Gomez MG, Langois CM et al (2012) Florbetapir PET analysis of amyloid-β deposition in the presenilin 1 E280A autosomal dominant Alzheimer's disease kindred: a cross-sectional study. Lancet Neurol 11:1057–1065. https://doi.org/10.1016/S1474-4422(12)70227-2
- Gal J, Katsumata Y, Zhu H, Srinivasan S, Chen J, Johnson LA et al (2022) Apolipoprotein E proteinopathy is a major dementiaassociated pathologic biomarker in individuals with or without the APOE Epsilon 4 Allele. Am J Pathol 192:564–578. https:// doi.org/10.1016/j.ajpath.2021.11.013
- Greve DN, Svarer C, Fisher PM, Feng L, Hansen AE, Baare W et al (2014) Cortical surface-based analysis reduces bias and variance in kinetic modeling of brain PET data. Neuroimage 92:225–236. https://doi.org/10.1016/j.neuroimage.2013.12.021
- Grubman A, Chew G, Ouyang JF, Sun G, Choo XY, McLean C et al (2019) A single-cell atlas of entorhinal cortex from individuals with Alzheimer's disease reveals cell-type-specific gene expression regulation. Nat Neurosci 22:2087–2097. https://doi.org/10.1038/s41593-019-0539-4
- Habib N, Avraham-Davidi I, Basu A, Burks T, Shekhar K, Hofree M et al (2017) Massively parallel single-nucleus RNA-seq with DroNc-seq. Nat Methods 14:955–958. https://doi.org/10.1038/ nmeth.4407
- Hanseeuw BJ, Betensky RA, Mormino EC, Schultz AP, Sepulcre J, Becker JA et al (2018) PET staging of amyloidosis using striatum. Alzheimers Dement 14:1281–1292. https://doi.org/10.1016/j. jalz.2018.04.011
- Huang M, Wang J, Torre E, Dueck H, Shaffer S, Bonasio R et al (2018) SAVER: gene expression recovery for single-cell RNA sequencing. Nat Methods 15:539–542. https://doi.org/10.1038/ s41592-018-0033-z
- Hyman BT, Phelps CH, Beach TG, Bigio EH, Cairns NJ, Carrillo MC et al (2012) National Institute on Aging-Alzheimer's Association guidelines for the neuropathologic assessment of Alzheimer's disease. Alzheimers Dement 8:1–13. https://doi.org/10.1016/j.jalz.2011.10.007
- Johnson KA, Schultz A, Betensky RA, Becker JA, Sepulcre J, Rentz D et al (2016) Tau positron emission tomographic imaging in aging and early Alzheimer disease. Ann Neurol 79:110–119. https://doi.org/10.1002/ana.24546
- Krasemann S, Madore C, Cialic R, Baufeld C, Calcagno N, El Fatimy R et al (2017) The TREM2-APOE pathway drives the transcriptional phenotype of dysfunctional microglia in neurodegenerative diseases. Immunity 47:566-581.e9. https://doi.org/10. 1016/j.immuni.2017.08.008
- Lake BB, Ai R, Kaeser GE, Salathia NS, Yung YC, Liu R et al (2016) Neuronal subtypes and diversity revealed by single-nucleus RNA sequencing of the human brain. Science 352:1586–1590. https://doi.org/10.1126/science.aaf1204
- Lake BB, Chen S, Sos BC, Fan J, Kaeser GE, Yung YC et al (2018) Integrative single-cell analysis of transcriptional and epigenetic states in the human adult brain. Nat Biotechnol 36:70–80. https://doi.org/10.1038/nbt.4038
- Leng K, Li E, Eser R, Piergies A, Sit R, Tan M et al (2021)
 Molecular characterization of selectively vulnerable neurons in



- Alzheimer's disease. Nat Neurosci 24:276–287. https://doi.org/ 10.1038/s41593-020-00764-7
- 22. Littau JL, Velilla L, Hase Y, Villalba-Moreno ND, Hagel C, Drexler D et al (2022) Evidence of Amyloid β independent small vessel pathology in familial Alzheimer's disease. Brain Pathol. https://doi.org/10.1111/bpa.13097
- Mathys H, Davila-Velderrain J, Peng Z, Gao F, Mohammadi S, Young JZ et al (2019) Single-cell transcriptomic analysis of Alzheimer's disease. Nature 570:332–337. https://doi.org/10.1038/s41586-019-1195-2
- McGinnis CS, Murrow LM, Gartner ZJ (2019) DoubletFinder: doublet detection in single-cell RNA sequencing data using artificial nearest neighbors. Cell Syst 8:329-337.e4. https://doi.org/10.1016/j.cels.2019.03.003
- Moreno-Jiménez EP, Flor-García M, Terreros-Roncal J, Rábano A, Cafini F, Pallas-Bazarra N et al (2019) Adult hippocampal neurogenesis is abundant in neurologically healthy subjects and drops sharply in patients with Alzheimer's disease. Nat Med 25:554–560. https://doi.org/10.1038/s41591-019-0375-9
- Mormino EC, Betensky RA, Hedden T, Schultz AP, Amariglio RE, Rentz DM et al (2014) Synergistic effect of β-amyloid and neurodegeneration on cognitive decline in clinically normal individuals. JAMA Neurol 71:1379–1385. https://doi.org/10.1001/jamaneurol.2014.2031
- Nichols JB, Malek-Ahmadi M, Tariot PN, Serrano GE, Sue LI, Beach TG (2021) Vascular lesions, APOE ε4, and tau pathology in Alzheimer disease. J Neuropathol Exp Neurol 80:240–246. https:// doi.org/10.1093/jnen/nlaa160
- Pikkarainen M, Kauppinen T, Alafuzoff I (2009) Hyperphosphorylated tau in the occipital cortex in aged nondemented subjects.
 J Neuropathol Exp Neurol 68:653–660. https://doi.org/10.1097/NEN.0b013e3181a6ee45
- Quiroz YT, Sperling RA, Norton DJ, Baena A, Arboleda-Velasquez JF, Cosio D et al (2018) Association between amyloid and tau accumulation in young adults with autosomal dominant Alzheimer disease. JAMA Neurol 75:548–556. https://doi.org/10. 1001/jamaneurol.2017.4907
- Sanchez JS, Becker JA, Jacobs HIL, Hanseeuw BJ, Jiang S, Schultz AP et al (2021) The cortical origin and initial spread of medial temporal tauopathy in Alzheimer's disease assessed with positron emission tomography. Sci Transl Med 13:eabc0655. https://doi.org/10.1126/scitranslmed.abc0655

- Sanchez JS, Hanseeuw BJ, Lopera F, Sperling RA, Baena A, Bocanegra Y et al (2021) Longitudinal amyloid and tau accumulation in autosomal dominant Alzheimer's disease: findings from the Colombia-Boston (COLBOS) biomarker study. Alzheimers Res Ther 13:27. https://doi.org/10.1186/s13195-020-00765-5
- Sepulveda-Falla D, Chavez-Gutierrez L, Portelius E, Vélez JI, Dujardin S, Barrera-Ocampo A et al (2021) A multifactorial model of pathology for age of onset heterogeneity in familial Alzheimer's disease. Acta Neuropathol 141:217–233. https://doi.org/ 10.1007/s00401-020-02249-0
- Thal DR, Rüb U, Orantes M, Braak H (2002) Phases of A betadeposition in the human brain and its relevance for the development of AD. Neurology 58:1791–1800. https://doi.org/10.1212/ wnl.58.12.1791
- Ulrich JD, Ulland TK, Mahan TE, Nyström S, Nilsson KP, Song WM et al (2018) ApoE facilitates the microglial response to amyloid plaque pathology. J Exp Med 215:1047–1058. https://doi.org/ 10.1084/jem.20171265
- Wang C, Xiong M, Gratuze M, Bao X, Shi Y, Andhey PS et al (2021) Selective removal of astrocytic APOE4 strongly protects against tau-mediated neurodegeneration and decreases synaptic phagocytosis by microglia. Neuron 109:1657-1674.e7. https://doi. org/10.1016/j.neuron.2021.03.024
- Williams S, Chalmers K, Wilcock GK, Love S (2005) Relationship of neurofibrillary pathology to cerebral amyloid angiopathy in Alzheimer's disease. Neuropathol Appl Neurobiol 31:414–421. https://doi.org/10.1111/j.1365-2990.2005.00663.x
- Xiong M, Jiang H, Serrano JR, Gonzales ER, Wang C, Gratuze M et al (2021) APOE immunotherapy reduces cerebral amyloid angiopathy and amyloid plaques while improving cerebrovascular function. Sci Transl Med 13:eabd7522. https://doi.org/10.1126/ scitranslmed.abd7522
- Yu G, Wang L-G, Han Y, He Q-Y (2012) clusterProfiler: an R package for comparing biological themes among gene clusters.
 OMICS 16:284–287. https://doi.org/10.1089/omi.2011.0118

Publisher's Note Springer Nature remains neutral with regard to jurisdictional claims in published maps and institutional affiliations.

Authors and Affiliations

Diego Sepulveda-Falla ¹ · Justin S. Sanchez · Maria Camila Almeida ^{3,4} · Daniela Boassa ^{5,6} · Juliana Acosta-Uribe · Clara Vila-Castelar · Liliana Ramirez-Gomez · Ana Baena · David Aguillon · Nelson David Villalba-Moreno · Jessica Lisa Littau · Andres Villegas · Thomas G. Beach · Charles L. White III · Mark Ellisman · Solution · Susanne Krasemann · Markus Glatzel · Keith A. Johnson · Reisa A. Sperling · Eric M. Reiman · Joseph F. Arboleda-Velasquez · Kenneth S. Kosik · Francisco Lopera · Yakeel T. Quiroz · Solution · Joseph · Solution · S

- Molecular Neuropathology of Alzheimer's Disease, Institute of Neuropathology, University Medical Center Hamburg-Eppendorf, Hamburg, Germany
- Department of Neurology, Massachusetts General Hospital, Harvard Medical School, Boston, MA, USA
- Department of Molecular, Cellular and Developmental Biology, Neuroscience Research Institute, University of California, Santa Barbara, CA 93106, USA
- ⁴ Center for Natural and Human Sciences, Federal University of ABC, São Bernardo do Campo, SP, Brazil
- National Center for Microscopy and Imaging Research (NCMIR), San Diego School of Medicine (UCSD), University of California, La Jolla, San Diego, CA 92093, USA
- Department of Neurosciences, San Diego School of Medicine (UCSD), University of California, La Jolla, San Diego, CA 92093, USA
- Department of Psychiatry, Massachusetts General Hospital, Harvard Medical School, Boston, MA, USA



- ⁸ Grupo de Neurociencias de Antioquia, Facultad de Medicina, Universidad de Antioquia, Medellín, Antioquia, Colombia
- Department of Neuropathology, Banner Sun Health Research Institute, Sun City, AZ, USA
- Department of Pathology, Neuropathology Laboratory, University of Texas Southwestern Medical Center, Dallas, USA
- Institute of Neuropathology, University Medical Center Hamburg-Eppendorf, Hamburg, Germany
- Experimental Pathology Core Facility, University Medical Center Hamburg-Eppendorf, Hamburg, Germany
- Department of Radiology, Massachusetts General Hospital, Harvard Medical School, Boston, MA, USA
- ¹⁴ The Banner Alzheimer's Institute, Phoenix, AZ, USA
- Schepens Eye Research Institute of Mass Eye and Ear and Department of Ophthalmology, Harvard Medical School, Boston, MA, USA

8. Publication II

nature medicine



Article

https://doi.org/10.1038/s41591-023-02318-3

Resilience to autosomal dominant Alzheimer's disease in a Reelin-COLBOS heterozygous man

Received: 18 October 2022

Accepted: 22 March 2023

Published online: 15 May 2023

Check for updates

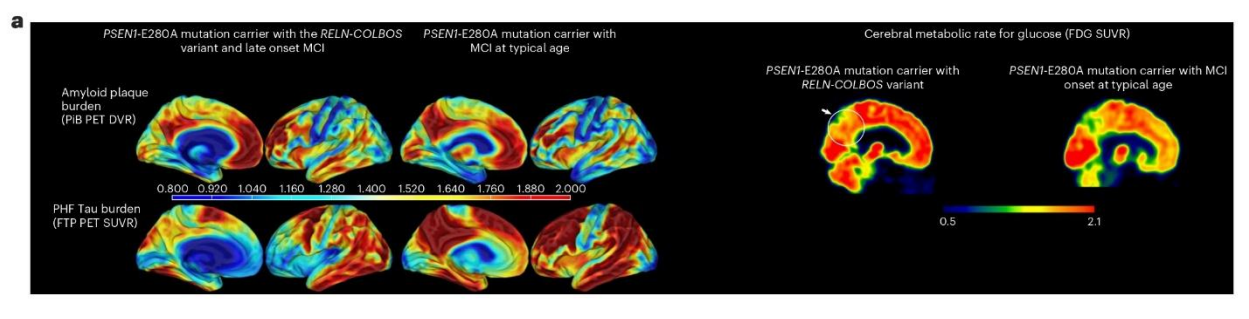
Francisco Lopera^{1,2,16}, Claudia Marino ^{3,16}, Anita S. Chandrahas^{3,16}, Michael O'Hare^{3,16}, Nelson David Villalba-Moreno^{4,16}, David Aguillon ^{1,2}, Ana Baena¹, Justin S. Sanchez ⁵, Clara Vila-Castelar ⁶, Liliana Ramirez Gomez⁵, Natalia Chmielewska³, Gabriel M. Oliveira^{3,6}, Jessica Lisa Littau⁴, Kristin Hartmann⁴, Kyungeun Park⁴, Susanne Krasemann ⁴, Markus Glatzel ⁶, Dorothee Schoemaker^{3,6}, Lucia Gonzalez-Buendia³, Santiago Delgado-Tirado³, Said Arevalo-Alquichire ³, Kahira L. Saez-Torres³, Dhanesh Amarnani³, Leo A. Kim ³, Randall C. Mazzarino ³, Harper Gordon ³, Yamile Bocanegra ¹, Andres Villegas^{1,2}, Xiaowu Gai^{7,8}, Moiz Bootwalla⁷, Jianling Ji ^{7,8}, Lishuang Shen⁷, Kenneth S. Kosik ⁹, Yi Su ¹⁰, Yinghua Chen ¹⁰, Aaron Schultz⁵, Reisa A. Sperling ¹¹, Keith Johnson ^{11,12}, Eric M. Reiman ^{10,13,14,15}, Diego Sepulveda-Falla ^{4,17}, Joseph F. Arboleda-Velasquez ^{3,17} & Yakeel T. Quiroz ^{1,5,6,17}

We characterized the world's second case with ascertained extreme resilience to autosomal dominant Alzheimer's disease (ADAD). Side-by-side comparisons of this male case and the previously reported female case with ADAD homozygote for the *APOE3* Christchurch (*APOECh*) variant allowed us to discern common features. The male remained cognitively intact until 67 years of age despite carrying a *PSENI*-E280A mutation. Like the *APOECh* carrier, he had extremely elevated amyloid plaque burden and limited entorhinal Tau tangle burden. He did not carry the *APOECh* variant but was heterozygous for a rare variant in *RELN* (H3447R, termed *COLBOS* after the Colombia–Boston biomarker research study), a ligand that like apolipoprotein E binds to the VLDLr and APOEr2 receptors. *RELN-COLBOS* is a gain-of-function variant showing stronger ability to activate its canonical protein target Dab1 and reduce human Tau phosphorylation in a knockin mouse. A genetic variant in a case protected from ADAD suggests a role for *RELN* signaling in resilience to dementia.

We have characterized about 1,200 individuals carrying the presenilin 1 (PSENI) E280A mutation from the world's largest known kindred with autosomal dominant Alzheimer's disease (ADAD). Carriers of the PSENI-E280A mutation develop mild cognitive impairment (MCI)

by the median age of 44 years (95% confidence interval (Cl) = 43–45) and dementia by 49 years (95% Cl = 49–50) 1 , with rare exceptions 2 . We previously reported a female carrying the *PSENI*-E280A mutation with two copies of the *APOE3* Christchurch (*APOECh*) (R136S) gene variant

A full list of affiliations appears at the end of the paper. Me-mail: d.sepulveda-falla@uke.uni-hamburg.de; joseph_arboleda@meei.harvard.edu; yquiroz@mgh.harvard.edu



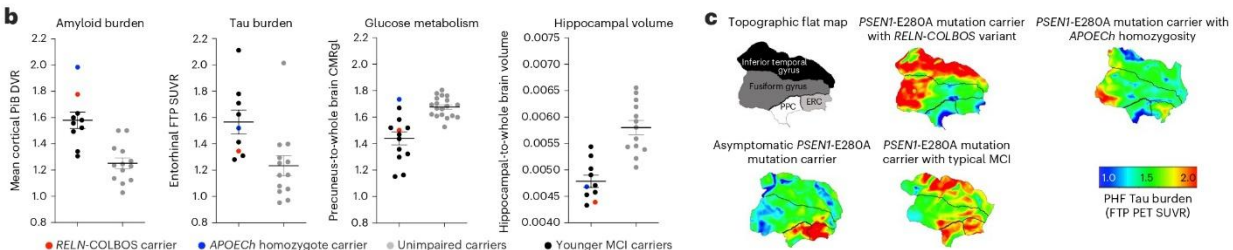


Fig. 1| PET imaging of the RELN-COLBOS (H3447R) carrier. a, Representative PiB PET amyloid and FTP Tau PET imaging of the male case with RELN-COLBOS (left) compared to a PSENI-E280A mutation carrier with MCl at a typical age (right). For both measurements, specific binding of the tracer is represented using a color-coded scale with blue being the lowest (DVR or SUVR = 0.8) and red being the highest (DVR or SUVR = 2.00) degree of binding. Right, representative FDG PET precuneus cerebral metabolic rate for glucose (CMRgI) of the male case with RELN-COLBOS (left) compared to a PSENI-E280A carrier with MCl at a typical age (right). Binding affinity of the dye is represented using a color-coded scale with blue being the lowest (SUVR = 0.5) and red being the highest (SUVR = 2.1) degree of binding. PHF, paired helical filament. b, Dot plot analysis of the imaging measurements shown in a for amyloid and Tau burden, glucose metabolism and hippocampal volume. Brain imaging measurements of the male case with RELN-COLBOS (red dot) compared to the previously published APOECh homozygote

female (blue dot), unimpaired PSENI-E280A carriers (gray dots, n=18 for the glucose metabolism panel, n=13 for all other panels) and younger carriers of the MCI PSENI-E280A mutation (black dots, n=7 for the Tau burden plot, n=8 for the amyloid burden and hippocampal volume plots, n=11 for glucose metabolism)². Some previously published data points are included in the figures because they are the only available data for comparison². Data are expressed as individual values with the mean \pm s.e.m. c, Anatomical details of Tau burden in the temporal cortex. Flat map representations of the right hemisphere temporal lobe cortex for regions of interest (ROIs) (top left, ERC), with Tau PET (FTP) overlay for four cases. The asymptomatic PSENI-E280A carrier was 38 years old; the PSENI-E280A carrier with typical MCI was 44 years old. The male carrier of RELN-COLBOS was notable for having relatively lower Tau burden in the medial temporal regions (ERC and PPC), compared to typical PSENI-E280A mutation carriers.

who remained cognitively unimpaired for nearly 30 years after the expected age at clinical onset 2 .

In this article, we report the clinical, in vivo neuroimaging, genetic and neuropathological characteristics of a male case with the *PSENI*-E280A mutation from the same population also presenting with an extreme phenotype of delayed age at clinical onset of ADAD.

Results

Case report

We identified a male carrier of the *PSENI*-E280A mutation who remained cognitively intact until age 67. He completed 5 years of formal education in his home country (Colombia) and worked until he retired in his early 60s. He was married and had two children. First cognitive assessment at age 67 revealed limited verbal learning skills and language difficulties in the context of functional independence. The patient was diagnosed with MCI, characterized by short-term memory and verbal fluency decline at age 70.

At age 72, his language had deteriorated further, progressing to mild dementia (Supplementary Table 1). Cognitive decline was preceded by a urinary tract infection-related episode of septic shock. At age 73, he required assistance with basic and instrumental activities of daily living, and met criteria for moderate dementia. He died at the age of 74 years from aspiration pneumonia; his relatives agreed to a brain donation for neuropathological study.

His sister also carried the *PSENI*-E280A mutation, had severe dementia when she was first evaluated at age 64 and progressed to

end-stage dementia at age 72 (see the pedigree in Supplementary Fig. 1). According to the family, she had hypothyroidism, hypertension, depression and cognitive decline at age 58 and developed dementia at age 61. Although less protected than her brother, her MCI began 14 years and her dementia 12 years later than expected for this population. Dementia was preceded by ocular trauma and tibial fracture after a fall, which required surgery under general anesthesia. She died at age 73 of sepsis of pulmonary origin. Additional clinical details about the cases can be found in the supplementary results section of the Supplementary Information.

The male patient was enrolled in the Colombia-Boston biomarker research study (COLBOS) and underwent neuroimaging examinations at the Massachusetts General Hospital (MGH) when he was 73 years old (see Supplementary Table 2 for the demographic information). Amyloid positron emission tomography (PET), measured using cortical-to-cerebellar Pittsburgh compound B (PiB), revealed that the individual's levels of cortical amyloid beta (Aβ) plaque burden were higher (distribution volume ratio (DVR) = 1.77) compared to that of younger impaired carriers from this kindred with a typical age at onset (mean DVR = 1.51 ± 0.13 ; Fig. 1a,b). Tau tangle burden in the inferior temporal lobe, measured by flortaucipir (FTP), was similar to that seen in younger PSEN1-E280A impaired carriers with typical age at onset (standardized uptake value ratio (SUVR) = 1.78). However, he had relatively limited Tau pathology in the entorhinal cortex (ERC) (SUVR = 1.34; Fig. 1a,c) and in other neocortical regions, such as the posterior cingulate cortex (PCC) and precuneus (SUVR PCC = 1.51; SUVR precuneus = 1.49; Fig. 1a), which usually show greater levels of Tau pathology in *PSENI*-E280A carriers who develop MCI and dementia at a typical age³ (Fig. 1, Supplementary Fig. 2 and Extended Data Figs. 1 and 2). Sparing of the ERC from Tau pathology is a salient feature in the case with *RELN-COLBOS* that could be critical for the protection phenotype.

Measurements of metabolic rate for glucose in the precuneus and whole brain region using ^{18}F -fluorodeoxyglucose (FDG) PET showed a slightly higher level of glucose metabolism compared to the mean levels of typical MCI carriers from the kindred, who were much younger (Fig.1a,b). He had brain atrophy, measured by magnetic resonance imaging (MRI)-based hippocampal and whole brain volume typical of MCI carriers. These imaging findings suggest that in this patient and in the APOECh homozygote case², protection against ADAD dementia occurred even in the face of high amyloid burden (Fig. 1a,b). Additional imaging and biomarker analyses are reported in the supplementary results of the Supplementary Information.

Our genetic analyses confirmed that the individual was a heterozygote carrier of the PSEN1-E280A mutation (confirmed by single-cell RNA sequencing (scRNA-seq); Supplementary Tables 3 and 4), ruled out the presence of the APOECh mutation (the individual was APOE3/APOE3 and had a normal blood lipid profile; Supplementary Table 5) and identified a heterozygous variant in RELN (chromosome 7:g.103113302T>C, H3447R; Supplementary Fig. 1b), which we named 'RELN-COLBOS', as the most promising missense variant potentially contributing to the phenotype in the protected individual. The RELN-COLBOS variant was only found in the individual and his sister (Supplementary Fig. 1), who also had late-onset cognitive decline. Both were APOE3/APOE3. We focused on the RFLN-COLBOS variant because it ranked in the top three candidate genes in the Genomizer priority score analysis and because the encoded protein RELN modulates Tau phosphorylation⁴ and is functionally closely related to APOE, the gene mutated in the other case with extreme protection against ADAD2. A more detailed description of the genetic analysis is reported in the genetic analysis section of the Supplementary Information.

Our genetic analyses also identified other variants of potential interest in the male individual including: (1) a noncoding variant in the amyloid beta precursor protein (*APP*) gene (3'-untranslated region, chromosome 21:g.27253263T>C; and (2) a noncoding variant in the calmodulin 2 (*CALM2*) gene (intronic, chromosome 2:g.47394764C>G). The levels of expression of *APP* in peripheral blood mononuclear cells from *RELN* H3447R carrier and noncarriers were very low and not substantially different. Therefore, the significance of the *APP* variant is uncertain, although it is unlikely to be implicated considering the robust amyloid pathology observed in the individual (Fig.1a,b). This *APP* variant (g.27253263T>C) was not seen in the *APOECh* case based on whole-genome sequencing (WGS). The *CALM2* variant is predicted as intronic for the canonical transcript encoding a protein with 149 amino acids (PODP24) and it would result in a Cys9Ser in a predicted

longer transcript encoding for a protein with 196 amino acids (E7EMB3). This *CALM2* variant has not been reported in the ClinVar database and has low in silico pathogenicity scores. We also could not find a per-variant regulatory score in the Encode database for this variant. The significance of this variant is uncertain, although it is unlikely to be implicated because there is no proteomic evidence of the region of the variant producing any detectable protein in the PeptideAtlas⁶. Further studies may be conducted to examine the extent to which these or other variants contribute to the observed phenotype.

To strengthen our understanding of the genetic implications of the *RELN-COLBOS* variant, we conducted both in vitro and in vivo molecular genetic studies. These studies aimed to provide further evidence to support our initial findings and increase confidence in our attribution of the variant's genetic effects. The binding of RELN results in the clustering and activation of VLDLr and APOEr2, initiating a signaling pathway that leads to the activation of Dab1 (refs. 4,7–9). Our studies found that RELN-COLBOS significantly increased Dab1 phosphorylation compared to wild-type (WT) RELN (Fig. 2a, P = 0.0246) in primary culture mouse cortical neurons (Supplementary Figs. 3 and 4). We also examined RELN-COLBOS binding to its receptors to better understand the potential mechanisms for the observed enhanced signaling. Our findings from cell-free binding assays suggest that RELN-COLBOS did not directly impact binding of RELN to VLDLr or APOEr2, suggesting that other mechanisms were involved (Supplementary Fig. 5).

The C-terminal region of RELN (CTR-RELN), where the H3447R variant is located, modulates signaling indirectly via interactions with previously unidentified coreceptors on cell membranes¹⁰. Recently, neuropilin 1 (NRP1) was identified as a coreceptor via binding to a fragment of CTR-RELN consisting of the last six amino acids. This fragment is removed by furin protease. The uncleaved 'long' CTR-RELN interacts with NRP1 and the cleaved 'short' CTR-RELN does not 11. CTR-RELN has many basic amino acids that are extremely well conserved across species¹⁰, which we hypothesized could also mediate interactions with glycosaminoglycans (GAGs) on cell membranes. Interactions with GAGs are a rate-limiting step in the interaction of the apolipoprotein E (APOE) protein with some receptors¹², whereas the role of GAGs in RELN activity has not been fully resolved 10,13. We used affinity chromatography to examine heparin (a type of GAG) binding of recombinant CTR-RELN peptides. WT CTR-RELN and H3447R CTR-RELN bound to heparin. H3447R CTR-RELN required higher NaCl concentrations to be released from the heparin column, suggesting increased binding affinity (Fig. 2b). Surface plasmon resonance (SPR) measures of kinetic constants showed that the affinity of CTR-RELN H3447R is about twice that observed in the WT CTR-RELN (Fig. 2c and Supplementary Fig. 6).

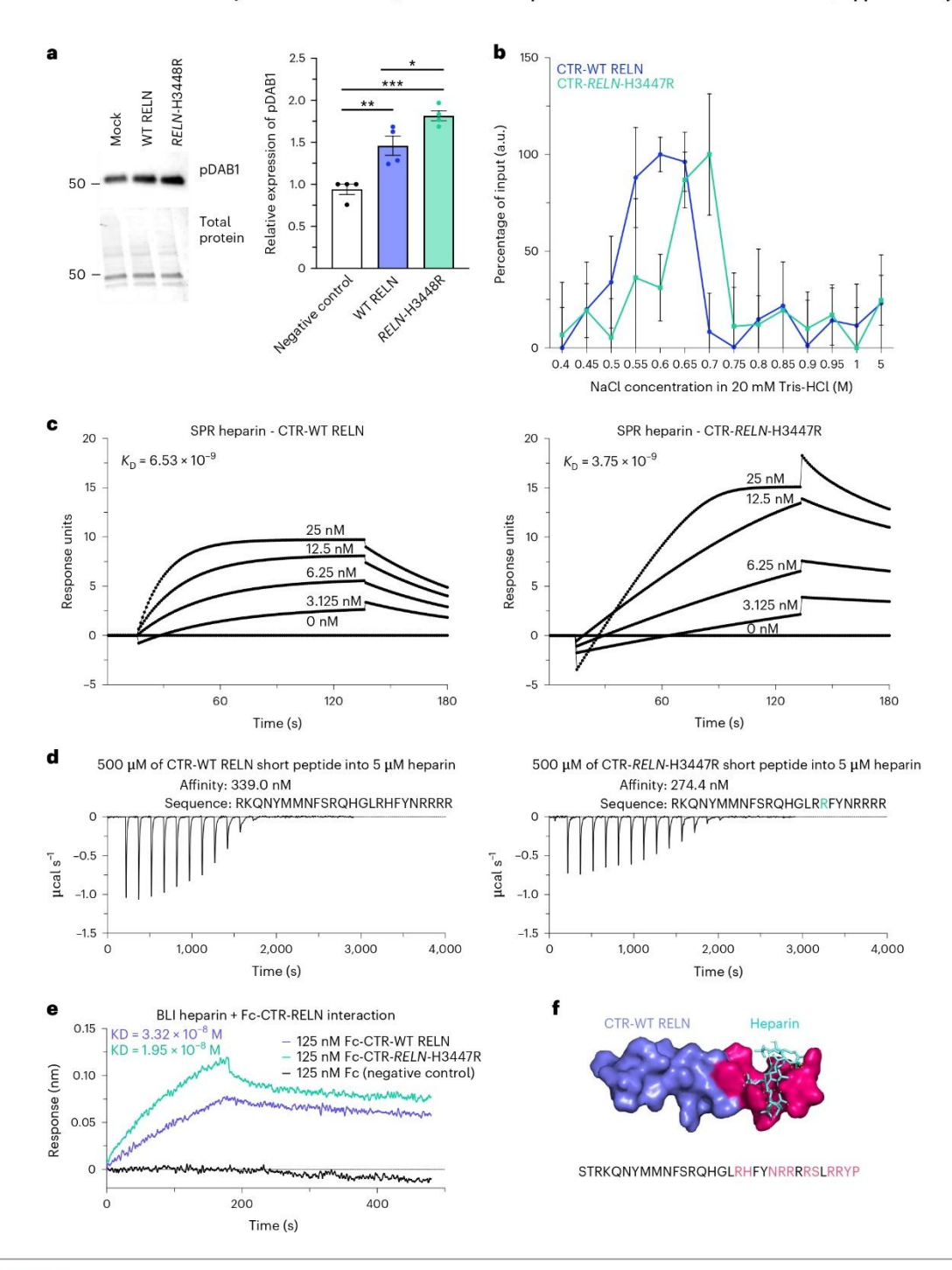
We confirmed enhanced interactions of H3447R CTR-RELN with heparin through the use of isothermal titration calorimetry (ITC) (Fig. 2d and Supplementary Table 6) and biolayer interferometry (BLI) (Fig. 2e). The association constant (K_a) was the main contributor to the

Fig. 2 | The RELN-H3448R variant enhances Dab1 signaling and the affinity of CTR-RELN to heparin. a, Representative western blotting of pDab1 levels (top) and total protein staining (bottom) levels in primary mouse cortical neurons treated with full-length WT RELN or RELN-H3448R, mouse ortholog of RELN-H3447R (mock, P < 0.0029 and WT RELN, P = 0.0246). Data are presented as the mean ± s.e.m. and were analyzed using a Kruskal-Wallis test with Dunn post hoc analysis for multiple comparisons of n = 4 independent biological $experiments. \ \textbf{b}, Spectroscopic analysis of heparin chromatography fractions$ of WT CTR-RELN (blue plot) and the CTR-RELN-H3447R mutant (green plot) eluted at increasing gradients of NaCl (0.05 M NaCl step gradient). Data are expressed as the percentage of input over 0.4-5 M NaCl gradient fractions. Data show that 0.55 M NaCl can displace WT CTR-RELN binding from a heparin column. The affinity for heparin of CTR-RELN increases in the presence of the H3447R mutation, as suggested by the shift of the peak with maximum height of the eluted fraction from 0.55 to 0.7 M NaCl. n = 3 independent chromatography experiments. The error bars represent the s.e.m. c. Representative sensorgrams

of the binding analysis between chip sensors coated with heparin and $0-25\,\text{nM}$ increasing concentrations of CTR-RELN variants. Data are expressed as response units per second. The equilibrium disassociation constant (K_D) for each SPR analysis are shown inside the graph and support the difference in affinity binding between heparin and the CTR-RELN variants: H3447R (right plot, $K_D=3.75\times 10^{-9}\,\text{M}^{-1}\,\text{s}^{-1})$. Has 347 (left plot, $K_D=6.53\times 10^{-9}\,\text{M}^{-1}\,\text{s}^{-1})$. The sensorgrams of CTR-RELN with the H3447K and H3447D control variants are reported in Supplementary Fig. 6 for comparison. **d**, Isothermal calorimetry measurements of short-variant WTCTR-RELN (left) and CTR-RELN-H3447R (right) titrated with 5 μ M heparin. Affinity calculations are reported above each plot. **e**, Binding analysis via BLI between Fc-fusion WT CTR-RELN and H3447R and a heparin-coated biosensor. Association (k_0) and dissociation constants (k_0) were used to calculate the K_D that is displayed in the plot. **f**, Docking of WT CTR-RELN (purple) with a representative heparin molecule (eyan). Amino acids in CTR-RELN that have polar contacts with heparin are highlighted in magenta.

difference in equilibrium dissociation constant ($\rm K_D$) values, and the mutant CTR-RELN had a more negative Gibbs free energy in comparison to WT, suggesting that the *COLBOS* mutation enables spontaneous CTR-RELN reactions with heparin (Supplementary Table 6). Our nuclear magnetic resonance (NMR) (Figs. 2f and 3a) study revealed that CTR-RELN may have an α -helix structure including a flexible region with a domain we named 'flexibility vertex' (Extended Data Fig. 3a) in the presence of trifluoroethanol, although it may be unstructured under native conditions as revealed by circular dichroism (Extended

Data Fig. 3b and Supplementary Table 7). Heparin-binding analyses of a library of mutant CTR-RELN peptides uncovered two binding sites for GAGs, which we named ' α -GAG binding site' and ' β -GAG binding site' (Fig. 3a). The α -GAG binding site is located in the last six amino acids and overlaps with a previously identified binding site for NRP1, which is released by furin. The β -GAG binding site is located upstream of the furin cleavage site and spans amino acids 3,446–3,451. Our research also found that CTR-RELN-COLBOS has a tenfold higher affinity for NRP1 compared to the WT version of CTR-RELN (Supplementary Table 8)



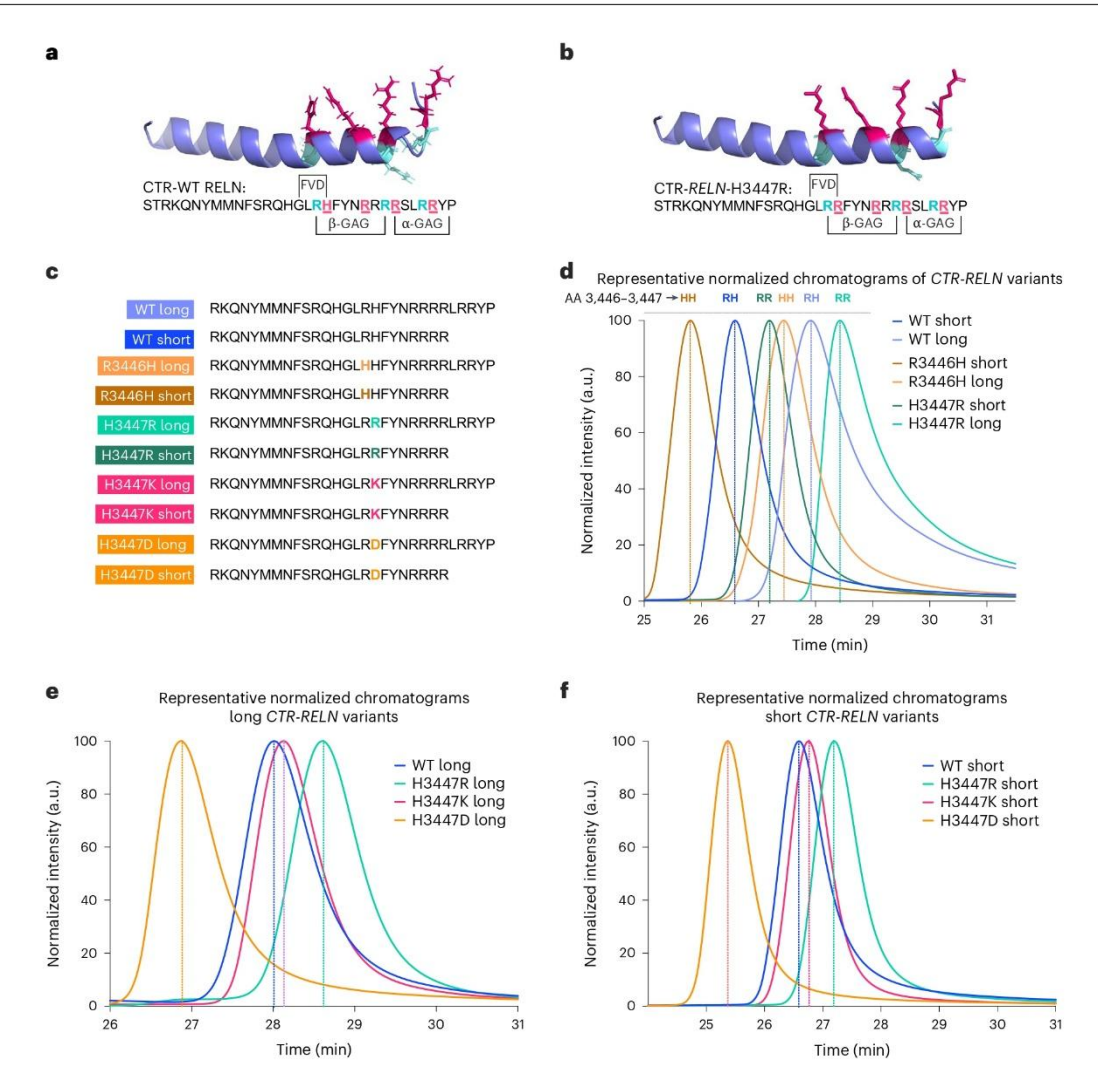


Fig. 3 | Binding profiles of CTR-RELN variants with heparin. a,b, Representative in silico models depicting the orientation of basic amino acids in the heparin-binding motif (highlighted with colors) using the WT CTR-RELN NMR structure (a). For the H3447R CTR-RELN variant (b) the model was determined by a homology-based model of WT CTR-RELN that was calculated by Swiss-Model. Position 3,447 orients in the same direction as most other arginines (magenta). Arginines in positions 3,446, 3,453 and 3,457 (cyan) may also interact with heparin as part of the heparin-binding motif but are oriented differently from most basic amino acids. c, RELN peptide variant sequences used for the HPLC analysis. d, Representative chromatographic profiles normalized to the maximum of each eluted peak of short or long CTR-RELN peptides with zero (R3446H, orange),

one (WT, blue) or two (H3447R, green) arginines in positions 3,446–3,447, which are predicted to contribute to increased interaction with heparin and are indicated by later peak retention time in the isocratic 1 M KCl elution. e.f., Long (e) or short (f) CTR-RELN peptides with zero (R3446H, orange), one (WT, blue) or two (H3447R, green) arginines in positions 3,446–3,447 showing increased interaction with heparin for the long variants, as indicated by later peak retention time in the isocratic 1 M KCl elution. Conversely, short RELN variants have earlier peak retention times compared to long *RELN* variants (e). n = 2 independent chromatographic repeats within <0.5 min of representative peaks. Data are expressed as normalized to the maximum emission wavelength for each peak.

due to the optimization of the β -GAG binding site. We conducted extensive studies of mutant CTR-RELN interactions with heparin by high-performance liquid chromatography (HPLC) (Fig. 3c-f), BLI (Fig. 2e) and NMR structure (Figs. 2f and 3a,b, Extended Data Fig. 3a and Supplementary Videos 1–3) to support these assertions.

Furthermore, we generated a knockin mouse model carrying the equivalent of the *RELN-COLBOS* variant (H3448R, *mRELN-H3448R* or *mRELN-COLBOS*¹⁰; Supplementary Fig. 7 and Supplementary Table 9) to increase confidence in our imputation of genetic implication, a common practice to study rare variants. This mouse model is viable, fertile and lacks overt structural and phenotypic brain

abnormalities of RELN loss-of-function mutants (for example, cortex lamination defects, abnormal neuronal migration and cerebellar hypotrophy; Extended Data Fig. 4a)^{14,15}. Our molecular analyses of cerebellum (CB) from mice with the *mRELN-COLBOS* confirmed our observation of a gain-of-function (GOF) in 6–12-month old mice for *RELN-H3448R* as determined by enhanced phosphorylation of Dab1 in males (Fig. 4a–c, P = 0.0284) and revealed a propensity for the formation of higher molecular protein oligomers for *RELN-COLBOS* (Supplementary Figs. 8 and 9), a feature that may be critical for enhanced activity ¹⁶. Morphological analysis revealed a mild, yet statistically significant increase in the number of cerebellar neurons in male mice

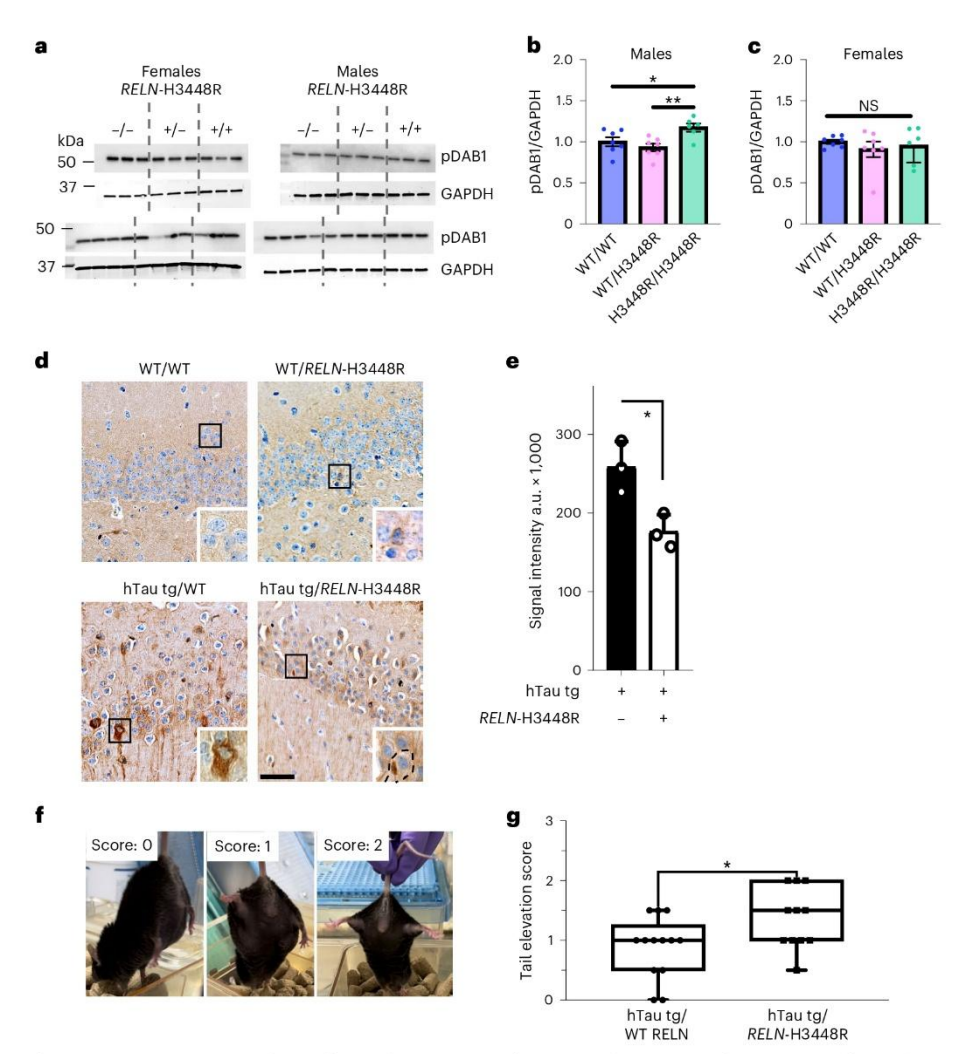


Fig. 4 | RELN-H3448R homozygosity promotes pDab1 signaling, reduces Tau hyperphosphorylation and preserves motor functions in mice. a, Representative western blots of pDab1 (top) and GAPDH levels (bottom) detected in the CB of both female (left) and male (right) mice either WT (WT/WT RELN), heterozygous (WT RELN/H3448R) or homozygous $(\textit{RELN-H}3448R/H3448R) for the \textit{mRELN-H}3448R \, mutation. \, Levels \, of \, pDab1$ were detected in 6-12-month-old mice. b,c, Quantifications of pDab1 levels normalized to GAPDH and expressed as the fold change of WT RELN showing a genotype effect in pDab1 levels in male mice (b) but not female mice (c). *P = 0.0284 for WT/WT, n = 7 mice versus H3448R/H3448R, n = 6 mice. t = 1.001. d.f. = 17; **P = 0.0037 for WT/H3448R, n = 7 mice versus H3448R/H3448R, n = 6 mice, t = 3.356, d.f. = 17, one-way analysis of variance (ANOVA). Data are expressed as the average ± s.e.m. Analyses of pDab1 levels in male mice at 3 months of age and in other brain regions are shown in Extended Data Fig. 5. Validation of the anti-pDab1 antibody used in a and e is reported in Supplementary Figs. 5 and 6. d, Representative immunohistochemistry (IHC) images from the HIC

of WT/WT, WT/RELN-H3448R, hTau tg/WT and hTau tg/RELN-H3448R mice stained with hyperphosphorylated Tau (pTau) T205 antibody. hTau tg/WT $mice showed \, neurofibrillary \, tangles \, and \, neuropil \, threads \, in \, the \, first \, region \, of \, and \, region \, of \, and \, region \, of \, region \, of$ $the \, hippocampal \, circuit \, (CA1) \, and \, dentate \, gyrus, while \, hTau \, tg/\textit{RELN-} H3448R$ showed Tau pathology to a lesser degree (soma of an affected neuron depicted with a dotted line). Bar scale, 100 μm. e, Bar graph for pTau T205 signal intensity values in hTau tg/WT (n = 3 mice) and hTau tg/RELN-H3448R mice (n = 3 mice). The latter showed significantly lower signal intensity. *P = 0.022, two-sided Student's t-test. The error bars represent the s.d. from the mean. f. Representative phenotype observed during the tail elevation test and relative score (0 = severely impaired, 1 = 50% impaired, 2 = normal). g, Tail elevation recorded on WT RELN/Tau-P301L (n = 13 male mice) and RELN-H3448R/Tau-P301L crossed male mice (n = 11 male mice) showed a significantly improved tail elevation score in the presence of the RELN-H3448R variant compared to Tau-P301L mice expressing WT RELN (*P = 0.0305, two-tailed unpaired t-test, t = 2.313, d.f. = 22). Box plots are expressed as minimum to maximum values around the average.

with the *RELN-COLBOS* variant. This supports the hypothesis of a GOF mechanism (Extended Data Fig. 4a,b), although the neuronal density phenotype was not observed in other brain regions (Supplementary Fig. 10).

This mouse model allowed us to examine sexually dimorphic effects of the *RELN-COLBOS* variant, a feature that has been described for conditions linked to genetic variation in *RELN*, including

schizophrenia, bipolar disease, autism and Alzheimer's disease $^{17-22}.$ Increased Dab1 phosphorylation and enhanced oligomerization of RELN were observed only in male mice (Fig. 4a–c, Extended Data Fig. 5 and Supplementary Figs. 8 and 9). This finding was consistent with our observation of optimal association of *RELN-COLBOS* with protection against ADAD in a male versus a female case. Homozygosity was required to detect changes in Dab1 and in GSK3 β activity

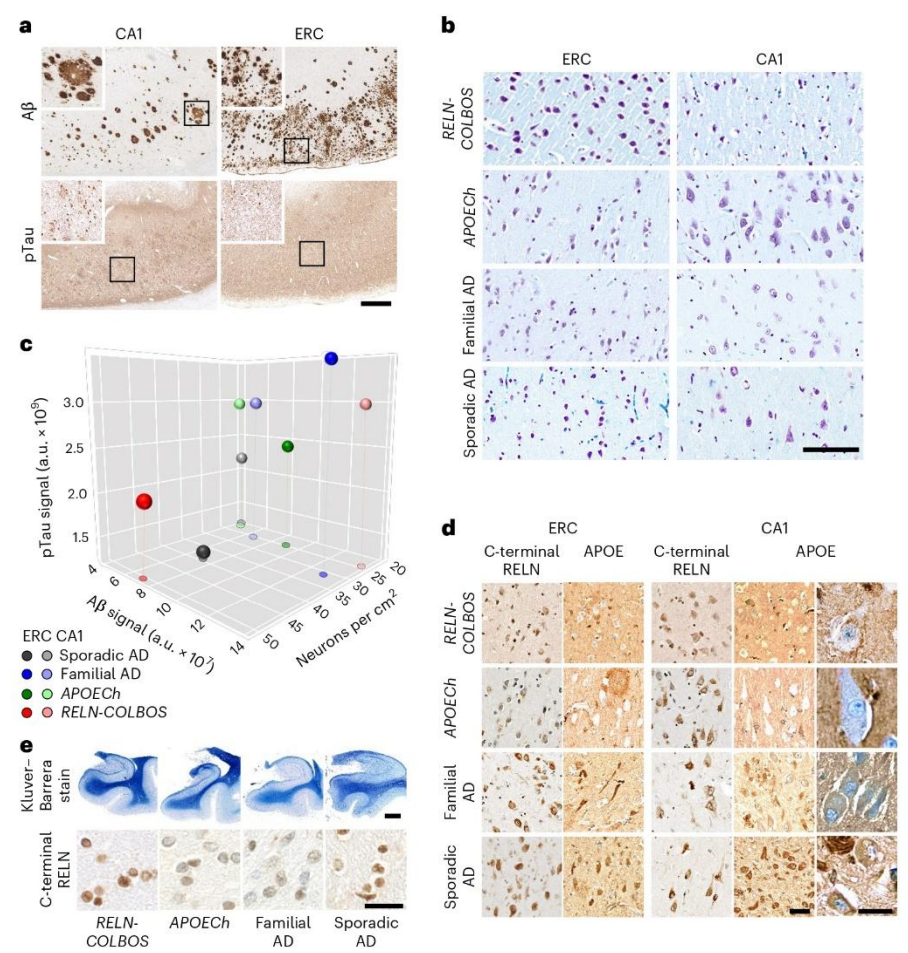


Fig. 5 | **Neuropathological characterization of the case with** *PSENI***-E280A**; *RELN***-H3447R. a**, Aβ and pTau pathologies in the CA1 and ERC. Both pathologies present wide distribution and intensity. Aβ pathology shows diffuse plaques with varied distribution and size (panels and insets). pTau pathology shows varied density of neurofibrillary tangles and diffuse Tau pathology. Scale bar, 500 μm. **b**, Neurons stained with Klüver–Barrera stain in the CA1 and ERC of the case with *PSENI*-E280A/*RELN*-COLBOS, the case with *PSENI*-E280A/*APOECh*, a case with average-onset *PSENI*-E280A familial AD and a case with sporadic AD. Scale bar, 125 μm. **c**, Three-dimensional scatter plot for Aβ, pTau and neuronal density for ERC and CA1 from cases with *RELN*-COLBOS, *APOECh*, familial AD (n = 5) and sporadic AD (n = 4). The ERC in the case with *RELN*-COLBOS shows the highest neuronal density, with low Aβ and pTau pathologies. **d**, C-terminal RELN and APOE staining of the cases with *RELN*-COLBOS, *APOECh*, familial AD and sporadic AD in the ERC and CA1. The case with *RELN*-COLBOS shows a

stronger background signal in both structures with lower intraneuronal signal for C-terminal RELN in the ERC. Similarly, the case with *APOECh* shows lower intraneuronal signal in ERC with the C-terminal RELN antibody and very low intraneuronal signal in both structures with the APOE antibody (magnified right). Finally, APOE staining shows noticeable plaque- and tangle-like signals in cases with familial and sporadic AD in both structures, the ERC and CAL Scale bars, 100 µm and 25 µm in the magnified panel. e, Klüver-Barrera staining of whole hippocampal and parahippocampal sections (top), together with representative magnified images of parahippocampal subcortical white matter stained with C-terminal RELN antibody in the cases with *RELN-COLBOS*, *APOECh*, familial and sporadic AD (bottom). The case with *RELN-COLBOS* showed increased white matter Luxol Fast Blue signal intensity, while the cases with *RELN-COLBOS* and sporadic AD showed increased intracellular C-terminal RELN signal in white matter. Scale bars, 2.5 mm for the top panel and 25 µm for the bottom panel.

(another downstream target of RELN signaling) associated with the *RELN-COLBOS* variant (Supplementary Figs. 11 and 12). Whether this homozygosity requirement is a species-specific effect or whether it depends on other factors such as age is to be examined. Altogether, these data indicate that *RELN-H3447R* is a GOF (hypermorph) variant.

To attempt to correlate the phenotypes of *RELN-COLBOS* in mice and humans, we used a crossbreeding strategy, using our knockin mouse model and a tauopathy mouse model, specifically the STOCK Tg(Prnp-MAPT*P301L)JNPL3HImc mouse from the Hutton's laboratory, distributed by Taconic Biosciences. This mouse model expresses a mutation in the Tau gene, leading to accumulation of Tau tangles

and neuronal loss in specific brain regions, commonly used to study tauopathies²³. The decision to use this mouse model was based on the known effects of RELN signaling on Tau phosphorylation²⁴ and our clinical observations of a relative reduction of tauopathy in certain brain regions from postmortem human brain samples of the protected case. Our study found that male P301L mice expressing the *RELN-COLBOS* allele had a significant reduction of human Tau phosphorylation (pTau205) in the hippocampus (HIC) (Fig. 4d,e) and medulla oblongata (MO) (Supplementary Fig. 13) compared to controls (Fig. 4d). We also observed that the abnormal limb-clasping response, which is a common consequence of tauopathy in mice, was significantly rescued

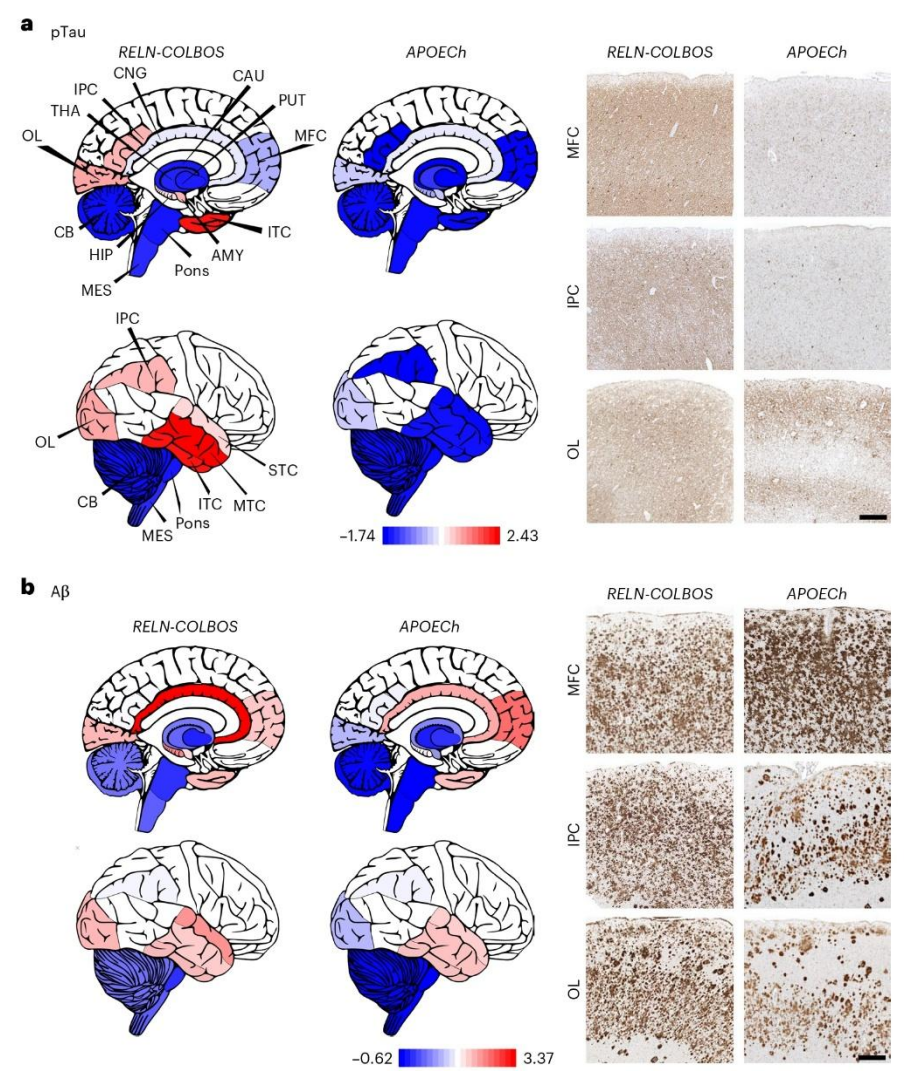


Fig. 6 | Brain distribution of AD hallmarks in the cases with RELN-COLBOS and APOECh. a,b, Graphic representation and representative images of the distribution and intensity of pTau (a) and $\Delta \beta$ (b) pathology signals with normalized minimum and maximum values shown in red and blue, respectively in the cases with RELN-COLBOS and APOECh. The case with APOECh showed distinct decreased pTau pathological profiles in all cortices compared to the case

with RELN-COLBOS. Despite some distribution differences, the A β pathology profile was similarly severe in both cases. AMY, amygdala; CAU, caudate; CNG, cingulate cortex; IPC, inferior parietal cortex; ITC, inferior temporal cortex; MES, mesencephalon; MFC, medial frontal cortex; MTC, middle temporal cortex; OL, occipital lobe; PUT, putamen; STC, superior temporal cortex; THA, thalamus. Scale bars, 250 μ m.

in *RELN-COLBOS* mice with the Tau transgene (Fig. 4f.g). Although additional studies of this model are necessary, our findings strongly support our hypothesis that *RELN-COLBOS* is a GOF mutation and it is probably genetically implicated in the resilience to tauopathy.

Postmortem examination of the case with *RELN-COLBOS* indicated neuropathological evidence of severe AD (brain weight = 745.4 g, classified as CERAD C, Braak VI stage and Thal phase 5) with extensive amyloid and Tau pathology, while showing some hippocampal formation-specific findings (Fig. 5, Extended Data Figs. 6 and 7, Supplementary Figs. 14–16 and extended description in the supplementary results). Recently, we reported the neuropathological profile of the *PSENI*-E280A carrier homozygous for the *APOECh* mutation. The Christchurch case showed a unique pathological phenotype among cases with *PSENI*-E280A, with remarkably low pTau pathology in

most brain regions except in the visual primary cortex \$^{25}\$. In contrast, side-by-side comparisons showed that the case with \$RELN-COLBOS\$ had more pTau pathology relative to the case with \$APOECh\$ except in specific regions (Fig. 6a and Supplementary Fig. 17). Both cases showed extensive \$A\beta\$ pathology in all evaluated areas, albeit with some individual differences (Fig. 6b and Supplementary Fig. 17). Microglial morphological assessment of the protected cases indicated that the \$APOECh\$ microglia were significantly more active in the studied areas (Extended Data Fig. 8).

We focused our analysis on the HIC and associated cortices because these structures are known to be affected early in AD 26 . Neurons in layer II of the ERC and ERC neurons in general are particularly vulnerable to aging and AD 27 . We measured neuronal density in hippocampal and parahippocampal areas of the cases with *RELN-COLBOS*,

the case with AD-resistant *APOECh*, cases with typical *PSENI*-E280A and cases with typical sporadic AD (Fig. 5b, Extended Data Figs. 9 and 10, Supplementary Figs. 18 and 19 and Supplementary Table 10). We found that lower AD pathology was associated with high neuronal density in the ERC of the case with *RELN-COLBOS* compared to the case with *APOECh* or the controls with familial and sporadic AD (Fig. 5c).

This association was not apparent in other subregions such as the CA1 (Fig. 5c and Supplementary Figs. 18 and 19). The cases with *RELN-COLBOS* and *APOECh* showed distinctively lower intraneuronal APOE signal than the controls with familial and sporadic AD (Fig. 5d and Supplementary Table 10) whereas the case with *RELN-COLBOS* showed higher Reelin intracellular signal in the white matter (Fig. 5e and Extended Data Fig. 10).

Neuropathological findings were consistent with our in vivo neuroimaging observations and confirmed a potential role for the ERC as a target of *RELN*-mediated mechanisms critical for the resilience to ADAD.

Discussion

We characterized a male heterozygous for the *RELN-COLBOS* variant who was resilient to the cognitive impairment associated with the *PSENI-E280A* mutation. The observation of low Tau pathology and increased neuronal density in the entorhinal cortex compared to other cases with AD implicates this brain region in *RELN*-mediated mechanisms relevant to protection against AD (Supplementary Table 1 and Figs. 1 and 5b,c). Because the comparative neuropathology was conducted in a relatively low number of cases, the results should not be considered definitive and they are only helpful as informative to generate hypotheses.

A female sibling carrier of the *RELN-COLBOS* and *PSENI*-E280A variants also presented with delayed age at onset of cognitive decline, although with less optimal protection compared to her brother and prolonged end-stage disease. The female sibling had a history of a severe head injury, which required reconstructive surgery, as well as a history of depression and hypothyroidism. These factors may have had an impact on her clinical profile and should be taken into consideration when evaluating her phenotype². In addition, *RELN*-specific sexual dimorphism may have contributed to her distinct features. We cannot rule out the possibility that other factors, including additional variants, may have contributed to the AD resilience phenotype in *RELN-COLBOS* carriers. Notwithstanding these potential limitations, others identified *RELN* as a candidate gene associated with AD pathology in cognitively healthy individuals²⁸ and *DABI* variants were linked to AD risk in *APOE4* homozygotes, further linking the *RELN/DABI* pathway to Alzheimer's²⁹.

We previously reported a female case homozygous for *APOECh* who was resistant to ADAD-related dementia, had widespread amyloid pathology and low Tau pathology in the ERC². Tauopathy was more extensive in the case with *RELN-COLBOS* compared to the *APOECh* homozygote, except for the ERC, which was largely spared in both, suggesting resilience in the case with *RELN-COLBOS*.

The hypermorphic effect of *RELN* is mild. This is the first known report of a *RELN* hypermorph and a stronger effect may not support proper development in this critical signaling process. The experimental evidence of a GOF mechanism for the *RELN-COLBOS* variant, and the fact that a patient with extreme protection against ADAD has it, establish a rationale for genetic implication in the observed phenotypes. Our hypothesis is that *RELN-COLBOS* is not a neutral variant and probably contributes to the phenotype of the individual. It is possible that other genetic variants may also contribute; if so, these variants and their effects will have to be interpreted and compared to the effect of *RELN-COLBOS* using the data we have provided.

The APOECh mutation impairs APOE binding to GAG and the APOE receptors^{2,30}. Conversely, the RELN-COLBOS variant enhances RELN

binding to GAG and NRP1, possibly giving it a competitive advantage for binding to its receptors? Interactions with GAG-containing proteins like heparan sulfate proteoglycans may enhance local concentration of RELN and amplify its signaling effect. Our analyses of the case with *RELN-COLBOS* revealed a mechanism potentially linking RELN interactions via GAG or other receptors to the protection against AD. Regulation of this RELN-protective pathway, particularly in the ERC, may have a profound therapeutic impact on the resistance to Tau pathology and neurodegeneration, and resilience against cognitive decline and dementia in AD.

Online content

Any methods, additional references, Nature Portfolio reporting summaries, source data, extended data, supplementary information, acknowledgements, peer review information; details of author contributions and competing interests; and statements of data and code availability are available at https://doi.org/10.1038/s41591-023-02318-3.

References

- Acosta-Baena, N. et al. Pre-dementia clinical stages in presenilin 1 E280A familial early-onset Alzheimer's disease: a retrospective cohort study. *Lancet Neurol.* 10, 213–220 (2011).
- Arboleda-Velasquez, J. F. et al. Resistance to autosomal dominant Alzheimer's disease in an APOE3 Christchurch homozygote: a case report. Nat. Med. 25, 1680–1683 (2019).
- Quiroz, Y. T. et al. Association between amyloid and tau accumulation in young adults with autosomal dominant Alzheimer disease. JAMA Neurol. 75, 548–556 (2018).
- Hiesberger, T. et al. Direct binding of Reelin to VLDL receptor and ApoE receptor 2 induces tyrosine phosphorylation of disabled-1 and modulates tau phosphorylation. *Neuron* 24, 481–489 (1999).
- Dunham, I. et al. An integrated encyclopedia of DNA elements in the human genome. Nature 489, 57–74 (2012).
- Schwenk, J. M. et al. The Human Plasma Proteome draft of 2017: building on the Human Plasma PeptideAtlas from mass spectrometry and complementary assays. J. Proteome Res. 16, 4299–4310 (2017).
- 7. D'Arcangelo, G. et al. Reelin is a ligand for lipoprotein receptors. Neuron 24, 471–479 (1999).
- Lane-Donovan, C. & Herz, J. ApoE, ApoE receptors, and the synapse in Alzheimer's disease. *Trends Endocrinol. Metab.* 28, 273–284 (2017).
- Sheldon, M. et al. Scrambler and yotari disrupt the disabled gene and produce a reeler-like phenotype in mice. *Nature* 389, 730–733 (1997).
- Nakano, Y. et al. The extremely conserved C-terminal region of Reelin is not necessary for secretion but is required for efficient activation of downstream signaling. J. Biol. Chem. 282, 20544–20552 (2007).
- Kohno, T. et al. Reelin-Nrp1 interaction regulates neocortical dendrite development in a context-specific manner. J. Neurosci. 40, 8248–8261 (2020).
- Mahley, R. W. & Ji, Z. S. Remnant lipoprotein metabolism: key pathways involving cell-surface heparan sulfate proteoglycans and apolipoprotein E. J. Lipid Res. 40, 1–16 (1999).
- Di Donato, V. et al. An attractive Reelin gradient establishes synaptic lamination in the vertebrate visual system. Neuron 97, 1049–1062 (2018).
- D'Arcangelo, G. et al. A protein related to extracellular matrix proteins deleted in the mouse mutant reeler. *Nature* 374, 719–723 (1995).
- Wasser, C. R. & Herz, J. Reelin: neurodevelopmental architect and homeostatic regulator of excitatory synapses. J. Biol. Chem. 292, 1330–1338 (2017).

- Utsunomiya-Tate, N. et al. Reelin molecules assemble together to form a large protein complex, which is inhibited by the function-blocking CR-50 antibody. Proc. Natl Acad. Sci. USA 97, 9729–9734 (2000).
- Shifman, S. et al. Genome-wide association identifies a common variant in the reelin gene that increases the risk of schizophrenia only in women. *PLoS Genet.* 4, e28 (2008).
- Ober, C., Loisel, D. A. & Gilad, Y. Sex-specific genetic architecture of human disease. Nat. Rev. Genet. 9, 911–922 (2008).
- Goes, F. S. et al. Sex-specific association of the reelin gene with bipolar disorder. Am. J. Med. Genet. B Neuropsychiatr. Genet. 153B, 549–553 (2010).
- 20. Seripa, D. et al. The RELN locus in Alzheimer's disease. J. Alzheimers Dis. **14**, 335–344 (2008).
- Fehér, Á., Juhász, A., Pákáski, M., Kálmán, J. & Janka, Z. Genetic analysis of the RELN gene: gender specific association with Alzheimer's disease. Psychiatry Res. 230, 716–718 (2015).
- Kelemenova, S. & Ostatnikova, D. Neuroendocrine pathways altered in autism. Special role of reelin. *Neuro. Endocrinol. Lett.* 30, 429–436 (2009).
- Lewis, J. et al. Neurofibrillary tangles, amyotrophy and progressive motor disturbance in mice expressing mutant (P301L) tau protein. *Nat. Genet.* 25, 402–405 (2000).
- Yu, N.-N., Tan, M.-S., Yu, J.-T., Xie, A.-M. & Tan, L. The role of Reelin signaling in Alzheimer's disease. *Mol. Neurobiol.* 53, 5692–5700 (2016).
- Sepulveda-Falla, D. et al. Distinct tau neuropathology and cellular profiles of an APOE3 Christchurch homozygote protected against autosomal dominant Alzheimer's dementia. Acta Neuropathol. 144, 589–601 (2022).
- Braak, H. & Braak, E. Evolution of the neuropathology of Alzheimer's disease. Acta Neurol. Scand. Suppl. 165, 3–12 (1996).

- Gómez-Isla, T. et al. Profound loss of layer II entorhinal cortex neurons occurs in very mild Alzheimer's disease. J. Neurosci. 16, 4491–4500 (1996).
- Kramer, P. L. et al. Alzheimer disease pathology in cognitively healthy elderly: a genome-wide study. Neurobiol. Aging 32, 2113–2122 (2011).
- 29. Bracher-Smith, M. et al. Whole genome analysis in *APOE4* homozygotes identifies the *DAB1-RELN* pathway in Alzheimer's disease pathogenesis. *Neurobiol. Aging* **119**, 67–76 (2022).
- Lalazar, A. et al. Site-specific mutagenesis of human apolipoprotein E. Receptor binding activity of variants with single amino acid substitutions. J. Biochem. 263, 3542–3545 (1988).

Publisher's note Springer Nature remains neutral with regard to jurisdictional claims in published maps and institutional affiliations.

Open Access This article is licensed under a Creative Commons Attribution 4.0 International License, which permits use, sharing, adaptation, distribution and reproduction in any medium or format, as long as you give appropriate credit to the original author(s) and the source, provide a link to the Creative Commons license, and indicate if changes were made. The images or other third party material in this article are included in the article's Creative Commons license, unless indicated otherwise in a credit line to the material. If material is not included in the article's Creative Commons license and your intended use is not permitted by statutory regulation or exceeds the permitted use, you will need to obtain permission directly from the copyright holder. To view a copy of this license, visit http://creativecommons.org/licenses/by/4.0/.

© The Author(s) 2023

¹Neuroscience Group of Antioquia, Medicine School, University of Antioquia, Medellín, Colombia. ²Medicine School, University of Antioquia, Medellín, Colombia. ³Schepens Eye Research Institute of Mass Eye and Ear and Department of Ophthalmology at Harvard Medical School, Boston, MA, USA. ⁴Institute of Neuropathology, University Medical Center Hamburg-Eppendorf, Hamburg, Germany. ⁵Department of Neurology at Harvard Medical School, Massachusetts General Hospital, Boston, MA, USA. ⁶Department of Psychiatry at Harvard Medical School, Massachusetts General Hospital, Boston, MA, USA. ⁷Center for Personalized Medicine, Department of Pathology and Laboratory Medicine, Children's Hospital Los Angeles, Los Angeles, CA, USA. ⁸Department of Pathology, Keck School of Medicine of University of Southern California, Los Angeles, CA, USA. ⁹Neuroscience Research Institute, Department of Molecular Cellular Developmental Biology, University of California, Santa Barbara, CA, USA. ¹⁰The Banner Alzheimer's Institute, Phoenix, AZ, USA. ¹¹Department of Neurology at Harvard Medical School, Brigham and Women's Hospital, Boston, MA, USA. ¹²Department of Radiology at Harvard Medical School, Massachusetts General Hospital, Boston, MA, USA. ¹³University of Arizona, Tucson, AZ, USA. ¹⁴Arizona State University, Tucson, AZ, USA. ¹⁵Neurogenomics Division, Translational Genomics Research Institute, Phoenix, AZ, USA. ¹⁶These authors contributed equally: Francisco Lopera, Claudia Marino, Anita S. Chandrahas, Michael O'Hare, Nelson David Villalba-Moreno. ¹⁷These authors jointly supervised this work: Diego Sepulveda-Falla, Joseph F. Arboleda-Velasquez, Yakeel T. Quiroz. ⊠e-mail: d.sepulveda-falla@uke.uni-hamburg.de; joseph_arboleda@meei.harvard.edu; yquiroz@mgh.harvard.edu

Methods

Clinical assessment

This research complies with all relevant ethical regulations. Written informed consent was obtained from all participants and the local institutional review boards for human research approved the study. This includes the institutional human research ethics committee of the University of Antioquia in Colombia and the Partners Human Research Committee in Boston.

In vivo neuroimaging

We used PiB and FTP PET to image cerebral A β and Tau burden, respectively. Structural MRI and both PET scans were conducted at MGH. The FDG PET was performed at the University of Antioquia and the procedures and data analyses were performed as described previously². Briefly, MRI images were processed with FreeSurfer (v.6.0) to identify surface boundaries and standard ROIs. PET data were acquired and processed according to previously published protocols ^{31,32}, whereby PiB data were expressed as DVR (Logan, 0–60 min) and FTP as SUVR (80–100 min), both using cerebellar gray matter as the reference region. PET images were affine coregistered to each individual's T1 images and visualized using FreeSurfer surface projections (sampled at the gray matter midpoint, surface-smoothed 8 mm). No partial volume correction was applied to PET images for the purposes of this study.

Genetic and molecular studies

We conducted whole-exome (WES), WGS and Genomizer (v.10.10) analysis of the individual to obtain a ranking of AD-related potential risk factors as shown previously 2 and as described in detail in the additional genome sequencing section of the Supplementary Information.

Cell culture

Plasmid encoding for the full-length murine recombinant RELN was a gift from T. Curran via Addgene (plasmid no. 122444 (ref. 14)). The plasmid was subsequently mutagenized to obtain the H3448R mutation homologous of human RELN-H3447R as fee-for-service by Custom DNA Constructs, Primary CD1 brain cortex mouse neurons (catalog no. M-CX-400, Lonza) were cultured in neurobasal medium (Gibco) supplemented with B-27 (Thermo Fisher Scientific), glutaMAX (Gibco) and normocin (Invivogen). Cells were plated on poly-L-lysine-coated (Sigma-Aldrich) wells and treated on day 6 after liquid nitrogen recovery. Treatments with recombinant RELN (WT RELN or RELN-H3448R, 4 μg ml⁻¹, produced by Innovagen) were incubated for either 5 min or 1 h at 37 °C, 5% CO_2 in the presence of 10 μM MG-132 proteasome inhibitor (catalog no. ab141003, Abcam), Cells were washed in ice-cold PBS (Gibco) and lysed in radioimmunoprecipitation assay (RIPA) (catalog no. 9806, Cell Signaling Technology) sup $plemented\ with\ 10\ \mu M\ Mg-132,\ Triton-X100\ (Sigma-Aldrich),\ cOmplete,$ Mini, EDTA-free protease inhibitor cocktail (catalog no. 4693159001, Merck Millipore) and phosphatase inhibitors (catalog no. 4906837001. Sigma-Aldrich; catalog no. P0044, Merck Millipore). Protein concentration was determined by Pierce bicinchoninic acid (BCA) protein assay kit (catalog no. 23227, Thermo Fisher Scientific) according to the manufacturer's instructions. Samples were prepared containing 10 µl Laemmli buffer (Boston Bioproducts) and $4 \mu l$ of 1 M dithiothreitol (DTT) (Sigma-Aldrich) and diluted to a final volume of 40 μ l with water and denatured 5 min at 90 °C.

Western blotting

A total of 20 μg of cell lysates were prepared in 4 μl of 1 M DTT and 10 μl Laemmli buffer to a final volume of 40 μl and denatured with heat for 5 min at 90 °C. Samples were separated electrophoretically for 1 h at 90 V using 4–20% precast gradient gels (Mini-PROTEANTGX, Bio-Rad Laboratories) and Tris-Glycine-SDS buffer (Bio-Rad Laboratories). Proteins were transferred to 0.45- μm nitrocellulose membranes for 1 h at 90 V in ice-cold 20% Tris-glycine-methanol buffer (Bio-Rad

Laboratories). To detect pDab1 levels, proteins were transferred onto polyvinylidene fluoride membranes using the iBlot 2 dry transfer system (catalog no. IB21002S, Thermo Fisher Scientific). Total protein levels were detected using LI-COR membranes were blocked for 1 h with Odyssey Blocking Buffer (LI-COR Biosciences) or for 2 h with 5% nonfat dry milk (catalog no. M17200-100.0, Research Products International); both protease and phosphatase inhibitor cocktails where blocked for anti-pDab1 western blotting. β-Tubulin (ms host; 1:2,000 dilution, catalog no. 86298S, Cell Signaling Technology), anti-pDab1 (recombinant; 1:7,500 dilution, catalog no. MBS8511213, MyBiorsorce), anti-pGSK3 β -Ser9 (1:1,000 dilution, catalog no. D85E12, Cell Signaling Technology), anti-pGSK3β-Tyr216/279 (1:1,000 dilution, catalog no. 05-413, Merck Millipore), anti-GSK3β (1,1,000 dilution, catalog no. 5558, Cell Signaling Technology), anti-GAPDH (1:5,000 dilution, catalog no. ab8245, Abcam) and anti-RELN (ms host, 1:1,000 dilution, clone CR-50, catalog no. D223-3, MBL) were used as primary antibodies and incubated in blocking buffer for either 2 h at room temperature or 18 h at 4 °C. After washing the blots three times with Tris-buffered saline with Tween 20 buffer (Pierce, Thermo Fisher Scientific); secondary antibodies were incubated either 1 h or 45 min at room temperature (IRDye 800CW donkey anti-mouse, catalog no. 925-32212 or IRDye 680CW donkey anti-rabbit; 1:10,000 dilution, catalog no. 925-68073, LI-COR Biosciences). Immunoreactive bands were detected using the Odyssey Infrared Imaging System and visualized on the Image Studio Acquisition Software (v.2.1, LI-COR Biosciences). Detection of pDab1 was obtained with anti-rabbit-horseradish peroxidase-conjugated antibody (catalog no. HAF008, R&D Systems) followed by a 5-min incubation with SuperSignal West Pico PLUS Chemiluminescent Substrate and acquisition on the Syngene G:BOX digital ECL detection system using the Genesys (v.1.5.3.0) software. Validation of DAB1-positive bands was conducted via immunoprecipitation (Supplementary Fig. 3) and mass spectrometry (Supplementary Fig. 4). All other western blot images were acquired using the Odyssey Infrared Imaging System and visualized with Image Studio v.2.1 (LI-COR Biosciences), PowerPoint 365 for macOS (v.16.69.1), Prism 9 (v.9.4.1) (GraphPad Software) and ImageJ v.2.3.0/1.53q. The blots are presented in Figs. 3a and 4a. Supplementary Figs. 10 and 11 were acquired using Genesys v.1.5.3.0.

Heparin-sepharose affinity chromatography

We tested changes in binding to heparin of RELN variants chromatographically using an optimized version of a protocol previously published by our laboratory². Briefly, after equilibration of the heparin column (catalog no. 6554-1, BioVision) at room temperature, columns were washed with five volumes of degassed 20 mM Tris-HCl buffer (pH 7.5). Recombinant C-terminal RELN peptides were produced and purified as fee-for-service by Innovagen: WT RKQNYMMNFSRQHGL-RHFYNRRRRSLRRYP and H3447R RKQNYMMNFSRQHGLRRFYNR-RRRSLRRYP. All synthetic peptides listed in Fig. 3 were also produced by Innovagen. One milliliter of 50 μg ml⁻¹ peptide (H3447 or WT and H3447R) was recycled through the column five times; the last flow through was collected for further analysis. The column was washed five times with the same buffer and the protein was eluted using a 0.05 M step gradient of NaCl in 20 mM Tris-HCl (0-1 M, 1 ml per fraction). To ensure the complete release of the protein, the column was washed with 5 M NaCl 20 mM Tris-HCl. Three independent experiments were conducted for C-terminal WT RELN and H3447R. All eluted fractions were analyzed spectroscopically by reading the absorbance at 280 nm with a NanoDrop 2000 Spectrophotometer. Blank-corrected fractions were subsequently analyzed with Prism 8.

HPLC

Fifty microliters of $0.3~\mu g~\mu l^{-1}$ Reelin peptides were injected at $0.3~ml~min^{-1}$ into a POROS Heparin 50 μm Column ($4.6\times50~mm$, 0.8~ml; Thermo Fisher Scientific) using 10 mM PBS and 0.15~M KCl as the mobile phase using a Shimadzu SCL-40 instrument. Loading of the sample to

the column was performed for 5 min. Affinity of the samples to heparin was tested using the following gradient steps: 0-13.5 min: at 0.15 M KCl to load the sample; 13.5-14.5 min: at isocratic conditions at 0.5 M KCl; 14.5-24.5 min: at a gradient of 0.5-1 M KCl (ramp); 24.5-45 min: at 1 M KCl (isocratic elution); 45-55 min: 1 M KCl at 0.6 ml min $^{-1}$ (wash); 55.0-56.0 min: ramp to 0.15 M KCl at 0.3 ml min $^{-1}$; 56.0-59.0 min: 0.15 M KCl (reset column). Fluorescence intensities were measured at an excitation wavelength of 260 nm and emission wavelength of 290 nm, based on the fluorescence properties of aromatic amino acids. Retention times were analyzed with LabSolutions v.5.106. Chromatogram intensities were normalized to the maximum peak intensity in Prism 9.

BLI

We used Fc-fusion Reelin CTR peptides because peptides alone would be smaller than the limit of detection in this experimental design. The fusion proteins were obtained by cloning DNA sequences encoding amino acids 3,429-3,460 of RELN-CTR into the pFUSEN-hG2Fc plasmid from InvivoGen. To assess the heparin-Fc-Reelin interaction, the Octet system was used to assess heparin-protein kinetics as a fee-for-service by Precision Antibody. A total of 50 $\mu g\,ml^{-1}$ biotinylated heparin (catalog no. 375054, Merck Millipore) was immobilized on the biosensor tip surface for 300 s on preconditioned biosensors. This was followed by quenching with biocytin at 50 μg ml⁻¹, baseline buffer dilution for 120 s, $200\,\text{nM}$ of analyte (Fc-fusion proteins) for $120\,\text{s}$ and disassociation in assay buffer for 120 s. BLI was additionally used to assess NRP1 protein kinetics at 30 °C and 1,000 rpm agitation; 1 mg ml⁻¹ NRP1 (catalog no. 3870-N1-025, R&D Systems) was biotinylated at a 1:2 molar ratio, desalted and immobilized on the streptavidin biosensor tip (Pall Forte-Bio) surface. This was followed by (1) 180 s of baseline buffer dilution, (2) loading of the ligand (NRP1), (3) 240 s association (analyte) and (4) 300 s disassociation in assay buffer. The assay buffer consisted of an SD Buffer (PBS, 0.05% Tween 20, 0.01% BSA, pH 7.4). The experimental data were fitted with the 1:1 binding model and analyzed with global fitting using the Octet Data Analysis software (v.9) to calculate KD.

ITC

Heparin and peptides were dissolved in Dulbecco's PBS buffer (pH 7.22) and spun for 5 min at 10,000 rpm. Then, 2 μ l of the 500 μ M peptide was successively injected into the cell containing 5 μ M heparin at 25 °C with 180 s between injections and at 1,000 rpm stirring speed (MicroCal iTC200). Data were evaluated using the MicroCal iTC200 Evaluation software (Malvern).

Mouse model and in vivo analyses

We generated the RELN-H3448R-Tg knockin mouse model carrying the RELN-COLBOS variant via homologous recombination as fee-for-service (Taconic-Cyagen) by introducing the H3448R (CAC>CGT) mutation into exon 64 in the 3' homology arm of the RELN gene. Mouse and human RELN have very high homology with 95.2% identity. Human RELN is missing a valine residue at position 15 resulting in it having 3,460 instead of 3,461 amino acids like its mouse counterpart. Structurally, the two proteins have similar domain structure consisting of a signal peptide, an F-spondin-like domain, eight Reelin repeats (RR1-8) and a positively charged sequence at the C terminus. The last 105 amino acids including the region impacted by RELN-COLBOS are identical between mice and human. Gene targeting was obtained using C57BL/6 embryonic stem (ES) cells. Knockin mice were generated by injecting targeted ES cells into blastocysts that were introduced into the foster mothers used to generate the mouse crossings (Supplementary Fig. 7). Mice were killed by placing them in chambers saturated with CO₂. HICs, midbrains, frontal cortices, parieto-occipital regions and CBs were dissected and stored at -80 °C upon cervical dislocation, ensuring a post $morteminterval\,of\,less\,than\,3\,min.\,Brain\,homogenates\,were\,obtained$ in modified RIPA buffer (Cell Signaling Technology) supplemented with protease (Roche) and phosphatase (Sigma-Aldrich) inhibitors, using a

tissue homogenizer (two times, 15 s pulses). Homogenized tissue was then vortexed for 20 s every 10 min for 1 h and centrifuged for 10 min at 10,000 rpm and 4 °C. The soluble protein fraction was then analyzed using a BCA assay (Pierce). Using western blotting, we measured the levels of RELN (clone CR-50), Dab1 (clone G-5, catalog no. sc-271136, Santa Cruz Biotechnology), pDab1 (Tyr232) in the CB of adult male and female mice (6-12 months, n=3 mice for 6-month-old (m.o.) and 12-m.o. homozygous, n = 4 mice for 12-m.o. WT and heterozygous) either WT, heterozygous or homozygous for the RELN-H3448R mutation. This knockin model was crossed with the Tau P301L model from Taconic Biosciences. Littermates were included for analyses throughout. Additional details about mouse model design and clone selection are reported in Supplementary Table 9 and Supplementary Fig. 7. Eighteen-month-old WT and RELN-COLBOS knockin mice, human Tau P301L transgenic mice and crossbred Tau P301L/RELN-COLBOS mice were tested for the behavioral analyses and their brains were collected and prepared for morphological and immunohistochemical studies (Cresyl violet, Klüver-Barrera and pTau T205 IHC, 1:10,000; catalog no. EPR23505-13, Abcam). Animal study protocols were approved by the Schepens Eye Research Institute and the Institutional Animal Care and Use Committee.

Behavioral studies

We used limb-clasping scoring to assess motor deficits in mice according to a previously published protocol 23 . Briefly, we habituated the animals to the user for 3 days and assessed the escape response when we elevated each mouse by the tail to promote the limb-clasping reflex while standing on a metal grid. We scored from 0 (observed legs in crossed position) to 2 (observed complete opening of the hind limbs).

Neuropathology characterization

The postmortem interval was 210 min after death. The brain presented frontal lobe-predominant atrophy; the weight of the brain and associated structures was 745.4 g and the interuncal distance was 2.3 cm. After 5 days of fixation in 4% paraformaldehyde and sample preparation in paraffin. 3-um-thick sections from the medial frontal gyrus, superior temporal gyrus, medial temporal gyrus, inferior temporal gyrus, HIC/collateral sulcus, HIC/uncus, AMY, insula, inferior parietal lobe, OL, cingulate gyrus, lentiform nucleus, caudate nucleus, thalamus/hypothalamus, CB, midbrain/pons and MO were cut, deparaffinized and stained with H&E or processed for IHC staining for AB (1:100; BAM-10. catalog no. Mob410, DBS Emergo Europe), pTau (1:100; AT8, catalog no. MN1020, Thermo Fisher Scientific), ionized calcium binding adapter molecule 1 (Iba1) (1:500; catalog no. 019-19741, Wako), glial fibrillary acidic protein (1:200; catalog no. M0761, DAKO), C-terminal Reelin (1:200; clone E-5, catalog no. sc-25346, Santa Cruz Biotechnology) and APOE (1:100; goat polyclonal, catalog no. AB947, Merck Millipore) and specific secondary antibodies: anti-mouse and anti-rabbit (P0260 and PO447, respectively. DAKO): and anti-neuronal nuclei antibody (clone A60; ms host, 1:100; catalog no. MAB377, Merck Millipore). Visualization was achieved with 3,3'-diaminobenzidine (DAB) (Ventana, Roche) and the Ultraview Universal Detection Kit (Roche) according to the manufacturer's instructions. Automatic immunostaining was performed with a Ventana BenchMark XT system (Roche) according to the manufacturer's instructions. Selected brain areas were also stained with Luxol Fast Blue (for myelin staining) and Klüver-Barrera staining. Cresyl violet staining was used for neuronal perikarya. The neuropathological workup was performed by experienced morphologists blinded to the origin of the sample (M.G. and D.S-F.). Sections were scanned using a Hamamatsu NanoZoomer automatic digital slide scanner (Hamamatsu Photonics) and obtained images and ROIs (cortex for cortical areas, whole stained sections for non-cortical areas) at a resolution of at least $1 \text{ px } \mu\text{m}^{-1}$. Signal intensity, together with particles and total area, were assessed after performing color deconvolution and thresholding in the brown (DAB) color channel using ImageJ (v.1.52p, NIH)³³. Neuronal counting was performed manually and normalized by area in selected ROIs in the hippocampal and parahippocampal structures. Information on the statistical analysis is reported in the dedicated section.

Statistical analysis

All data presented are expressed as averaged values and errors are expressed either as s.e.m. or s.d. Statistical analyses were performed using Prism 8 or 9.P < 0.05 and an α of 0.05 were considered statistically significant. We used a Kruskal-Wallis test with Dunn post hoc analysis $for \, multiple \, comparisons \, of \, four \, independent \, experiments \, to \, compare$ changes between primary cortical neurons treated with either mock. WT RELN or RELN-H3448R and presented data as the mean \pm s.e.m. For the SPR data (Fig. 3c and Supplementary Fig. 4), we verified the accuracy of the results with a chi-squared test and compared the sensorgrams obtained experimentally with the sensorgrams generated mathematically by the BIAnalysis software (black line). Values ranging from 1 to 2 were interpreted as significant (accurate), and those below 1 as highly significant (highly accurate). Western blot analyses or neuronal counting of Cresyl violet-stained slides were done using a one-way ANOVA followed by Fisher's least significant difference test for multiple comparisons using Prism 9 (v.9.4.1) as reported in the figure legends. The neuropathological data (Fig. 2) were analyzed and graphs were generated with Prism 8 (v.8.1.1) and the R (v.3.6.3) statistical software (R Foundation for Statistical Computing), Distribution and correlation analyses were performed using a Spearman correlation test. The brain color maps were created with the cerebroViz package for R. The statistical significance of all analyses was determined with * $P \le 0.05$, ** $P \le 0.01$ and *** $P \le 0.001$. Statistical comparisons of two groups were performed using a two-sided Student's t-test.

Inclusion and ethics in global research

The study received institutional review board approval from the MGH, the Mass Eye and Ear and the local ethics committee at the School of Medicine at the Universidad the Antioquia, Medellín, Colombia. This work involved a collaboration between scientists in multiple countries including Colombia, the United States of America and Germany. Contributors from all sites are included as coauthors or in acknowledgements according to their contributions. Researchers residing in $Colombia\ have\ been\ involved\ in\ study\ design, study\ implementation,$ data ownership and intellectual property as appropriate. The research is locally relevant due to the high prevalence of ADAD. Roles and responsibilities were agreed among collaborators ahead of the research. Local ethics committees approved all research involving human participants. To prevent any stigmatization, any and all identifying information has been removed to preserve the privacy of individuals. The Colombian $team\ has\ retained\ ownership\ of\ any\ and\ all\ human\ biological\ material$ shared for research purposes.

Reporting summary

Further information on research design is available in the Nature Portfolio Reporting Summary linked to this article.

Data availability

Anonymized clinical, genetic and imaging data are available upon request during working hours, subject to an internal review by F.L., J.F.A.-V. and Y.T.Q. to ensure that participant confidentiality and *PSENI*-E280A carrier or noncarrier status are protected, completion of a data sharing agreement and in accordance with the University of Antioquia's and MGH's institutional review board and institutional guidelines. Experimental data are available upon request, subject to the MGH and Schepens Eye Research Institute of Mass, Eye and Ear institutional guidelines. Material and data requests will be considered based on a proposal review, completion of a material transfer agreement or a data use agreement (or both) and in accordance with the MGH and Schepens

Eye Research Institute of Mass, Eye and Ear institutional guidelines. Please submit requests for participant-related clinical and imaging data and samples to Y.T.Q. (yquiroz@mgh.harvard.edu); requests for experimental data and materials, genetic and scRNA-seg data should be sent to J.F.A.-V. (joseph_arboleda@meei.harvard.edu); and requests for neuropathology specimens should be forwarded to F.L. (francisco. lopera@gna.org.co). The RELN-COLBOS mouse model will be made freely available to the community via the Mutant Mouse Resource and Research Centers repository. The CTR-RELN NMR structure is available via the Protein Data Bank (PDB) platform (https://doi.org/10.2210/ pdb8g21/pdb). WES and WGS data were analyzed with the following resources: hs37d5 genome (ftp://ftp.1000genomes.ebi.ac.uk/vol1/ftp/ technical/reference/phase2_reference_assembly_sequence/hs37d5. fa.gz); SW Edico Genome DRAGEN Pipeline v.01.011.231.02.05.01.40152; HW Edico Genome DRAGEN Pipeline v. 01.011.231; BCFtools v. 1.9 (http:// samtools.github.io/bcftools/); Ensembl Variant Eeffector Predictor v.94 (https://uswest.ensembl.org/info/docs/tools/vep/index.html); gnomAD v.2.0.1 (http://gnomad.broadinstitute.org/downloads); bcbio-nextgen suite v.1.1.2 (https://github.com/bcbio/bcbio-nextgen); Exomiser v.10.1.0; Cartagenia v.5.0 (https://www.genomeweb.com/ resources/new-product/cartagenia-bench-lab-50); QIAGEN HGMD Professional Database v.2018.2; OMIM latest version at the time of the data analysis; ExAC release 0.3 and gnomAD latest online version http:// $gnomad. broad in stitute.org/. \, Source \, data are \, provided \, with \, this \, paper. \,$

References

- Desikan, R. S. et al. Automated MRI measures identify individuals with mild cognitive impairment and Alzheimer's disease. *Brain* 132, 2048–2057 (2009).
- Johnson, K. A. et al. Tau positron emission tomographic imaging in aging and early Alzheimer disease. Ann. Neurol. 79, 110–119 (2016).
- Schneider, C. A., Rasband, W. S. & Eliceiri, K. W. NIH Image to ImageJ: 25 years of image analysis. *Nat. Methods* 9, 671–675 (2012).

Acknowledgements

We thank the Colombian families with ADAD for contributing their time to this study and for their continued commitment to this research. This work was made possible by a gift from Open Philantrophy and Good Ventures to J.F.A.-V. J.F.A.-V. received philantrophic support from the Remondi Family Foundation. This work was supported by the US National Institutes of Health (NIH) Office of the Director (grant no. DP5 OD019833) and US National Institute on Aging (NIA) (grant no. R01 AG054671), the MGH Executive Committee on Research (MGH Research Scholar Award) and the Alzheimer's Association (no. AARGD-591030) to Y.T.Q. Y.T.Q. and F.L. received funding from the NIA (no. RF1AG077627). F.L. received funding from the NIH, Roche and the Banner Foundation for the API Colombia Registry and ADAD clinical trial. J.F.A.-V. was funded by the US National Institute of Neurological Disorders and Stroke (NINDS) and NIA cofunded grant nos. UH3 NS100121 and RF1 NS110048. C.V.-C. was funded by a grant from the Alzheimer's Association (no. AARF 2019A005859) and the NIA (no. K99AG073452); D.S.-F. was also funded by NINDS and NIA cofunded grant no. RF1 NS110048. D.S.-F. and S.K. were jointly funded by a gift from Open Philanthropy and Good Ventures, and by a grant from the Werner Otto Foundation, A.S.C. received funding from National Science Foundation Graduate Research Fellowship Program grant no. DGE1745303. D.S. received postdoctoral fellowships from the Fonds de recherche du Québec-Santé (Canada, award no. 254389) and the American Heart Association (award no. 20POST35110047). M.G. and D.S.-F. received funding from the German Federal Ministry of Education and Research, UndoAD-Project; M.G. received funding from the German Research Foundation (no. SFB877), K.S.K. received grant support from the Rainwater foundation, NIH, W.M. Keck Foundation

and the Alzheimer's Association. L.A.K. is supported in part by the National Eye Institute grant no. R01EY027739. R.A.S. received funding from the Harvard Aging Brain Study P01 NIA. E.M.R. received funding from NIH grant nos. RF1 AG041705, R01 AG058468, P30 AG072980 and R01 AG054671, the Banner Alzheimer's Foundation, the NOMIS Foundation and anonymous foundations (state of Arizona). We also thank J. Acosta-Uribe for help with the genetic studies, C. Dwumfour for histological preparations, A. Koutoulas from the Broad Institute of MIT and Harvard for technical support with DNA sequencing and Y. Alekseyev from the Boston University Department of Medicine Single Cell Sequencing Core and Boston University Microarray and Sequencing Resource Core Facilities for reagents and technical support for scRNA-seq.

Author contributions

F.L., J.F.A.-V. and Y.T.Q. initiated this work and directed and supervised the study. F.L., C.M., A.S.C., D.S.-F., J.F.A.-V. and Y.T.Q. drafted the manuscript. F.L., Y.T.Q., A.B., J.S.S., C.V.-C., L.R.G., K.S.K., Y.B., D.Aguillon, L.A.K., S.D.-T., Y.S., Y.C., A.S., R.A.S., K.J., E.M.R. and L.G.-B. collected and analyzed the biomarker and imaging data. D.S.-F., J.L.L., N.D.V.-M., K.H., K.P., S.K., A.V. and M.G. conducted and analyzed the neuropathology work. J.F.A.-V., K.L.S.-T., X.G., M.B., J.J. and L.S. collected and analyzed the genetic data. J.F.A.-V., C.M., A.S.C., M.O.H., N.C., G.M.O., D.S., A.S.C., K.L.S.-T., R.C.M., H.G., S.J.A.-A. and D.Amarnani conducted and analyzed the laboratory, cell culture and biochemistry work. C.M. and A.S.C. analyzed the data and contributed to finalizing the manuscript. F.L., J.F.A.-V., Y.T.Q. and D.S.-F. had direct access to and verified the data reported in the manuscript. F.L., C.M., A.S.C., M.O.H. and N.D.V.-M. are equal contributors listed as first coauthors. J.F.A.-V., Y.T.Q. and D.S.-F. are senior and corresponding authors.

Competing interests

None of the authors were precluded from accessing data in the study; they accept responsibility to submit the manuscript for publication. J.F.A.-V. and L.A.K. are cofounders of Epoch Biotech, a company developing resilient case-inspired therapeutics. Y.T.Q., J.F.A.-V. and F.L. serve as consultants for Biogen. K.S.K. consults with Expansion Therapeutics, ADRx Pharma and Herophilus, and serves on the board of directors of the Tau Consortium. E.M.R. is a compensated scientific advisor to Alzheon, Aural Analytics, Denali, Retromer Therapeutics and Vaxxinity, and a cofounder and advisor to ALZpath, which was not involved in this study. The other authors declare no competing interests.

Additional information

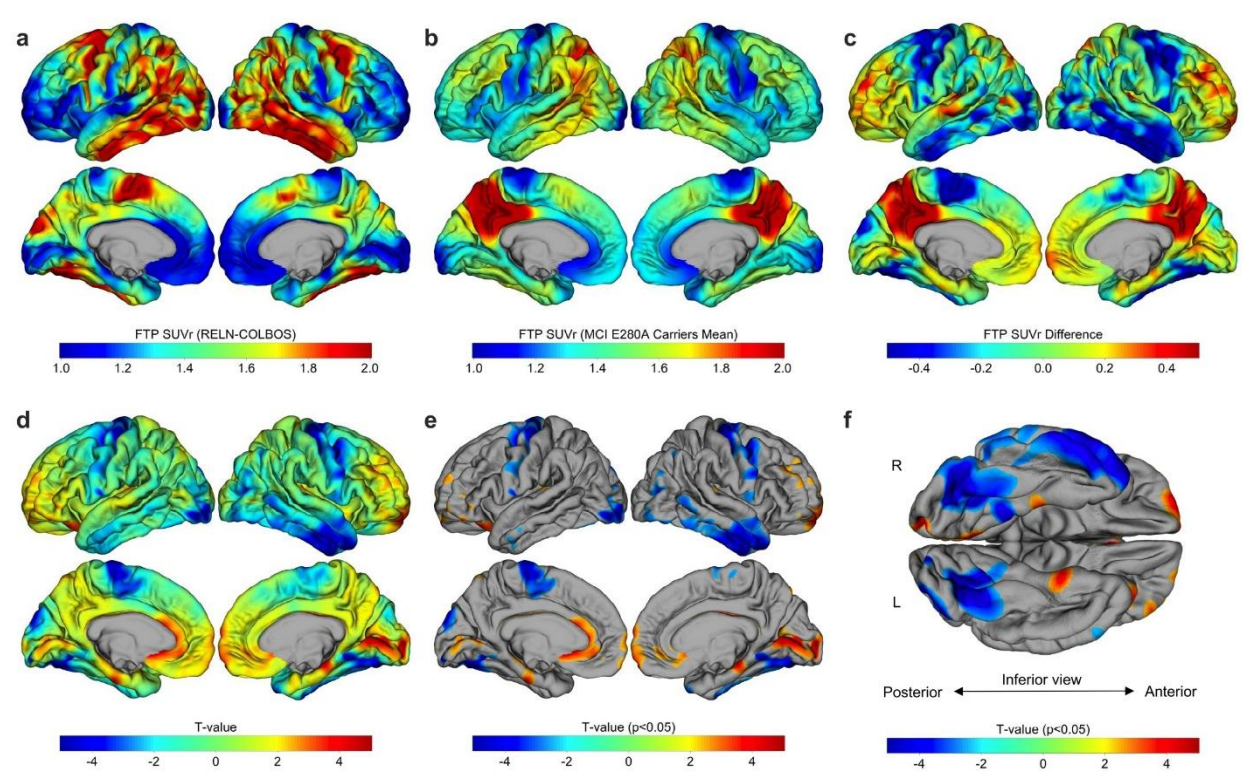
Extended data is available for this paper at https://doi.org/10.1038/s41591-023-02318-3.

Supplementary information The online version contains supplementary material available at https://doi.org/10.1038/s41591-023-02318-3.

Correspondence and requests for materials should be addressed to Diego Sepulveda-Falla, Joseph F. Arboleda-Velasquez or Yakeel T. Quiroz

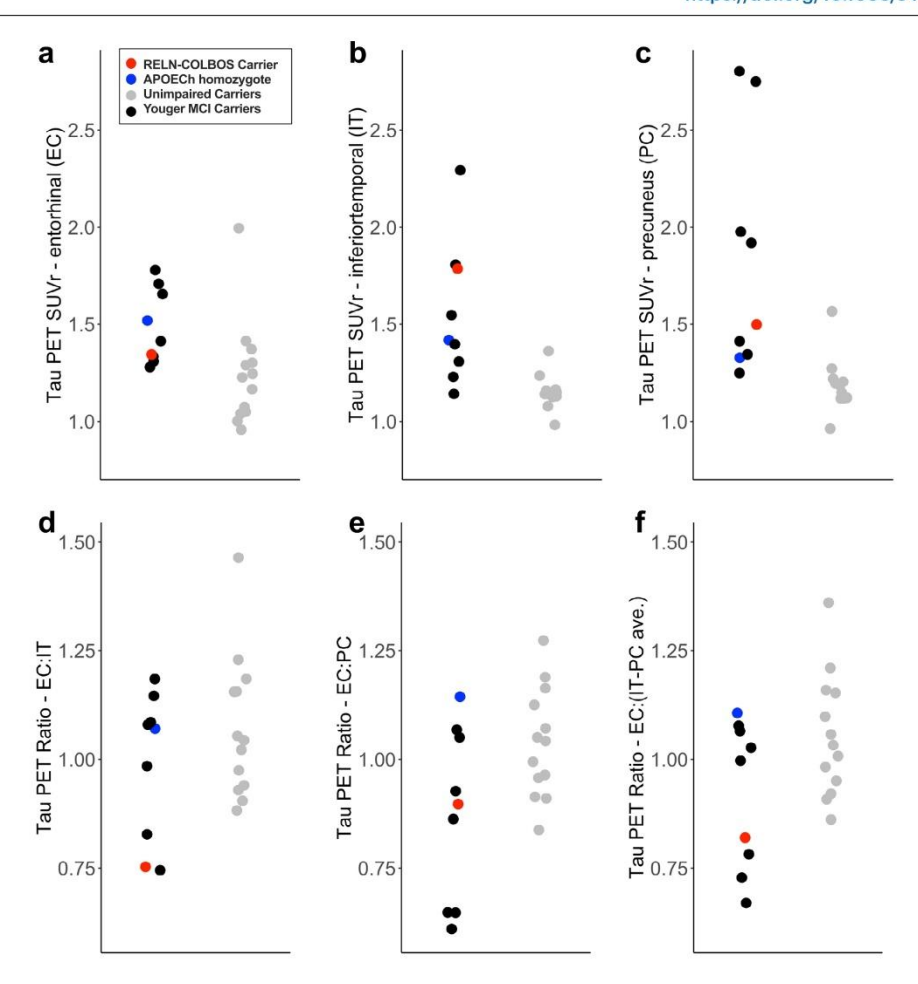
Peer review information *Nature Medicine* thanks Yadong Huang, Jacob Vogel and the other, anonymous, reviewer(s) for their contribution to the peer review of this work. Primary Handling Editor: Jerome Staal, in collaboration with the *Nature Medicine* team.

Reprints and permissions information is available at www.nature.com/reprints.



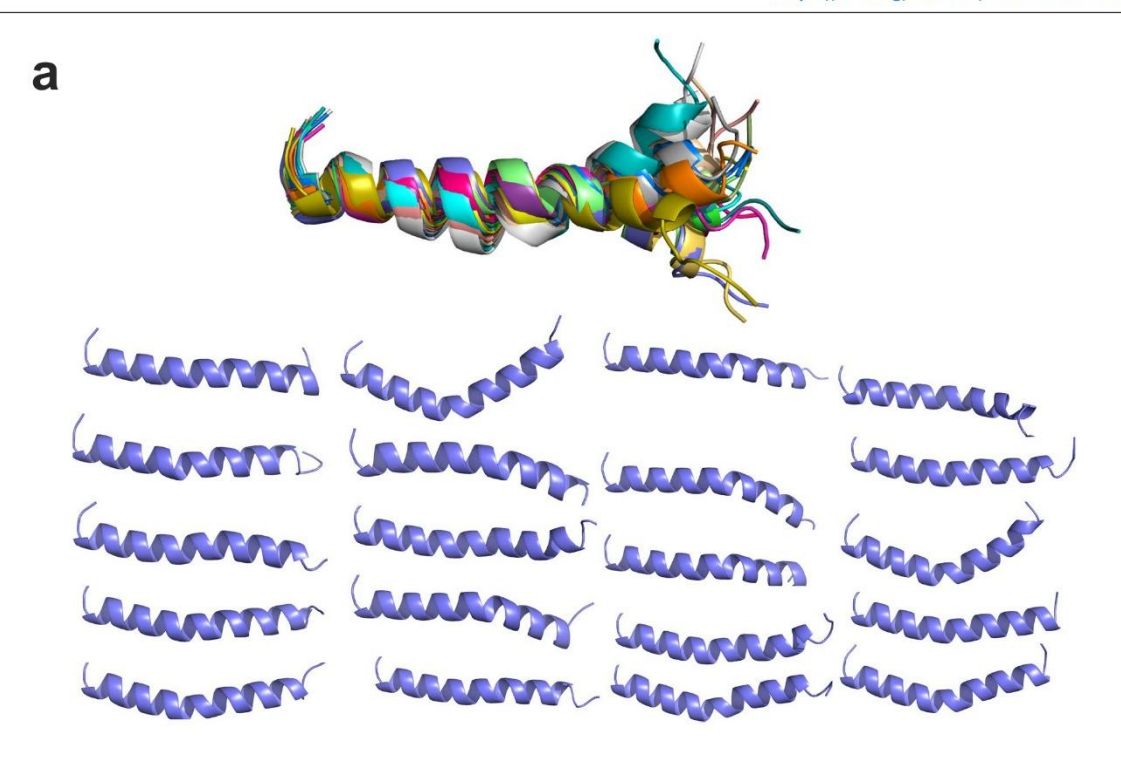
Extended Data Fig. 1 | Whole-cortex (vertex-wise) comparison of *RELN-COLBOS* carrier to typical MCI *PSENI E280A* carriers' tau PET. This analysis confirmed that compared to other *PSENI* E280A carriers who developed MCI at younger ages, the *RELN-COLBOS* carrier had relatively spared tau PET signal in the medial temporal lobe (entorhinal cortex / parahippocampal gyrus), but not in other areas including temporal neocortex. a, Cortical surface projection of vertex-wise tau PET (Flortaucipir, FTP) standardized uptake value ratio (SUVr) in the *RELN-COLBOS* carrier. b, Mean tau PET image of typical MCI *PSENI* E280A

carriers (n = 7). **c**, difference analysis between images (**b**) and (**a**): negative values indicate areas where RELN-COLBOS carrier had higher tau PET signal compared to other carriers, and vice-versa. **d**, T-value for one-sample 2-sided t-tests comparing other PSENI E280A carriers to the RELN-COLBOS patient. Directionality of effect size is the same as (**c**). Panel **e** shows T-values as in (**d**) masked by p value < 0.05 (uncorrected). **f**, Inferior / close-up view of surfaces shown in (**e**).

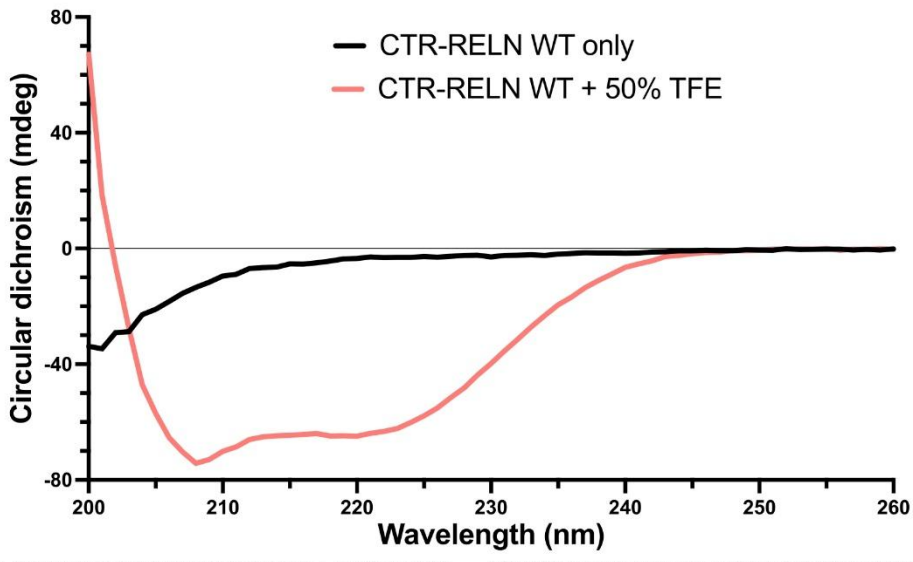


Extended Data Fig. 2 | Regional comparison of tau PET burden in RELN-COLBOS carrier versus other PSENI E280A carriers. This analysis confirmed that compared to other PSENI E280A carriers who developed MCI at younger ages, the RELN-COLBOS carrier had relatively spared tau pathology in the medial temporal lobe (entorhinal cortex / parahippocampal gyrus), but not in other areas including temporal neocortex (inferior temporal). a-c, Regional tau PET signal (Flortaucipir, FTP) standardized uptake value ratio (SUVr) in three regions

of interest: entorhinal (EC, a), inferior temporal (IT, b), and precuneus (PC, C). d-f, Ratios of tau PET uptake in medial temporal (EC) and neocortical (IT, PC) regions. d, EC:IT ratio, e, EC:PC ratio, f, ratio of EC to average of IT and PC (neocortical average). The tau pattern of the RELN-COLBOS patient was notable for the relative involvement of medial temporal versus temporal neocortex, particularly given the older age of the RELN-COLBOS patient compared to other carriers.

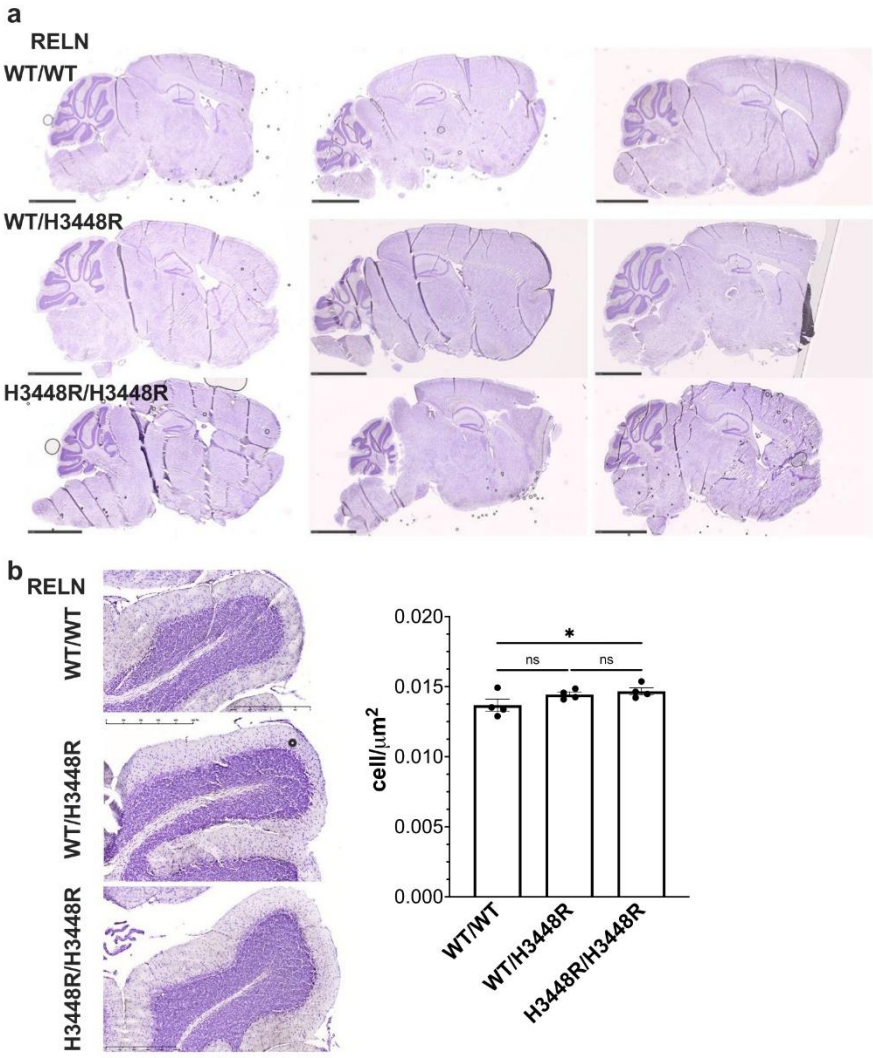


b Circular dichroism of CTR-RELN WT with 50% TFE



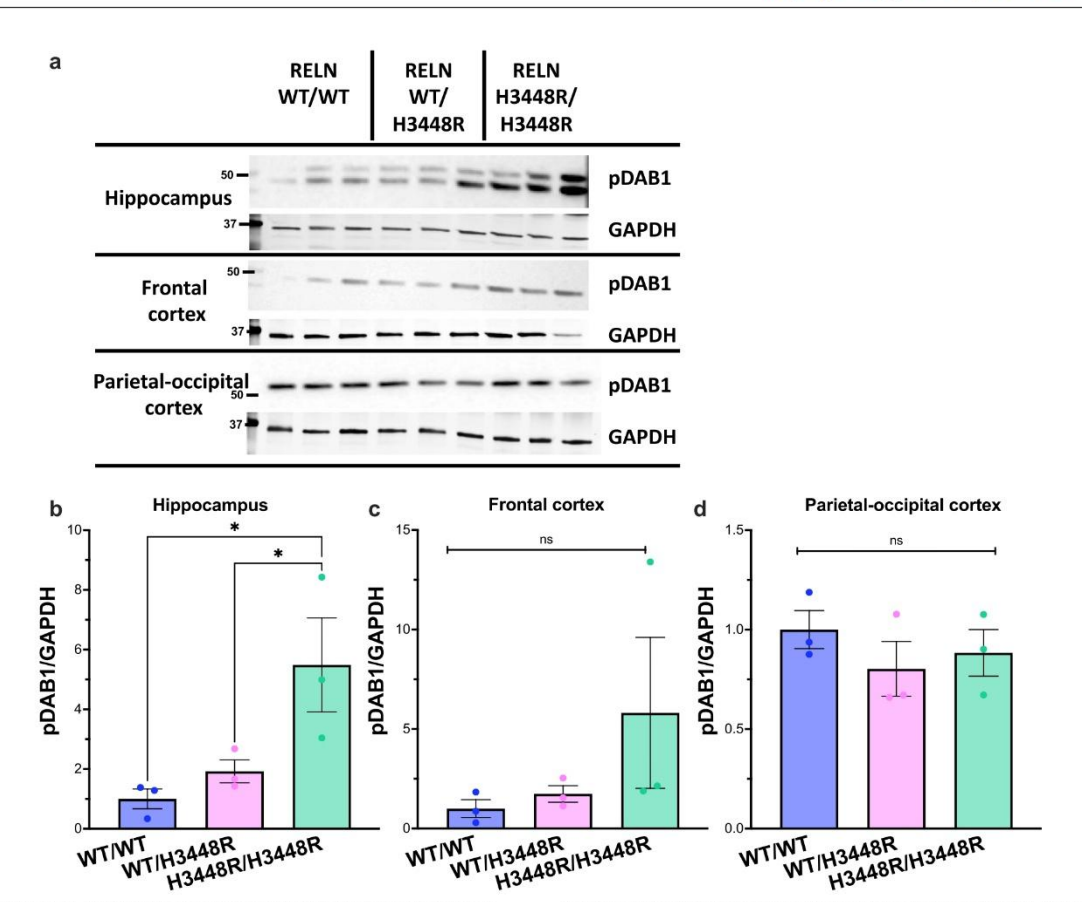
 $\label{lem:condition} \textbf{Extended Data Fig. 3} | \textbf{RELN CTR structural determination. a}, \textit{In silico} \ \textbf{models} \\ \text{for the 20 lowest energy structures of CTR-RELN produced by 2D NMR.} \\ \textbf{b}, \text{Representative CD spectra of CTR-RELN without heating showing that the CTR-RELN has primarily an alpha helical structure while the peptide without 50%} \\$

 $2,2,2 - Trifluoro ethanol \ has a spectrum closest to a random coil. \ Data is presented as the average of four spectra. Secondary structure analysis is reported in Supplementary Table 7.$



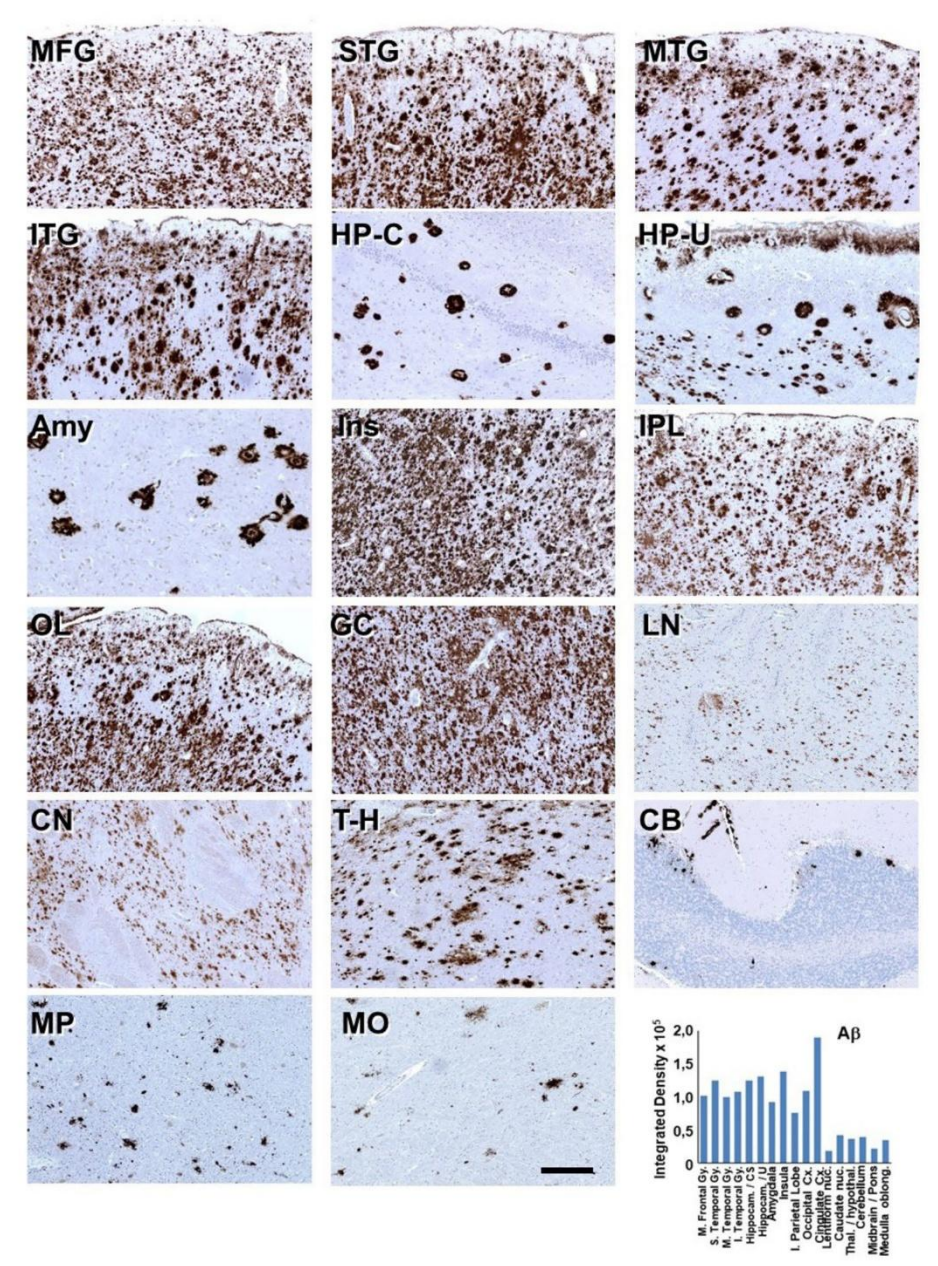
Extended Data Fig. 4 | Increased neuronal density in the cerebellum's granular layer in the presence of the H3448R *RELN* mice. presence of the H3448R *RELN* mice. a, Representative Cresyl violet staining of n=3 midsagittal sections from male *RELN* mice (WT/WT, WT/H3448R, H3448R/H3448R, 5-6-month-old mice). Data is showing that the H3448R variant does not affect qualitatively the gross anatomy, nor neuronal distribution in the whole brain. Scale bar, 2.5 mm. b, Cresyl violet staining of the granular region of the cerebellum, indicating an increased neuronal density in the homozygotes

 $(H3448R/H3448R) \ as compared to wild type (WT/WT) \ and heterozygote (WT/H3448R) mice. Scale bar, 500 \ \mu m. \ c$, Neuron density analysis of the granular layer of the *RELN*-H3448R cerebellum in comparisons to wild type. Data indicates a significantly increased neuron counting (*p = 0.0470, n1 = n2 = 4, t = 2.300, DF = 9) in homozygotes (H3448R/H3448R) as compared with wild type (WT/WT). One-way ANOVA, followed by Fisher's LSD test post-hoc analysis for multiple comparison of n = 4 specimens for each genotype. Data is presented as mean \pm S.D. At least 2 sections and 5 fields per section were analyzed for each specimen.



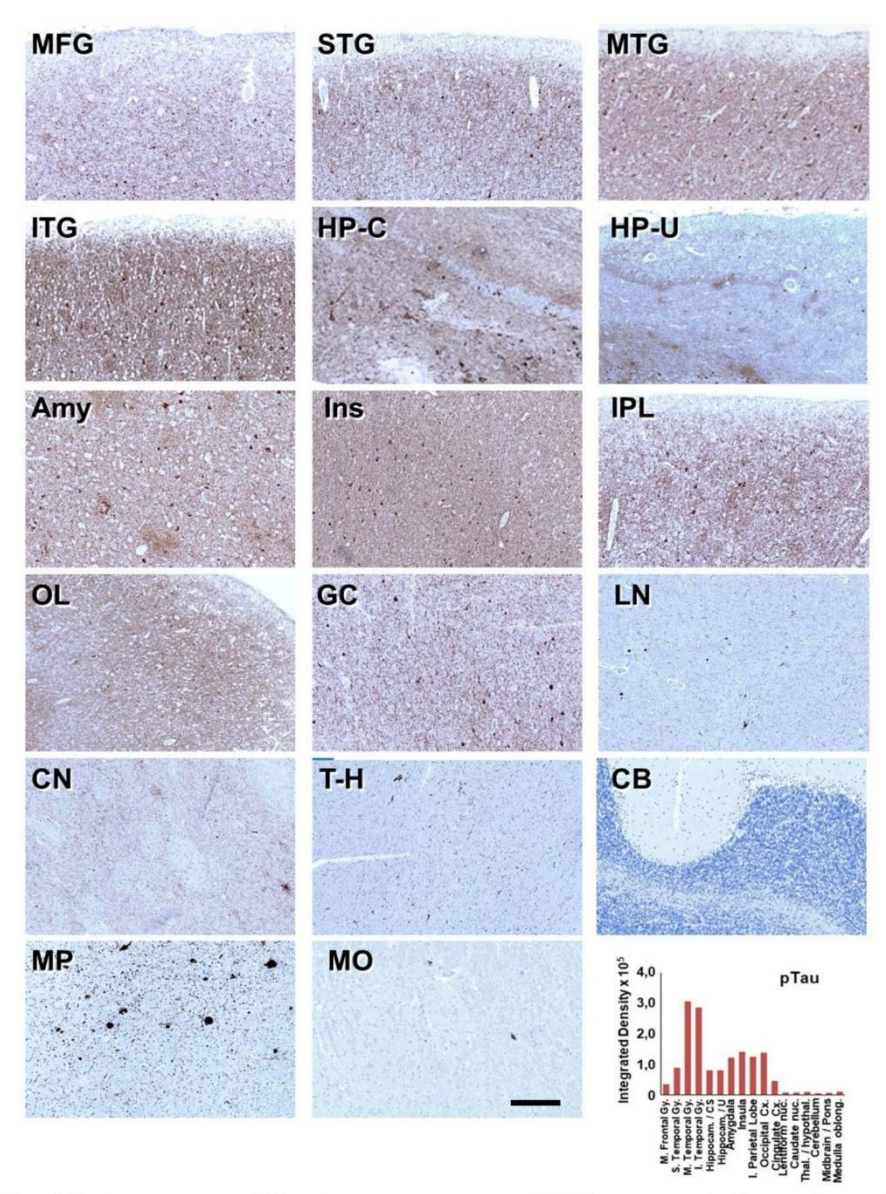
Extended Data Fig. 5 | pDab1 levels in different brain regions of the novel H3448R-RELN transgenic mouse model. a, Representative blots of pDab1 and GAPDH levels in hippocampus, frontal cortex and parietal-occipital cortex of total homogenate obtained from RELN WT/WT, RELN WT/H3448R and RELN H3448R/H3448R brains (n = 3). b-c, Quantification of normalized to GAPDH levels of pDab1 positive bands detected in the hippocampus (b), frontal cortex (c), and parietal-occipital cortex (d) from RELN WT/WT, RELN WT/H3448R and RELN H3448R/H3448R male mice at 16 weeks of age, n = 3 mice. Data is

showing that there are significantly increased pDab1 levels in the presence of the homozygous H3448R mutation compared to heterozygous and WT hippocampus (b, 'p = 0.03866, WT/WT vs. WT/H3448R, nl = n2 = 3, t = 3.32, DF = 6). *p = 0.01596, WT/WT vs. H3448R/H3448R, nl = n2 = 3, t = 2.63773, DF = 6). For all quantification, we used one-way ANOVA, followed by Fisher's Least Significant difference (LSD) test for multiple comparisons. All data is presented as average \pm s. e. m.



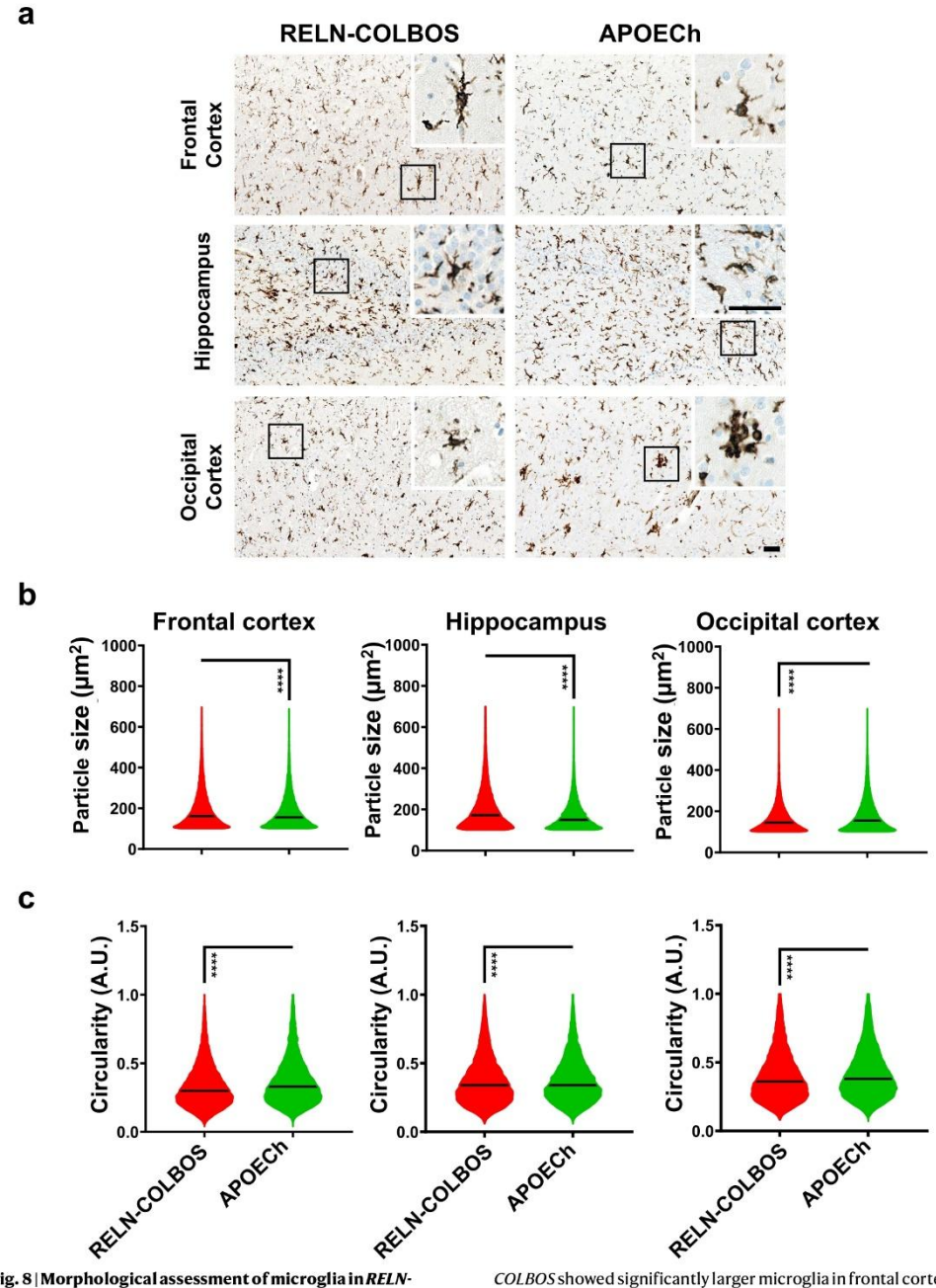
Extended Data Fig. 6 | IHC staining for Amyloid \beta. MFG = Medial frontal gyrus, STG = Superior temporal gyrus, MTG = Medial temporal gyrus, ITG = Inferior temporal gyrus, HP-C = Hippocampus/collateral sulcus, HPUncus = Hippocampus/uncus, Amy = Amygdala, Ins = Insula, IPL = Inferior

 $parietal\ lobe,\ OL=Occipital\ lobe,\ GC=Gyrus\ cinguli,\ LN=Lentiform\ nucleus,\ CN=Caudate\ nucleus,\ T-H=Thalamus/Hypothalamus,\ CB=Cerebellum,\ MP=Midbrain/pons,\ MO=Medulla\ oblongata.\ Scale\ bar=100\ \mu m.$



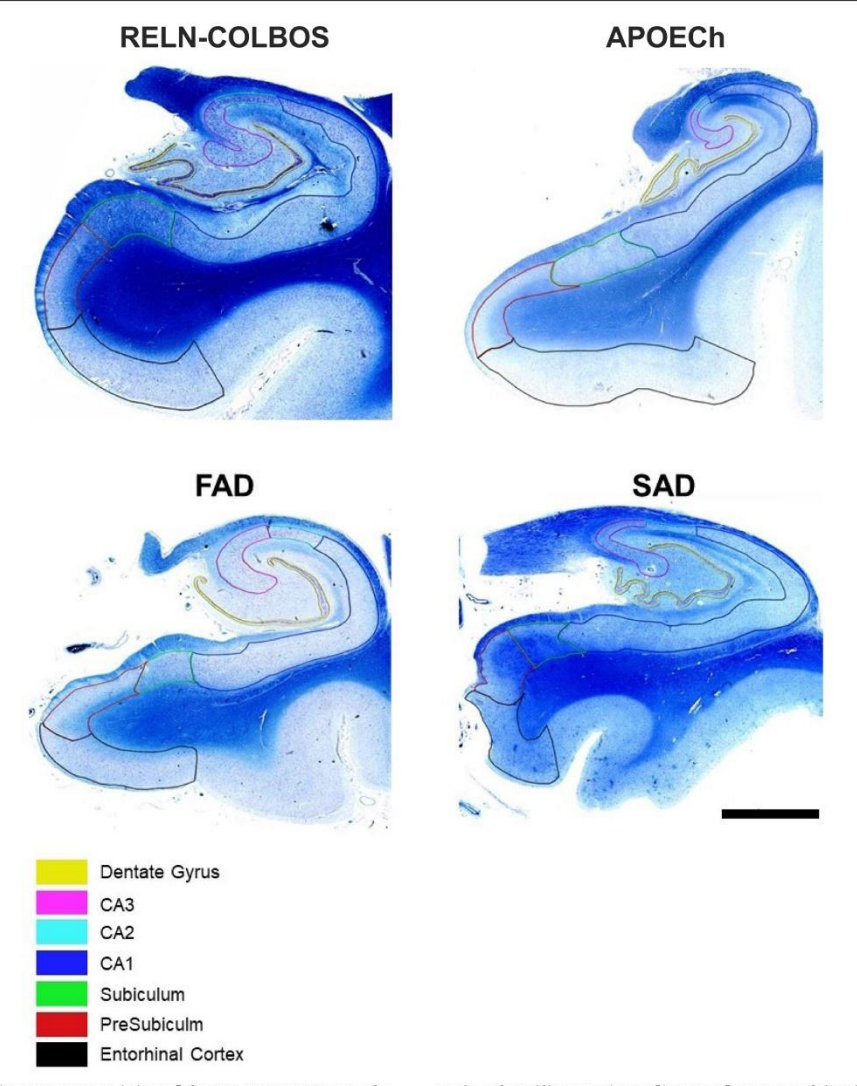
 $\label{eq:continuous} \textbf{Extended Data Fig. 7} | \textbf{IHC staining for ptau.} \ MFG = \textbf{Medial frontal gyrus,} \\ \textbf{STG} = \textbf{Superior temporal gyrus,} \ MTG = \textbf{Medial temporal gyrus,} \ \textbf{ITG} = \textbf{Inferior temporal gyrus,} \ \textbf{HP-C} = \textbf{Hippocampus/collateral sulcus,} \ \textbf{HP-Uncus} = \textbf{Hippocampus/uncus,} \ \textbf{Amy} = \textbf{Amygdala,} \ \textbf{Ins} = \textbf{Insula,} \ \textbf{IPL} = \textbf{Inferior parietal lobe,} \\ \ \textbf{Medial frontal gyrus,} \ \textbf{Medi$

OL = Occipital lobe, GC = Gyrus cinguli, L = Lentiform nucleus, CN = Caudate nucleus, T-H = Thalamus/Hypothalamus, CB = Cerebellum, MP = Midbrain/pons, MO = Medulla oblongata. Scale bar = 100 $\,\mu$ m.



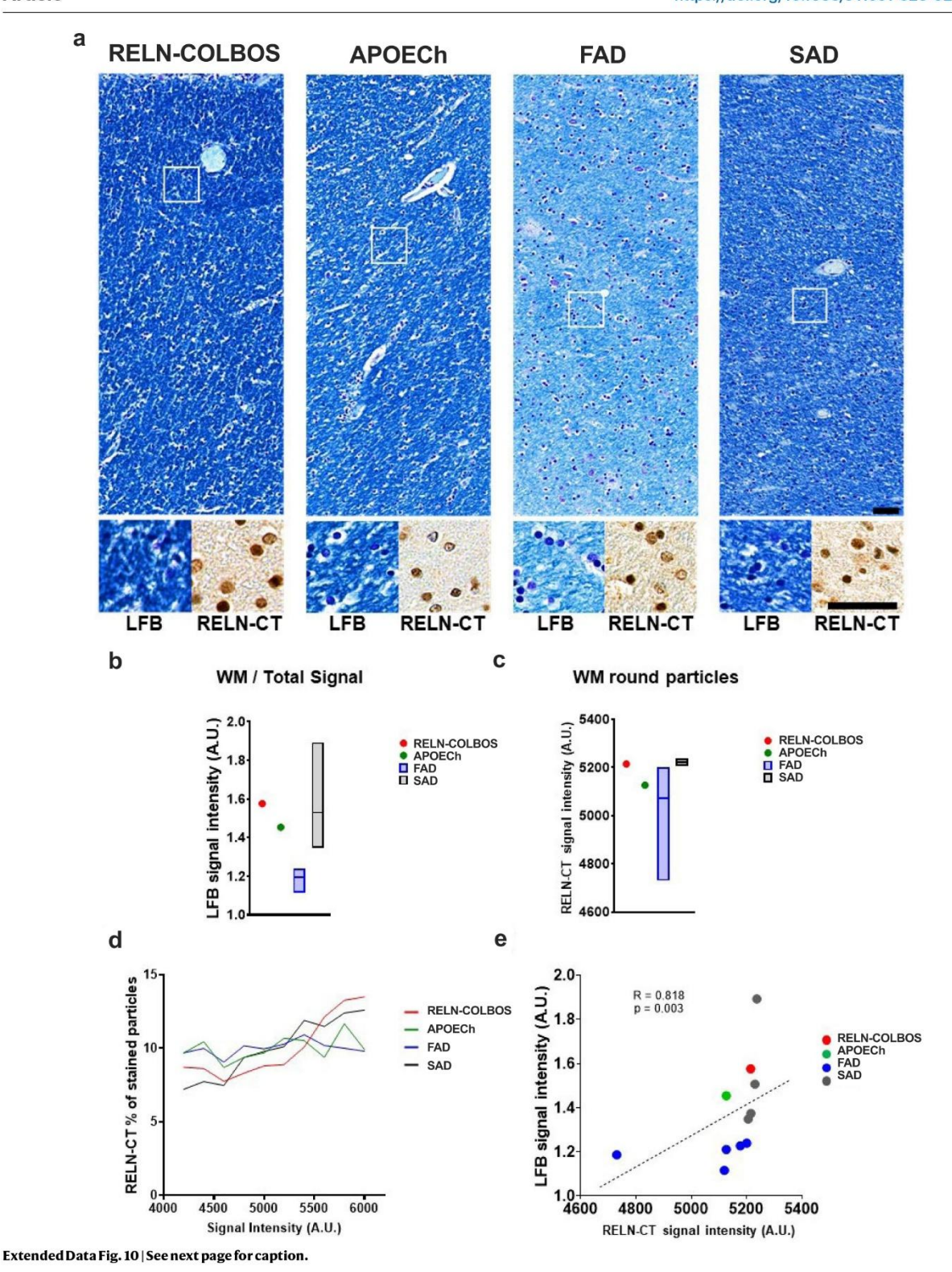
Extended Data Fig. 8 | Morphological assessment of microglia in RELN-COLBOS and APOECh protected cases. a, Representative pictures of ionized calcium binding adaptor molecule1 (IBA1) stained microglia in frontal cortex, hippocampus, and occipital cortex from both, PSENI E280A RELN-COLBOS case and the PSENI E280A APOECh homozygous case. Bar, 50 μ m. b, c, Violin plots for size and circularity assessment in RELN-COLBOS and APOECh cases. The RELN-

COLBOS showed significantly larger microglia in frontal cortex (FC, number of particles, np = 45679) and hippocampus (Hip, np = 21407), and smaller microglia in the occipital cortex (OC, np = 22365). Microglial circularity was higher in the APOECh case in all areas (np values for APOECh: FC = 18537, Hip = 14265, OC = 23845). $P \le 0.001^{****}$. Two-sided Student's test was used for analysis.



Extended Data Fig. 9 | Klüver Barrera staining of the RELN-COLBOS case, the APOECh case, a representative PSENI E280A FAD case and a representative SAD case. Klüver-Barrera staining using luxol fast blue staining for myelin and cresyl violet staining for neuronal perikaryal in selected brain regions.

 $Code-colored\ lines, regions\ of interest\ for\ neuronal\ density\ measurements\ in\ Cornu\ Ammonis\ (CA)\ structures\ CA1,\ CA2,\ and\ CA3,\ together\ with\ the\ Dentate\ Gyrus,\ Subiculum,\ Presubiculum\ and\ Entorhinal\ cortex.\ Scale\ bar,\ 3\ mm.$



Extended Data Fig. 10 | **Analysis of the white matter signal in the** *RELN-COLBOS* **in comparisons to other AD cases. a**, Representative images for luxol fast blue (LFB) staining (large panel and small left panels) and RELN-CT (small right panel) of the sub hippocampal white matter of the *RELN-COLBOS* case, the *APOECh* case, a representative *PSENI* E280A FAD case and a representative SAD case. Scale bars, 50 μm. **b**, Bar graph for normalized measurement of white matter relative to total LFB signal of the *RELN-COLBOS* case, the *APOECh* case, *PSENI* E280A FAD cases (n = 5) and SAD cases (n = 4). Both the *RELN-COLBOS* case and the *APOECh* case show relative higher white matter signal than the other FAD cases. **c**, Bar graph for the quantification of RELN-CT signal in round particles

in the sub-hippocampal white matter of the RELN-COLBOS case, the APOECh case, PSENI E280A FAD cases (n = 5) and SAD cases (n = 4). The RELN-COLBOS case shows higher RELN-CT signal intensity than all FAD cases, including the APOECh one. **d**, Line graph for RELN-CT positive round particles signal intensity distribution in the RELN-COLBOS case, the APOECh case, PSENI E280A FAD cases (n = 5) and SAD cases (n = 4). The RELN-COLBOS case showed a larger percentage of particles with higher RELN-CT signal intensity when compared with the other AD cases. **e**, Scatter plot of Spearman's Rho correlation analysis for LFB signal intensity and RELN-CT round particles signal intensity in all analyzed AD cases. A statistically significant positive correlation was identified (p = 0.003, R = 0.818).

9. Publication III

The NEW ENGLAND JOURNAL of MEDICINE

ORIGINAL ARTICLE

APOE3 Christchurch Heterozygosity and Autosomal Dominant Alzheimer's Disease

Y.T. Quiroz, D. Aguillon, D.C. Aguirre-Acevedo, D. Vasquez, Y. Zuluaga, A.Y. Baena, L. Madrigal, L. Hincapié, J.S. Sanchez, S. Langella, R. Posada-Duque, J.L. Littau, N.D. Villalba-Moreno, C. Vila-Castelar, L. Ramirez Gomez, G. Garcia, E. Kaplan, S. Rassi Vargas, J.A. Ossa, P. Valderrama-Carmona, P. Perez-Corredor, S. Krasemann, M. Glatzel, K.S. Kosik, K. Johnson, R.A. Sperling, E.M. Reiman, D. Sepulveda-Falla, F. Lopera, and J.F. Arboleda-Velasquez

ABSTRACT

BACKGROUND

Variants in *APOE* and *PSEN1* (encoding apolipoprotein E and presenilin 1, respectively) alter the risk of Alzheimer's disease. We previously reported a delay of cognitive impairment in a person with autosomal dominant Alzheimer's disease caused by the *PSEN1*^{E280A} variant who also had two copies of the apolipoprotein E3 Christchurch variant (*APOE3*^{Ch}). Heterozygosity for the *APOE3*^{Ch} variant may influence the age at which the onset of cognitive impairment occurs. We assessed this hypothesis in a population in which the *PSEN1*^{E280A} variant is prevalent.

METHODS

We analyzed data from 27 participants with one copy of the *APOE3*^{ch} variant among 1077 carriers of the *PSENI*^{E280A} variant in a kindred from Antioquia, Colombia, to estimate the age at the onset of cognitive impairment and dementia in this group as compared with persons without the *APOE3*^{ch} variant. Two participants underwent brain imaging, and autopsy was performed in four participants.

DECILIT

Among carriers of *PSEN1*^{E280A} who were heterozygous for the *APOE3*^{Ch} variant, the median age at the onset of cognitive impairment was 52 years (95% confidence interval [CI], 51 to 58), in contrast to a matched group of *PSEN1*^{E280A} carriers without the *APOE3*^{Ch} variant, among whom the median age at the onset was 47 years (95% CI, 47 to 49). In two participants with the *APOE3*^{Ch} and *PSEN1*^{E280A} variants who underwent brain imaging, ¹⁸F-fluorodeoxyglucose positron-emission tomographic (PET) imaging showed relatively preserved metabolic activity in areas typically involved in Alzheimer's disease. In one of these participants, who underwent ¹⁸F-flortaucipir PET imaging, tau findings were limited as compared with persons with *PSEN1*^{E280A} in whom cognitive impairment occurred at the typical age in this kindred. Four studies of autopsy material obtained from persons with the *APOE3*^{Ch} and *PSEN1*^{E280A} variants showed fewer vascular amyloid pathologic features than were seen in material obtained from persons who had the *PSEN1*^{E280A} variant but not the *APOE3*^{Ch} variant.

CONCLUSIONS

Clinical data supported a delayed onset of cognitive impairment in persons who were heterozygous for the *APOE3*^{Ch} variant in a kindred with a high prevalence of autosomal dominant Alzheimer's disease. (Funded by Good Ventures and others.)

The authors' full names, academic degrees, and affiliations are listed in the Appendix. Dr. Quiroz can be contacted at yquiroz@mgh.harvard.edu. Dr. Lopera can be contacted at francisco.lopera@gna.org.co. Dr. Arboleda-Velasquez can be contacted at joseph_arboleda@meei.harvard.edu or at Schepens Eye Research Institute, Mass Eye and Ear, 20 Staniford St., Boston, MA 02114.

Drs. Quiroz, Aguillon, Aguirre-Acevedo, and Vasquez and Drs. Lopera and Arboleda-Velasquez contributed equally to this article.

This article was updated on June 19, 2024, at NEIM.org.

N Engl J Med 2024;390:2156-64.
DOI: 10.1056/NEJMoa2308583
Copyright © 2024 Massachusetts Medical Society.

2156

N ENGL J MED 390;23 NEJM.ORG JUNE 20, 2024

N ANTIOQUIA, COLOMBIA, THERE IS A large family of approximately 6000 blood relatives, including more than 1000 carriers of the E280A variant of the PSEN1 gene (encoding the protein presenilin 1). Autosomal dominant Alzheimer's disease is destined, with near 100% certainty, to develop in these carriers of PSEN1^{E280A}. Most of the carriers in this kindred have mild cognitive impairment in their midforties and dementia in their late forties.¹

Common variants of the apolipoprotein E gene (APOE) influence the risk of Alzheimer's disease: APOE4 is linked to high risk, APOE3 is considered to confer a neutral risk, and APOE2 is associated with relative protection.2-5 In addition to APOE, several other genes, when variant, cause susceptibility to Alzheimer's disease; one of these is PSEN1.6 We previously reported the case of a person with the PSEN1E280A variant who also had two copies of the rare Christchurch variant (R136S) in APOE3 (APOE3Ch); in this person, mild cognitive impairment developed during her seventies — almost three decades after the expected age at onset.7 In vivo and postmortem analyses showed that the APOE3^{Ch} variant was linked to reduced tau accumulation and reduced neuroinflammation, which led to less neurodegeneration and less cerebral amyloid angiopathy within the context of higher cortical amyloid burden than is observed in persons with the PSEN1E280A variant and without the APOE3^{Ch} variant.^{7,8} We aimed to ascertain whether heterozygosity for the APOE3^{Ch} variant (APOE3^{Ch/e3}, APOE3^{Ch/e2}, or APOE3^{Ch/e4}) would delay the age at onset of mild cognitive impairment or dementia in 27 persons with this genotype among members of the Colombian kindred with the PSEN1E280A variant, which is associated with autosomal dominant Alzheimer's disease.

METHODS

STUDY DESIGN

In this retrospective study, we investigated data from a cohort of 1077 descendants in a family with the *PSEN1*^{E280A} variant,⁹ which was assessed by our group from 1995 to 2022 (Fig. S1 in the Supplementary Appendix, available with the full text of this article at NEJM.org). The study was approved by the institutional review boards of the University of Antioquia, Colombia, and the Mass General Brigham integrated health care

system. All the participants (or their representatives) provided written informed consent before the initiation of study procedures. (The document was read to participants who were unable to read, and they were asked to sign, if possible, or to provide a fingerprint.) Enrolled participants were 18 years of age or older and had at least one parent with the *PSENI* E280A variant, and therefore, mild cognitive impairment followed by autosomal dominant Alzheimer's disease was destined to occur. During data collection, investigators were unaware of the genetic status of the participants.

Participants underwent regular clinical and neuropsychological assessments. The intervals between testing have been analyzed previously and were homogeneous across *APOE3*^{ch} carriers and noncarriers. In one report involving this kindred, testing in a group of 309 persons with the *PSENI*^{E280} variant took place at a mean interval of 2 years (range, 1 to 11), and in another report, at a median interval of 2 years (interquartile range, 1 to 3).

Neuropsychological assessments were conducted in Spanish with the use of a battery that has been adapted and validated for the detection of Alzheimer's disease-related cognitive impairment in this kindred, which included the Consortium to Establish a Registry for Alzheimer's Disease (CERAD), the Trail Making Test, and the Rey-Osterrieth complex figure, among other assessments. 10-12 Using these data, neurologists and neuropsychologists, who were unaware of the genetic variants in the specific participants, retrospectively classified participants as having normal cognitive status, mild cognitive impairment, or dementia, according to the National Institute on Aging and the Alzheimer's Association Workgroup criteria for mild cognitive impairment due to Alzheimer's disease13 and the related Workgroup criteria for dementia due to Alzheimer's disease.14

We also used the Functional Assessment Staging (FAST) system, which is a scale to assess the level of functional impairment in patients with dementia (scores range from 1 [no impairment] to 7 [total dependence]), and the Mini-Mental State Examination (MMSE; scores range from 0 to 30, with lower scores indicating greater cognitive impairment). The criteria for mild cognitive impairment were as follows: for persons with less than 9 years of education, a FAST score

of at least 3 and an MMSE score of no more than 24; and for persons with 9 or more years of education, an MMSE score of no more than 26. The criteria for mild dementia were as follows: for persons with less than 9 years of education, a FAST score of at least 4 and an MMSE score of no more than 22; and for persons with 9 or more years of education, an MMSE score of no more than 24.

PARTICIPANTS

In an extended family of 1077 PSEN1E280A carriers in whom autosomal dominant Alzheimer's disease was destined to develop, we identified 121 carriers of the APOE3^{Ch} variant (Fig. S2), among whom 1 had the previously reported PSEN1E280A variant and was homozygous for APOE3ch and 27 were carriers of PSEN1E280A and were heterozygous for the APOE3^{Ch} variant. Of these 27 persons who were heterozygous for PSEN1E280A and APOE3^{ch}, 1 died at 57 years of age without cognitive symptoms (last examination at 2 years before death), 13 had mild cognitive impairment or dementia, and 13 did not meet the criteria for mild cognitive impairment or dementia (and are not identified in the family tree in order to protect privacy) (see the Supplementary Appendix).

These 27 persons who were heterozygous for the *APOE3*^{Ch} and *PSEN1*^{E280A} variants (i.e., the group of interest) had extensive clinical data and underwent neuropsychological testing. Two participants also had neuroimaging data, and 4 also underwent postmortem brain examinations. Genotyping was performed for the *PSEN1*^{E280A} and *APOE* variants, as previously described.⁷

NEUROIMAGING METHODS

One participant underwent amyloid (11C-Pittsburgh compound B) and tau (18F-flortaucipir) positron-emission tomographic (PET) imaging at Massachusetts General Hospital in Boston. Two participants (Participants 1 and 2) underwent structural magnetic resonance imaging and 18F-fluorodeoxyglucose (FDG) PET imaging at the Hospital Pablo Tobón Uribe in Medellín, Colombia.

NEUROPATHOLOGICAL METHODS

Neuropathological material, which was obtained with the use of previously described techniques, was available from four persons who were heterozygous for the PSENI^{E280A} and APOE3^{Ch} variants

(Participants 3 through 6), from five carriers of *PSEN1*^{E280A} and *APOE3* (Participants 7 through 11), and from one person who was a *PSEN1*^{E280A} carrier and was homozygous for *APOE3*^{Ch} (Participant 12). Immunohistochemical staining was performed uniformly for pathological markers of Alzheimer's disease in cortical areas, followed by quantitative morphologic evaluation of vascular pathologic features in all the participants. ImageJ software, version 1.52p (National Institutes of Health), was used for image analysis for all findings. A description of these methods is provided in the Supplementary Appendix.

STATISTICAL ANALYSIS

We retrospectively estimated the cumulative incidence function, which represents the probability of mild cognitive impairment or dementia over time, considering the time from the date of birth to the onset of mild cognitive impairment or dementia in all the participants available from the cohort described above. We calculated the restricted mean and median survival times (i.e., the time to mild cognitive impairment or dementia) with the standard error and 95% confidence intervals, respectively, with categorization according to APOE3^{Ch} genotype. For participants with censored data, the times to these end points were calculated to the date of the last medical evaluation. We considered death to be a competing event for the analyses because death could occur before the onset of mild cognitive impairment or dementia.

To control for potential confounding factors of sex, APOE genotype, and years of formal education, we established a matched sample between carriers and noncarriers of the APOE3^{ch} variant. For this matching, we used the nearestneighbor method with the propensity score as a measure of similarity,15 resulting in a ratio of approximately 12 noncarriers to 1 APOE3^{Ch} carrier, which was determined by the MatchIt package in R software, after the maximum ratio was initially set at 20:1. To examine the balance of the groups before and after matching, we used a standard mean (or proportion) difference (Fig. S3). A subhazard ratio¹⁶ was calculated in an exploratory analysis to estimate the association between APOE3^{ch} status and the time to mild cognitive impairment or dementia (Table S1 and Fig. S4). Statistical analyses were performed with the use of R software, version 4.3.1.17

RESULTS

CLINICAL AND NEUROIMAGING FINDINGS IN TWO LIVING PERSONS HETEROZYGOUS FOR APOE3^{CH}

The first participant was a man with the genotype PSEN1E280A-APOE3Ch/e3 and 11 years of formal education. At 47 years of age, he had no subjective or objective cognitive problems or changes in daily functioning, and neurologic examinations and testing were normal (FAST score, 1; MMSE score, 28). At 49 years of age, his cognitive test performance was within normal limits for his age and educational level, and he reported having mild subjective memory concerns (FAST score, 2; MMSE score, 27). At 51 years of age, he received a diagnosis of mild cognitive impairment (FAST score, 3; MMSE score, 25) and had a decline in semantic fluency (decline in the CERAD Animal Fluency score from the 79th to 53rd percentile [range in normal populations, 25th to 75th]), executive functioning (decline in the Trail Making Test score from the 45th to 42nd percentile [range in normal populations, 25th to 75th]) and memory recall (decline in the CERAD Word List Recall score from the 23rd to 1st percentile [range in normal populations, 25th to 75th]). At 54 years of age, he received a diagnosis of mild dementia (FAST score, 4; MMSE score, 21).

PET imaging in this participant at 51 years of age showed slightly higher levels of brain cortical amyloid plaque $(A\beta)$ burden than was seen in PSEN1^{E280A} carriers in whom Alzheimer's disease had developed at the expected age in this kindred (distribution volume ratio [DVR], 1.68 vs. a mean [±SD] of 1.50±0.12 among PSEN1E280A carriers with cognitive impairment) but a more limited tau burden in brain regions related to Alzheimer's disease, including the entorhinal cortex (standardized uptake value ratio [SUVR], 1.33 vs. a mean of 1.60±0.29) (Fig. 1 and Fig. S5). When this participant was 53 years of age, 18F-FDG PET imaging showed a cerebral metabolic rate for glucose in the precuneus within the range of younger PSEN1 variant carriers in whom mild cognitive impairment had developed at a typical age in this kindred (SUVR, 1.15 vs. a mean of 1.23±0.17) (Fig. 1).

The second participant was a man with genotype *PSEN1*^{E280A}—*APOE3*^{Ch/e2} who was illiterate and had received no formal education. His evaluation at 38 years of age showed slow processing speed and low verbal memory recall, although the scores

were within the normal limits for his educational level (FAST score, 2; MMSE score, 27). He reported subjective cognitive concerns at 42 years of age, and his performance on the MMSE was reduced as compared with previous scores (FAST score, 2; MMSE score, 22) in the context of depression (Geriatric Depression Scale-15 score, 6; on a scale from 0 to 15, with a score above 5 indicating depression). His overall objective performance, however, was within the normal limits for his age and educational level. His scores were similar to those on previous verbal and nonverbal memory tests, and he did not have functional decline, so he did not meet the criteria for mild cognitive impairment at that time.

At 52 years of age, with no intervening testing after the previous battery, this participant had a decline in verbal memory, and his family reported having increased concerns about his cognitive condition despite preserved functional independence. At that time, he met the criteria for mild cognitive impairment (FAST score, 3; MMSE score, 25). (When the numerical results on the MMSE and FAST diverged, the clinical study team placed more emphasis on the FAST score because it reflects functional capabilities; the study team retrospectively classified this person as having mild cognitive impairment at this time point.) When this participant was 57 years of age, functional decline led to a diagnosis of mild dementia (FAST score, 4; MMSE score, not available). At 62 years of age, his memory skills declined further, although his naming and semantic fluency skills remained similar to the results on previous tests. He required more support to complete instrumental activities of daily living and had progression to moderate dementia (FAST score, 5; MMSE score, 18). When this participant was 64 years of age, FDG PET imaging showed a relatively preserved cerebral metabolic rate for glucose in the precuneus (SUVR, 1.35) (Fig. 1) as compared with PSEN1E280A carriers in whom mild cognitive impairment had developed at the expected age. Imaging for $A\beta$ and tau was not conducted owing to a lack of local availability and travel restrictions to the United States.

AGE AT ONSET IN PERSONS WITH PSEN1E280A HETEROZYGOUS FOR APOE3^{CH}

To evaluate the time to mild cognitive impairment or dementia, with accounting for known

influencing factors, we matched *APOE3*^{Ch} carriers with noncarriers on the basis of sex, educational level, and *APOE* genotype, as described above. This matching process yielded a subgroup of 353

participants for this part of the study (Table S2). Figures 2A and 2B show the time to mild cognitive impairment or dementia among the 1077 PSEN1^{E280A} carriers, including 27 carriers of the

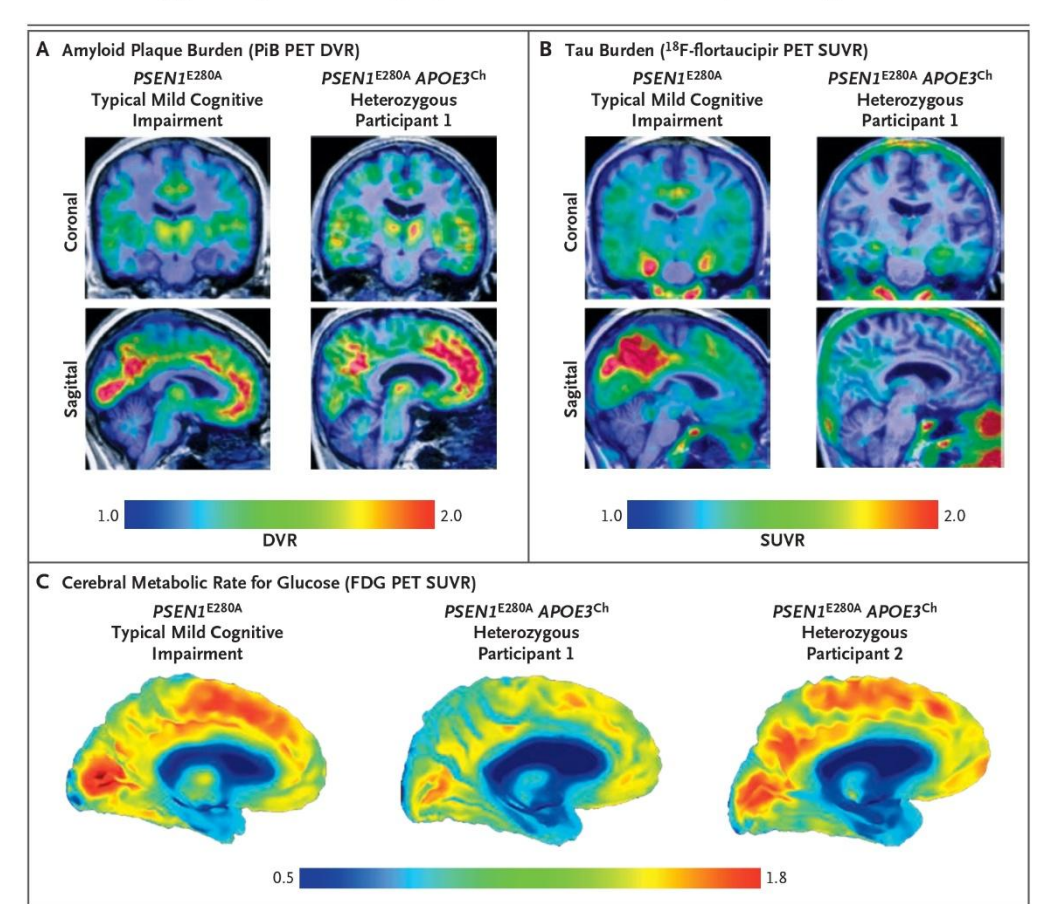


Figure 1. Limited Tau Pathological Findings and Relatively Preserved Regional Cerebral Metabolic Activity in Persons Heterozygous for the *PSEN1*^{E280A} and *APOE3*^{Ch} Variants.

Shown are baseline amyloid-eta positron-emission tomographic (PET) images (Panel A; 11 C-Pittsburgh compound B [PiB]) and tau PET images (Panel B; 18F-flortaucipir). Sample coronal views (upper images) and sagittal views (lower images) are shown for each. For visual comparison, samples that were obtained from two participants are shown: from a typical person with the E280A variant of presenilin 1 (PSEN1E280A) who had mild cognitive impairment (Panels A and B, left images), and from a person with the PSEN1E280A variant who was also heterozygous for the APOE3Ch variant (right images). The color-coded scale bar indicates the PiB distribution volume ratio (DVR) or flortaucipir standardized uptake value ratio (SUVR) values; blue represents the lowest binding and red represents the highest binding, with values ranging from 1.0 to 2.0. The person who was heterozygous for the APOE3^{ch} variant had greater amyloid- β plaque burden and a relatively limited tau burden as compared with persons with the PSEN1^{E280A} variant in whom the onset of mild cognitive impairment occurred at the typical age in this kindred, as exemplified by the person whose images are shown here. Panel C shows ¹⁸F-fludeoxyglucose (FDG) PET images indicating the precuneus cerebral metabolic rate for glucose. In all three panels, the sample was obtained from a person with the PSE-N1E280A variant. The leftmost image in Panel C shows the sample of a person in whom the onset of mild cognitive impairment occurred at a typical age in this kindred, the middle image a sample from a person heterozygous for the APOE3^{ch} variant, and the rightmost image a sample from a second person heterozygous for the APOE3^{ch} variant. The color-coded scale bar indicates FDG SUVR values; blue represents lowest values and red represents highest values, with values ranging from 0.5 to 1.8. SUVR values represent the regional cerebral metabolic rate for glucose.

data for the matched samples that had been obtained from 326 persons who did not have the APOE3^{ch} variant and from 27 carriers of the APOE3^{ch} variant.

Survival analyses of the matched samples showed that the median age at the onset of mild cognitive impairment was 52 years (95% CI, 51 to 58) among APOE3^{Ch} carriers, as compared with approximately 47 years (95% CI, 47 to 49) in the matched sample of noncarriers. The median age at the onset of dementia among APOE3^{Ch} carriers was 54 years (95% CI, 49 to 57), which indicated an apparent delay as compared with the noncarriers, among whom the median age at onset was 50 years (95% CI, 48 to 51) (Table S3). Some imprecision in the ages at the onset of mild cognitive impairment and dementia in both groups may have been introduced by gaps in testing that could have been as long as 5 years.

PATHOLOGICAL FINDINGS IN PERSONS WITH APOE3CH

The four participants who were heterozygous for APOE3ch and had available autopsy material had a greater amyloid- β plaque burden and a relatively limited tau burden as compared with PSEN1E280A variant carriers in whom mild cognitive impairment had occurred at the kindred's typical age as determined by qualitative visual inspection, but this observation was not quantified. The regional distribution patterns of amyloid and tau in the participants were typical of those in persons with Alzheimer's disease. In our previous article, we reported that the participant, who was homozygous for the APOE3^{ch} variant, had a distribution of tau deposition in the cortex that largely spared the frontal lobe and was prominent in the occipital lobe.^{7,8} In contrast, the brains of the APOE3^{Ch} heterozygous carriers in the current study did not show this pattern of tau deposition. Findings were within the expected range of tau deposition variation and without visible association between the extent of tau pathological findings and the age at onset of dementia (Table S4 and Fig. S6).

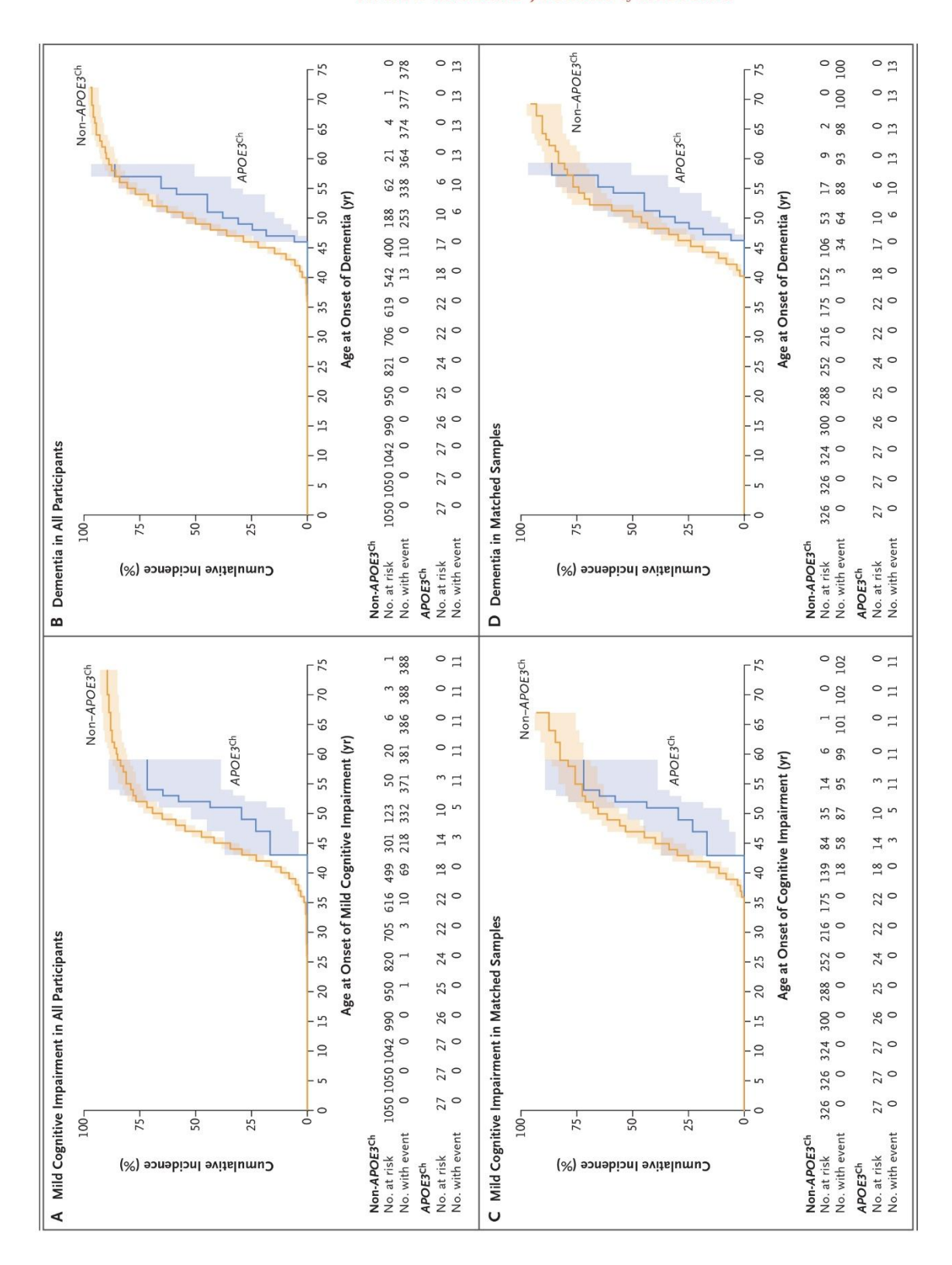
Pathological findings of cerebral amyloid angiopathy were less prominent in the frontal cortex in APOE3^{ch} carriers (Fig. S7A) than in noncarriers. In addition, APOE3^{ch} carriers had a numerically lower percentage of partial involvement of vessel walls (present only in a portion the an- population who was homozygous for APOE3^{Ch7}

APOE3^{ch} variant. Figures 2C and 2D show the nular circumferences of walls) than noncarriers, with pathological findings of cerebral amyloid angiopathy in frontal and occipital cortexes (Figs. S7B and S7C). The participant in the earlier study, who was homozygous for the APOE3ch variant, was less affected in all these measurements of cerebral amyloid angiopathy than the current cohort of participants who were heterozygous for the variant. However, direct comparisons between homozygous and heterozygous participants cannot be made because the homozygous participant in the earlier case report was much older than the participants in the current cohort. Furthermore, vessels that were analyzed in participants who were heterozygous or homozygous for APOE3^{ch} showed greater similarity to controls in terms of length, branching pattern, and spacing between them than those obtained from PSEN1E280A carriers without the APOE3Ch variant (Fig. S8).

DISCUSSION

We report clinical, cognitive testing, neuroimaging, and neuropathological data from heterozygous APOE3^{ch} variant carriers among participants with familial Alzheimer's disease due to PSEN1^{E280A} from an extensively studied group of persons in Colombia. Within the limits of confidence that could be extracted from the data obtained from 27 participants who were heterozygous for the APOE3^{ch} variant, as compared with 1050 participants who did not have this variant, we found that they had an onset of mild cognitive impairment and dementia, analyzed retrospectively, that was approximately 5 years later for mild cognitive impairment and 4 years later for dementia; we also found that they had different patterns on PET imaging. The precision of these estimates was probably not affected by irregular intervals between testing for the reasons noted above, including homogeneity of intervals across the entire group of persons with the PSEN1E280A variant. The apparent delay in the onset of clinical features that were attributable to autosomal dominant Alzheimer's disease in participants who were heterozygous for the APOE3^{ch} variant was less than that observed in a previously reported case of APOE3^{ch} homozygosity.

Our original report about one person in this



2162 N ENGL J MED 390;23 NEJM.ORG JUNE 20, 2024

The New England Journal of Medicine is produced by NEJM Group, a division of the Massachusetts Medical Society.

Downloaded from nejm.org on March 31, 2025. For personal use only.

No other uses without permission. Copyright © 2024 Massachusetts Medical Society. All rights reserved.

Figure 2 (facing page). Cumulative Incidence of Mild Cognitive Impairment and Dementia among Persons with the *PSEN1*^{E280A} Variant.

Shown are the cumulative incidence functions of mild cognitive impairment and dementia among persons with the *PSENI*^{E280A} variant, 27 of whom had the *APOE3*^{Ch} variant and 1050 of whom did not. The analyses of mild cognitive impairment shown in Panel A and of dementia shown in Panel B included all the participants. The analyses of mild cognitive impairment shown in Panel C and of dementia shown in Panel D included matched samples from 27 persons with the *APOE3*^{Ch} variant and 326 persons without this variant. Participants were matched for sex, *APOE* genotype, and years of formal education. Death without a diagnosis of mild cognitive impairment or dementia was a competing risk. Shading indicates the 95% confidence interval.

also discussed four persons with the *PSEN1*^{E280A} variant who were heterozygous for *APOE3*^{Ch}, and we did not describe a delay in the age at onset of cognitive impairment. This finding led us⁷ and others¹⁸ to initially conclude that *APOE3*^{Ch} heterozygosity was not protective. The analyses that we present here encompassed a larger cohort with *APOE3*^{Ch} and *PSEN1*^{E280A} variants, with more comprehensive longitudinal clinical characterization, and indicated that *APOE3*^{Ch} heterozygosity is apparently linked to delay in the expected cognitive impairment.

The PET imaging findings in two participants heterozygous for the $APOE3^{\rm Ch}$ variant, which showed limited tau pathological findings and relatively preserved glucose metabolism, suggest that the delayed clinical onset that is associated with the $APOE3^{\rm Ch}$ variant may involve mechanisms that limit tau pathologic conditions and neurodegeneration, even in the presence of a high burden of $A\beta$ amyloid plaque. These findings are consistent with our observations in the previously reported case of a person who was homozygous for the $APOE3^{\rm Ch}$ variant, but these are speculations and were not systematically studied owing to the small sample.

Limitations of this study arise from the relatively small number of persons who have both the APOE3^{Ch} and PSEN1^{E280A} variants, as well as the homogeneity of the population belonging to a genetic isolate.19 These limitations increase uncertainty around differences in the point estimates for the ages at the onset of mild cognitive impairment and dementia. Further studies involving larger and more ethnically diverse samples of persons with Alzheimer's disease may shed light on any apparent protective effect of the APOE3^{ch} variant. Furthermore, the biologic insight that the APOE3ch variant is protective in this group of persons from the Antioquia, Colombia, cohort may not translate to sporadic Alzheimer's disease or to other groups.

The clinical, cognitive, neuroimaging, and neuropathological data that we present here provide evidence that *APOE3*^{ch} heterozygosity delayed the onset of cognitive impairment in a form of autosomal dominant Alzheimer's disease and may have a protective effect against Alzheimer's disease and neurodegeneration in this population.

Supported by grants from Good Ventures (to Drs. Krasemann and Sepulveda-Falla and to Dr. Arboleda-Velasquez), by the Remondi Family Foundation (to Dr. Arboleda-Velasquez), by grants (R01AG054671, to Dr. Quiroz; RF1AG077627, to Drs. Quiroz and Lopera; K99AG073452, to Dr. Vila-Castelar; and P30AG072980, to Dr. Reiman) from the National Institute on Aging (NIA), by the Massachusetts General Hospital (MGH) Executive Committee on Research (MGH Research Scholar Award, to Dr. Quiroz), by the Alzheimer's Association (to Dr. Quiroz), by a grant (RM1NS132996, to Drs. Quiroz, Lopera, and Arboleda-Velasquez) from the National Institute of Neurological Disorders and Stroke (NINDS), by the National Institutes of Health (to Dr. Lopera), by Roche (to Dr. Lopera), by the Banner Alzheimer's Foundation for the Alzheimer's Prevention Initiative Colombia Registry and the Alzheimer's Prevention Initiative (API) and the API ADAD Colombia Trial (to Drs. Reiman and Lopera), by a joint grant (RF1NS110048, to Dr. Sepulveda-Falla) from NINDS and NIA, by a grant from the Werner Otto Foundation (to Drs. Krasemann and Sepulveda-Falla), by the German Federal Ministry of Education and Research (UndoAD-Project, to Drs. Glatzel and Sepulveda-Falla), by grants (KR 1737/2-1, to Dr. Krasemann; and SFB877, to Dr. Glatzel) from the German Research Foundation, by an Alzheimer's Association Research Fellowship (to Dr. Langella), and by the NOMIS Foundation (to Dr. Reiman).

Disclosure forms provided by the authors are available with the full text of this article at NEJM.

APPENDIX

The authors' full names and academic degrees are as follows: Yakeel T. Quiroz, Ph.D., David Aguillon, M.D., Ph.D., Daniel C. Aguirre-Acevedo, Ph.D., Daniel Vasquez, M.D., Yesica Zuluaga, M.A., Ana Y. Baena, M.A., Lucia Madrigal, Ph.D., Liliana Hincapié, B.S., Justin S. Sanchez, B.A., Stephanie Langella, Ph.D., Rafael Posada-Duque, Ph.D., Jessica L. Littau, M.Sc., Nelson D. Villalba-Moreno, M.Sc., Clara Vila-Castelar, Ph.D., Liliana Ramirez Gomez, M.D., Gloria Garcia, M.S., Elizabeth Kaplan, B.S., Sofia Rassi Vargas, M.D., Alejandro Ossa, B.S., Pablo Valderrama-Carmona, B.S., Paula Perez-Corredor, M.S., Susanne Krasemann, Ph.D., Markus Glatzel, M.D., Kenneth S. Kosik, M.D., Keith Johnson, M.D., Reisa A. Sperling, M.D., Eric M. Reiman, M.D., Diego Sepulveda-Falla, M.D., Francisco Lopera, M.D., and Joseph F. Arboleda-Velasquez, M.D., Ph.D.

2163

The authors' affiliations are as follows: Massachusetts General Hospital (Y.T.Q., J.S.S., S.L., C.V.-C., L.R.G., E.K., K.J., R.A.S.), the Departments of Neurology (Y.T.Q., J.S.S., L.R.G., K.J., R.A.S.), Psychiatry (Y.T.Q., S.L., C.V.-C., E.K.), and Ophthalmology (P.P.-C., J.F.A.-V.), Harvard Medical School, Brigham and Women's Hospital (K.J., R.A.S.), and Schepens Eye Research Institute, Mass Eye and Ear (P.P.-C., J.F.A.-V.) — all in Boston; Grupo de Neurociencias de Antioquia, Facultad de Medicina, Universidad de Antioquia, Medellín, Colombia (Y.T.Q., D.A., D.C.A-A., D.V., Y.Z., A.Y.B., L.M., L.H., R.P.-D., G.G., S.R.V., J.A.O., P.V.-C., F.L.); the Institute of Neuropathology, University Medical Center Hamburg–Eppendorf, Hamburg, Germany (J.L.L., N.D.V.-M., S.K., M.G., D.S-F.); the Neuroscience Research Institute, Department of Molecular Cellular Developmental Biology, University of California, Santa Barbara, Santa Barbara (K.S.K.); and the Banner Alzheimer's Institute, Phoenix, the University of Arizona, Tucson, and Arizona State University, Tempe — all in Arizona (E.M.R.).

DECEDENCE

- Acosta-Baena N, Sepulveda-Falla D, Lopera-Gómez CM, et al. Pre-dementia clinical stages in presenilin 1 E280A familial early-onset Alzheimer's disease: a retrospective cohort study. Lancet Neurol 2011;10:213-20.
- Strittmatter WJ, Saunders AM, Schmechel D, et al. Apolipoprotein E: high-avidity binding to beta-amyloid and increased frequency of type 4 allele in late-onset familial Alzheimer disease.
 Proc Natl Acad Sci U S A 1993;90:1977-81.
- 3. Corder EH, Saunders AM, Strittmatter WJ, et al. Gene dose of apolipoprotein E type 4 allele and the risk of Alzheimer's disease in late onset families. Science 1993:261:921-3.
- Reiman EM, Arboleda-Velasquez JF, Quiroz YT, et al. Exceptionally low likelihood of Alzheimer's dementia in APOE2 homozygotes from a 5,000-person neuropathological study. Nat Commun 2020; 11:667.
- 5. Corder EH, Saunders AM, Risch NJ, et al. Protective effect of apolipoprotein E type 2 allele for late onset Alzheimer disease. Nat Genet 1994;7:180-4.
- **6.** Sherrington R, Rogaev EI, Liang Y, et al. Cloning of a gene bearing missense mutations in early-onset familial Alzheimer's disease. Nature 1995;375:754-60.
- 7. Arboleda-Velasquez JF, Lopera F, O'Hare M, et al. Resistance to autosomal dominant Alzheimer's disease in an APOE3

- Christchurch homozygote: a case report. Nat Med 2019;25:1680-3.
- 8. Sepulveda-Falla D, Sanchez JS, Almeida MC, et al. Distinct tau neuropathology and cellular profiles of an APOE3 Christchurch homozygote protected against autosomal dominant Alzheimer's dementia. Acta Neuropathol 2022;144:589-601.
- Lopera F, Ardilla A, Martínez A, et al. Clinical features of early-onset Alzheimer disease in a large kindred with an E280A presenilin-1 mutation. JAMA 1997;277:793-9.
 Aguirre-Acevedo DC, Lopera F, Henao E, et al. Cognitive decline in a Colombian kindred with autosomal dominant Al-
- kindred with autosomal dominant Alzheimer disease: a retrospective cohort study. JAMA Neurol 2016;73:431-8.
- 11. Aguirre-Acevedo DC, Jaimes-Barragán F, Henao E, et al. Diagnostic accuracy of CERAD total score in a Colombian cohort with mild cognitive impairment and Alzheimer's disease affected by E280A mutation on presenilin-1 gene. Int Psychogeriatr 2016;28:503-10.
- 12. Torres VL, Vila-Castelar C, Bocanegra Y, et al. Normative data stratified by age and education for a Spanish neuropsychological test battery: results from the Colombian Alzheimer's prevention initiative registry. Appl Neuropsychol Adult 2021; 28:230-44.
- 13. Albert MS, DeKosky ST, Dickson D, et al. The diagnosis of mild cognitive impairment due to Alzheimer's disease: recommendations from the National Insti-

- tute on Aging-Alzheimer's Association workgroups on diagnostic guidelines for Alzheimer's disease. Alzheimers Dement 2011;7:270-9.
- 14. McKhann GM, Knopman DS, Chertkow H, et al. The diagnosis of dementia due to Alzheimer's disease: recommendations from the National Institute on Aging-Alzheimer's Association workgroups on diagnostic guidelines for Alzheimer's disease. Alzheimers Dement 2011;7:263-9. 15. Austin PC. Balance diagnostics for comparing the distribution of baseline
- 15. Austin PC. Balance diagnostics for comparing the distribution of baseline covariates between treatment groups in propensity-score matched samples. Stat Med 2009;28:3083-107.
- Austin PC, Fine JP. Practical recommendations for reporting Fine-Gray model analyses for competing risk data. Stat Med 2017;36:4391-400.
- 17. R Core Team. R: a language and environment for statistical computing. Vienna: R Foundation for Statistical Computing, 2023.
- 18. Cochran JN, Acosta-Uribe J, Esposito BT, et al. Genetic associations with age at dementia onset in the PSEN1 E280A Colombian kindred. Alzheimers Dement 2023;19:3835-47.
- 19. Bedoya G, Montoya P, García J, et al. Admixture dynamics in Hispanics: a shift in the nuclear genetic ancestry of a South American population isolate. Proc Natl Acad Sci U S A 2006;103:7234-9.
- Copyright © 2024 Massachusetts Medical Society.

10. Publication IV



TYPE Original Research PUBLISHED 20 March 2024 DOI 10.3389/fnmol.2024.1373568



OPEN ACCESS

EDITED BY Tsuneya Ikezu, Mayo Clinic Florida, United States

REVIEWED BY
Jing Zhao,
Mayo Clinic Florida, United States
Yonghe Li,
Mayo Clinic Florida, United States
Hayk Davtyan,
University of California, Irvine, United States

*CORRESPONDENCE

Joseph F. Arboleda-Velasquez

☑ Joseph_Arboleda@meei.harvard.edu
Randall C. Mazzarino

☑ Mazzarino.randall@gmail.com

RECEIVED 20 January 2024 ACCEPTED 22 February 2024 PUBLISHED 20 March 2024

CITATION

Perez-Corredor P, Vanderleest TE, Vacano GN, Sanchez JS, Villalba-Moreno ND, Marino C, Krasemann S, Mendivil-Perez MA, Aguillón D, Jiménez-Del-Río M, Baena A, Sepulveda-Falla D, Lopera F, Quiroz YT, Arboleda-Velasquez JF and Mazzarino RC (2024) APOE3 Christchurch modulates β-catenin/Wnt signaling in iPS cell-derived cerebral organoids from Alzheimer's cases.

Front. Mol. Neurosci. 17:1373568.
doi: 10.3389/fnmol.2024.1373568

COPYRIGHT

© 2024 Perez-Corredor, Vanderleest, Vacano. Sanchez, Villalba-Moreno, Marino, Krasemann, Mendivil-Perez, Aguillón, Jiménez-Del-Río, Baena, Sepulveda-Falla, Lopera, Quiroz, Arboleda-Velasquez and Mazzarino. This is an open-access article distributed under the terms of the \subset commons Attribution License (CC BY). The use, distribution or reproduction in other forums is permitted, provided the original author(s) and the copyright owner(s) are credited and that the original publication in this journal is cited, in accordance with accepted academic practice. No use, distribution or reproduction is permitted which does not comply with these terms.

APOE3 Christchurch modulates β-catenin/Wnt signaling in iPS cell-derived cerebral organoids from Alzheimer's cases

Paula Perez-Corredor¹, Timothy E. Vanderleest¹, Guido N. Vacano², Justin S. Sanchez³, Nelson D. Villalba-Moreno⁴, Claudia Marino¹, Susanne Krasemann⁵, Miguel A. Mendivil-Perez⁶, David Aguillón⁶, Marlene Jiménez-Del-Río⁶, Ana Baena⁶, Diego Sepulveda-Falla⁴, Francisco Lopera⁶, Yakeel T. Quiroz^{3,6,7}, Joseph F. Arboleda-Velasquez¹⁴ and Randall C. Mazzarino¹⁴

¹Schepens Eye Research Institute of Mass Eye and Ear and Department of Ophthalmology at Harvard Medical School, Boston, MA, United States, ²Vacano Informatics LLC, Arvada, CO, United States, ³Massachusetts General Hospital and Department of Neurology at Harvard Medical School, Boston, MA, United States, ⁴Molecular Neuropathology of Alzheimer's Disease, Institute of Neuropathology, University Medical Center Hamburg-Eppendorf, Hamburg, Germany, ⁵Institute of Neuropathology, University Medical Center Hamburg-Eppendorf, Hamburg, Germany, ⁶The Neuroscience Group of Antioquia, University of Antioquia, Medellin, Colombia, ⁷Massachusetts General Hospital and Department of Psychiatry at Harvard Medical School, Boston, MA, United States

A patient with the *PSEN1* E280A mutation and homozygous for *APOE3* Christchurch (*APOE3Ch*) displayed extreme resistance to Alzheimer's disease (AD) cognitive decline and tauopathy, despite having a high amyloid burden. To further investigate the differences in biological processes attributed to *APOE3Ch*, we generated induced pluripotent stem (iPS) cell-derived cerebral organoids from this resistant case and a non-protected control, using CRISPR/ Cas9 gene editing to modulate *APOE3Ch* expression. In the *APOE3Ch* cerebral organoids, we observed a protective pattern from early tau phosphorylation. ScRNA sequencing revealed regulation of Cadherin and Wnt signaling pathways by *APOE3Ch*, with immunostaining indicating elevated β -catenin protein levels. Further *in vitro* reporter assays unexpectedly demonstrated that ApoE3Ch functions as a Wnt3a signaling enhancer. This work uncovered a neomorphic molecular mechanism of protection of ApoE3 Christchurch, which may serve as the foundation for the future development of protected case-inspired therapeutics targeting AD and tauopathies.

KEYWORDS

Wnt signaling, ApoE, iPS cells, CRISPR, Alzheimer's disease, ApoE Christchurch, Presenilin

Introduction

Alzheimer's disease (AD) is the most common cause of dementia among older adults. AD affects an estimated 55 million people worldwide with numbers expected to exceed 152 million people by the year 2050 (Patterson, 2018). AD is characterized by the formation of amyloid plaques and tau tangles in the brain as well as calcium and mitochondrial dysregulation that

manifests in neuronal death and memory deficits (Nunomura et al., 2001; Mosconi, 2013; Knopman et al., 2021). Autosomal dominant Alzheimer's disease (ADAD) accounts for approximately 1% of diagnosed patients (Sims et al., 2020), with approximately 70% of ADAD patients having a Presenilin-1 (*PSEN1*) mutation (Sun et al., 2017).

Recently, a member of the Colombian *PSEN1* E280A (Paisa) kindred was identified as being resistant to ADAD. Carriers of the *PSEN1* E280A mutation develop mild cognitive impairment at 43–45 and dementia at 49–50 years of age (95% confidence intervals); the identified female patient did not develop mild cognitive impairment until her seventies. She had very limited levels of tau pathology, neuroinflammation, and neurodegeneration but extremely high levels of amyloid plaque burden (Arboleda-Velasquez et al., 2019; Sepulveda-Falla et al., 2022; Lopera et al., 2023).

She was also found to be homozygous for the Apolipoprotein E3 Christchurch (APOE3Ch) variant (R136S), which was identified as a candidate variant responsible for her resistance to ADAD (Arboleda-Velasquez et al., 2019). Genetic imputation of causality could not be confirmed because only a single APOE3Ch homozygote case with resistance was identified. We hypothesized that the iPS system devised here would be an informative model to identify biological pathways influenced by the Christchurch variant in APOE that will shed light on her remarkable AD resistance. In this study, we used cells from the resistant and a non-resistant patient to generate iPS cells, used genomic editing to introduce or remove the APOE3Ch or PSEN1 E280A mutations, and identified the Cadherin/Wnt/ β -catenin signaling pathways as plausibly regulated by the APOE3Ch variant.

Methods

Patient selection and sample collection

We have selected two patients for this study, and they will be known in this study as Patient α and Patient ω to ensure patient privacy. Patient α was previously described as being a protected patient from familial Alzheimer's disease (Arboleda-Velasquez et al., 2019). Patient α was part of the Paisa PSENI E280A kindred in her seventies at a time of mild cognitive impairment. She was found to have the APOE3 R136S Christchurch variant that provided her resistance to Alzheimer's development. Patient ω was also selected as a Paisa kindred female with the development of ADAD at the expected age of onset and which PET imaging data were available with expected brain pathology.

Blood samples from each individual were obtained by venipuncture. Peripheral blood mononuclear cells were separated by Ficoll–Hypaque 1077 and submitted for reprogramming and genetic editing.

In vivo neuroimaging

Structural magnetic resonance imaging (MRI), Pittsburgh compound B (PiB), and Flortaucipir (FTP) positron emission tomography (PET) were performed at Massachusetts General Hospital, as described elsewhere (Quiroz et al., 2018). In brief, MRI images were processed with FreeSurfer (FS, v 6.0) to identify surface

boundaries and standard regions of interest (Desikan et al., 2009). PET data were acquired and processed according to previously published protocols (Johnson et al., 2016), whereas PiB data were expressed as distribution volume ratios (DVR, Logan, 0–60 min) and FTP as standardized uptake value ratios (SUVR, 80–100 min), both using cerebellar gray matter as the reference region. PET images were affine co-registered to each subject's T1 images and visualized using FS surface projections (sampled at the midpoint of gray matter, surface-smoothed 8 mm). No partial volume correction was applied to PET images for the purposes of this study.

Reprogramming and genetic editing

Cell services were performed using the Harvard Stem Cell Core: whole blood was reprogrammed via Cytotune 2.0 (Thermo Fisher), and colonies were allowed to grow and were then assessed for the iPS markers SSEA, Oct4, Tra-1-60, and Nanog using immunocytochemistry and qPCR for trilineage. Successful screened colonies were then processed further for genetic editing. Guide RNA (gRNA) and single-stranded oligodeoxynucleotide (ssODN) sequences were determined (Supplementary Table 1) using the CRISPOR suite through the highest specificity score and lowest off-target homology, and then, colonies were karyotyped. Normal karyotype colonies were sequenced for their inclusion of the desired genetic mutation, and isogenic controls were also selected (Supplementary Figure 2).

Cell culture

Reprogrammed and edited cells were cultured on human embryonic stem cell (hESC)-qualified Matrigel (Corning #354277) using mTeSR Plus (StemCell Technologies #100-0276) supplemented with the antimicrobial Normocin (Invivogen #ant-nr-1) and clump passaged weekly using ReLeSR (StemCell Technologies #05872) according to the manufacturer's recommended protocols. Cell clumps were sparsely plated to allow for easy physical removal of spontaneously differentiated cells. Cells were grown at 37°C and 5% CO₂.

Differentiation

Cells were cultured as described above. Regions of spontaneously differentiated cells were identified and physically removed. Organoids were made using Stemdiff Cerebral Organoid Kit (StemCell Technologies #08570) and Normocin using the manufacturer's recommended protocol; however, iPS cell spheroids were made using EB formation media (Stem Cell Technologies #05893) with Normocin. In brief, cells were detached to single cell using Accutase (StemCell Technologies #07920) and counted (Countess II) using Trypan Blue. In total, 9,000 cells/well were plated into low retention 96-well U-bottom plates (S-Bio #MS-9096UZ) placed in EB formation media with γ-27632 (ATCC #ACS-3030) in addition to regular fresh media. After 5 days, spheroids were transferred to a 24-well flat bottom low retention plate (Corning #3473) to induce differentiation. Organoids were then embedded into individual hESC-qualified Matrigel droplets and plated into 6-well flat bottom low retention plates (Corning

#3471) for expansion. Organoids were then placed onto a shaker plate inside the incubator with regular media exchanges (2–3 days) until downstream analysis 29 days after initial EB spheroid formation.

Immunostaining

Organoids for immunofluorescence analyses were fixed in 4% PFA for 2h, then washed in dPBS thrice, and then infiltrated with 30% sucrose until they dropped then frozen in OCT and sectioned at 15 µm. Sections were washed with 1xdPBS and blocked for 1 h (PBS, 3% BSA, 0.2% Triton X-100, and 0.02% sodium azide). Middle sections were preferentially selected for IF analysis. Then, they were incubated in primary antibody diluted in blocking buffer using the following primary antibodies: anti-Phospho-Tau (Ser396) (1:500, 44-752G, Invitrogen), anti-β-catenin (E-5) (1:50, sc-7963, Santa Cruz), and anti-Reelin (CR-50) (1:100, D223-3, MBL Life Science) overnight at 4°C. After washing the sections with 1xdPBS, they were incubated in the following secondary antibodies: Donkey anti-rabbit IgG Alexa Fluor 647 (1:500, A-31573, Thermo Fisher) and Donkey anti-mouse IgG Alexa Fluor 488 (1:500, A-21202, Thermo Fisher). DAPI solution was used for nuclei staining. Images were taken at $63\mathrm{X}$ magnification using a ZEISS Axioscope digital microscope. A total of 3-4 organoids were imaged and used for quantification. The Shapiro-Wilk normality test was performed followed by a one-way ANOVA and Tukey's multiple comparison for post-hoc analysis.

Immunofluorescence staining was performed on the formalinfixed paraffin-embedded (FFPE) brain tissue from the frontal cortex, hippocampus, and occipital cortex from a previously described PSEN1 E280A carrier homozygous for the APOE3Ch mutation (Sepulveda-Falla et al., 2022). In total, 4-µm thick sections were mounted on Superfrost plus slides and further processed for immunofluorescence staining for β-catenin (1:200; 05-665, Sigma Aldrich) and RNA binding protein, fox-1 homolog 3 (NeuN, 1:200; 26975-1-AP, Protein Tech). After deparaffinization, heat-induced epitope retrieval was performed using R-Universal buffer (AP0530-500; Aptum Biologics, Southampton, United Kingdom) in a pressure cooker for 20 min, and sections were then blocked for 1h with blocking medium (MAXblockTM, 15252; Active Motif GmbH) followed by incubation with primary antibodies at 4°C overnight. For the detection of specific binding, secondary antibodies were incubated at room temperature for 1 h. After washing, mounting was performed with 4',6-Diamidino-2-phenylindole (DAPI) Fluoromount-G for nuclear counterstaining. High-resolution images were obtained with a Leica TCS SP8 confocal laser scanning microscope (Leica Microsystems, Mannheim, Germany) using a 20X immersion oil lens objective.

scRNA-seq

Six organoids from each individual cell line (eight lines in total) were pooled and processed using MACS papain neural tissue dissociation kit (Miltenyi Biotec #130-092-628) according to the manufacturer's protocol and resuspended in 0.22 μm filter-sterilized dPBS 0.04%BSA solution. Cells were serially filtered through a 70- μm (Miltenyi Biotec #130-110-916) and then a 40- μm (Bel-Art #H136800040) strainer to remove clumped cells. Samples were kept on wet ice and assessed at the BioMicroCenter core facility

(Massachusetts Institute of Technology) for viability, cell density, and quality. Samples were processed on 10X Genomics Chromium Controller at the BMC Core facility. Sequences were then processed through the 10X Genomics Cell Ranger Suite.

Transcriptomic analysis

The h5 files were read with the Seurat Read10X_h5() function [Seurat (Hao et al., 2021), an R package for scRNA-seq clustering and integration]. The DoubletFinder (McGinnis et al., 2019) doubletFinder_v3() function was employed to identify and remove likely multiplets in each sample, and the predicted multiplet rate was 0.8% per "Targeted Cell Recovery" of 1,000 cells (Chromium). QC cutoffs were employed to remove cells with nFeature_RNA>8,000 or<200, nCount_RNA>50,000, or percent.mito >20%. Sample subsets of 6,400 cells were processed via DietSeurat() (default values) and saved as RDS files.

Sample integration was accomplished by merging Seurat objects with merge(), v.1 SCTransform() (Hafemeister and Satija, 2019) with FindClusters (resolution=0.3) and Harmony integration [RunHarmony()] (Korsunsky et al., 2019). Seurat objects were saved as RDS files.

Aggregate gene expression [AverageExpression()] in clusters was employed to compare gene expression between samples (log2 adjusted sample ratios).

Comparison groups were established (Table 1) reflecting log2(fc>1 and<-1) and pathway analysis run using PANTHER Pathways Overrepresentation Test version (PANTHER version 17.0 released 2022-02-22) with *Homo sapiens* (all genes in database) reference genome using Binomial test type and Bonferroni correction.

Gene Set Enrichment Analysis (GSEA) (Subramanian et al., 2005) was performed using fgsea to facilitate cell type identification. The MSigDB (v2023.1.Hs) C8 cell type signature gene set database¹ was queried (after filtering to retain only brain-relevant entries; La Manno et al., 2016; Fan et al., 2018; Zhong et al., 2018; Cao J. et al., 2020). NES (enrichment score normalized to mean enrichment of random samples of the same size) scores ≥7.5 were considered significant and informed cell type assignment. Clusters were further classified by general cell type into "superclusters." These are "neuronal," "neuroblast," "radial glial," "progenitor," "oligodendrocyte," and "neuro endothelial." We also employed SCSA (Cao Y. et al., 2020; https:// github.com/bioinfo-ibms-pumc/SCSA) using output from the Seurat FindAllMarkers function and the most recent SCSA database (whole_ v2.db) to validate cell type identifications based on GSEA, and we refined our list to designate clusters 5 and 7 as "radial glia/early astrocyte" based on this analysis. Post-hoc cell identities were determined for transcript expression of TUBB3 for neuronal and HES1, FABP7, and VIM for radial glia.

Monocle (Qiu et al., 2017) was employed for single-cell trajectory analysis and identification of genes that change as a function of pseudotime. The Seurat object from the SCTransform/Harmony

¹ https://www.gsea-msigdb.org/gsea/msigdb/index.jsp

TABLE 1 Cell lines used for the study.

Reprogrammed cell line	Base genotype	CRISPR target	Mutation success	Final genotype
iPS patient α	E3Ch PS1mut	PS1mut → PS1WT	Successful	E3Ch PS1WT
		PS1mut → PS1WT	Unsuccessful	E3Ch PS1mut
iPS patient α	E3Ch PS1mut	E3Ch → E3WT	Successful	E3WT PS1mut
		E3Ch → E3WT	Unsuccessful	E3Ch PS1mut
iPS patient ω	E3WT PS1mut	PS1mut → PS1WT	Successful	E3WT PS1WT
		PS1mut → PS1WT	Unsuccessful	E3WT PS1mut
iPS patient ω	E3WT PS1mut	E3WT → E3Ch	Successful	E3Ch PS1mut
		E3WT → E3Ch	Unsuccessful	E3WT PS1mut

Patient cells were reprogrammed to generate iPS cells and then subjected to CRISPR gene editing to produce the cell lines used for the study. For this table, E3Ch, APOE3Ch; E3WT, APOE3WT; PSImut, PSEN1 E280A; and PSIWT. PSEN1WT.

analysis (see above) was converted to a Monocle3 cell dataset and processed as described.²

Immunofluorescence image quantification

Rosette β -catenin quantification was implemented in MATLAB 2021a with the use of the Image Processing Toolbox. We quantified the average channel intensity in two types of rosette regions of interest (ROIs): the Body and the Ribbon. The masks (or binary image representations) of the Body and the Ribbon were produced via a combination of hand-drawing (to get the outer boundary and inner luminal boundary lines) and Otsu thresholding to remove background pixels from the hand-drawn regions. The hand-drawn mask for the rosette body was defined as the region between the inner and outer boundaries eroded by $1.8\,\mu m$ (to ensure that the Ribbon and Body's outer edges were not included in the Body ROI). The rosette ribbon ROI was defined as the inner luminal boundary line dilated by $1.8\,\mu m$ to approximately capture the full ribbon thickness.

Rosette area was measured by summing the number of pixels within the rosette Body and Ribbon ROIs. The rosette aspect ratio was defined as the major axis length divided by the minor axis length. We used MATLAB function *regionprops* to measure the major and minor axis lengths.

In both pTau S396 and Reelin fluorescence imaging, background intensity was subtracted via a top-hat filter to remove non-uniform background illumination. Top-hat filtering was accomplished with a large structuring element (54 μm radius disk) so as not to remove the signal from large features of interest. After background removal, we used Otsu's threshold method to find the foreground and computed the mean intensity over the foreground.

Wnt signaling reporter assay

TCF/LEF Reporter HEK 293 cell line (BPS Bioscience #60501) was designed to stably contain firefly luciferase under the control of a TCF/LEF reporter element and commercially validated against Wnt3a

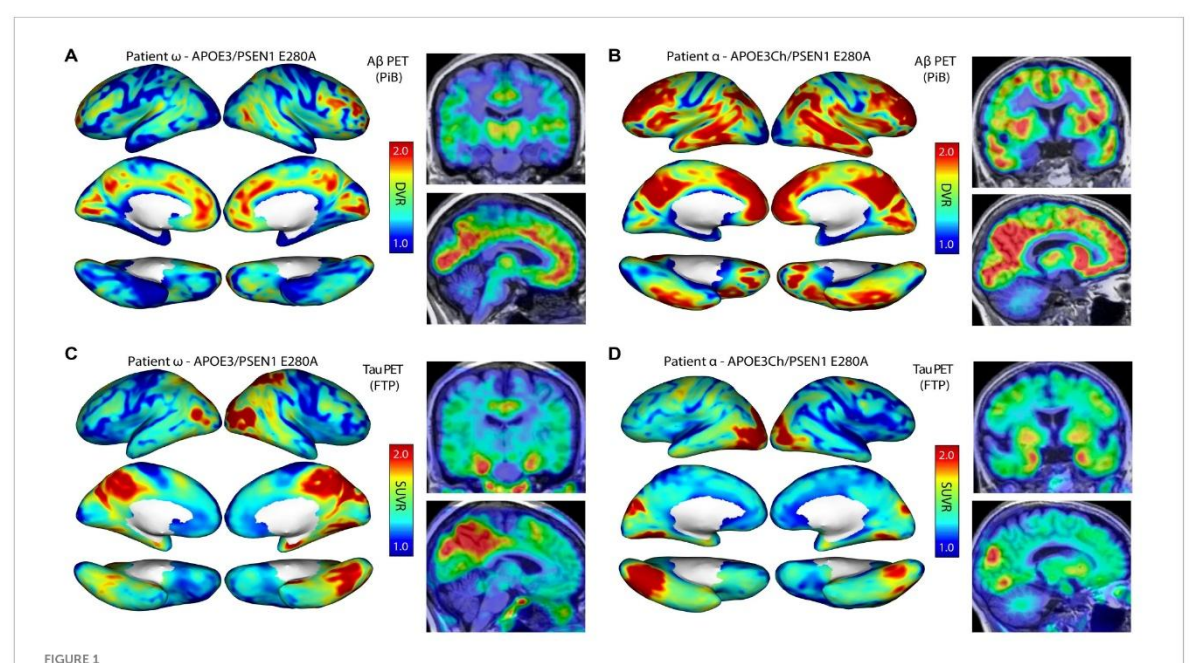
(RND systems #5036-WN-010). Wnt ligands huWnt16b (RND Systems #7790-WN-025) and hu/msWnt5a (RND Systems #645-WN-010) were also tested. Recombinant ApoE proteins were sourced as a fee-for-service from Innovagen AB produced in E. coli. We performed this assay according to the BPS Bioscience recommended protocol. In short, 35,000 cells/well were plated in a 96-well white wall clear bottom TC plate. Cells were treated with a final concentration of 10 µM LiCl in media overnight. All wells were treated with LiCl, including vehicle control. The next day, test compounds were sterile prepared in assay media and incubated at room temperature for 15 min and then added to wells in triplicate to final concentrations indicated. Treated cells were incubated at 37°C and 5%CO2 for 5 h. Media were removed, and wells were washed with 1x dPBS. Firefly luciferase was assessed using a commercially available kit (Promega #E1910) and measured on a BioTek Synergy H1 microplate reader. Data were analyzed via GraphPad PRISM and statistical significance using a one-way ANOVA and post-hoc Tukey's test to consider a p-value of <0.05 significance.

Results

Patient cases selected for analysis

We identified two informative patients for this study (named α and ω to protect privacy): Patient α was previously described as the homozygote APOE3Ch protected case (Arboleda-Velasquez et al., 2019), and Patient ω who was not previously described was selected as a control for this study. Both individuals are from the Paisa PSEN1 E280A kindred and women, though not closely related. Patient α developed mild cognitive impairment (MCI) in her seventies, suggesting protection against ADAD, while Patient ω developed MCI and dementia in her forties, as expected for the Paisa kindred. PET imaging of each patient was performed (Figures 1A-D) to evaluate amyloid and tau burden. Pittsburgh compound B PET imaging for amyloid plaques revealed elevated burden in Patient α versus Patient ω, while [18F]Flortaucipir PET imaging displayed a significant burden in the medial temporal and parietal regions of Patient ω, which is markedly reduced in Patient α . Patient ω was selected as an appropriate control for this experiment based on the following criteria: (1) being a PSEN1 E280A mutation carrier, (2) being symptomatic, (3) having PET imaging data available for this patient, (4) being female, (5)

² https://cole-trapnell-lab.github.io/monocle3/docs/trajectories



Autosomal dominant Alzheimer's disease (ADAD) patient *in vivo* neuroimaging. Patient ω is a non-protected, Paisa kindred control patient and was scanned for amyloid β (**A**) and tau burden (**C**). Patient α is an AD-protected Paisa kindred patient and was previously described and scanned for amyloid β (**B**) and tau burden (**D**) (Arboleda-Velasquez et al., 2019). Scans indicated elevated amyloid β burden in patient α (**B**) compared to patient ω (**A**). Tau burden was elevated in patient ω (**C**) over patient α (**D**), with a marked increase in medial temporal and parietal regions. PiB, Pittsburgh Compound B; FTP, Flortaucipir; DVR, Distribution volume ratio; and SUVR, Standardized uptake value ratio.

having a *APOE3/3* wild-type genotype, and (6) having provided informed consent for this study. Taken together, these individuals were selected as an informative pairing for protected and non-protected cases.

Patient-derived iPS cell generation and gene editing

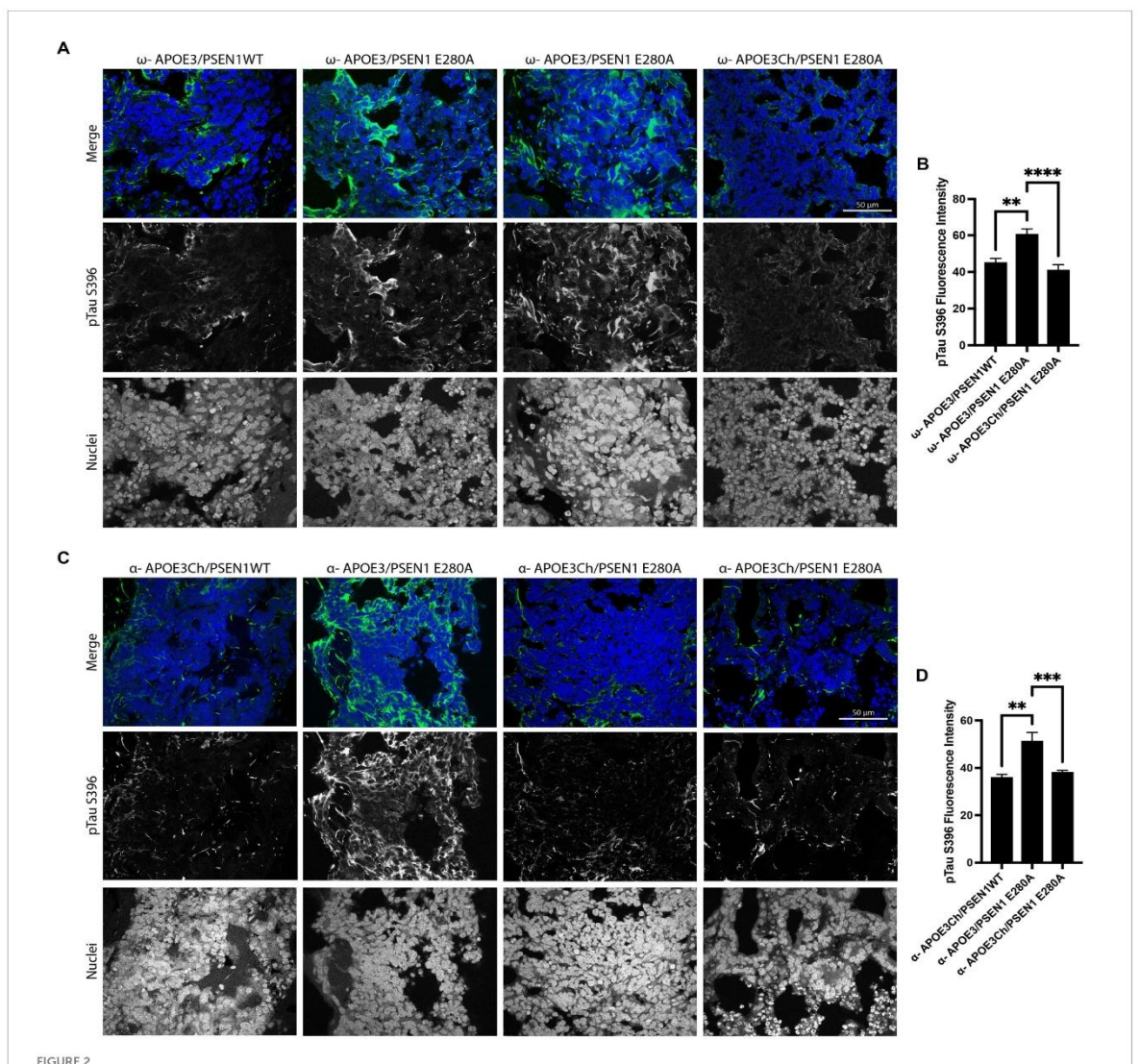
We generated patient-derived iPS cell lines to examine the effects of the *APOE3Ch* R136S and *PSEN1* E280A mutation (Supplementary Figure 1A). Patient blood samples were successfully reprogrammed and subcloned, as tested by immunofluorescence (IF) staining of pluripotency markers (Supplementary Figure 1B). Reprogrammed subclones were then edited using CRISPR/Cas9 to knock in gene variants to both add and remove the putative *APOE3Ch* protective factor as well as remove the *PSEN1* E280A AD causality factor, generating eight cell lines for the study (Table 1; Supplementary Figure 1A).

Sanger sequencing was performed and successful genetically edited cells were selected while isogenic controls were also selected from reprogrammed cells that underwent the CRISPR editing process but were unsuccessful in genomic editing (Supplementary Figure 2). Altogether, eight cell lines were generated for this study (four from each case). Karyotyping was performed, and all cell lines generated showed 46 chromosomes without overt abnormalities (Supplementary Figure 1C). Cell lines

showed success for trilineage; embryoid bodies were formed and differentiated toward ectoderm, mesoderm, and endoderm for 2 weeks and assessed by a three gene qPCR panel: ectoderm—EN1, MAP2, and NR2F2, mesoderm—SNAIL2, RGS4, and HAND2, and endoderm—SST, Klf5, and AFP (Data available on request).

APOE3 iPS cell cerebral organoids produce differential phospho-tau patterns

We first asked whether our genetically engineered cerebral organoids display an early AD phenotype to validate our model. Therefore, we conducted immunofluorescence analyses to confirm the genetic link between specific patterns of tau phosphorylation and APOE3Ch using anti-pTau S396 antibody. pTau S396 is an early marker of pathological tau phosphorylation (Mondragón-Rodríguez et al., 2014). pTau S396 staining was similar in Patient ω's isogenic control organoids with the PSEN1 E280A mutation and was reduced in PSEN1WT organoids (Figures 2A,B). When the APOE3Ch variant was introduced to Patient ω, pTau S396 staining was significantly reduced compared to isogenic patient controls and corrected tau phosphorylation to PSEN1WT levels (Figures 2A,B). This staining pattern was consistent in Patient a, whereby the removal of the APOE3Ch variant led to a significant increase in pTau S396 staining compared to all other Patient α cell lines (Figures 2C,D). We concluded that the APOE3Ch variant was able to produce a protective pattern of early tau phosphorylation defined as low pTau S396 in cerebral



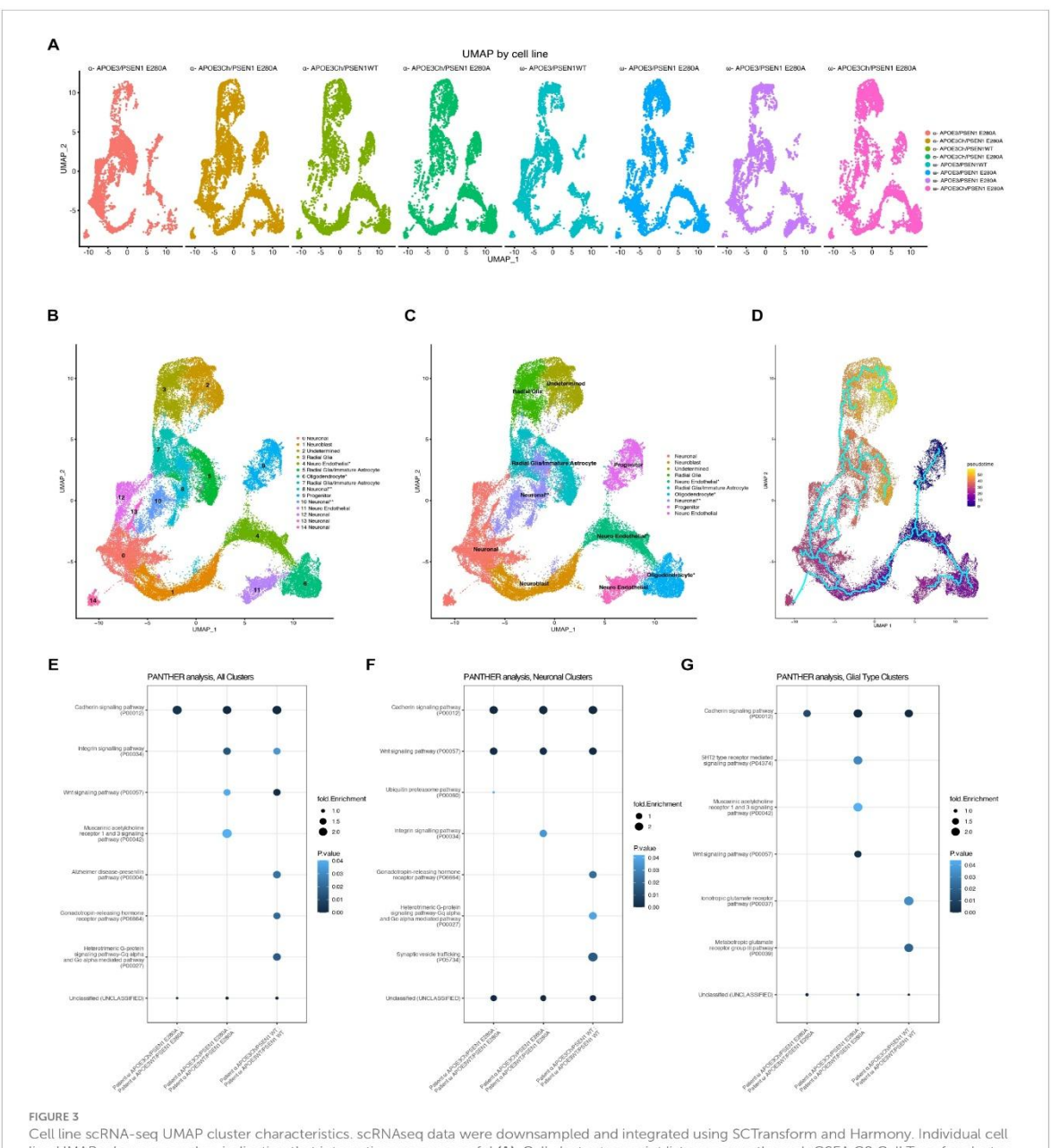
APOE3Ch decreases pTau S396. Cerebral organoids were formed and stained for nuclei and pTau S396 and imaged at 63X. Representative images from patient ω . (A) and patient α (C) depicted, scale bars = 50 μ m. pTau S396 signal intensity was measured, and isogenic controls for each individual patient were averaged together (B,D). Quantification was performed on three to four organoids per line with n=31–159 measurements for patient ω and n=25–47 measurements for patient ω .

organoids derived from an AD-protected and non-protected patient within the PSEN1 E280A background. Overall, the effects of APOE genotypes on tau phosphorylation were independent from PSEN1 genotypes, suggesting a direct effect of APOE genotypes on the status of tau phosphorylation.

Single-cell RNA sequencing of cerebral organoids reveals Wnt signaling differences

We conducted scRNA sequencing to identify potential dominant effects associated with APOE genotypes. The quality of

datasets was confirmed within Seurat using standard QC measures (Supplementary Figure 3) and threshold set. To be able to compare the results within and between all cell lines, we downsampled all datasets to 6,400 cells after thresholding and QC and then integrated all scRNA-seq output using Harmony and SCTransform. UMAPs for both patients exhibit an overlap of cluster and cell types, indicating that integration was successful (Figure 3A). By using GSEA C8 Cell Type Signature Gene Sets, SCSA, and *post-hoc* transcript analysis, we were able to identify cell types (Figures 3B,C). Cell type identities in the SCSA analysis were mostly identical to the results obtained by GSEA C8 analysis; however, SCSA analysis revealed that clusters 5 and 7 are likely astrocyte or early astrocyte. We noticed a difference



Cell line scRNA-seq UMAP cluster characteristics. scRNAseq data were downsampled and integrated using SCTransform and Harmony. Individual cell line UMAPs show an overlap, indicating that integration was successful (A). Cell cluster transcript lists were run through GSEA C8 Cell Type for cluster identity (B). * represents cell cluster identities defined by the second highest hit in GSEA C8 Cell Type analysis and the post hoc transcript expression profile. Similar cluster identities were combined to form reference groups for downstream analysis (C). Asterisk denotes cell cluster identity that was second hit in fGSEA due to its better representation of transcriptomic profile and differentiation protocol used (B,C). Pseudotime was performed using the Monocle analysis suite to represent the differentiation timing to cell identity, initiating the analysis at Cluster 9 (Progenitor) as time zero (D). PANTHER pathways analysis was performed on total cells, all clusters (E), neuronal clusters 0, 1, 8, 10, 12, 13, and 14 (F), and glia-type clusters 3, 5, and 7 (G).

in cell clustering that any organoid containing *APOE3Ch* was more populated in the cluster 2 and 3 regions of the integrated uMAPs. We have identified that clusters 2 and 3 were also the last clusters in

our developmental pattern and trajectory pseudotime analysis (Figure 3D), indicating that APOE3Ch likely influences cell developmental timings or cell type identity.

Next, we assessed the transcriptome of genes of interest to Alzheimer's disease and resistance (Arboleda-Velasquez et al., 2019; Lopera et al., 2023), APOE, APP, MAPT, PSEN1, and RELN and found no notable differences across cell lines (Supplementary Figure 4). It should be noted that APOE displays minimal transcript expression in neuronal clusters and is enriched in glial Clusters 5 and 8 (Supplementary Figure 4), as expected.

Owing to the complexity and diverse genetic backgrounds of our cell lines, we first sought to identify differences across the datasets and to streamline workflow by converting datasets to pseudo-bulk to identify broad changes. Here, we identified that the Christchurch variant has a profound effect on Wnt signaling and Cadherin signaling pathways (Figure 3E), both of which utilize β -catenin. Next, we sought to assess pathway differences seen in the neuron clusters. When assessing neuronal-specific clusters, PANTHER pathways analysis yielded that the APOE3Ch variant influences Wnt signaling and Cadherin signaling, as well as others (Figure 3F). Due to the expression of APOE from glial cells, we queried these cell clusters revealing also Wnt signaling and Cadherin signaling, among others (Figure 3G). We then assessed the successful gene hits through the datasets and found that, for each patient, APOE3Ch drastically decreases transcript levels of WNT2B, WNT4, and WNT7B in our cerebral organoids but does not influence β-catenin transcript (Supplementary Figure 5). We also traced the WNT2B, WNT4, and WNT7B to maximum intensities in glial cell-type clusters (Supplementary Figure 5).

β -Catenin is elevated in *APOE3Ch* cerebral organoids

Cerebral organoids have a high level of cellular heterogeneity, and we, therefore, focused on the characterization of rosettes, which are structures commonly observed in cerebral organoids resembling neural tubes that include pseudostratified epithelium with apico-basal polarity (Di Lullo and Kriegstein, 2017). Rosettes are an ideal morphogenetic model of brain development, with inner layers containing progenitors and more mature neurons toward the outer layers. Rosettes were smaller within APOE3/PSEN1 E280A organoids compared to their PSEN1WT or APOE3Ch counterparts, suggesting a differential maturation phenotype. Consistent with a more mature phenotype, APOE3Ch organoids stained prominently with Reelin, a marker of more mature neurons (Figures 4A-D; Lancaster et al., 2013; Di Lullo and Kriegstein, 2017). Canonical Wnt activation leads to the accumulation of β-catenin and inhibition of GSK3β, a critical modulator of tau phosphorylation (Jackson et al., 2002; De Ferrari et al., 2014). Thus, we hypothesized that Wnt/β-catenin/Cadherin pathway regulation could link APOE genotypes to tau phosphorylation via modulation of β -catenin. Distribution of β -catenin was prominent in apical regions close to the rosette's lumen (ribbon-like) and more homogenously localized within the pseudostratified epithelium of organoids with APOE3Ch variant (Figure 4E). We segmented the body of the rosette and ribbon for the quantification of β -catenin expression (Figures 4F-H). Rosette body and ribbon features show a significant increase of β-catenin expression in APOE3Ch variant carrier organoids vs. control. This phenotype was not impacted by PSEN1 genotypes, suggesting a direct effect of the APOE genotype on tau phosphorylation phenotypes. We observed a marked decrease in the

rosette area within *APOE3/PSEN1* E280A organoids compared to *APOE3Ch* rosettes (Figure 4I). This observation did not carry into the rosette aspect ratio (Figure 4I).

Increased nuclear $\beta\text{-catenin}$ in neurons of protected brain regions of patient α

Previously, we have reported a comprehensive postmortem analysis of brain tissue collected from a homozygous APOE3Ch PSEN1 E280A carrier. Three brain areas were selected as representative for the degree of protection conferred by this APOE mutation: frontal cortex (FC), hippocampus (Hipp), and occipital cortex (OC) (Sepulveda-Falla et al., 2022). As a validation of our current results in brain organoids derived from the same patient, we performed colocalization analysis between β-catenin, DAPI as a nuclear marker, and NeuN as a neuronal marker. We found that the FC showed a significantly higher thresholded volume of colocalization (TVC) for β-catenin in nuclei when compared to Hip and OC (Figures 5A,B), indicating a higher level of activation of the β -catenin pathway in this brain region. On the other hand, TVC for β-catenin in neuronal cells only showed statistically significant differences between Hip and OC (Figures 5A,C), possibly reflecting neuronal loss and general neurodegeneration described in this brain area from this patient. These results indicate a potential link between Wnt signaling, β-catenin, and AD protection.

ApoE3Ch acts as a Wnt3a signaling enhancer

Together, our findings revealed an intriguing correlation: a reduced expression of multiple Wnt ligands alongside a significant increase in β -catenin protein expression. This correlation prompted us to investigate the presence of a hypothetical activator of the pathway in our system. If a putative activator was present, the Wnt ligand downregulation may arise as a compensatory mechanism.

Therefore, we examined whether the ApoE3Ch protein could directly influence Wnt signaling. To explore this influence, we utilized a Wnt reporter cell line, validated for Wnt3a. Our initial investigations indicated that ApoE3WT and ApoE3Ch alone did not induce Wnt signaling. However, when combined with Wnt3a ligands, ApoE3Ch acted as a Wnt signaling activator, while ApoE3WT functioned as a Wnt signaling inhibitor (Figure 6A). This finding was further confirmed through a repeated experiment, which also revealed a dose-dependent relationship (Figure 6B). Notably, while the inhibitory effect of ApoE on Wnt signaling, attributed to competitive binding to LRP receptors, has been reported before with ApoE4 being the stronger inhibitor compared to ApoE3 and ApoE2 (Caruso et al., 2006), the discovery of ApoE3Ch as a Wnt3a activator represents a new and unexpected gain-of-function property of this rare variant (neomorphism).

We tested other Wnt ligands including Wnt5a and Wnt16b, but they could not be accurately measured in our assay (data not shown). Taken together, these findings suggest that ApoE3Ch might operate through multiple mechanisms upstream of tau phosphorylation, including the regulation of Wnt signaling.

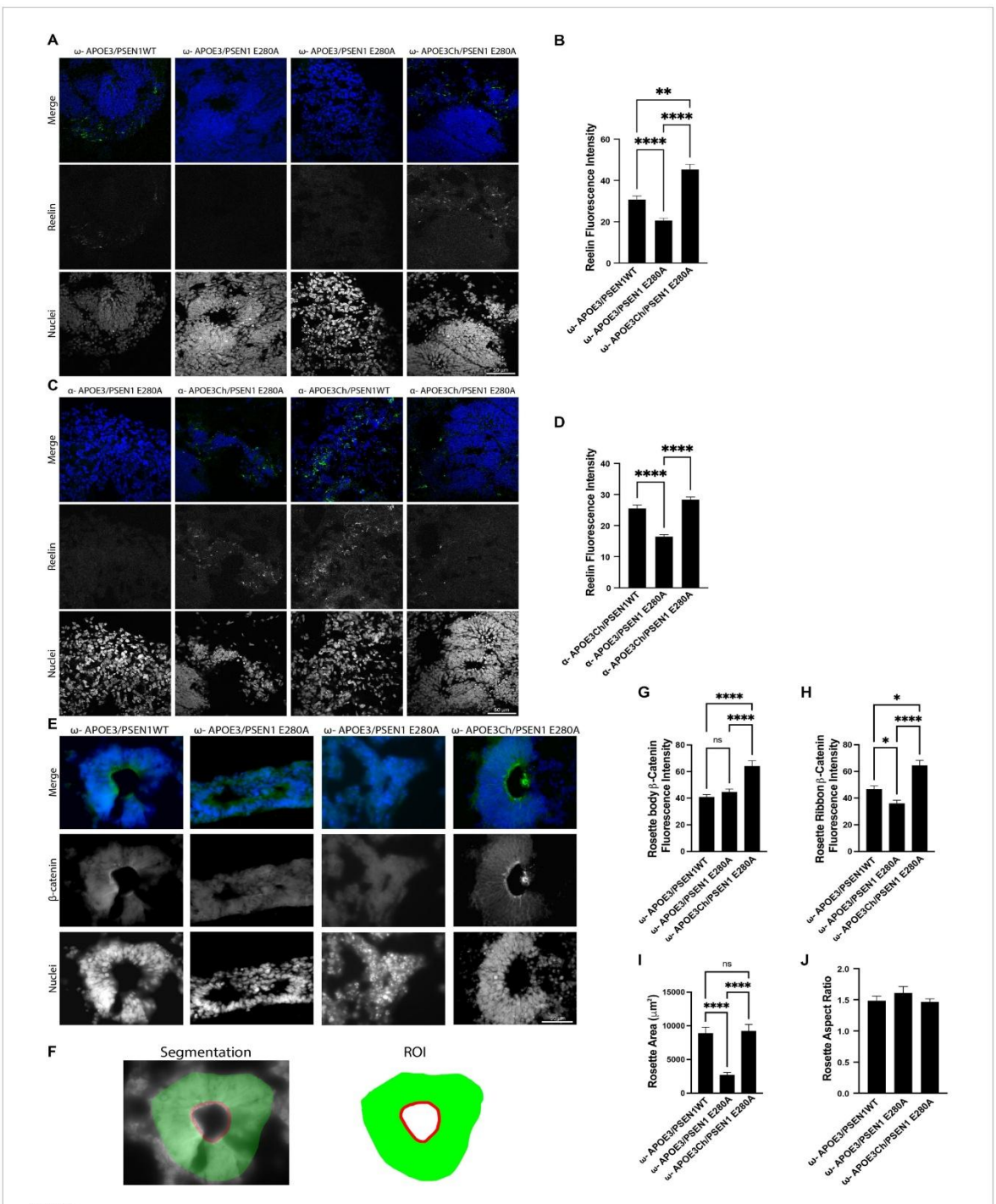
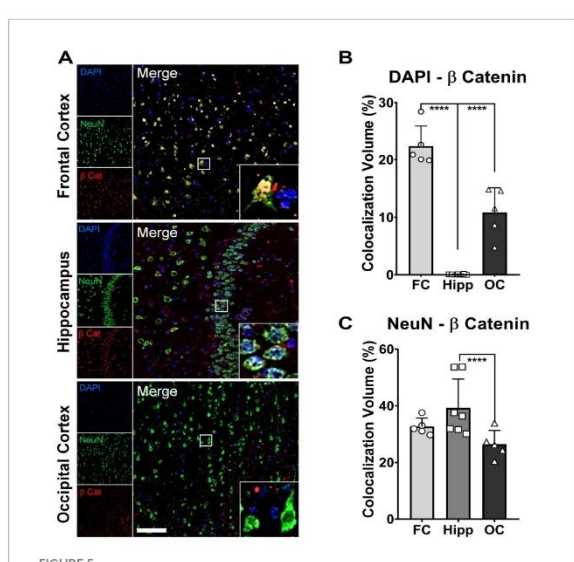


FIGURE 4 APOE3Ch influences reelin, β -catenin, and neural rosette features. Immunofluorescence staining was performed on cerebral organoids to identify changes in protein of interest and physical data. Organoids were imaged at 63X and quantified. Representative images of patient ω (A) and patient α (C) stained for reelin and nuclei. Reelin channel intensity was averaged, with isogenic controls averaged together for patient ω (n = 28 - 64 measurements per line) (B) and patient α (n = 44 - 120 measurements per line) (D) using three to four organoids per line. Cerebral organoids were stained for β -catenin using three to four organoids re line rosettes and were identified in patient ω (n = 17 - 29 measurements per line) and imaged at 63X (E). Segmentation was performed, and regions of interest were defined (F). β -catenin was quantified for both rosette body (G) and rosette ribbon (H). Rosette physical features were then measured for area (I) and aspect ratio (3). Scale bars for panels A, C, and E=50 μ m.

frontiersin.org



Increased nuclear β -catenin in neurons of protected brain regions of patient α . Representative immunofluorescence (IF) micrographs of the frontal cortex (FC), hippocampus (Hipp), and occipital cortex (OC) stained for β -catenin (red), NeuN (green), and cell nuclei (DAPI, blue). Insets present magnified images of neurons showing the degree of colocalization between the three markers. Scale bar = 100 μ m. (A). Bar graphs for colocalization analysis depicting thresholded colocalization volumes (TCVs) between DAPI and β -catenin in FC, Hipp, and OC. The percentage of β -catenin colocalizing in nuclei is significantly higher in FC than in both structures, Hipp and OC (oneway ANOVA, ρ < 0.0001 for both) (B). Bar graphs for colocalization analysis depicting TCVs between DAPI and β -catenin in FC, Hipp, and OC. The percentage of β -catenin colocalizing with neurons is significantly higher only in Hipp when compared to OC (one-way ANOVA, ρ = 0.025) (C).

Discussion

We have developed novel iPS cell lines derived from the ADAD Paisa kindred, used genetic engineering to correct the PSEN1 E280A mutation as well as editing native APOE3 to either add or remove the Christchurch variant, formed cerebral organoids, identified pathways through scRNA-seq, and supported these findings through immunostaining. While it is well documented that iPS cell systems can model aspects of AD pathology (Penney et al., 2020; Nelson et al., 2023), we have also demonstrated here that the iPS system is also capable of accurately identifying cellular processes differentially regulated by the APOE3Ch variant. We have found that the APOE3Ch variant alters the translational landscape to promote changes in Cadherin and Wnt signaling, which affects β -catenin, irrespective of the PSEN1 background. We have also found that ApoE3Ch is an enhancer of Wnt signaling. Taken together, this system has accurately identified cellular processes historically implicated in AD pathogenesis that are affected by the APOE3Ch variant. Additional studies will be required to provide therapeutic intent to AD as well as other neurodegenerative diseases and tauopathies.

Our findings in the *postmortem* tissue of Patient α, a homozygous APOE3Ch PSEN1 E280A carrier, confirm the relevance of the Wnt/βcatenin pathway as a putative mechanism of protection. A pathological downregulation of this pathway has been described in *postmortem* studies in the frontal cortex of Alzheimer's patients (Folke et al., 2019). Interestingly, the frontal cortex, the most protected brain region with the highest *APOE* expression levels in the Patient α *APOE3Ch PSEN1* E280A carrier showed higher activation of the Wnt/ β -catenin pathway. This finding bolsters our previous suggestion for an *APOE* dosedependent protective effect (Sepulveda-Falla et al., 2022).

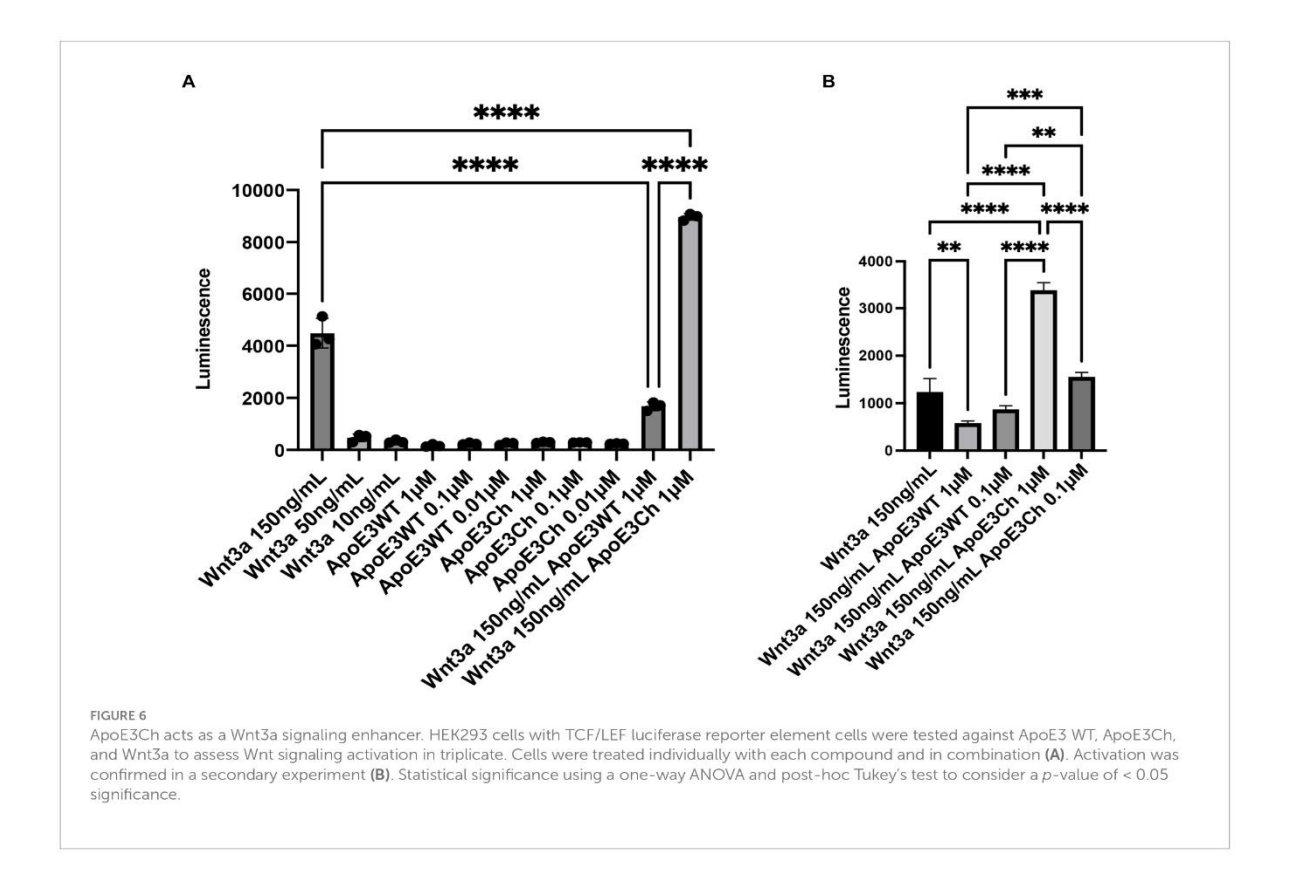
We were puzzled by the finding of Wnt ligand downregulation in the context of increased β -catenin signaling. To further explore this apparent discrepancy, we hypothesized that the changes arose from the presence of a hypothetical Wnt activator in our system that led to the compensatory decrease of endogenous Wnt ligands. As a first suspect, we tested whether ApoE3Ch could itself act as a Wnt activator using a reporter assay. This turned out to be the case as indicated by our data. ApoE3Ch protection may operate via multiple mechanisms, one of which is a neomorphism.

Our findings revealed a novel and unexpected gain-of-function property of ApoE3Ch, showing its ability to enhance Wnt3a signaling activity. While ApoE3Ch alone did not induce Wnt signaling, intriguingly, when combined with the Wnt3a ligand, it acted as a Wnt3a signaling activator. In contrast, ApoE3 WT displayed a Wnt signaling inhibitory effect under the same conditions. Our study sheds light on the intricate regulatory roles of ApoE isoforms in modulating the Wnt signaling pathway, providing insights into potential mechanisms underlying the resistance to tauopathy observed in Patient α, the ApoE3Chcarrying individual with the PSEN1 E280A mutation. These findings may have significant implications for the development of therapeutic strategies targeting Wnt signaling in Alzheimer's disease and other tauopathies. Further investigations are warranted to fully elucidate the molecular mechanisms underlying ApoE3Chmediated Wnt activation and its relevance to neuroprotection in the context of tau-related pathologies.

PSEN1 mutations can affect neuronal differentiation in iPS cell-derived systems, such as cerebral organoids, through reduced Notch signaling and premature aging phenotypes (Arber et al., 2021). Our study found developmental differences in organoids carrying the *PSEN1* E280A genotype, including abnormal tau phosphorylation at a young developmental stage. This suggests that young cerebral organoids can be used as pathological models for AD and as a tool to study the mechanisms of protection.

The effects of *APOE3Ch* on Wnt and Cadherin signaling uncovered by scRNA sequencing of cerebral organoids were unexpected and may operate via multiple mechanisms, ultimately resulting in β -catenin upregulation. Cadherins are a family of calcium-dependent transmembrane adhesion proteins that link β - and α -catenin to the actin cytoskeletal network (Punovuori et al., 2021) and also regulate cellular homeostasis through signaling mediating development, proliferation, apoptosis, and disease pathology (Yulis et al., 2018). Cadherins regulate calcium-dependent cell–cell adherent junctions, where the chelation of calcium abolishes adhesive activity and allows proteolytic degradation of cadherins (Nagar and Overduint, 1996; Kim et al., 2011). Thus, proper calcium levels play a vital role in cell–cell dynamics as well as maintaining a pool of cadherin.

Wnt signaling influences multiple cellular processes such as cell fate determination, cell polarity, organogenesis, stem cell renewal (Komiya and Habas, 2008), neuronal health (Inestrosa and



Varela-Nallar, 2014), autophagy (Pérez-Plasencia et al., 2020), and phagocytosis and ferroptosis (Wang et al., 2022). Wnt signaling has also been implicated in neurological aging (Inestrosa et al., 2020) and neurological aging disorders such as AD (Palomer et al., 2019). ApoE has also been implicated in Wnt signaling regulation (Zhao et al., 2023). ApoE is known to be produced in both radial glia and other glia cell populations (Zhao et al., 2023); however, neurons are known to produce ApoE under stress (Konings et al., 2021). Our scRNA-seq analysis revealed that our cerebral organoids produced ApoE but displayed minimal expression in neuronal clusters and selective enrichment in glial population clusters.

Wnt signaling can be assigned into two pathways, canonical Wnt signaling or the non-canonical planar cell polarity (PCP) and Wnt/calcium pathway subdivisions. Canonical Wnt signaling requires extracellular Wnt binding to LRP5/6 and Frizzled for signal transduction across the cell membrane to Disheveled. Once internalized, the signal is passed to the β -catenin destruction complex, a proteinaceous structure composed of GSK3 β and other proteins, resulting in the release of β -catenin by the inhibition of GSK3 β . Free β -catenin is then able to translocate to the nucleus and activate TCF/LEF transcription. In the PCP pathway, Wnt directly binds to Frizzled and transduces the signal to Disheveled, which in turn activates RhoA and Rac1 and eventual JNK pathways. In the non-canonical calcium-dependent subpathway, Wnt binds directly to Frizzled, transduces the signal to Disheveled, and interacts with trimeric G proteins and phospholipase C, increasing intracellular calcium concentration

inducing CamKII and calcineurin activation (Inestrosa and Varela-Nallar, 2014). CaMKII is vital in controlling NMDA receptor activity (Incontro et al., 2018), which also acts as a calcium channel (Lau et al., 2009).

GSK3 β is a protein kinase that phosphorylates and primes tau for inclusion in paired helical filaments and fibrils (Hooper et al., 2008). Indeed, GSK3 β is known to phosphorylate tau at the early pathology site S396 (Li and Paudel, 2006), and GSK3 β is also a vital component of the β -catenin destruction complex. It is responsible for phosphorylating β -catenin for ubiquitination and proteosomal degradation (Inestrosa and Varela-Nallar, 2014). This persistent degradation maintains low levels of free cytoplasmic β -catenin and inhibits gene transcription. Cerebral GSK3 β stimulation by phosphorylation at Y216 is mediated by intracellular calcium levels and calcium-dependent PYK2 (Hartigan and Johnson, 1999; Hartigan et al., 2001; Sayas et al., 2006).

APOE is the most significant known risk factor for sporadic Alzheimer's disease, ApoE4 exhibits the strongest receptor binding and is considered a high-risk allele, while ApoE2 exhibits the weakest receptor binding and is considered protective (Yamazaki et al., 2019). The ApoE3Ch variant was found in a protected ADAD subject and was shown to have weaker binding than its ApoE3 WT counterpart to heparin sulfate proteoglycans (Arboleda-Velasquez et al., 2019). However, imputation of genetic causality was also not feasible because of the rarity of the Christchurch variant. Thus, the need for genetic analyses ex vivo was conducted here.

In this study, we have demonstrated that APOE3Ch produces a reduction of pTau S396 phosphorylation in an AD cerebral organoid model and that ApoE3Ch enhances Wnt signaling. However, it is important to note that further studies with more mature organoids will be necessary to confirm the protective tau phosphorylation pattern persists over time to determine efficacy within the PSEN1 E280A background. Wnt signaling is also modulated by additional factors such as Wnt ligand, Fzd receptors, sFRP, R-Spondin, and Dkk, where our validation study relied on the HEK293 system only; therefore, further studies will be required to understand the secretome of APOE3Ch cerebral organoids and functional mechanisms of signaling enhancement (e.g., HSPG binding; Marino et al., 2023). CRISPR was employed to generate the genetic edits desired for this study, and while optimal guidance motifs were selected to reduce off-target edits, we cannot rule out any potential off-target effects, though isogenic controls were used to minimize this potential limitation. Developmental patterns of tau phosphorylation may also present a confounding factor. Due to the dynamic nature of a developing system and that gene expression patterns are on a continuum, cluster cell identification has its limitations.

In sum, our data suggest that iPS-derived cerebral organoids can be informative in the identification of biological processes influenced by protective mutations. Our model shows a link between APOE3Ch and a protective pattern of early pathogenic tau phosphorylation. Importantly, our data showed a prominent role for Wnt and Cadherin signaling in the presence of the APOE3Ch variant. β -catenin is differentially regulated in APOE3Ch cerebral organoids, which is known to affect Wnt/Cadherin signaling and GSK3 β activity, and confirmed by postmortem analysis of the ApoE3Ch patient. Furthermore, we confirmed scRNA-seq findings through ApoE3Ch enhancement of Wnt signaling. These findings are relevant in informing the sphere of influence associated with AD protection mediated by the APOE3Ch variant and serve to build the toolbox for identifying therapeutic targets against AD.

Data availability statement

The names of the repository/repositories and accession number(s) can be found in the article/Supplementary material. Sequencing data used in this manuscript are available through Gene Expression Omnibus (GEO) (Accession GSE241453) at https://www.ncbi.nlm.nih.gov/geo/query/acc.cgi?acc=GSE241453.

Ethics statement

The studies involving humans were approved by University of Antioquia IRB and Mass General Hospital IRB. The studies were conducted in accordance with the local legislation and institutional requirements. The participants provided their written informed consent to participate in this study.

Author contributions

PP: Data curation, Formal analysis, Investigation, Methodology. TV: Formal analysis, Investigation. GV: Formal analysis, Investigation.JS:

Formal analysis, Investigation. NV-M: Formal analysis, Investigation. CM: Formal analysis, Investigation. SK: Investigation, Formal analysis. MMP: Resources. DA: Resources. MJ-D-R: Resources. AB: Resources. DS-F: Formal analysis, Investigation. FL: Project administration, Resources, Supervision. YTQ: Project administration, Investigation, Supervision. JFA-V: Conceptualization, Investigation, Methodology, Project administration, Supervision. RM: Conceptualization, Formal analysis, Investigation, Methodology, Project administration.

Funding

The author(s) declare that financial support was received for the research, authorship, and/or publication of this article. This study was made possible by a gift from Good Ventures and Open Philanthropy to JFA-V. JFA-V was the recipient of philanthropic support from the Remondi Family Foundation and federal support from the USA National Institute of Neurological Disorders and Stroke and the National Institute on Aging co-funded grants UH3 NS100121 and RF1 NS110048. FL was funded by the API Colombia registry and clinical trial. YTQ was funded by the US National Institutes of Health (NIH) Office of the Director grant DP5 OD019833 and the US National Institute on Aging (R01 AG054671, RF1AGO77627), the Massachusetts General Hospital Executive Committee on Research (MGH Research Scholar Award), and a grant from the USA Alzheimer's Association. DS-F was also funded by the U.S. National Institute of Neurological Disorders and Stroke and the National Institute on Aging co-funded grant RF1 NS110048. DS-F and SK also received a gift from Good Ventures and Open Philanthropy. None of the authors were precluded from accessing data in the study, and they accept responsibility to submit for publication. SK was supported by the DFG grant KR1737/2-1. YTQ, JFA-V, and FL were funded by the US National Institute of Neurological Disorders and Stroke (NINDS) and NIA co-funded grant RM1NS132996.

Acknowledgments

The authors thank the Colombian families with ADAD for their contributions and extraordinary commitment to research. The authors would like to thank L. Daheron and the Harvard Stem Cell Institute for their effort and support. The authors also thank A. Koutoulas for technical support with genome sequencing, K. Hartmann and C. Dwumfour for technical support with immunohistochemical staining, and S. Levine and S. Mildrum of the BMC core at the Massachusetts Institute of Technology.

Conflict of interest

JFA-V, YTQ, and FL are listed as inventors on a patent application addressing Christchurch-inspired therapeutics filed by Mass General Brigham. JFA-V is a co-founder of Epoch Biotech, a company developing ApoE Christchurch-inspired therapeutics. YTQ serves as a consultant for Biogen. FL received consulting fees from Biogen and Tecnoquimicas. GV is employed by the company Vacano Informatics LLC of Arvada, CO, USA and was contracted by JFA-V.

The remaining authors declare that the research was conducted in the absence of any commercial or financial relationships that could be construed as a conflict of interest.

The author(s) declared that they were an editorial board member of Frontiers, at the time of submission. This had no impact on the peer review process and the final decision.

Publisher's note

All claims expressed in this article are solely those of the authors and do not necessarily represent those of their affiliated organizations, or those of the publisher, the editors and the reviewers. Any product that may be evaluated in this article, or claim that may be made by its manufacturer, is not guaranteed or endorsed by the publisher.

Supplementary material

The Supplementary material for this article can be found online at: https://www.frontiersin.org/articles/10.3389/fnmol.2024.1373568/full#supplementary-material

References

Arber, C., Lovejoy, C., Harris, L., Willumsen, N., Alatza, A., Casey, J. M., et al. (2021). Familial Alzheimer's disease mutations in PSEN1 lead to premature human stem cell neurogenesis. *Cell Rep.* 34:108615. doi: 10.1016/j.celrep.2020.108615

Arboleda-Velasquez, J. F., Lopera, F., O'Hare, M., Delgado-Tirado, S., Marino, C., Chmielewska, N., et al. (2019). Resistance to autosomal dominant Alzheimer's disease in an APOE3 Christchurch homozygote: a case report. *Nat. Med.* 25, 1680–1683. doi: 10.1038/s41591-019-0611-3

Cao, J., O'Day, D. R., Pliner, H. A., Kingsley, P. D., Deng, M., Daza, R. M., et al. (2020). A human cell atlas of fetal gene expression. *Science* 370:eaba7721. doi: 10.1126/science.aba7721

Cao, Y., Wang, X., and Peng, G. (2020). SCSA: a cell type annotation tool for single-cell RNA-seq data. Front. Genet. 11:490. doi: 10.3389/fgene.2020.00490

Caruso, A., Motolese, M., Iacovelli, L., Caraci, F., Copani, A., Nicoletti, F., et al. (2006). Inhibition of the canonical Wnt signaling pathway by apolipoprotein E4 in PC12 cells. J. Neurochem. 98, 364–371. doi: 10.1111/j.1471-4159.2006.03867.x

De Ferrari, G. V., Avila, M. E., Medina, M. A., Perez-Palma, E., Bustos, B. I., and Alarcon, M. A. (2014). Wnt/b-catenin signaling in Alzheimer's disease. CNS Neurol. Disord. Drug Targets 13, 745–754. doi: 10.2174/1871527312666131223113900

Desikan, R. S., Cabral, H. J., Hess, C. P., Dillon, W. P., Glastonbury, C. M., Weiner, M. W., et al. (2009). Automated MRI measures identify individuals with mild cognitive impairment and Alzheimer's disease. *Brain* 132, 2048–2057. doi: 10.1093/brain/awn123

Di Lullo, E., and Kriegstein, A. R. (2017). The use of brain organoids to investigate neural development and disease. *Nat. Rev. Neurosci.* 18, 573–584. doi: 10.1038/nrn.2017.107

Fan, X., Dong, J., Zhong, S., Wei, Y., Wu, Q., Yan, L., et al. (2018). Spatial transcriptomic survey of human embryonic cerebral cortex by single-cell RNA-seq analysis. *Cell Res.* 28, 730–745. doi: 10.1038/s41422-018-0053-3

Folke, J., Pakkenberg, B., and Brudek, T. (2019). Impaired Wnt signaling in the prefrontal cortex of Alzheimer's disease. *Mol. Neurobiol.* 56, 873–891. doi: 10.1007/s12035-018-1103-z

Hafemeister, C., and Satija, R. (2019). Normalization and variance stabilization of single-cell RNA-seq data using regularized negative binomial regression. *Genome Biol.* 20:296. doi: 10.1186/s13059-019-1874-1

Hao, Y., Hao, S., Andersen-Nissen, E., Mauck, W. M., Zheng, S., Butler, A., et al. (2021). Integrated analysis of multimodal single-cell data. *Cell* 184, 3573–3587.e29. doi: 10.1016/j.cell.2021.04.048

Hartigan, J. A., and Johnson, G. V. W. (1999). Transient increases in intracellular calcium result in prolonged site-selective increases in tau phosphorylation through a glycogen synthase kinase 3β-dependent pathway. *J. Biol. Chem.* 274, 21395–21401. doi: 10.1074/jbc.274.30.21395

Hartigan, J. A., Xiong, W. C., and Johnson, G. V. W. (2001). Glycogen synthase kinase 3β is tyrosine phosphorylated by PYK2. *Biochem. Biophys. Res. Commun.* 284, 485–489. doi: 10.1006/bbrc.2001.4986

Hooper, C., Killick, R., and Lovestone, S. (2008). The GSK3 hypothesis of Alzheimer's disease: GSK3 and Alzheimer's disease. *J. Neurochem.* 104, 1433–1439. doi: 10.1111/j.1471-4159.2007.05194.x

Incontro, S., Díaz-Alonso, J., Iafrati, J., Vieira, M., Asensio, C. S., Sohal, V. S., et al. (2018). The CaMKII/NMDA receptor complex controls hippocampal synaptic transmission by kinase-dependent and independent mechanisms. *Nat. Commun.* 9:2069. doi: 10.1038/s41467-018-04439-7

Inestrosa, N. C., Tapia-Rojas, C., Lindsay, C. B., and Zolezzi, J. M. (2020). Wnt signaling pathway dysregulation in the aging brain: lessons from the *Octodon degus*. Front. Cell Dev. Biol. 8:734. doi: 10.3389/fcell.2020.00734

Inestrosa, N. C., and Varela-Nallar, L. (2014). Wnt signaling in the nervous system and in Alzheimer's disease. J. Mol. Cell Biol. 6, 64–74. doi: $10.1093/\mathrm{jmcb/mjt051}$

Jackson, G. R., Wiedau-Pazos, M., Sang, T. K., Wagle, N., Brown, C. A., Massachi, S., et al. (2002). Human wild-type tau interacts with wingless pathway components and produces neurofibrillary pathology in Drosophila. *Neuron* 34, 509–519. doi: 10.1016/S0896-6273(02)00706-7

Johnson, K. A., Schultz, A., Betensky, R. A., Becker, J. A., Sepulcre, J., Rentz, D., et al. (2016). Tau positron emission tomographic imaging in aging and early Alzheimer disease: tau PET in aging and early AD. *Ann. Neurol.* 79, 110–119. doi: 10.1002/ana.24546

Kim, S. A., Tai, C. Y., Mok, L. P., Mosser, E. A., and Schuman, E. M. (2011). Calcium-dependent dynamics of cadherin interactions at cell-cell junctions. *Proc. Natl. Acad. Sci. USA* 108, 9857–9862. doi: 10.1073/pnas.1019003108

Knopman, D. S., Amieva, H., Petersen, R. C., Chételat, G., Holtzman, D. M., Hyman, B. T., et al. (2021). Alzheimer disease. *Nat. Rev. Dis. Prim.* 7:33. doi: 10.1038/s41572-021-00269-y

Komiya, Y., and Habas, R. (2008). Wnt signal transduction pathways. Organ~4, 68-75.~doi: 10.4161/org.4.2.5851

Konings, S. C., Torres-Garcia, L., Martinsson, I., and Gouras, G. K. (2021). Astrocytic and neuronal apolipoprotein E isoforms differentially affect neuronal excitability. Front. Neurosci. 15:734001. doi: 10.3389/fnins.2021.7344001

Korsunsky, I., Millard, N., Fan, J., Slowikowski, K., Zhang, F., Wei, K., et al. (2019). Fast, sensitive, and accurate integration of single-cell data with harmony. *Nat. Methods* 16, 1289–1296. doi: 10.1038/s41592-019-0619-0

La Manno, G., Gyllborg, D., Codeluppi, S., Nishimura, K., Salto, C., Zeisel, A., et al. (2016). Molecular diversity of midbrain development in mouse, human, and stem cells. *Cell* 167, 566–580.e19. doi: 10.1016/j.cell.2016.09.027

Lancaster, M. A., Renner, M., Martin, C. A., Wenzel, D., Bicknell, L. S., Hurles, M. E., et al. (2013). Cerebral organoids model human brain development and microcephaly. *Nature* 501, 373–379. doi: 10.1038/nature12517

Lau, C. G., Takeuchi, K., Rodenas-Ruano, A., Takayasu, Y., Murphy, J., Bennett, M. V. L., et al. (2009). Regulation of NMDA receptor Ca2+ signalling and synaptic plasticity. *Biochem. Soc. Trans.* 37, 1369–1374. doi: 10.1042/BST0371369

Li, T., and Paudel, H. K. (2006). Glycogen synthase kinase 3β phosphorylates Alzheimer's disease-specific Ser396 of microtubule-associated protein tau by a sequential mechanism. *Biochemistry* 45, 3125–3133. doi: 10.1021/bi051634r

Lopera, F., Marino, C., Chandrahas, A. S., O'Hare, M., Villalba-Moreno, N. D., Aguillon, D., et al. (2023). Resilience to autosomal dominant Alzheimer's disease in a Reelin-COLBOS heterozygous man. *Nat. Med.* 29, 1243–1252. doi: 10.1038/s41591-023-02318-3

Marino, C., Perez-Corredor, P., O'Hare, M., Heuer, A., Chmielewska, N., Gordon, H., et al. (2023). APOE Christchurch-mimetic therapeutic antibody reduces APOE-mediated toxicity and tau phosphorylation. *Alzheimers Dement.* 20, 819–836. doi: 10.1003/eji.13436

McGinnis, C. S., Murrow, L. M., and Gartner, Z. J. (2019). DoubletFinder: doublet detection in single-cell RNA sequencing data using artificial nearest neighbors. *Cell Syst.* 8, 329–337.e4. doi: 10.1016/j.cels.2019.03.003

Mondragón-Rodríguez, S., Perry, G., Luna-Muñoz, J., Acevedo-Aquino, M. C., and Williams, S. (2014). Phosphorylation of tau protein at sites Ser 396-404 is one of the earliest events in Alzheimer's disease and down syndrome: phosphorylation was found to be the earliest event in AD and down syndrome. *Neuropathol. Appl. Neurobiol.* 40, 121–135. doi: 10.1111/nan.12084

Mosconi, L. (2013). Glucose metabolism in normal aging and Alzheimer's disease: methodological and physiological considerations for PET studies. $Clin.\ Translat.\ Imaging$ 1, 217–233. doi: 10.1007/s40336-013-0026-y

Nagar, B., and Overduint, M. (1996). Structural basis of calcium-induced E-cadherin rigidification and dimerization. *Nature* 380, 360–364. doi: 10.1038/380360a0

Nelson, M. R., Liu, P., Agrawal, A., Yip, O., Blumenfeld, J., Traglia, M., et al. (2023). The APOE-R136S mutation protects against APOE4-driven tau pathology,

neurodegeneration, and neuroinflammation. Nat. Neurosci. 26, 2104–2121. doi: 10.1038/s41593-023-01480-8

Nunomura, A., Perry, G., Aliev, G., Hirai, K., Takeda, A., Balraj, E. K., et al. (2001). Oxidative damage is the earliest event in Alzheimer disease. *J. Neuropathol. Exp. Neurol.* 60, 759–767. doi: 10.1093/jnen/60.8.759

Palomer, E., Buechler, J., and Salinas, P. C. (2019). Wnt signaling deregulation in the aging and Alzheimer's brain. *Front. Cell. Neurosci.* 13:227. doi: 10.3389/fncel.2019.00227

Patterson, C. (2018). World Alzheimer report 2018—the state of the art of dementia research; new frontiers. Alzheimer's disease International.

Penney, J., Ralvenius, W. T., and Tsai, L. H. (2020). Modeling Alzheimer's disease with iPSC-derived brain cells. *Mol. Psychiatry* 25, 148–167. doi: 10.1038/s41380-019-0468-3

Pérez-Plasencia, C., López-Urrutia, E., García-Castillo, V., Trujano-Camacho, S., López-Camarillo, C., and Campos-Parra, A. D. (2020). Interplay between autophagy and Wnt/β-catenin signaling in cancer: therapeutic potential through drug repositioning. Front. Oncol. 10:1037. doi: 10.3389/fonc.2020.01037

Punovuori, K., Malaguti, M., and Lowell, S. (2021). Cadherins in early neural development. Cell. Mol. Life Sci. 78, 4435–4450. doi: 10.1007/s00018-021-03815-9

Qiu, X., Mao, Q., Tang, Y., Wang, L., Chawla, R., Pliner, H. A., et al. (2017). Reversed graph embedding resolves complex single-cell trajectories. *Nat. Methods* 14, 979–982. doi: 10.1038/nmeth.4402

Quiroz, Y. T., Sperling, R. A., Norton, D. J., Baena, A., Arboleda-Velasquez, J. F., Cosio, D., et al. (2018). Association between amyloid and tau accumulation in young adults with autosomal dominant Alzheimer disease. *JAMA Neurol.* 75, 548–556. doi: 10.1001/jamaneurol.2017.4907

Sayas, C. L., Ariaens, A., Ponsioen, B., and Moolenaar, W. H. (2006). GSK-3 is activated by the tyrosine kinase Pyk2 during LPA $_1$ -mediated neurite retraction. *MBoC* 17, 1834–1844. doi: 10.1091/mbc.e05-07-0688

Sepulveda-Falla, D., Sanchez, J. S., Almeida, M. C., Boassa, D., Acosta-Uribe, J., Vila-Castelar, C., et al. (2022). Distinct tau neuropathology and cellular profiles of an APOE3 Christchurch homozygote protected against autosomal dominant Alzheimer's dementia. *Acta Neuropathol.* 144, 589–601. doi: 10.1007/s00401-022-02467-8

Sims, R., Hill, M., and Williams, J. (2020). The multiplex model of the genetics of Alzheimer's disease. Nat. Neurosci. 23, 311–322. doi: 10.1038/s41593-020-0599-5

Subramanian, A., Tamayo, P., Mootha, V. K., Mukherjee, S., Ebert, B. L., Gillette, M. A., et al. (2005). Gene set enrichment analysis: a knowledge-based approach for interpreting genome-wide expression profiles. *Proc. Natl. Acad. Sci. USA* 102, 15545–15550. doi: 10.1073/pnas.0506580102

Sun, L., Zhou, R., Yang, G., and Shi, Y. (2017). Analysis of 138 pathogenic mutations in presenilin-1 on the in vitro production of A β 42 and A β 40 peptides by γ -secretase. Proc. Natl. Acad. Sci. USA 114, E476–E485. doi: 10.1073/pnas.1618657114

Wang, Y., Zheng, L., Shang, W., Yang, Z., Li, T., Liu, F., et al. (2022). Wnt/beta-catenin signaling confers ferroptosis resistance by targeting GPX4 in gastric cancer. *Cell Death Differ.* 29, 2190–2202. doi: 10.1038/s41418-022-01008-w

Yamazaki, Y., Zhao, N., Caulfield, T. R., Liu, C. C., and Bu, G. (2019). Apolipoprotein E and Alzheimer disease: pathobiology and targeting strategies. *Nat. Rev. Neurol.* 15, 501–518. doi: 10.1038/s41582-019-0228-7

Yulis, M., Kusters, D. H. M., and Nusrat, A. (2018). Cadherins: cellular adhesive molecules serving as signalling mediators: Cadherins as signalling mediators. *J. Physiol.* 596, 3883–3898. doi: 10.1113/JP275328

Zhao, J., Ikezu, T. C., Lu, W., Macyczko, J. R., Li, Y., Lewis-Tuffin, L. J., et al. (2023). APOE deficiency impacts neural differentiation and cholesterol biosynthesis in human iPSC-derived cerebral organoids. $Stem\ Cell\ Res\ Ther\ 14:214.\ doi: 10.1186/s13287-023-03444-y$

Zhong, S., Zhang, S., Fan, X., Wu, Q., Yan, L., Dong, J., et al. (2018). A single-cell RNA-seq survey of the developmental landscape of the human prefrontal cortex. *Nature* 555, 524–528. doi: 10.1038/nature25980

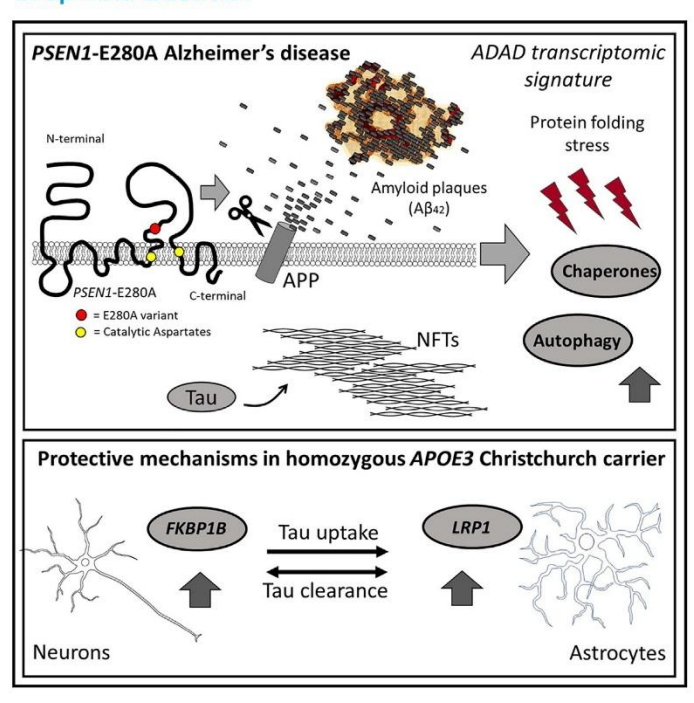
11. Publication V

Article

Neuron

Single-nucleus RNA sequencing demonstrates an autosomal dominant Alzheimer's disease profile and possible mechanisms of disease protection

Graphical abstract



Authors

Maria Camila Almeida, Sarah J. Eger, Caroline He, ..., Diego Sepulveda-Falla, Francisco Lopera, Kenneth S. Kosik

Correspondence

francisco.lopera@gna.org.co (F.L.), kosik@ucsb.edu (K.S.K.)

In brief

Almeida, Eger, and colleagues find specific autophagy and chaperone gene signatures that distinguish autosomal dominant Alzheimer's disease (ADAD) from sporadic cases. Protection from dementia due to the APOE3-Christchurch variant may arise from increased LRP1 expression in astrocytes and, consequently, their increased TAU uptake.

Highlights

- An autophagy gene profile distinguishes PSEN1-E280A
 ADAD cases from sporadic AD
- A possible mechanism for the PSEN1-E280A Christchurch variant effect observed
- Unique cellular responses in ADAD and sporadic AD may impact clinical trial design







Article

Single-nucleus RNA sequencing demonstrates an autosomal dominant Alzheimer's disease profile and possible mechanisms of disease protection

Maria Camila Almeida,^{1,2,8} Sarah J. Eger,^{1,8} Caroline He,¹ Morgane Audouard,^{1,6} Arina Nikitina,¹ Stella M.K. Glasauer,^{1,6} Dasol Han,^{1,6} Barbara Mejía-Cupajita,^{1,3} Juliana Acosta-Uribe,^{1,3} Nelson David Villalba-Moreno,⁴ Jessica Lisa Littau,⁴ Megan Elcheikhali,^{5,7} Erica Keane Rivera,¹ Daniel Carneiro Carrettiero,^{1,2} Carlos Andrés Villegas-Lanau,³ Diego Sepulveda-Falla,⁴ Francisco Lopera,^{3,*} and Kenneth S. Kosik^{1,9,*}

SUMMARY

Highly penetrant autosomal dominant Alzheimer's disease (ADAD) comprises a distinct disease entity as compared to the far more prevalent form of AD in which common variants collectively contribute to risk. The downstream pathways that distinguish these AD forms in specific cell types have not been deeply explored. We compared single-nucleus transcriptomes among a set of 27 cases divided among *PSEN1*-E280A ADAD carriers, sporadic AD, and controls. Autophagy genes and chaperones clearly defined the *PSEN1*-E280A cases compared to sporadic AD. Spatial transcriptomics validated the activation of chaperone-mediated autophagy genes in *PSEN1*-E280A. The *PSEN1*-E280A case in which much of the brain was spared neurofibrillary pathology and harbored a homozygous *APOE3*-Christchurch variant revealed possible explanations for protection from AD pathology including overexpression of *LRP1* in astrocytes, increased expression of *FKBP1B*, and decreased *PSEN1* expression in neurons. The unique cellular responses in ADAD and sporadic AD require consideration when designing clinical trials.

INTRODUCTION

Alzheimer's disease (AD) is a progressive neurodegenerative disorder that ultimately impairs the ability to carry out the simplest activities of daily living. Although more granular classifications of AD genotypes and phenotypes are described, the disease can be broadly discriminated as highly penetrant autosomal dominant AD (ADAD) or sporadic AD due to a complex interplay of genetic risks and environmental contributions. While sporadic AD is often subdivided into late-onset AD (LOAD) and early-onset AD (EOAD), genetic evidence suggests that they represent a continuum rather than two distinct groups, ¹ and there can be overlap in age at onset with ADAD. ² PSEN1, PSEN2, and APP are the three genes that carry multiple different ADAD mutations. Variants in these genes are often highly penetrant with most carriers

developing AD by midlife. A glutamic acid-to-alanine mutation at codon 280 in *PSEN1* (NM_000021:c.839A>C, p.Glu280Ala, here referred as *PSEN1*-E280A) (rs63750231) discovered in Antioquia, Colombia, affects the largest kindred in the world with ADAD. A.5 *PSEN1*-E280A mutation carriers usually develop memory deficits, followed by gradual impairments in other cognitive skills, such as verbal fluency and executive function. The median lifespan after onset of dementia (~49 years old) is approximately 10 years. Although ADAD cases represent fewer than 1% of all AD cases, patients with these variants have greatly informed mechanistic studies of the disease. Nevertheless, the dysregulated pathways that lead to sporadic AD versus ADAD are unknown, as are the molecular consequences of the somewhat distinct co-pathologies associated with these conditions. Greater degrees of neuritic plaques, neurofibrillary tangle (NFT)



¹Neuroscience Research Institute and Department of Molecular, Cellular and Developmental Biology, University of California, Santa Barbara, Santa Barbara, CA 93106, USA

²Center for Natural and Humans Sciences, Federal University of ABC, Sao Bernardo do Campo, SP 09608020, Brazil

³Grupo de Neurociencias de Antioquia, School of Medicine, Universidad de Antioquia, Medellín 050010, Colombia

⁴Molecular Neuropathology of Alzheimer's Disease, Institute of Neuropathology, University Medical Center Hamburg-Eppendorf, 20246 Hamburg, Germany

⁵Department of Statistics and Applied Probability, University of California, Santa Barbara, Santa Barbara, CA 93106, USA

⁶Present address: Altos Labs, Inc., Redwood City, CA 94065, USA

⁷Present address: Slavov Lab, Bioengineering Department, Northeastern University, Boston, MA 02115, USA

⁸These authors contributed equally

⁹Lead contact

^{*}Correspondence: francisco.lopera@gna.org.co (F.L.), kosik@ucsb.edu (K.S.K.) https://doi.org/10.1016/j.neuron.2024.02.009

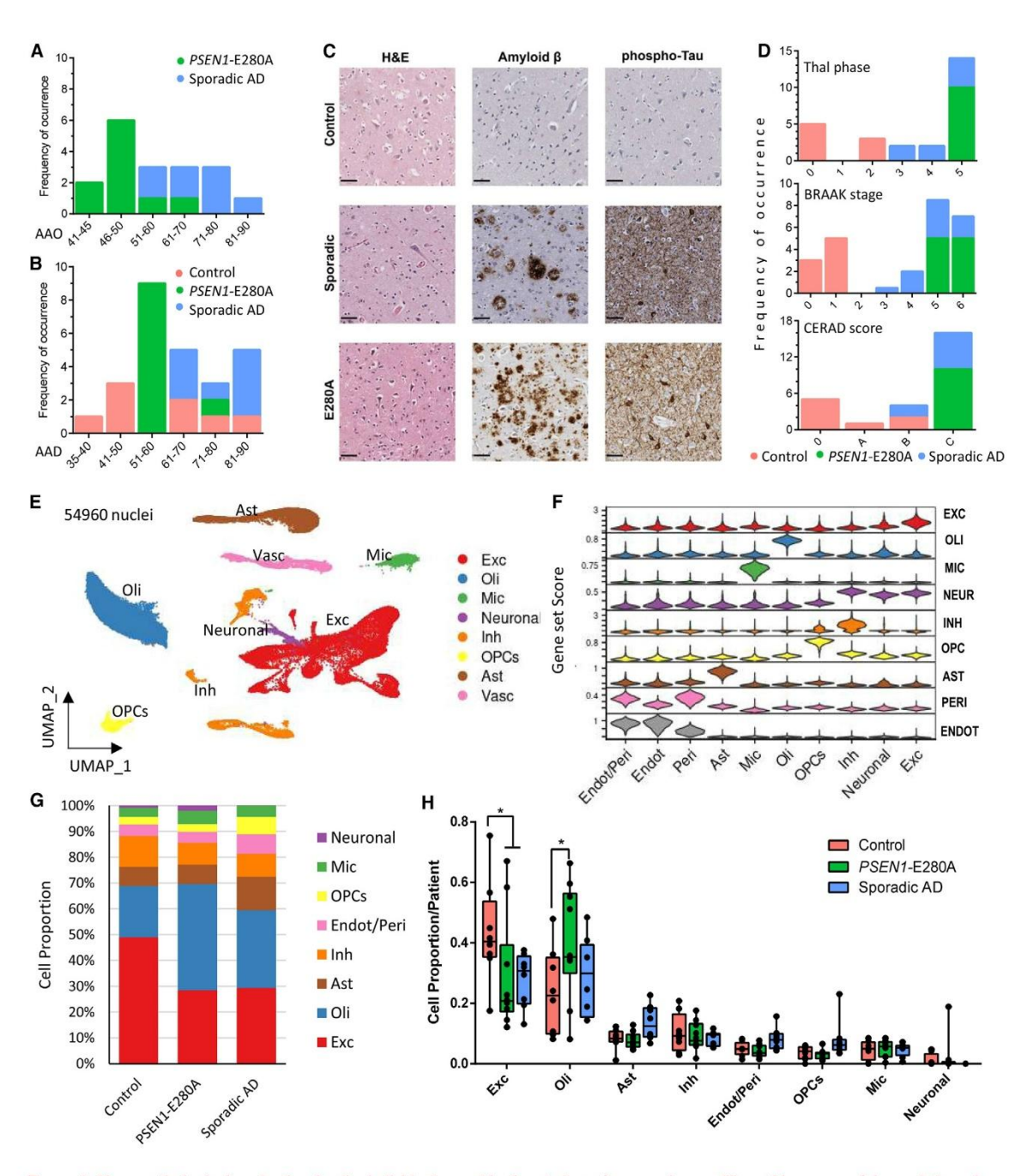


Figure 1. Neuropathological evaluation for the individuals used in the study and expression profiling of human nuclei populations from frozen, postmortem frontal cortex

(A and B) Frequency of occurrence of age at onset (AAO; A) of cognitive decline and age at death (AAD; B) among individuals from three different diagnosis: control, *PSEN1*-E280A, and sporadic AD.

(legend continued on next page)

Neuron 112, 1778-1794, June 5, 2024 1779

⁽C) Representative images of histological characterization of frontal cortex tissue from control, *PSEN1*-E280A, and sporadic AD individuals. Hematoxylin and eosin staining (column 1); immunohistochemistry for A β peptides (column 2), and phosphorylated TAU (AT8) (column 3). Each row represents one set representative image for each diagnosis. Scale bars, 50 μ m.

⁽D) Neuropathological status (Thal phase, BRAAK stage, and CERAD score) for each diagnosis.





formation, and cerebral amyloid angiopathy were found in ADAD.⁷ Highly prevalent AD co-pathologies are not restricted to the oldest-old but are common even in early-onset AD.⁸ AD pathology unrelated to plaques and tangles is well known to occur in ADAD; particularly, the coexistence of Lewy bodies composed primarily of alpha-synuclein filaments occurs frequently.^{9–11}

Our hypothesis is that single-cell gene expression vulnerabilities in ADAD, as exemplified by *PSEN1*-E280A, differ from sporadic AD, including LOAD. Because clinical and pathological variation do exist among cases with different *PSEN1* variants, focusing on a single *PSEN1* mutation will reduce that variation. The very large *PSEN1*-E280A kindred precisely provides the opportunity to do this. Understanding the cellular and molecular differences between these forms of AD is critical because ADAD cases are often utilized in "prevention" trials that take advantage of the strong genetic predisposition to identify participants before the onset of clinical symptoms; however, the results from such trials remain of questionable application to the larger LOAD population. Identification of differences between these conditions may spur separate treatment limbs in clinical trials and provide a better-informed route toward precision medicine.

In this study, we performed single-nucleus RNA sequencing (snRNA-seg) from postmortem frontal cortex in non-AD controls, sporadic AD patients, and ADAD patients to detect a PSEN1-E280A transcriptomic profile that can distinguish ADAD from sporadic AD and controls. We also performed a spatial transcriptomics analysis in samples from frontal cortex and the CA1 hippocampal region in PSEN1-E280A cases compared with nondiseased control individuals to validate our findings. Finally, we compared single-nucleus transcriptomes from the frontal cortex of the PSEN1-E280A case carrying the APOE3 homozygous Christchurch variant (PSEN1-E280A_APOE3-CC-hom) with the variety of PSEN1-E280A mutation settings in which prominent AD pathology was observed, including occipital cortex from PSEN1-E280A_APOE3-CC-hom, seven PSEN1-E280A carriers that do not have the Christchurch variant (PSEN1-E280A_A-POE3-CC-negative), and three PSEN1-E280A APOE3-Christchurch heterozygotes (PSEN1-E280A_APOE3-CC-het).

RESULTS

snRNA-seq of frontal cortex

The samples under study were from ten carriers of *PSEN1*-E280A, eight non-*PSEN1*-E280A carriers with sporadic AD, and eight non-AD controls, both male and female subjects with a range of *APOE* genotypes (E2/E3, E3/3, E3/4, and E4/4), plus one additional patient carrying two alleles of the *APOE3*-Christchurch variant (Table S1). Although age at onset in sporadic AD cases skewed older, there was significant overlap in the two groups (Figures 1A and 1B; Table S1). All brains were neuropathologically examined by immunohistochemistry for β -amyloid (A β) and pathological TAU (AT8). Virtually no AD-related neuro-

pathological markers were detected in controls, while both *PSEN1*-E280A carriers and sporadic AD cases were positive for both markers (Figures 1C and S1). Disease stage, as assessed by Thal phase, BRAAK stage, and CERAD scores were similarly advanced in both *PSEN1*-E280A and sporadic AD individuals (Figure 1D; Table S1). snRNA-seq was performed on the frontal pole from all individuals (Figures S2A and S2B). After quality-control filtering, 54,960 nuclei with an average of 4,128 transcripts and 2,074 genes per nucleus were detected (Figure S2C; Table S1). After integrating data from the occipital cortex and frontal pole of the patient carrying two alleles of the *APOE3*-Christchurch variant (*PSEN1*-E280A_*APOE3*-CC-hom), the total count of nuclei analyzed summed to 66,250, with an average of 4,163 transcripts and 2,076 genes per nucleus (Table S1).

The postmortem time to brain retrieval did not correlate with the number of transcripts or genes detected per cell (Figure S2D). The cells clustered as inhibitory neurons, excitatory neurons, astrocytes, microglia, oligodendrocytes, oligodendrocyte precursor cells (OPCs), endothelial cells, and pericytes (Figures S3A, S3B, 1E, and 1F). The nuclei types, markers, and proportions of nuclei types matched previous snRNA-seq data from adult human cortex. 12-15

All the cell types were detected in the three sample groups (Figure 1G). To assess whether the proportions of broad cell types were affected by diagnosis (control, PSEN1-E280A, and sporadic AD), we computed the relative abundance of each cell type for each individual according to diagnosis. Statistical significance was determined using beta regression. The relative abundance of oligodendrocytes in PSEN1-E280A (p = 1.2E-2) compared to controls was increased, whereas sporadic AD did not differ from controls in oligodendrocyte abundance (p = 6.5E-2). However, a direct comparison between PSEN1-E280A cases and sporadic AD cases was not significant (p = 5.3E-1) for oligodendrocyte abundance. Both PSEN1-E280A and sporadic AD cases showed a decrease in the excitatory neuron population compared to controls (Figure 1H). No sample variable, such as donor control, disease status, sex, age at death, postmortem interval time to brain retrieval, or neuropathological staging, was exclusively associated with any cluster (Figure S3C).

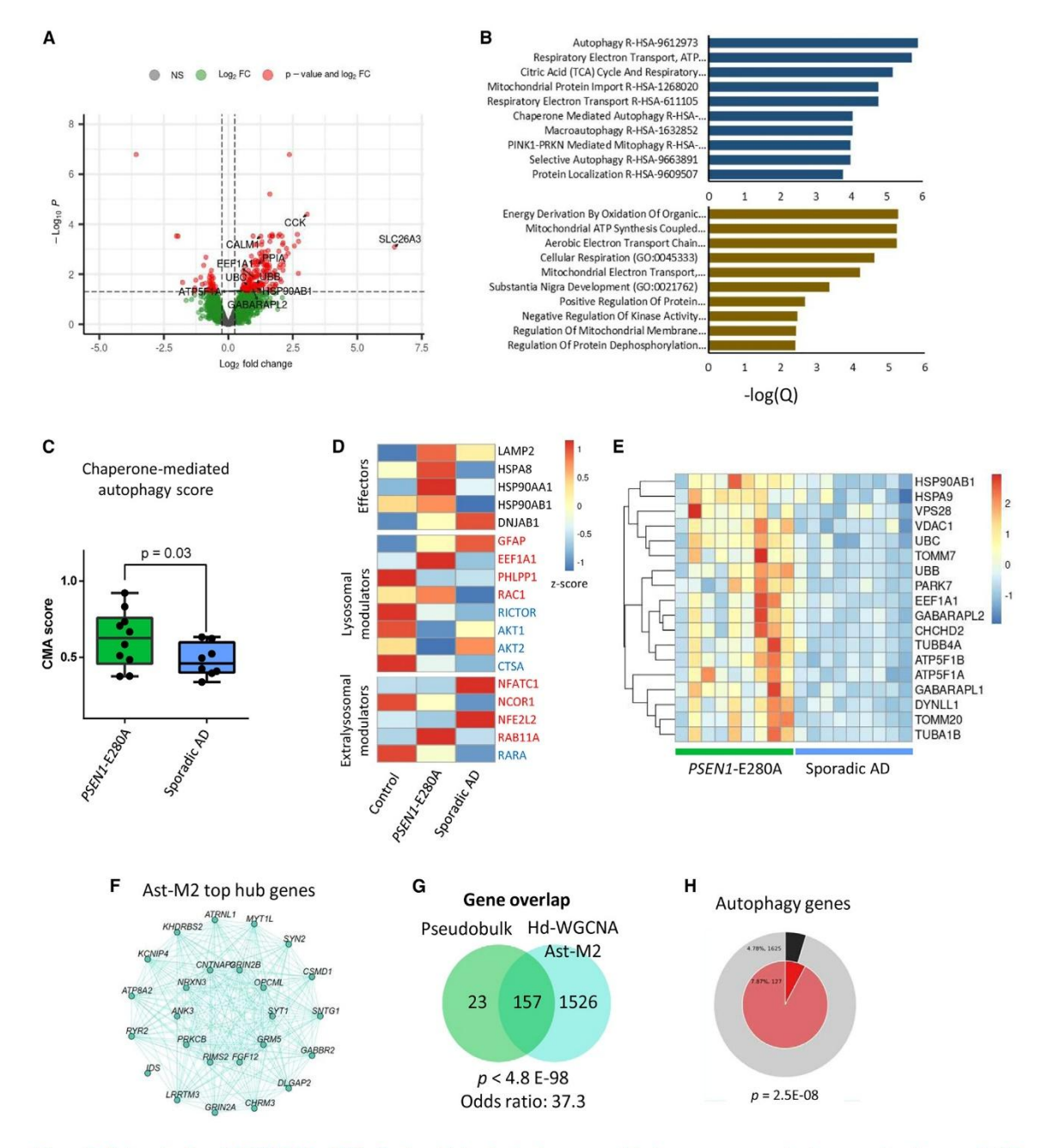
Cellular systems dysregulated in PSEN1-E280A AD astrocytes

Of 3,958 nuclei from diseased patients annotated as astrocytes (2,101 from *PSEN1*-E280A and 1,857 from sporadic AD), we assessed differential gene expression (DGE) within the total astrocytic population in *PSEN1*-E280A versus sporadic AD by aggregating the counts for a pseudobulk DGE analysis. ¹⁶ We identified 186 genes upregulated and 53 genes downregulated in *PSEN1*-E280A when compared to the sporadic AD cases (Figure 2A; Table S2).

Among the gene set enriched terms associated with the genes overexpressed in *PSEN1*-E280A, the top terms included

(E) UMAP of cells from control, *PSEN1*-E280A, and sporadic AD individuals colored by cell type annotation. Neur, neuronal; Inh, inhibitory neurons; OPCs, oligodendrocyte precursor cells; Oli, oligodendrocytes; Mic, microglia; Ast, astrocytes; Peri, pericytes; Endot, endothelial. (F) Violin plots showing the gene set score for the cell types identified in the dataset.

(G and H) Abundance of cell type per diagnosis (G) or individuals (H) from different diagnosis. The boxes represent the interquartile range, with the line inside indicating the median. Whiskers extend to the minimum and maximum values. The asterisk indicates significant difference (p_adjusted < 0.05). See also Figures S1–S3.



 $Figure \ 2. \ A strocytes from \textit{PSEN1}-280 A \ exhibit mitochondrial and autophagy-associated gene overexpression in comparison to sporadic AD \ and \ an autophagy-associated gene overexpression in comparison to sporadic AD \ and \ an autophagy-associated gene overexpression in comparison to sporadic AD \ and \ an autophagy-associated gene overexpression in comparison to sporadic AD \ and \ an autophagy-associated gene overexpression in comparison to sporadic AD \ and \ an autophagy-associated gene overexpression in comparison to sporadic AD \ and \ an autophagy-associated gene \ autophagy-a$

(A) Volcano plots showing up- and downregulated genes in PSEN1-E280A astrocytes compared to sporadic AD.

(B) Gene set enrichment annotation of differentially overexpressed genes in astrocytes. Bar graph representing annotation into two categories: Reactome (top) and GO biological processes (bottom).

(C) Scores for the chaperone-mediated autophagy (CMA) according to diagnosis. CMA scores for both *PSEN1*-E280A and sporadic AD are normalized by the CMA score for non-diseased individuals. The boxes represent the interquartile range, with the line inside indicating the median. Whiskers extend to the minimum and maximum values

(D) Heatmap and hierarchical clustering of the genes (rows) associated with autophagy overexpressed in PSEN1-E280A. Columns show individual cases.

(legend continued on next page)

Neuron 112, 1778-1794, June 5, 2024 1781





autophagy (which was accompanied by other related terms such as "macroautophagy," "mitophagy," and "chaperone-mediated autophagy" [CMA]) and respiratory electron transport-related terms (which included genes encoding for mitochondrial complexes I, III, IV, and V) (Figure 2B). Computing a CMA score 17 from the changes in the mRNA levels of components of the CMA network in astrocytes revealed a significantly higher score in PSEN1-E280A versus sporadic AD cases (Figures 2C and 2D). The overexpressed genes associated with autophagy in astrocytes from PSEN1-E280A included two heat shock genes (HSP90AB1 and HSPA9), the heat shock inducer EEF1A1, cytoskeleton-associated genes (DYNLL1, TUBA1B, and TUBA4A), the members of the ATG8 family (GABARAPL2 and GABAR-APL1), and the mitochondrial-associated genes (VDAC1, TOMM20, TOMM7, ATP5F1A, ATP5F1B, and CHCHD2). Interestingly, several genes associated with "regulation of protein modification process" were also overexpressed in PSEN1-E280A and include the molecular chaperone known to regulate protein isomerization at proline residues (PPIA) and ubiquitin B and C (UBB and UBC), suggesting that the transcriptional activation of protein degradation and autophagic responses in PSEN1-E280A cases qualitatively differs from that which occurs in sporadic AD (Figure 2E).

Next, we ran high-dimensional weighted gene co-expression analysis (hd-WGCNA), which groups together co-regulated genes as modules, in astrocytes from controls (916 nuclei), PSEN1-E280A, and sporadic AD. Among the ten modules identified, two modules (Ast-M1, green module; Ast-M2, turquoise module) were significantly upregulated in PSEN1-E280A compared to sporadic AD cases, while Ast-M8 (purple module) modules were significantly downregulated in PSEN1-E280A compared to sporadic AD cases by eigengene expression values (Wilcoxon rank-sum p value < 0.01, effect size > 0.3; Figures 2F and S4A-S4C; Table S3). A significant overlap between Ast-M2 genes and overexpressed DGEs found by pseudobulk analysis was found (p = 4.8E-98, odds ratio = 37.3; Table S3), with 157 out of the 180 DGEs identified by pseudobulk also presented in Ast-M2 (Figure 2G). Ast-M2 contained 127 genes that matched the membership term "autophagy" (p = 2.5E-08), which included 25 genes significantly overexpressed in PSEN1-E280A compared to sporadic AD (Figure 2H). These results were consistent with the DGE results described above and further support the observation that transcriptional activation of protein degradation and autophagy in PSEN1-E280A cases qualitatively differs from the sporadic AD profile.

Unique and shared transcriptional regulation in *PSEN1*-E280A and sporadic AD neurons

Nuclei assigned as neuronal (control: 7,233 control, *PSEN1*-E280A: 10,382, and sporadic AD: 5,447) clustered into 14 sub-populations (Neu-0 to Neu-13, Figures 3A and S5A), including ten clusters of excitatory neurons (78.2%) that shared the

expression of the pan-excitatory marker *SLC17A7* and four clusters of inhibitory neurons (21.8%) positive for the pan-inhibitory *GAD1* marker (Figure 3B). Among excitatory subtypes, we identified layers 2–3 (Neu-0 and Neu-2, expressing *CUX2/LAMP5* and *CUX2/COL5A2*, respectively), layers 4–5 *RORB* positive (*RORB/PCP4*, *RORB/IL1RAPL2*, *RORB/PLCH1/MME*, Neu-1, Neu-3, and Neu-9), layers 5–6 (*NFIA/THEMIS* and Neu-5), layer 6 (*TRPM3/SEMA5A*, *THEMIS/NTNG2/NR4A2*, Neu-6, and Neu-13), deeper layer 6b (*FEZF2/CTGF/SEMA3D* and Neu-10), and deep-layer glutamatergic neuron (Neu-12). Inhibitory nuclei consisted of *LHX6*-expressing neurons (Neu-7 and Neu-8) and were comprised of *PVALB* and *SST* subtypes, while the other inhibitory clusters were positive for *ADARB2* (Neu-4 and Neu-11) and included *VIP/CALB2* and *LAMP5/KIT* subclusters (Figures S5B and S5C; Table S4).

A significant reduction in the relative abundance of nuclei in the inhibitory subpopulation expressing SST (Neu-8) was observed for both PSEN1-E280A (p = 4.0E-2) and sporadic AD (p < 1.0E-3) individuals when compared to controls (Figure 3C). Inhibitory neurons expressing VIP/CALB2/PROX1 (Neu-4) were significantly reduced only in sporadic AD (p = 6.0E-3). Thus, the susceptibility of these interneuron subclass populations differs between PROX1 and SST clusters, with PSEN1-E280A cases limited in their inhibitory neuronal loss to the SST subpopulation. Both PSEN1-E280A and sporadic AD individuals showed a significant reduction in layer 4–5 RORB-positive excitatory neurons, as shown for sporadic AD. 19

In inhibitory neurons, DGE analysis revealed 494 genes overexpressed and 291 genes underexpressed in PSEN1-E280A compared to sporadic AD. In excitatory neurons, 1,452 genes were upregulated and 833 genes downregulated in PSEN1-E280A compared to sporadic AD (Figure 3D). To check whether neurons also exhibited an autophagy-related gene difference, as seen in astrocytes, we calculated the CMA score. The CMA score was significantly higher in PSEN1-E280A when compared to sporadic AD for both excitatory (p = 4.4E-2) and inhibitory (p =2.9E-2; Figures 3E and 3F) neurons. Gene set enrichment analysis on the genes overexpressed in both inhibitory and excitatory neurons from PSEN1-E280A revealed several molecular chaperones potentially involved with protein folding and degradation, autophagy, and cellular respiration (Figure 3G; Table S2). Widespread changes of genes encoding the mitochondrial electron transport chain components were recently reported in brains from sporadic AD patients.20 The upregulation of MT3 is also of interest. MT3 can control lysosomal pH by moving zinc to lysosomes and can control the expression levels of the lysosomal membrane proteins LAMP1/2 by glycosylation, thus balancing the lysosomal biogenesis, making autophagy possible under various stress situations and inducing a smooth fusion of autophagosomes and lysosomes.2

Hd-WGCNA was performed in excitatory neurons. One module (Exc-M2, turquoise) out of the five modules found was significantly

⁽E) Network plot showing the top 25 hub genes associated with module Ast-M2 identified by hd-WGCNA.

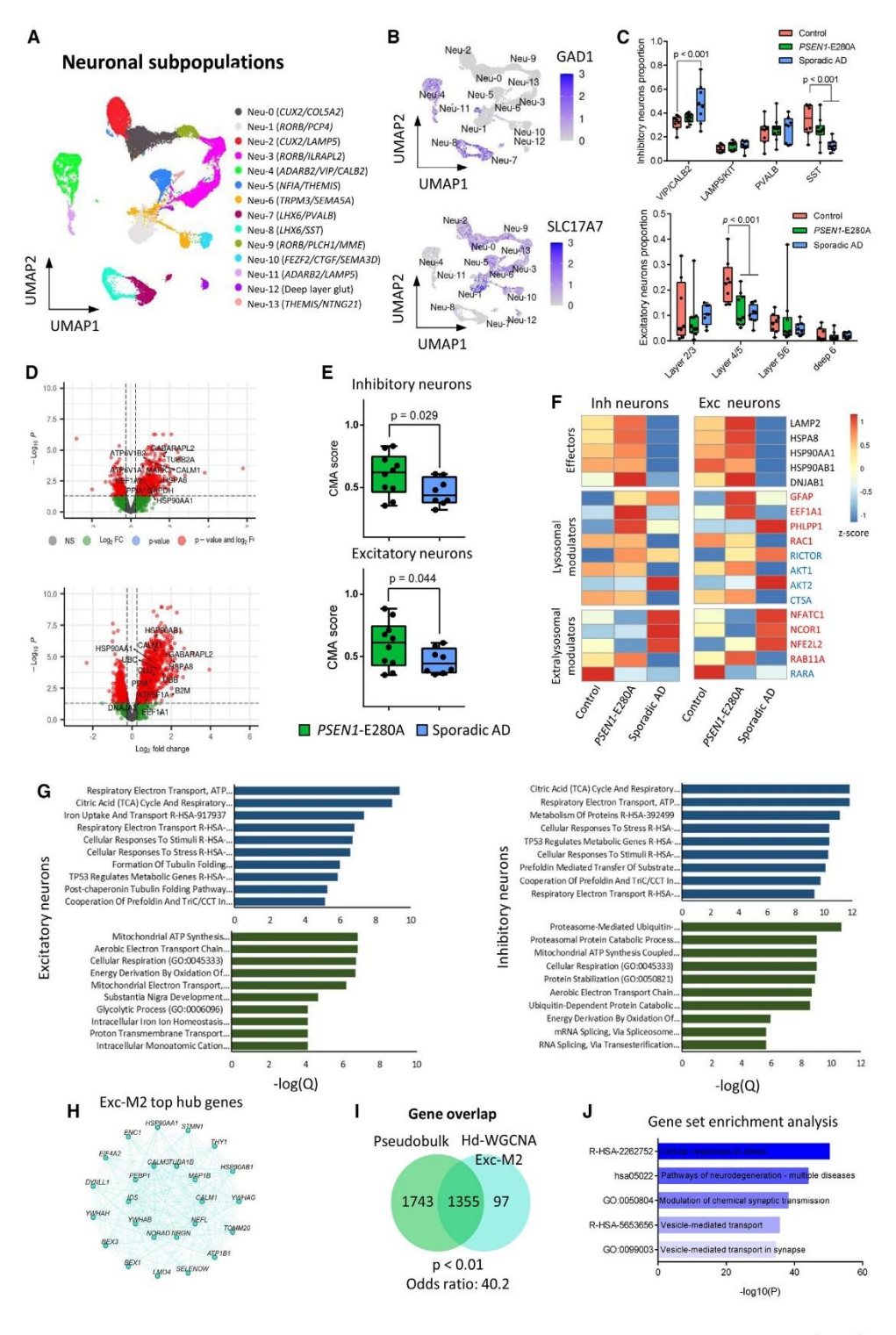
⁽F) Overlap of genes differentially expressed revealed by pseudobulk analysis and genes in Ast-M2 module revealed by hd-WGCNA.

⁽G) Enrichment of genes matching membership term: autophagy. The outer pie shows the number and the percentage of genes in the background that are associated with the membership (in black); the inner pie shows the number and the percentage of genes in the individual input gene list that are associated with the membership. The p value indicates whether the membership is statistically significantly enriched in the list.

See also Figures S2 and S4.







(legend on next page)

Neuron 112, 1778-1794, June 5, 2024 1783





upregulated in *PSEN1*-E280A compared to sporadic AD cases by eigengene expression values (Figures S4D–S4F). The genes in module Exc-M2 significantly overlapped with upregulated DGEs in *PSEN1*-E280A identified by pseudobulk (Figures 3H–3J), further confirming the findings.

To further characterize transcriptional changes in NFTbearing gray matter, we performed spatial transcriptomics on postmortem samples from hippocampus and frontal pole of two PSEN1-E280A carriers and one control (Figure 4A). Immunostaining of adjacent slices showed positive labeling for AT8 (which may stain multiple forms of TAU pathology, including neuritic plaque-associated TAU in dystrophic axons and neuropil threads) and Aβ plagues (Figure S6A). A total of 13.538 capture spots remained after quality-control filtering, 7,540 from PSEN1-E280A and 5,998 from control. Spots from the same sample were clustered at a low resolution (res = 0.1) for all five samples individually, yielding two clusters that corresponded to white and gray matter in every sample (Figures 4B, 4C, S6B, and S6C). All spots were integrated and jointly clustered (res = 0.1). Integrated cluster identities corresponded with the gray (n = 5,945) and white (n = 6,435)matter spot sample-level assignments (Figures 4D-4G). 1,158 spots were not assigned to white or gray matter. Those spots contained low expressed neuronal and oligodendrocyte markers that could not be assigned to a distinct cluster (Figure 4F). Clustering did not separate spots by brain region or diagnosis (Figures 4E and S6D).

Using a generalized linear mixed model (GLMM) to compare PSEN1-E280A and control, we identified 2,083 gray matter and 1,071 white matter significant differentially expressed genes (DEGs) (Figures 5H and 5I; Table S5). There was a significant overlap of 306 genes that were differentially expressed in both gray and white matter (Fisher's exact test p = 4.7E-2; Table S5), The significant Gene Ontology (GO) terms for genes upregulated in PSEN1-E280A white matter compared to control included "signaling by Rho GTPases, Miro GTPases and RHOBTB3" and "pathways of neurodegeneration." For genes downregulated in PSEN1-E280A white matter compared to control, "membrane lipid metabolic process" and "amyloid precursor protein metabolic process" were among the top significant GO terms. For gray matter, "signaling by Rho GTPases, Miro GTPases and RHOBTB3" and "regulation of cellular response to stress" were also upregulated in PSEN1-E280A.

Given that all *PSEN1*-E280A patients were AT8⁺ in our immunohistochemical analysis, NFTs are likely abundant throughout their gray matter. As such, of the 227 synaptic genes that Otero-Garcia et al.²² identified as differentially expressed in AT8⁺ excitatory neuron clusters, 58 were also dysregulated in *PSEN1*-E280A gray matter. We performed a gene set enrichment analysis (GSEA) by ranking genes significantly differentially expressed in *PSEN1*-E280A patients' gray matter compared to controls by their z value. This ranked list of 2,083 genes was significantly enriched for the 227 synaptic genes (normalized enrichment score = -1.96, p = 3.5E-4). The negative value meant that the NFT genes were located among the gray matter DEGs with low z values (Figure S6E).

Oligodendrocyte transcriptomic signatures do not differ between *PSEN1*-E280A and sporadic AD

18,009 nuclei were annotated as oligodendrocytes. Pseudobulk analysis revealed only six genes significantly overexpressed and three genes underexpressed in the comparison between *PSEN1*-E280A and sporadic AD cases (Table S2). Hd-WGCNA in oligodendrocytes revealed seven distinct modules of co-regulated genes (Figure S7A), but no module presented eigengene expression values that were significantly different between *PSEN1*-E280A and sporadic AD cases (Wilcoxon rank-sum p value < 0.01, effect size > 0.3; Figures S7B and S7C).

A more pronounced human Alzheimer microglia profile in sporadic AD patients compared to *PSEN1*-E280A AD

We annotated 2,663 nuclei as microglia. A direct comparison of PSEN1-E280A with sporadic cases in microglia did not yield a significant number of DEGs to conclude that specific biological pathways distinguish these conditions (Table S2). Nevertheless. using the gene set associated with a human AD microglia (HAM) profile previously published, 23 we calculated a HAM score (see STAR Methods) and found that compared to controls, the set of upregulated HAM genes was only modestly increased in PSEN1-E280A (p = 4.5E-2), but significantly enhanced in sporadic AD cases (p < 1E-4). The HAM score was also significantly higher in sporadic AD cases when directly compared to PSEN1-E280A (p = 3.1E-3) (Figures S7D and S7E), while differences among downregulated HAM genes were minimal. These results quantitatively distinguish PSEN1-E280A microglial transcriptomes from those of sporadic AD cases.

Figure 3. Excitatory neuronal loss is detected in both PSEN1-E280A and sporadic AD

- (A) UMAP plot of neuronal nuclei colored by neuronal subpopulation and split by diagnosis.
- (B) UMAP plot colored by the levels of expression of the pan-excitatory and -inhibitory markers SLC17A7 and GAD1.
- (C) Subpopulations' proportion of excitatory and inhibitory neurons across controls, PSEN1-E280A, and sporadic AD. The boxes represent the interquartile range, with the line inside indicating the median. Whiskers extend to the minimum and maximum values.
- (D) Volcano plots showing up- and downregulated genes in PSEN1-E280A excitatory and inhibitory neurons compared to sporadic AD.
- (E) Scores for the chaperone-mediated autophagy (CMA) according to diagnosis in excitatory and inhibitory neurons. CMA scores for both PSEN1-E280A and sporadic AD are normalized by the CMA score for non-diseased individuals. The boxes represent the interquartile range, with the line inside indicating the median. Whiskers extend to the minimum and maximum values.
- (F) Gene set enrichment annotation of differentially overexpressed genes in excitatory and inhibitory neurons. Bar graph representing annotation into two categories: Reactome (top) and GO biological processes (bottom).
- (G) Network plot showing the top 25 hub genes associated with module Ast-M2 identified by hd-WGCNA.
- (H) Overlap of genes differentially expressed revealed by pseudobulk analysis and genes in Exc-M2 module revealed by hd-WGCNA.
- (I) Gene set enrichment annotation of genes within hd-WGCNA module Exc-M2. Bar graph represents annotation into Reactome, Kegg pathway, and GO biological processes ranked by p value.

See also Figures S2-S5.

1784 Neuron 112, 1778-1794, June 5, 2024

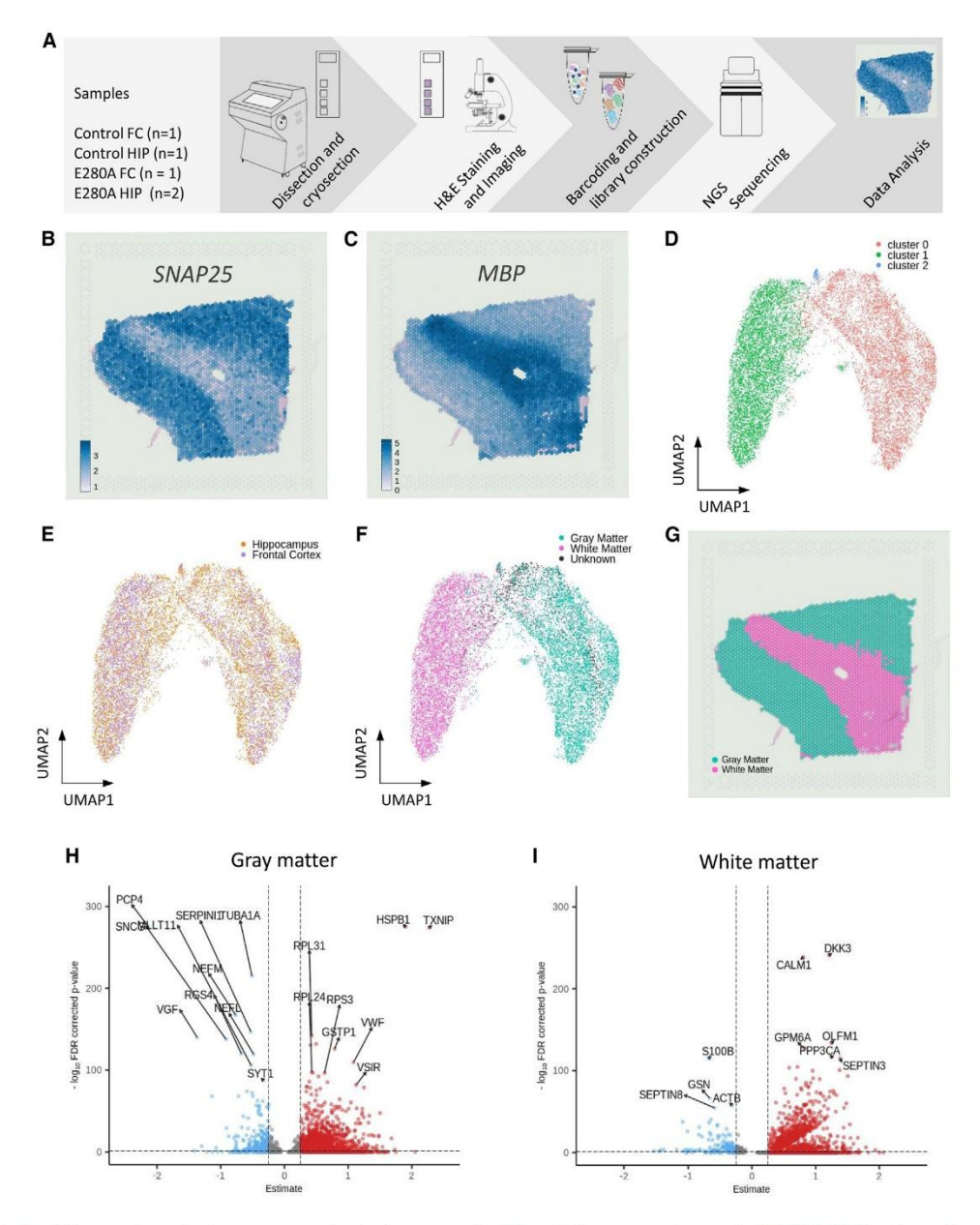


Figure 4. Spatial transcriptomics in postmortem brain tissue reveals differentially expressed genes in *PSEN1*-E280A patients that are specific to white and gray matter regions

(A) Spatial transcriptomics overview.

(B and C) Expression of neuron (SNAP25; B) and oligodendrocyte (MBP; C) markers delineates gray and white matter in frontal cortex.

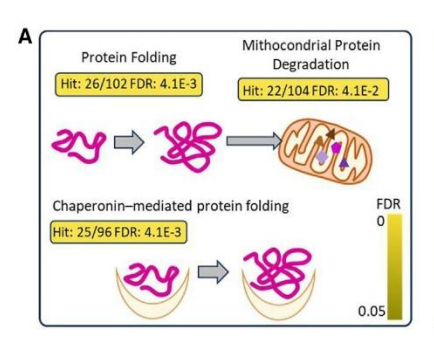
(D-F) UMAP of spots from PSEN1-E280A and control individuals colored by cluster identity (D), brain region (E), and white/gray matter (F).

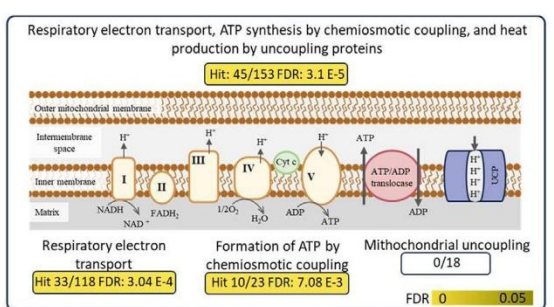
(G) Spots colored by white/gray matter on frontal cortex sample.

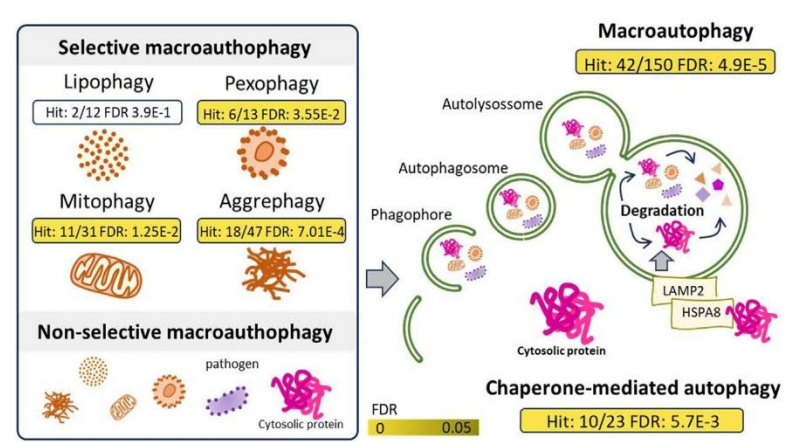
(H and I) Volcano plots for genes differentially expressed in E280A patients as compared to controls (H) in gray matter (H) and white matter (I). See also Figure S6.











Cell type	pathway	padj	log2err	ES	NES	size
Astrocytes	Abetaset	0.091	0.322	0.397	1.449	33
Excitatory	Abetaset	0.005	0.432	0.483	1.825	34
Inhibitory	Abetaset	0.005	0.432	0.483	1.825	34
Oligodendrocytes	Abetaset	0.009	0.407	0.459	1.846	27
Microglia	Abetaset	0.011	0.407	0.464	1.836	25
Astrocytes	NFTset	0.070	0.557	0.371	1.772	141
Excitatory	NFTset	0.194	0.175	0.228	1.217	197
Inhibitory	NFTset	0.134	0.185	0.284	1.280	187
Oligodendrocytes	NFTset	0.089	0.231	0.245	1.423	145
Microglia	NFTset	0.087	0.234	0.241	1.421	138

Figure 5. Mechanistic insight into sets of differentially expressed genes in PSEN1-E280A compared to sporadic AD

(A) Schematics showing the results of the hypergeometric distribution test showing top Reactome pathways overrepresented in the overexpressed DEGs in PSEN1-E280A versus sporadic AD astrocytes, excitatory neurons, and inhibitory neurons.

(B) Table displaying results from gene set enrichment analysis; the rows represent gene sets and the columns provide information about enrichment results. Gene sets represent Aβ production and secretion genes (Abetaset) and NFT-associated genes (NFTset). The statistics represent the results from the DEGs in *PSEN1*-E280A compared to sporadic AD by their z value. ES, enrichment score; NES, normalized enrichment score.

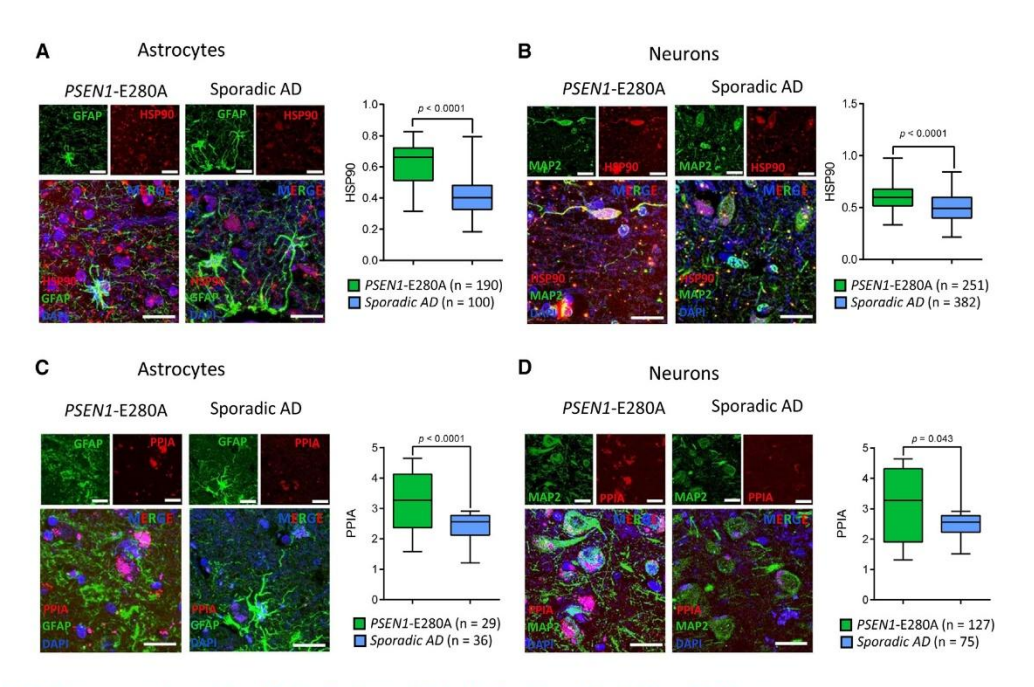


Figure 6. Protein expression profile validates the transcriptional alterations detected by snRNA- seq

- (A) Representative immunofluorescence micrographs of frontal cortex GFAP and HSP90 labeling from *PSEN1*-E280A and sporadic AD cases, as well as quantification of HSP90 expression in astrocytes.
- (B) Representative immunofluorescence micrographs of frontal cortex MAP2 and HSP90 labeling from PSEN1-E280A and sporadic AD cases, as well as quantification of HSP90 expression in neurons.
- (C) Representative immunofluorescence micrographs of frontal cortex GFAP and PPIA labeling from PSEN1-E280A and sporadic AD cases, as well as quantification of PPIA expression in astrocytes.
- (D) Representative immunofluorescence micrographs of frontal cortex MAP2 and PPIA labeling from *PSEN1*-E280A and sporadic AD cases, as well as quantification of PPIA expression in astrocytes.

Scale bars, $20 \, \mu m$. n represents the number of cells analyzed in each group. The boxes represent the interquartile range, with the line inside indicating the median. Whiskers extend to the minimum and maximum values.

The PSEN1-E280A mutation affects A β -associated pathways but not TAU

To provide mechanistic insight into sets of DEGs in PSEN1-E280A compared to sporadic AD across cell types, we performed pathway enrichment analysis in Reactome²⁴ on overexpressed genes in astrocytes and excitatory and inhibitory neurons. The top significantly enriched pathways identified were related to protein folding, respiratory electron transport, and autophagy (Table S6; Figure 5A). In another analysis, we used a curated set of 45 genes associated with Aβ production 18 that are known to regulate Aß production and secretion across various cell types. Using the ranked DEGs (PSEN1-E280A versus sporadic AD) according to their z values, we observed enrichment for these Aβ-associated genes in four of the five cell types analyzedexcitatory neurons, inhibitory neurons, oligodendrocytes, and microglia; in astrocytes, the enrichment did not reach statistical significance (p = 9.1E-2, Figure 5B). This distinctive pattern of Aβ-associated gene enrichment across multiple cell types relative to sporadic AD suggests a homeostatic response to APP degradation intended to maintain levels of APP and in contrast to sporadic AD in which AB accumulation is driven not by increased production but instead by failure of resorption.²⁵ Interestingly, a similar GSEA analysis of NFT-associated gene enrichment²² with a ranked list of genes in neurons did not result in significant enrichment when comparing genes differentially expressed in *PSEN1*-E280A to those in sporadic AD (Figure 5B). This result provides a sanity check for the well-known relationship between the *PSEN*-related pathway and amyloidogenesis.

Protein expression validation of snRNA-seq

We validated the results in postmortem formalin-fixed paraffinized brain tissue slices from PSEN1-E280A and sporadic AD cases. We selected HSP90 (Figures 6A and 6B) and PPIA (Figures 6C and 6D) because of their relative higher expression and specificity and performed a cell-wise co-localization analysis in neurons and astrocytes. Both HSP90 and PPIA expression were significantly increased in astrocytes (p < 1.0E-4 for both) and neurons (p < 1.0E-4 for HSP90 and p = 4.3E-2 for PPIA) from PSEN1-E280A compared to sporadic AD.

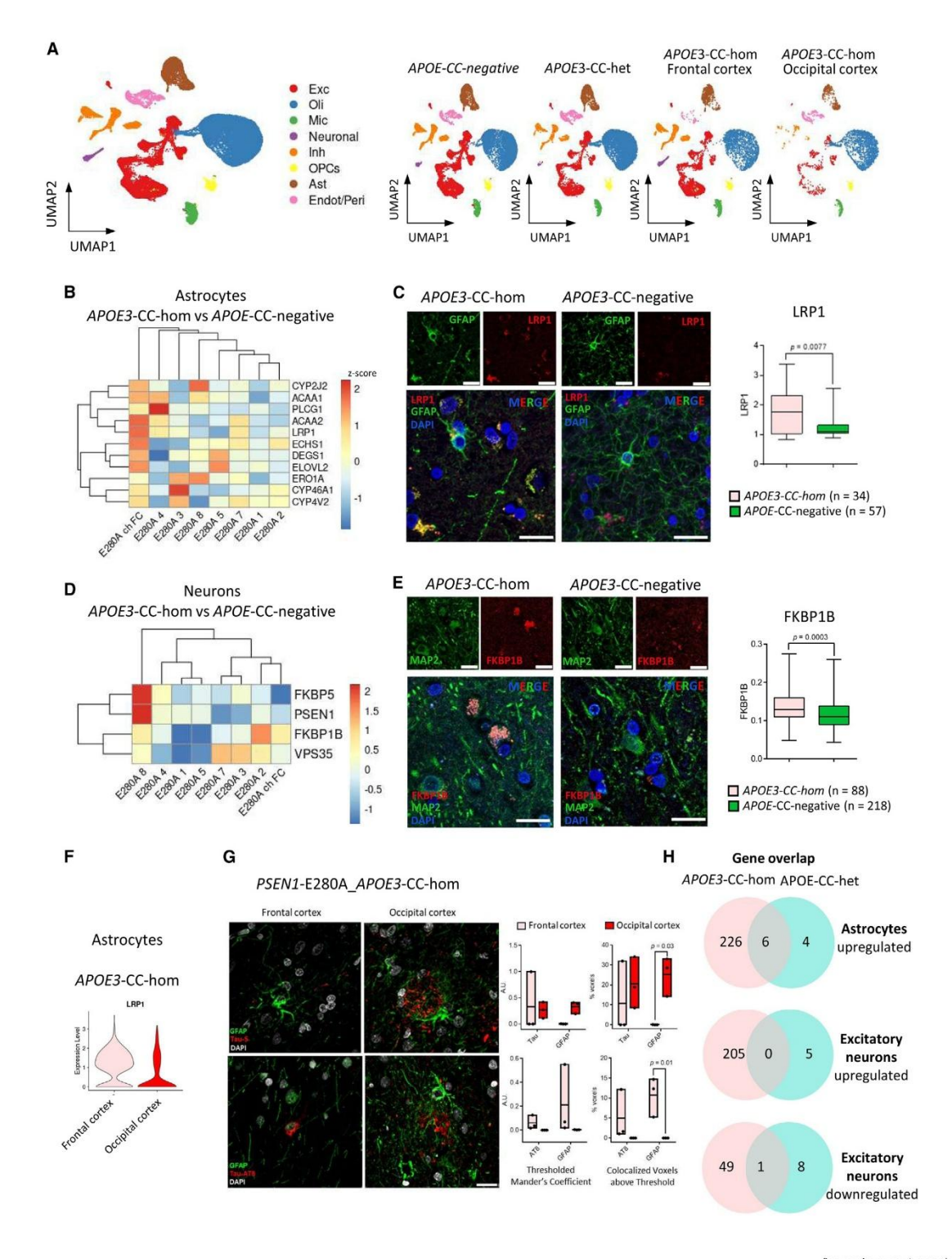
A protective profile of *PSEN1*-E280A_*APOE3*Christchurch

In the large PSEN1-E280A kindred a single individual, homozygous for the Christchurch variant on an APOE3 background

Neuron 112, 1778-1794, June 5, 2024 1787







(legend on next page)

Neuron Article



(NM_000041:c.460C>A Arg154Ser, rs121918393) was found to be relatively spared of dementia well into her 70s. 26 She showed minimal NFT pathology in the expected distribution²⁷; specifically, her NFT pathology was mostly and atypically restricted to the occipital cortex while the frontal cortex was spared. The protective effect of APOE3-R154S was recently confirmed in two independent animal studies.^{28,29} We sought to detect DGE associated with APOE3-R154S homozygosity. Given the inherent limitations of data from a single individual, albeit the only known individual in the world with this genotypic/phenotypic presentation, we conducted multiple types of analyses: (1) a comparison of frontal cortex from PSEN1-E280A_APOE3-CC-hom to all seven PSEN1-E280A carriers that do not have the Christchurch variant (PSEN1-E280A A-POE3-CC-negative) using a GLMM to estimate the fixed effect of the homozygous genotype while accounting for pseudo-replication bias with a random effect for patient30; (2) a comparison of the relatively spared frontal cortex to the heavily affected occipital cortex in PSEN1-E280A_APOE3-CC-hom; (3) a comparison of all seven PSEN1-E280A_APOE3-CC-negative to the three PSEN1-E280A_APOE3-CC-het using a GLMM; although a larger sample of the heterozygotes has recently revealed a modest delay in age at onset (under review), this subset of patients was not delayed in their age at onset (Table S1), and therefore, we hypothesized that they would not show the DGE profile observed in PSEN1-E280A_APOE3-CC-hom; and (4) immunohistochemical validation of the gene expression differences in PSEN1-E280A_APOE3-

To undertake these analyses, we integrated our dataset with snRNA-seq from the frontal and occipital cortices of this patient who was homozygous for the *APOE3*-Christchurch variant (*PSEN1*-E280A_*APOE3*-CC-hom) (Figure 7A). A total of 11,190 nuclei, with 8,247 nuclei from the frontal cortex and 3,043 nuclei from the occipital cortex, were integrated into our dataset. All seven major cell types identified in our dataset, i.e., inhibitory neurons, excitatory neurons, astrocytes, microglia, oligodendrocytes, OPCs, endothelial cells, and pericytes, were also identified in both frontal and occipital cortices of the *PSEN1*-E280A_*A-POE3*-CC-hom individual (Figure 7A).

A comparison of PSEN1-E280A_APOE3-CC-hom to all seven carriers of PSEN1-E280A without the Christchurch variant (PSEN1-E280A_APOE3-CC-negative) (Table S7) revealed 232 genes in astrocytes that were significantly upregulated and 60 genes downregulated. Consistent with a role for APOE3 Christchurch in lipid metabolism,31 astrocytic genes involved in cholesterol and lipid synthesis (CYP46A1, CYP2J2, CYP4V2, DEGS1, ACAA1, and PLCG1) and metabolism (ACAA1, ACAA2, ECHS1, and ELOVL2) (Figure 7B) increased their expression. For example, CYP46A1 regulates the conversion of cholesterol to 24S-hydroxycholesterol, which controls cholesterol efflux from the brain and thereby plays a major role in regulating brain cholesterol homeostasis. In mouse, decreased expression of the Cyp46a1 gene increased the amounts of cholesterol in neurons, leading to apoptotic death of neurons and thereby cognitive impairments.³² Oxidoreductase-activity-related genes (ERO1A, CYP2J2, DEGS1, CYP46A1, and CYP4V2) were also overexpressed in astrocytes from PSEN1-E280A_APOE3-CC-hom and may serve as possible protective mechanisms to cope with the increased oxidative stress in neurons resulting from the PSEN1-E280A variant.33 Notably, in astrocytes from PSEN1-E280A_APOE3-CC-hom, lipoprotein receptor-related protein 1 (LRP1) was also upregulated (estimate = 0.5, p_adjusted = 4.1E-2, Figure 7B). To validate this result, we performed immunofluorescence labeling of LRP1, which revealed significantly higher expression of LRP1 in astrocytes from PSEN1-E280A A-POE3-CC-hom compared to PSEN1-E280A_APOE3-CC-negative (Figure 7C).

The transcriptional profiles of neurons provided additional possible mechanisms of PSEN1-E280A_APOE3-CC-hom protection (Figure 7D). Vacuolar sorting protein 35 (VPS35), a key component of the retromer that, when dysfunctional, is a risk factor for AD, ³⁴ was upregulated in PSEN1-E280A_APOE3-CC-hom compared to PSEN1-E280A_APOE3-CC-negative (estimate = 0.25 ± 0.03 , p_adjusted = 1.2E-11). Furthermore, excitatory neurons in PSEN1-E280A_APOE3-CC-hom showed significant downregulation of PSEN1 (estimate = -0.19 ± 0.04 , p_adjusted = 1.9E-4) and FKBP5 (estimate = -0.88 ± 0.22 , p_adjusted =

Figure 7. A protective profile in NFT-free frontal cortex of a PSEN1-E280A_APOE3-Christchurch homozygous carrier

(A) UMAP of dataset integrated with data obtained from snRNA-seq of frontal cortex and occipital cortex of a patient carrier of *PSEN1*-E280A, who was also homozygous for the APOE3 Christchurch (*PSEN1*-E280A_APOE3-CC-hom). Left UMAP shows cells from all patients, and right plots show the projection of nuclei split by *PSEN1*-E280A carriers negative for the APOE3-Christchurch variant (*PSEN1*-E280A_APOE3-CC-hom) and by *PSEN1*-E280A carrier heterozygotes for the APOE3-Christchurch variant (*PSEN1*-E280A_APOE3-CC-het).

(B) Heatmap showing the Z score for the levels of expression of selected genes upregulated in astrocytes from PSEN1-E280A_APOE3-CC-hom compared to PSEN1-E280A_APOE-CC-negative.

(C) Representative immunofluorescence micrographs of frontal cortex GFAP and LRP1 labeling from PSEN1-E280A_APOE-CC-hom and PSEN1-E280A_APOE-CC-negative cases, as well as quantification of LRP1 expression in astrocytes. Scale bar, 20

µm. n represents the number of cells analyzed in each group. The boxes represent the interquartile range, with the line inside indicating the median. Whiskers extend to the minimum and maximum values.

(D) Heatmap showing the Z score for the levels of expression of selected genes upregulated in excitatory neurons from PSEN1-E280A_APOE3-CC-hom compared to PSEN1-E280A_APOE-CC-negative.

(E) Representative immunofluorescence micrographs of frontal cortex MAP2 and FKBP1 labeling from *PSEN1*-E280A_*APOE*-CC-hom and *PSEN1*-E280A_*APOE*-CC-negative cases, as well as quantification of FKBP1 expression in astrocytes. Scale bar, 20 µm. n represents the number of cells analyzed in each group. (F) Violin plots showing levels of expression of *LRP1* in astrocytes from *APOE3*-CC_hom frontal cortex and occipital cortex samples.

(G) Representative immunofluorescence micrographs of frontal and occipital cortex of PSEN1-E280A_APOE3-CC-hom, and quantification represented by boxplots showing levels of colocalization of Tau-5 (top) or pathological TAU (AT8, bottom) with GFAP. Volume of GFAP colocalizing with thresholded Tau-5-positive signal is higher in occipital than in frontal cortex, while GFAP colocalizing with thresholded AT8-positive signal is significantly smaller in occipital than in frontal cortex of PSEN1-E280A_APOE3-CC-hom. Data from the analysis of three slices/brain regions from the patient PSEN1-E280A_APOE3-CC-hom. The boxplots represent minimum and maximum values, while lines in the centers represent the median.

(H) Venn diagrams showing the overlap of significant genes differentially expressed when comparing either PSEN1-E280A_APOE3-CC-hom or PSEN1-E280A_APOE3-CC-het with PSEN1-E280A carriers negative for the APOE3-Christchurch variant.





3.9E-3) and upregulation of *FKBP1B* (estimate = 0.60 ± 0.07 , p_adjusted = 2.0E-16) compared to *PSEN1*-E280A_*APOE3*-CC-negative excitatory neurons. Increased expression of FKBP1B, a peptidyl-prolyl *cis-trans* isomerase and member of the FK506-binding protein family, has an ameliorative effect on TAU inclusions, $^{35-37}$ while age-associated FKBP51 increase (encoded by *FKBP5*) and its engagement with HSP90 have been described to promote accumulation of neurotoxic TAU. 38 To confirm the transcriptional result described above, we verified protein expression levels of FKBP1B by immunofluorescence, with significantly higher levels in *PSEN1*-E280A_*APOE3*-CC-hom neurons than the *PSEN1*-E280A_*APOE3*-CC-negative neurons (Figure 7E), which may contribute to the *PSEN1*-E280A_*APOE3*-CC-hom individual's TAU pathology resistance.

In a comparison of astrocytes from the spared frontal cortex to the intensely affected occipital cortex in PSEN1-E280A_APOE3-CC-hom, we observed overlapping genes also expressed in the comparison with all seven PSEN1-E280A cases that lack any Christchurch allele. These genes included ones involved in fatty acid metabolism (ACAA2, ECHS1, ELOVL2, and ACAA1) and in oxidoreductase activity (CYP2J2 and CYP46A1) (Table S7). In neurons, the upregulation of FKBP1B (log2FC = 0.4, p_adjusted = 2.6E-24) and the downregulation of FKBP5 (log2FC = -1.4, p_adjusted = 5.9E-11) were replicated in the frontal cortex TAU-sparing region. We again found LRP1 upregulated in frontal cortex (log2FC = -0.55, p_adjusted = 3.1E-15) (Figure 7F; Table S7). Because LRP1 mediates TAU uptake and is involved in TAU spread in neurons, 39 we hypothesized that neuronal TAU spread might be prevented by its uptake in astrocytes. Thus, we performed immunofluorescence staining of either TAU (Tau-5) or pathological TAU (AT-8) and quantified its levels in astrocytes in samples from both frontal cortex and occipital cortex from PSEN1-E280A_APOE3-CC-hom case (Figure 7G). While levels of co-localization of Tau-5 with GFAP are lower in samples from frontal than occipital cortex, pathological TAU, as stained by AT8, presents higher levels of co-localization in astrocytes from frontal than occipital cortex (Figure 7G), further suggesting that pathological TAU spread might be prevented by its uptake in astrocytes.

Finally, to check whether heterozygosity for APOE3-Christchurch variant is sufficient to activate a protective transcriptomic profile, as observed by homozygosity, we compared three PSEN1-E280A_APOE3-CC-hets to all seven carriers of PSEN1-E280A without the Christchurch variant (PSEN1-E280A_APOE3-CC-negative) (Figure 7H; Table S7). This subset of PSEN1-E280A_APOE3-CC-hets did not have delayed onset (Table S1); therefore, we expected their profiles to resemble those cases without either Christchurch allele. In astrocytes, only 10 and 45 genes in PSEN1-E280A APOE3-CC-het compared to PSEN1-E280A_APOE3-CC-negative patients, respectively, were significantly differentially overexpressed or underexpressed (Figure 7H; Table S7). None of these DEGs included any of the cholesterol and lipid synthesis genes of the oxidoreductase-activity-related genes, which suggests that this astrocyte profile seen in the PSEN1-E280A APOE3-CC-hom was not shared by the three PSEN1-E280A_APOE3-CC-het cases. Furthermore, LRP1 was not significantly upregulated in the PSEN1-E280A APOE3-CChet astrocytes compared to PSEN1-E280A_APOE3-CC-negative. In neurons, the *PSEN1*-E280A_*APOE3*-CC-hom profile was also not observed in the *PSEN1*-E280A_*APOE3*-CC-het patients. In the excitatory neurons of the *PSEN1*-E280A_*APOE3*-CC-het patients, *PSEN1* and *FKBP5* were not downregulated, and the genes *FKBP1B* and *VPS35*, which are protective when upregulated, were not upregulated compared to *PSEN1*-E280A cases without a Christchurch allele. Overall, the absence of a shared transcriptomic profile in astrocytes for DEGs in *PSEN1*-E280A_*APOE3*-CC-hom likely indicates that heterozygotes without delayed disease onset do not activate the protective network seen in *PSEN1*-E280A_*APOE3*-CC-hom astrocytes.

DISCUSSION

Unraveling the distinct mechanisms by which ADAD and sporadic AD lead to convergent phenotypes is a broadly relevant question, especially with regard to clinical trials that attempt to extrapolate treatment-efficacy conclusions across distinct AD etiologies. In this study, we have studied multiple cases of the same ADAD mutation and therefore limited variation related to the mutation. PSEN1 mutations other than PSEN1-E280A may not show this same pattern. The exceptionally large PSEN1-E280A kindred and their generosity toward brain donation made it possible to obtain these data. 5 Some PSEN1 mutations, even those in the same protein domain such as PSEN1 (NM_000021:c.851C>T p.Pro284Leu) (rs63750863), present with spastic paraparesis along with cognitive decline and with cotton wool $A\beta$ plaques $^{40-42}$ that may induce a distinct transcriptional profile. We recognize that variation remains among the sporadic AD cases.

What most distinguishes this cohort of identical PSEN1 mutations from sporadic AD is the increased expression of autophagy genes and chaperones. Considering the complexity of presenilin folding, the PSEN1-E280A mutation may trigger a host of celltype-specific homeostatic corrective measures that include multiple chaperones and related folding catalysts required to position and shape an active y-secretase catalytic complex. Full-length presenilins undergo endoproteolysis but remain physically associated as a high-molecular-weight, stable complex in which the two catalytically essential aspartates in separate fragments must come into proximity⁴³ to form a catalytically active γ -secretase complex with the additional proteins nicastrin (NCT), anterior-pharynx defective-1 (APH1), and presenilinenhancer-2 (PEN2).44,45 The active site lies at the interface between the two presenilin subunits, and the active site conformation is altered by AD-causing *PSEN1* mutations, 45 possibly necessitating additional chaperone mitigation.

From these data, we can infer that sporadic AD and ADAD caused by the *PSEN1*-E280A variant have distinct molecular signatures largely defined by cell-type-specific increases in chaperone/autophagy gene expression. Spatial transcriptomics and immunofluorescence in tissue further validated the activation of chaperone-mediated autophagy genes in *PSEN1*-E280A compared to controls. While proteostatic networks have been noted to contribute to disease progression, ^{46,47} the *PSEN1*-E280A mutation further activates this pathway in a qualitatively and cell-type-specific manner.

Neuron Article



The very large family also made it possible to spot the highly improbable individual who carried not only the rare PSEN1-E280A variant but also two copies of a second rare variant. APOE3 Christchurch. The snRNA-seq results suggest a mechanism that might explain the most striking feature of this individual, a relative paucity of NFT pathology. The expected spread of TAU inclusions in a pattern described by Braak et al.48 did not occur in this patient. Therefore, it was remarkable that LRP1, which mediates TAU spread, was increased in astrocytes from the PSEN1-E280A_APOE3-CC-hom in the frontal cortex, but not in the occipital cortex, which carried a heavy NFT burden. This observation raises the surprising possibility that TAU uptake in astrocytes can prevent TAU spread possibly in combination with protein degradation machinery that is made selectively available in the astrocytes. The known association of APOE with LRP1 49,50 might induce upregulation of LRP1 when APOE3 Christchurch is present in the homozygous condition. Other possible protective mechanisms that might explain the paucity of NFT in PSEN1-E280A_APOE3-CC-hom occur in excitatory neurons, among them upregulation of the TAU peptidyl-prolyl cis-trans isomerase FKBP1B and downregulation of FKBP5, which could reduce the pathogenicity of TAU.

E280A is one of 13 different PSEN1 mutations that have been reported in the Colombian population.⁵¹ We have previously speculated that the apparent high prevalence of PSEN1 mutations became fixed in the population because of positive selection from infectious diseases during the conquest and colonial period.⁵¹ The increased production of Aβ that occurs in carriers of PSEN1 mutations could function as an anti-microbial. Upregulation of SOD1 and PRDX3 in the PSEN1-E280A cases may also be related to their action as peptide anti-microbials, and similarly, the upregulation of SERF2, along with ITM2B, can enhance Aβ aggregation.⁵² Astrocytes from PSEN1-E280A carriers overexpress genes implicated in the immune response to bacterial pathogens, such as CALM1, CALM3, CLTA, DNM1, and YWHAH, as well genes potentially involved with T cell activation (PAK3 and PRKCB). In the same vein, genes known to regulate inflammatory responses to viral infection, such as PARP1 and AKT1, and VPS4A, VPS28, CHMP5, CHMP3, and CHMP4B, all of which are part of the ESCRT pathway, which may contribute to cellular response to viral infection, are upregulated in PSEN1-E280A excitatory neurons, suggesting a unique immunophenotype in these individuals that may influence their susceptibility or response to AD pathology (Table S7).

Many studies have implicated TAU in the APOE network. 53–55 Most compelling regarding this link is the case from Colombia with the Christchurch variant of *APOE3* and two follow-up studies in animal models that support the protective effects of this variant. 28,29 However, the mechanism for the protection is unknown. We suggest a broad-based protection affecting several pathways and several cell types. For example, heparan sulfate proteoglycan (HSPG) has been proposed to facilitate the aggregation of Aβ and the neuronal uptake of extracellular TAU, while the binding of APOE may be a requisite factor for some of these observed effects. 50,51 When comparing the transcriptomic profiles of the frontal cortex from *PSEN1*-E280A, *APOE3*-CC-hom with *PSEN1*-E280A carriers negative for the Christchurch variant, *B3GAT3*, which is involved in heparan syn-

thesis, was found to be upregulated in excitatory neurons and *EXTL2*, another participant in heparan synthesis, was found to be upregulated in inhibitory neurons and astrocytes. These findings suggest that upregulation of *B3GAT3* and *EXTL2* in specific cell types could potentially indicate a broad regulatory response in *PSEN1*-E280A_APOE3-CC-hom. Hopefully, these studies will lead to a more precise understanding of AD genotypes that can become incorporated into precision medicine clinical trials.

STAR*METHODS

Detailed methods are provided in the online version of this paper and include the following:

- KEY RESOURCES TABLE
- RESOURCE AVAILABILITY
 - Lead contact
 - Materials availability
 - O Data and code availability
- EXPERIMENTAL MODEL AND STUDY PARTICIPANT DETAILS
 - Postmortem human cohort
- METHOD DETAILS
 - Genetic sequencing
 - O Neuropathological and immunohistochemical analysis
 - Single-nucleus RNA sequencing
 - O Hd-WGCNA
 - Spatial transcriptomics
 - Immunofluorescence
 - Multi dataset analyses
- QUANTIFICATION AND STATISTICAL ANALYSIS
 - Statistics
 - O Cell-specific co-localization analysis
 - Immunofluorescence
 - Calculation of CMA activation score
 - Beta regression
 - O Gene set HAM (human AD microglia) score
 - Overlap analysis
 - Negative binomial generalized linear mixed-effect model
 - Randomization
 - Sample size estimation

SUPPLEMENTAL INFORMATION

Supplemental information can be found online at https://doi.org/10.1016/j.neuron.2024.02.009.

ACKNOWLEDGMENTS

We thank the individuals and the families who participated in this study. We thank the Grupo Neurociencias de Antioquia (GNA) staff who helped with the participant recruitment, evaluation, and sample processing and especially Duvan Cardona and Brian Vicaño from the BrainBank. We thank Alexander Franks for expert statistical advice, Ana Maria Cuervo for gene lists involved in chaperone-mediated autophagy, and Davis Westover for assisting with code annotation. The authors acknowledge the use of the DNA Technologies and Expression Analysis Core at the UC Davis Genome Center, supported by NIH Shared Instrumentation Grant 1510OD010786-01, and the use of the Neuroscience Research Institute, Molecular, Cell and Developmental Biology





Microscopy Facility. This work was supported by the Center for Alzheimer's and Related Dementias, within the Intramural Research Program of the National Institute on Aging and the National Institute of Neurological Disorders and Stroke, National Institutes of Health, Department of Health and Human Services (ZIA AG000545). This study was funded by NIH 1RF1AG062479-01 grant to K.S.K. and F.L., FAPESP grant 2019/22819-8 to M.C.A., and FAPESP grant 2019/22708-1 to D.C.C.

AUTHOR CONTRIBUTIONS

Conceptualization, M.C.A., F.L., and K.S.K.; investigation, M.C.A., D.H., M.A., J.A.-U., D.C.C., C.A.V.-L., B.M.-C., J.L.L., N.D.V.-M., D.S.-F., and E.K.R.; data curation, M.C.A., S.J.E., C.H., D.C.C., and D.S.-F.; formal analysis, M.C.A., S.J.E., C.H., A.N., C.A.V.-L., and M.E.; visualization, M.C.A., S.J.E., C.H., D.S.-F., and D.C.C.; writing – original draft, M.C.A., S.J.E., and K.S.K.; writing – review & editing, M.C.A., S.J.E., S.M.K.G., C.H., D.H., J.A.-U., F.L., and K.S.K.; resources, F.L. and K.S.K. All authors approved the final version of the manuscript.

DECLARATION OF INTERESTS

K.S.K. consults for ADRx and Expansion Therapeutics and is a member of the Tau Consortium board of directors. F.L. consults for Biogen and Viewmind and has grants from the NIH, Red-Lat, Alzheimer's Association, Biogen, DIAN-TU, DIAN-Obs, Large PD, and Enroll-HD. J.A.-U .is a consultant for the pharmaceutical company Tecnoquimicas (Colombia).

DECLARATION OF GENERATIVE AI AND AI-ASSISTED TECHNOLOGIES IN THE WRITING PROCESS

During the preparation of this work, the authors used ChatGPT to condense text and enhance clarity. After using this tool, the authors reviewed and edited the content as needed and take full responsibility for the content of the publication.

Received: May 16, 2023 Revised: January 7, 2024 Accepted: February 9, 2024 Published: February 27, 2024

REFERENCES

- Cruchaga, C., Del-Aguila, J.L., Saef, B., Black, K., Fernandez, M.V., Budde, J., Ibanez, L., Deming, Y., Kapoor, M., Tosto, G., et al. (2018). Polygenic risk score of sporadic late-onset Alzheimer's disease reveals a shared architecture with the familial and early-onset forms. Alzheimers Dement. 14, 205–214. https://doi.org/10.1016/j.jalz.2017.08.013.
- Zetterberg, H., and Mattsson, N. (2014). Understanding the cause of sporadic Alzheimer's disease. Expert Rev. Neurother. 14, 621–630. https://doi.org/10.1586/14737175.2014.915740.
- Ryman, D.C., Acosta-Baena, N., Aisen, P.S., Bird, T., Danek, A., Fox, N.C., Goate, A., Frommelt, P., Ghetti, B., Langbaum, J.B.S., et al. (2014). Symptom onset in autosomal dominant Alzheimer disease: A systematic review and meta-analysis. Neurology 83, 253–260. https://doi.org/10. 1212/WNIL.000000000000000596.
- Acosta-Baena, N., Sepulveda-Falla, D., Lopera-Gómez, C.M., Jaramillo-Elorza, M.C., Moreno, S., Aguirre-Acevedo, D.C., Saldarriaga, A., and Lopera, F. (2011). Pre-dementia clinical stages in presenilin 1 E280A familial early-onset Alzheimer's disease: a retrospective cohort study. Lancet Neurol. 10, 213–220. https://doi.org/10.1016/S1474-4422(10)70323-9.
- Lopera, F., Ardilla, A., Martínez, A., Madrigal, L., Arango-Viana, J.C., Lemere, C.A., Arango-Lasprilla, J.C., Hincapíe, L., Arcos-Burgos, M., Ossa, J.E., et al. (1997). Clinical Features of Early-Onset Alzheimer Disease in a Large Kindred With an E280A Presenilin-1 Mutation. JAMA 277, 793–799. https://doi.org/10.1001/jama.1997.03540340027028.
- Robinson, J.L., Richardson, H., Xie, S.X., Suh, E., Van Deerlin, V.M., Alfaro, B., Loh, N., Porras-Paniagua, M., Nirschl, J.J., Wolk, D., et al. (2021). The

- development and convergence of co-pathologies in Alzheimer's disease. Brain 144, 953–962. https://doi.org/10.1093/brain/awaa438.
- Ringman, J.M., Monsell, S., Ng, D.W., Zhou, Y., Nguyen, A., Coppola, G., Van Berlo, V., Mendez, M.F., Tung, S., Weintraub, S., et al. (2016). Neuropathology of Autosomal Dominant Alzheimer Disease in the National Alzheimer Coordinating Center Database. J. Neuropathol. Exp. Neurol. 75, 284–290. https://doi.org/10.1093/jnen/nl/028.
- Beach, T.G., and Malek-Ahmadi, M. (2021). Alzheimer's Disease Neuropathological Comorbidities Are Common in the Younger-Old. J. Alzheimers Dis. 79, 389–400. https://doi.org/10.3233/JAD-201213.
- Lippa, C.F., Fujiwara, H., Mann, D.M., Giasson, B., Baba, M., Schmidt, M.L., Nee, L.E., O'Connell, B., Pollen, D.A., St. George-Hyslop, P., et al. (1998). Lewy Bodies Contain Altered α-Synuclein in Brains of Many Familial Alzheimer's Disease Patients with Mutations in Presentlin and Amyloid Precursor Protein Genes. Am. J. Pathol. 153, 1365–1370. https://doi.org/10.1016/S0002-9440(10)65722-7.
- Rosenberg, R.N. (2005). New Presenilin 1 Mutation With Alzheimer Disease and Lewy Bodies. Arch. Neurol. 62, 1808. https://doi.org/10. 1001/archneur.62.12.1808.
- Leverenz, J.B., Fishel, M.A., Peskind, E.R., Montine, T.J., Nochlin, D., Steinbart, E., Raskind, M.A., Schellenberg, G.D., Bird, T.D., and Tsuang, D. (2006). Lewy Body Pathology in Familial Alzheimer Disease: Evidence for Disease- and Mutation-Specific Pathologic Phenotype. Arch. Neurol. 63, 370–376. https://doi.org/10.1001/archneur.63.3.370.
- Grubman, A., Chew, G., Ouyang, J.F., Sun, G., Choo, X.Y., McLean, C., Simmons, R.K., Buckberry, S., Vargas-Landin, D.B., Poppe, D., et al. (2019). A single-cell atlas of entorhinal cortex from individuals with Alzheimer's disease reveals cell-type-specific gene expression regulation. Nat. Neurosci. 22, 2087–2097. https://doi.org/10.1038/s41593-019-0539-4
- Mathys, H., Davila-Velderrain, J., Peng, Z., Gao, F., Mohammadi, S., Young, J.Z., Menon, M., He, L., Abdurrob, F., Jiang, X., et al. (2019). Single-cell transcriptomic analysis of Alzheimer's disease. Nature 570, 332–337. https://doi.org/10.1038/s41586-019-1195-2.
- Zhou, Y., Song, W.M., Andhey, P.S., Swain, A., Levy, T., Miller, K.R., Poliani, P.L., Cominelli, M., Grover, S., Gilfillan, S., et al. (2020). Human and mouse single-nucleus transcriptomics reveal TREM2-dependent and TREM2-independent cellular responses in Alzheimer's disease. Nat. Med. 26, 131–142. https://doi.org/10.1038/s41591-019-0695-9.
- Brase, L., You, S.-F., D'Oliveira Albanus, R., Del-Aguila, J.L., Dai, Y., Novotny, B.C., Soriano-Tarraga, C., Dykstra, T., Fernandez, M.V., Budde, J.P., et al. (2023). Single-nucleus RNA-sequencing of autosomal dominant Alzheimer disease and risk variant carriers. Nat. Commun. 14, 2314. https://doi.org/10.1038/s41467-023-37437-5.
- Squair, J.W., Gautier, M., Kathe, C., Anderson, M.A., James, N.D., Hutson, T.H., Hudelle, R., Qaiser, T., Matson, K.J.E., Barraud, Q., et al. (2021). Confronting false discoveries in single-cell differential expression. Nat. Commun. 12, 5692. https://doi.org/10.1038/s41467-021-25960-2.
- Bourdenx, M., Martín-Segura, A., Scrivo, A., Rodriguez-Navarro, J.A., Kaushik, S., Tasset, I., Diaz, A., Storm, N.J., Xin, Q., Juste, Y.R., et al. (2021). Chaperone-mediated autophagy prevents collapse of the neuronal metastable proteome. Cell 184, 2696–2714.e25. https://doi.org/10.1016/j. cell.2021.03.048.
- Gazestani, V., Kamath, T., Nadaf, N.M., Dougalis, A., Burris, S.J., Rooney, B., Junkkari, A., Vanderburg, C., Pelkonen, A., Gomez-Budia, M., et al. (2023). Early Alzheimer's disease pathology in human cortex involves transient cell states. Cell 186, 4438–4453.e23. https://doi.org/10.1016/j.cell. 2023.08.005.
- Leng, K., Li, E., Eser, R., Piergies, A., Sit, R., Tan, M., Neff, N., Li, S.H., Rodriguez, R.D., Suemoto, C.K., et al. (2021). Molecular characterization of selectively vulnerable neurons in Alzheimer's disease. Nat. Neurosci. 24, 276–287. https://doi.org/10.1038/s41593-020-00764-7.
- Mathys, H., Peng, Z., Boix, C.A., Victor, M.B., Leary, N., Babu, S., Abdelhady, G., Jiang, X., Ng, A.P., Ghafari, K., et al. (2023). Single-cell

Neuron Article



- atlas reveals correlates of high cognitive function, dementia, and resilience to Alzheimer's disease pathology. Cell *186*, 4365–4385.e27. https://doi.org/10.1016/j.cell.2023.08.039.
- Lee, S.J., Park, M.H., Kim, H.J., and Koh, J.Y. (2010). Metallothionein-3 regulates lysosomal function in cultured astrocytes under both normal and oxidative conditions. Glia 58, 1186–1196. https://doi.org/10.1002/ glia.20998.
- Otero-Garcia, M., Mahajani, S.U., Wakhloo, D., Tang, W., Xue, Y.-Q., Morabito, S., Pan, J., Oberhauser, J., Madira, A.E., Shakouri, T., et al. (2022). Molecular signatures underlying neurofibrillary tangle susceptibility in Alzheimer's disease. Neuron 110, 2929–2948.e8. https://doi.org/10. 1016/j.neuron.2022.06.021.
- Srinivasan, K., Friedman, B.A., Etxeberria, A., Huntley, M.A., van der Brug, M.P., Foreman, O., Paw, J.S., Modrusan, Z., Beach, T.G., Serrano, G.E., and Hansen, D.V. (2020). Alzheimer's Patient Microglia Exhibit Enhanced Aging and Unique Transcriptional Activation. Cell Rep. 31, 107843. https://doi.org/10.1016/j.celrep.2020.107843.
- Fabregat, A., Sidiropoulos, K., Viteri, G., Forner, O., Marin-Garcia, P., Arnau, V., D'Eustachio, P., Stein, L., and Hermjakob, H. (2017). Reactome pathway analysis: a high-performance in-memory approach. BMC Bioinf. 18, 142. https://doi.org/10.1186/s12859-017-1559-2.
- Mawuenyega, K.G., Sigurdson, W., Ovod, V., Munsell, L., Kasten, T., Morris, J.C., Yarasheski, K.E., and Bateman, R.J. (2010). Decreased Clearance of CNS β-Amyloid in Alzheimer's Disease. Science 330, 1774. https://doi.org/10.1126/science.1197623.
- Arboleda-Velasquez, J.F., Lopera, F., O'Hare, M., Delgado-Tirado, S., Marino, C., Chmielewska, N., Saez-Torres, K.L., Amarnani, D., Schultz, A.P., Sperling, R.A., et al. (2019). Resistance to autosomal dominant Alzheimer's disease in an APOE3 Christchurch homozygote: a case report. Nat. Med. 25, 1680–1683. https://doi.org/10.1038/s41591-019-0611-3.
- Sepulveda-Falla, D., Sanchez, J.S., Almeida, M.C., Boassa, D., Acosta-Uribe, J., Vila-Castelar, C., Ramirez-Gomez, L., Baena, A., Aguillon, D., Villalba-Moreno, N.D., et al. (2022). Distinct tau neuropathology and cellular profiles of an APOE3 Christchurch homozygote protected against autosomal dominant Alzheimer's dementia. Acta Neuropathol. 144, 589–601. https://doi.org/10.1007/s00401-022-02467-8.
- Chen, Y., Song, S., Parhizkar, S., Lord, J., Zhu, Y., Strickland, M.R., Wang, C., Park, J., Tabor, G.T., Jiang, H., et al. (2023). APOE3ch alters microglial response and suppresses Aβ-induced tau seeding and spread. Cell 187, 428–445.e20. https://doi.org/10.1016/j.cell.2023.11.029.
- Nelson, M.R., Liu, P., Agrawal, A., Yip, O., Blumenfeld, J., Traglia, M., Kim, M.J., Koutsodendris, N., Rao, A., Grone, B., et al. (2023). The APOE-R136S mutation protects against APOE4-driven Tau pathology, neurodegeneration and neuroinflammation. Nat. Neurosci. 26, 2104–2121. https:// doi.org/10.1038/s41593-023-01480-8.
- Zimmerman, K.D., Espeland, M.A., and Langefeld, C.D. (2021). A practical solution to pseudoreplication bias in single-cell studies. Nat. Commun. 12, 738. https://doi.org/10.1038/s41467-021-21038-1.
- Koopal, C., Marais, A.D., Westerink, J., and Visseren, F.L.J. (2017).
 Autosomal dominant familial dysbetalipoproteinemia: A pathophysiological framework and practical approach to diagnosis and therapy. J. Clin. Lipidol. 11, 12–23.e1. https://doi.org/10.1016/j.jacl.2016.10.001.
- Djelti, F., Braudeau, J., Hudry, E., Dhenain, M., Varin, J., Bièche, I., Marquer, C., Chali, F., Ayciriex, S., Auzeil, N., et al. (2015). CYP46A1 inhibition, brain cholesterol accumulation and neurodegeneration pave the way for Alzheimer's disease. Brain 138, 2383–2398. https://doi.org/10.1093/brain/awy166.
- Soto-Mercado, V., Mendivil-Perez, M., Velez-Pardo, C., Lopera, F., and Jimenez-Del-Rio, M. (2020). Cholinergic-like neurons carrying PSEN1 E280A mutation from familial Alzheimer's disease reveal intraneuronal sAPPβ fragments accumulation, hyperphosphorylation of TAU, oxidative stress, apoptosis and Ca2+ dysregulation: Therapeutic implications. PLoS One 15. e0221669. https://doi.org/10.1371/journal.pone.0221669.

- Wen, L., Tang, F.-L., Hong, Y., Luo, S.-W., Wang, C.-L., He, W., Shen, C., Jung, J.-U., Xiong, F., Lee, D.h., et al. (2011). VPS35 haploinsufficiency increases Alzheimer's disease neuropathology. J. Cell Biol. 195, 765–779. https://doi.org/10.1083/jcb.201105109.
- Chambraud, B., Sardin, E., Giustiniani, J., Dounane, O., Schumacher, M., Goedert, M., and Baulieu, E.-E. (2010). A role for FKBP52 in Tau protein function. Proc. Natl. Acad. Sci. USA 107, 2658–2663. https://doi.org/10. 1073/onas.0914957107.
- Jinwal, U.K., Koren, J., Borysov, S.I., Schmid, A.B., Abisambra, J.F., Blair, L.J., Johnson, A.G., Jones, J.R., Shults, C.L., O'Leary, J.C., et al. (2010). The Hsp90 Cochaperone, FKBP51, Increases Tau Stability and Polymerizes Microtubules. J. Neurosci. 30, 591–599. https://doi.org/10. 1523/JNEUROSCI.4815-09.2010.
- Ikura, T., and Ito, N. (2013). Peptidyl-prolyl isomerase activity of FK506 binding protein 12 prevents tau peptide from aggregating. Protein Eng. Des. Sel. 26, 539–546. https://doi.org/10.1093/protein/gzt033.
- Blair, L.J., Nordhues, B.A., Hill, S.E., Scaglione, K.M., O'Leary, J.C., Fontaine, S.N., Breydo, L., Zhang, B., Li, P., Wang, L., et al. (2013). Accelerated neurodegeneration through chaperone-mediated oligomerization of tau. J. Clin. Invest. 123, 4158–4169. https://doi.org/10.1172/ ICIGO003
- Rauch, J.N., Luna, G., Guzman, E., Audouard, M., Challis, C., Sibih, Y.E., Leshuk, C., Hemandez, I., Wegmann, S., Hyman, B.T., et al. (2020). LRP1 is a master regulator of tau uptake and spread. Nature 580, 381–385. https://doi.org/10.1038/s41586-020-2156-5.
- Dumois-Petersen, S., Gallegos-Arreola, M.P., Magaña-Torres, M.T., Perea-Díaz, F.J., Ringman, J.M., and Figuera, L.E. (2020). Autosomal dominant early onset Alzheimer's disease in the Mexican state of Jalisco: High frequency of the mutation PSEN1 c.1292C>A and phenotypic profile of patients. Am. J. Med. Genet. C Semin. Med. Genet. 184, 1023-1029. https://doi.org/10.1002/ajmg.c.31865.
- Tabira, T., Chui, D.H., Nakayama, H., Kuroda, S., and Shibuya, M. (2002).
 Alzheimer's disease with spastic paresis and cotton wool type plaques.
 Neurosci. Res. 70, 367–372. https://doi.org/10.1002/jnr.10392.
- 42. Ryan, N.S., Nicholas, J.M., Weston, P.S.J., Liang, Y., Lashley, T., Guerreiro, R., Adamson, G., Kenny, J., Beck, J., Chavez-Gutierrez, L., et al. (2016). Clinical phenotype and genetic associations in autosomal dominant familial Alzheimer's disease: a case series. Lancet Neurol. 15, 1326–1335. https://doi.org/10.1016/S1474-4422(16)30193-4.
- Tolia, A., Chávez-Gutiérrez, L., and De Strooper, B. (2006). Contribution of Presenilin Transmembrane Domains 6 and 7 to a Water-containing Cavity in the γ-Secretase Complex. J. Biol. Chem. 281, 27633–27642. https://doi. org/10.1074/jbc.M604997200.
- 44. Oikawa, N., and Walter, J. (2019). Presentlins and γ -Secretase in Membrane Proteostasis. Cells 8, 209. https://doi.org/10.3390/cells8030209.
- Wolfe, M.S. (2013). Toward the structure of presenilin/γ-secretase and presenilin homologs. Biochim. Biophys. Acta 1828, 2886–2897. https:// doi.org/10.1016/j.bbamem.2013.04.015.
- Balch, W.E., Morimoto, R.I., Dillin, A., and Kelly, J.W. (2008). Adapting Proteostasis for Disease Intervention. Science 319, 916–919. https://doi. org/10.1126/science.1141448.
- Labbadia, J., and Morimoto, R.I. (2015). The Biology of Proteostasis in Aging and Disease. Annu. Rev. Biochem. 84, 435–464. https://doi.org/ 10.1146/annurev-biochem-060614-033955.
- Braak, H., Alafuzoff, I., Arzberger, T., Kretzschmar, H., and Del Tredici, K. (2006). Staging of Alzheimer disease-associated neurofibrillary pathology using paraffin sections and immunocytochemistry. Acta Neuropathol. 112, 389–404. https://doi.org/10.1007/s00401-006-0127-z.
- Bu, G. (2009). Apolipoprotein E and its receptors in Alzheimer's disease: pathways, pathogenesis and therapy. Nat. Rev. Neurosci. 10, 333–344. https://doi.org/10.1038/nrn2620.
- Zlokovic, B.V., Deane, R., Sagare, A.P., Bell, R.D., and Winkler, E.A. (2010). Low-density lipoprotein receptor-related protein-1: a serial





- clearance homeostatic mechanism controlling Alzheimer's amyloid β -peptide elimination from the brain. J. Neurochem. 115, 1077–1089. https://doi.org/10.1111/j.1471-4159.2010.07002.x.
- Acosta-Uribe, J., Aguillón, D., Cochran, J.N., Giraldo, M., Madrigal, L., Killingsworth, B.W., Singhal, R., Labib, S., Alzate, D., Velilla, L., et al. (2022). A neurodegenerative disease landscape of rare mutations in Colombia due to founder effects. Genome Med. 14, 27. https://doi.org/ 10.1186/s13073-022-01035-9.
- Cleverley, K., Lee, W.C., Mumford, P., Collins, T., Rickman, M., Cunningham, T.J., Cleak, J., Mianne, J., Szoke-Kovacs, Z., Stewart, M., et al. (2021). A novel knockout mouse for the small EDRK-rich factor 2 (Serf2) showing developmental and other deficits. Mamm. Genome 32, 94–103. https://doi.org/10.1007/s000335-021-09864-6.
- Shi, Y., Yamada, K., Liddelow, S.A., Smith, S.T., Zhao, L., Luo, W., Tsai, R.M., Spina, S., Grinberg, L.T., Rojas, J.C., et al. (2017). ApoE4 markedly exacerbates tau-mediated neurodegeneration in a mouse model of tauopathy. Nature 549, 523–527. https://doi.org/10.1038/nature24016.
- Dincer, A., Chen, C.D., McKay, N.S., Koenig, L.N., McCullough, A., Flores, S., Keefe, S.J., Schultz, S.A., Feldman, R.L., Joseph-Mathurin, N., et al. (2022). APOE ε4 genotype, amyloid-β, and sex interact to predict tau in regions of high APOE mRNA expression. Sci. Transl. Med. 14, eabl7646. https://doi.org/10.1126/scitranslmed.abl7646.
- 55. Wang, C., Xiong, M., Gratuze, M., Bao, X., Shi, Y., Andhey, P.S., Manis, M., Schroeder, C., Yin, Z., Madore, C., et al. (2021). Selective removal of astrocytic APOE4 strongly protects against tau-mediated neurodegeneration and decreases synaptic phagocytosis by microglia. Neuron 109, 1657–1674.e7. https://doi.org/10.1016/j.neuron.2021.03.024.
- Stuart, T., Butler, A., Hoffman, P., Hafemeister, C., Papalexi, E., Mauck, W.M., Hao, Y., Stoeckius, M., Smibert, P., and Satija, R. (2019). Comprehensive Integration of Single-Cell Data. Cell 177, 1888– 1902.e21. https://doi.org/10.1016/j.cell.2019.05.031.
- McGinnis, C.S., Murrow, L.M., and Gartner, Z.J. (2019). DoubletFinder: Doublet Detection in Single-Cell RNA Sequencing Data Using Artificial Nearest Neighbors. Cell Syst. 8, 329–337.e4. https://doi.org/10.1016/j. cels.2019.03.003.
- Bankhead, P., Loughrey, M.B., Fernández, J.A., Dombrowski, Y., McArt, D.G., Dunne, P.D., McQuaid, S., Gray, R.T., Murray, L.J., Coleman, H.G., et al. (2017). QuPath: Open source software for digital pathology image analysis. Sci Rep 7, 16878. https://doi.org/10.1038/s41598-017-17204-5.
- Zhou, Y., Zhou, B., Pache, L., Chang, M., Khodabakhshi, A.H., Tanaseichuk, O., Benner, C., and Chanda, S.K. (2019). Metascape provides a biologistoriented resource for the analysis of systems-level datasets. Nat. Commun. 10, 1523. https://doi.org/10.1038/s41467-019-09234-6.
- Bates, D., Mächler, M., Bolker, B., and Walker, S. (2015). Fitting Linear Mixed-Effects Models Using Ime4. J. Stat. Soft. 67, 1–48. https://doi. org/10.18637/jss.v067.i01.
- Korotkevich, G., Sukhov, V., Budin, N., Shpak, B., Artyomov, M.N., and Sergushichev, A. (2016). Fast gene set enrichment analysis. Preprint at bioRxiv. https://doi.org/10.1101/060012.
- Almeida, M.C., Eger, S., He, C., Westover, D., Acosta-Uribe, J., and Kosik, K.S. (2024). Single Nucleus & Spatial Transcriptomics Analyses in

- Autosomal Dominant Alzheimer's Disease Brain Tissue. https://doi.org/ 10.5281/ZENODO.10460116.
- 63. Habib, N., Avraham-Davidi, I., Basu, A., Burks, T., Shekhar, K., Hofree, M., Choudhury, S.R., Aguet, F., Gelfand, E., Ardlie, K., et al. (2017). Massively parallel single-nucleus RNA-seq with DroNc-seq. Nat. Methods 14, 955–958. https://doi.org/10.1038/nmeth.4407.
- 64. McKenzie, A.T., Wang, M., Hauberg, M.E., Fullard, J.F., Kozlenkov, A., Keenan, A., Hurd, Y.L., Dracheva, S., Casaccia, P., Roussos, P., and Zhang, B. (2018). Brain Cell Type Specific Gene Expression and Co-expression Network Architectures. Sci. Rep. 8, 8868. https://doi.org/10.1038/s41598-018-27293-5.
- 65. Zhang, Y., Chen, K., Sloan, S.A., Bennett, M.L., Scholze, A.R., O'Keeffe, S., Phatnani, H.P., Guarnieri, P., Caneda, C., Ruderisch, N., et al. (2014). An RNA-Sequencing Transcriptome and Splicing Database of Glia, Neurons, and Vascular Cells of the Cerebral Cortex. J. Neurosci. 34, 11929–11947. https://doi.org/10.1523/JNEUROSCI.1860-14.2014.
- Darmanis, S., Sloan, S.A., Zhang, Y., Enge, M., Caneda, C., Shuer, L.M., Hayden Gephart, M.G., Barres, B.A., and Quake, S.R. (2015). A survey of human brain transcriptome diversity at the single cell level. Proc. Natl. Acad. Sci. USA 112, 7285–7290. https://doi.org/10.1073/pnas.1507125112.
- Franzén, O., Gan, L.-M., and Björkegren, J.L.M. (2019). PanglaoDB: a web server for exploration of mouse and human single-cell RNA sequencing data. Database. https://doi.org/10.1093/database/baz046.
- He, L., Davila-Velderrain, J., Sumida, T.S., Hafler, D.A., Kellis, M., and Kulminski, A.M. (2021). NEBULA is a fast negative binomial mixed model for differential or co-expression analysis of large-scale multi-subject single-cell data. Commun. Biol. 4, 629–717. https://doi.org/10.1038/ s42003-021-02146-6.
- Sherman, B.T., Hao, M., Qiu, J., Jiao, X., Baseler, M.W., Lane, H.C., Imamichi, T., and Chang, W. (2022). DAVID: a web server for functional enrichment analysis and functional annotation of gene lists (2021 update). Nucleic Acids Res. 50, W216–W221. https://doi.org/10.1093/nar/gkac194.
- Morabito, S., Miyoshi, E., Michael, N., Shahin, S., Martini, A.C., Head, E., Silva, J., Leavy, K., Perez-Rosendahl, M., and Swarup, V. (2021). Singlenucleus chromatin accessibility and transcriptomic characterization of Alzheimer's disease. Nat. Genet. 53, 1143–1155. https://doi.org/10. 1038/s41588-021-00894-z.
- Maynard, K.R., Collado-Torres, L., Weber, L.M., Uytingco, C., Barry, B.K., Williams, S.R., Catallini, J.L., Tran, M.N., Besich, Z., Tippani, M., et al. (2021). Transcriptome-scale spatial gene expression in the human dorsolateral prefrontal cortex. Nat. Neurosci. 24, 425–436. https://doi.org/10. 1038/s41593-020-00787-0.
- Schindelin, J., Arganda-Carreras, I., Frise, E., Kaynig, V., Longair, M., Pietzsch, T., Preibisch, S., Rueden, C., Saalfeld, S., Schmid, B., et al. (2012). Fiji: an open-source platform for biological-image analysis. Nat. Methods 9, 676–682. https://doi.org/10.1038/nmeth.2019.
- Olah, M., Menon, V., Habib, N., Taga, M.F., Ma, Y., Yung, C.J., Cimpean, M., Khairallah, A., Coronas-Samano, G., Sankowski, R., et al. (2020). Single cell RNA sequencing of human microglia uncovers a subset associated with Alzheimer's disease. Nat. Commun. 11, 6129. https://doi. org/10.1038/s41467-020-19737-2.





STAR*METHODS

KEY RESOURCES TABLE

REAGENT or RESOURCE	SOURCE	IDENTIFIER
Antibodies		
mouse beta amyloid monoclonal antibody (BAM-10)	Thermo Fisher Scientific	Cat# MA1-91209; RRID: AB_1954846
Phospho-Tau (Ser202, Thr205) Monoclonal Antibody (AT8)	Thermo Fisher Scientific	Cat# MN1020; RRID: AB_223647
GFAP antibody	Synaptic Systems	Cat# 173 308; RRID: AB_2905596
HSP90 alpha-recombinant rabbit nonoclonal antibody (4D1)	Thermo Fisher Scientific	Cat# MA5-33174; RRID: AB_2811990
Tau Monoclonal Antibody (TAU5)	Thermo Fisher Scientific	Cat# AHB0042; RRID: AB_2536235
Rabbit Anti-MAP2 Polyclonal Antibody, Unconjugated	Abcam	Cat# ab32454; RRID: AB_776174
Anti-LRP1 (N-terminal) antibody produced in rabbit	Sigma Aldrich	Cat# L2295; RRID: AB_10610711
Cyclophilin A Polyclonal Antibody	Thermo Fisher Scientific	Cat# PA1-025; RRID: AB_2169124
FKBP1B antibody	Proteintech	Cat# 15114-1-AP; RRID: AB_11182817
Biological samples		
Human, PostMortem Frontal Cortex Samples from Alzheimer's Disease (familial and sporadic) and Non-Symptomatic Patients	Grupo de Neurociencias de Antioquia brain bank	https://www.gna.org.co/
Human, PostMortem Hippocampal Samples from Alzheimer's Disease (familial) and Non-Symptomatic Patients	Grupo de Neurociencias de Antioquia brain bank	https://www.gna.org.co/
Human, PostMortem occipital cortex sample	Grupo de Neurociencias de Antioquia	https://www.gna.org.co/
Chemicals, peptides, and recombinant proteins		
Glycerin (Glycerol), 50% (v/v) Aqueous Solution	Thermo Fisher	Cat# 329032
ow TE Buffer	Thermo Fisher	Cat#12090-015
Sytox green nucleic acid stain	Life Tech	Cat# S7020
Molecular biology grade ethanol	Fisher	Cat# BP2818500
RNAse inhibitor	Lucigen	Cat# 30281-1
Nuclei Isolation Kit: Nuclei EZ Prep	Millipore Sigma	Cat# NUC101-1KT
SPRI Select beads	Beckman Coulter	Cat# B23318
Kylene	Millipore-Sigma	Cat# 534056-4L; CAS: 1330-20-7
2-propanol	Millipore-Sigma	Cat# I9516
N	Millipore-Sigma Ventana Medical Systems, Inc.	Cat# 19516 Cat# 05279801001
001		
CC1 CC2	Ventana Medical Systems, Inc.	Cat# 05279801001
CC1 CC2 Shandon Instant Hematoxylin	Ventana Medical Systems, Inc. Ventana Medical Systems, Inc.	Cat# 05279801001 Cat# 05279798001
CC1 CC2 Shandon Instant Hematoxylin Eosin yellowish	Ventana Medical Systems, Inc. Ventana Medical Systems, Inc. Thermo Fisher	Cat# 05279801001 Cat# 05279798001 Cat# 12687926
CC1 CC2 Shandon Instant Hematoxylin Eosin yellowish Consul-Mount™ Histology Media, Medium Viscosity	Ventana Medical Systems, Inc. Ventana Medical Systems, Inc. Thermo Fisher PanReac	Cat# 05279801001 Cat# 05279798001 Cat# 12687926 Cat# 348111; CAS: 17372-87-1
CC1 CC2 Shandon Instant Hematoxylin Eosin yellowish Consul-Mount™ Histology Media, Medium Viscosity Reaction Buffer Concentrate (10X)	Ventana Medical Systems, Inc. Ventana Medical Systems, Inc. Thermo Fisher PanReac Thermo Fisher	Cat# 05279801001 Cat# 05279798001 Cat# 12687926 Cat# 348111; CAS: 17372-87-1 Cat# 9990440
CC1 CC2 Shandon Instant Hematoxylin Eosin yellowish Consul-Mount™ Histology Media, Medium Viscosity Reaction Buffer Concentrate (10X)	Ventana Medical Systems, Inc. Ventana Medical Systems, Inc. Thermo Fisher PanReac Thermo Fisher Ventana Medical Systems, Inc.	Cat# 05279801001 Cat# 05279798001 Cat# 12687926 Cat# 348111; CAS: 17372-87-1 Cat# 9990440 Cat# 5353955001
CC1 CC2 Shandon Instant Hematoxylin Eosin yellowish Consul-Mount™ Histology Media, Medium Viscosity Reaction Buffer Concentrate (10X) .CS .OX EZ PREP SOLUTION, 2L	Ventana Medical Systems, Inc. Ventana Medical Systems, Inc. Thermo Fisher PanReac Thermo Fisher Ventana Medical Systems, Inc. Ventana Medical Systems, Inc.	Cat# 05279801001 Cat# 05279798001 Cat# 12687926 Cat# 348111; CAS: 17372-87-1 Cat# 9990440 Cat# 5353955001 Cat# 5264839001
CC1 CC2 Shandon Instant Hematoxylin Eosin yellowish Consul-Mount™ Histology Media, Medium Viscosity Reaction Buffer Concentrate (10X) .CS 0X EZ PREP SOLUTION, 2L PROTEASE 1	Ventana Medical Systems, Inc. Ventana Medical Systems, Inc. Thermo Fisher PanReac Thermo Fisher Ventana Medical Systems, Inc. Ventana Medical Systems, Inc. Ventana Medical Systems, Inc.	Cat# 05279801001 Cat# 05279798001 Cat# 12687926 Cat# 348111; CAS: 17372-87-1 Cat# 9990440 Cat# 5353955001 Cat# 5264839001 Cat# 5279771001
CC1 CC2 Shandon Instant Hematoxylin Eosin yellowish Consul-Mount™ Histology Media, Medium Viscosity Reaction Buffer Concentrate (10X) .CS IOX EZ PREP SOLUTION, 2L PROTEASE 1 ANTIBODY DILUENT	Ventana Medical Systems, Inc. Ventana Medical Systems, Inc. Thermo Fisher PanReac Thermo Fisher Ventana Medical Systems, Inc. Ventana Medical Systems, Inc. Ventana Medical Systems, Inc. Ventana Medical Systems, Inc.	Cat# 05279801001 Cat# 05279798001 Cat# 12687926 Cat# 348111; CAS: 17372-87-1 Cat# 9990440 Cat# 5353955001 Cat# 5264839001 Cat# 5279771001 Cat# 5266688001
Z-propanol CC1 CC2 Shandon Instant Hematoxylin Eosin yellowish Consul-Mount™ Histology Media, Medium Viscosity Reaction Buffer Concentrate (10X) _CS 10X EZ PREP SOLUTION, 2L PROTEASE 1 ANTIBODY DILUENT Methanol, for HPLC, ≥ 99.9% Eosin Y solution, aqueous	Ventana Medical Systems, Inc. Ventana Medical Systems, Inc. Thermo Fisher PanReac Thermo Fisher Ventana Medical Systems, Inc.	Cat# 05279801001 Cat# 05279798001 Cat# 12687926 Cat# 348111; CAS: 17372-87-1 Cat# 9990440 Cat# 5353955001 Cat# 5264839001 Cat# 5279771001 Cat# 5266688001 Cat# 5261899001
CC1 CC2 Shandon Instant Hematoxylin Eosin yellowish Consul-Mount™ Histology Media, Medium Viscosity Reaction Buffer Concentrate (10X) CCS IOX EZ PREP SOLUTION, 2L PROTEASE 1 ANTIBODY DILUENT Methanol, for HPLC, ≥ 99.9%	Ventana Medical Systems, Inc. Ventana Medical Systems, Inc. Thermo Fisher PanReac Thermo Fisher Ventana Medical Systems, Inc. Millipore Sigma	Cat# 05279801001 Cat# 05279798001 Cat# 12687926 Cat# 348111; CAS: 17372-87-1 Cat# 9990440 Cat# 5264839001 Cat# 5279771001 Cat# 5266688001 Cat# 5261899001 Cat# 34860

(Continued on next page)





Continued		
REAGENT or RESOURCE	SOURCE	IDENTIFIER
Tris Base	Thermo Fisher Scientific	Cat# BP152-500
Potassium Hydroxide Solution, 8M	Millipore Sigma	Cat# P4494-50ML
SSC Buffer 20X Concentrate	Millipore Sigma	Cat# S66391L
Hydrochloric Acid Solution, 0.1N	Fisher Chemical	Cat# SA54-1
Qiagen Buffer EB	Qiagen	Cat# 19086
KAPA SYBR FAST qPCR Master Mix	Roche	KK4600
Critical commercial assays		
Visium Spatial Gene Expression Slide & Reagent Kit	10x Genomics	Cat # 1000187
Chromium Next GEM Single Cell 3′ GEM, Library & Gel Bead Kit v3.1	10x Genomics	Cat # 1000121
UltraView Universal DAB Detection Kit	Ventana Medical Systems, Inc.	Cat# 5269806001
Deposited data		
Single Nucleus RNA Sequencing Data	This study	GEO: GSE222494, GSE222495
Spatial Transcriptomic Sequencing Data	This study	GEO: GSE221365
Single Nucleus RNA Sequencing Data	Sepulveda-Falla et al.,27	GEO: GSE206744
Software and algorithms		
Prism (version 6.1.0)	GraphPad	https://www.graphpad.com/ scientificsoftware/prism/; RRID: SCR_002798
Microsoft Excel	Microsoft 365	https://microsoft.com; RRID: SCR_016137
Cell Ranger (version 3.0)	10x Genomics	https://support.10xgenomics.com/ single-cell-gene-expression/software/ pipelines/latest/what-is-cell-ranger; RRID: SCR_017344
RStudio	Posit	https://RStudio.com; RRID: SCR_000432
Seurat (version 4.1.1)	Stuart et al. ⁵⁶	https://satijalab.org/seurat/index.html; RRID: SCR_016341
Doubletfinder (version 2.0.3)	McGinnis et al. ⁵⁷	https://github.com/chris- mcginnis-ucsf/DoubletFinder
QPath (v.0.1.2)	Bankhead et al. ⁵⁸	https://qupath.github.io/; RRID: SCR_018257
Inkscape (v1.2.1)	The Inkscape Project	https://inkscape.org/; RRID: SCR_014479
Metascape	Zhou et al. ⁵⁹	https://metascape.org; RRID: SCR_016620
Space Ranger (version 1.3.1)	10x Genomics	https://support.10xgenomics.com/ spatial-gene-expression/software/ pipelines/latest/what-is-space-ranger
Libra	Squair et al. 16	https://github.com/neurorestore/Libra
lme4 package	Bates et al. ⁶⁰	http://www.jstatsoft.org/v67/i01/
fgsea	Korotkevich et al.61	https://github.com/ctlab/fgsea
Custom computer code used in this manuscript	Almeida et al. ⁶²	https://doi.org/10.5281/zenodo.10460116

RESOURCE AVAILABILITY

Lead contact

Further information and requests for resources and reagents should be directed to and will be fulfilled by the lead contact, Kenneth S. Kosik (kosik@ucsb.edu).

Materials availability

This study did not generate new unique reagents.





Data and code availability

- Raw single nucleus RNA sequencing have been deposited at GEO under accession numbers GSE222494 and GSE222495 and
 are publicly available as of the date of publication. Raw spatial transcriptomics sequencing data have been deposited at GEO
 under accession number GSE221365 and are publicly available as of the date of publication. Accession numbers are listed in
 the key resources table. Microscopy data reported in this paper will be shared by the lead contact upon request.
- All original code has been deposited at Zenodo and is publicly available as of the date of publication.⁶² DOI is listed in the key resources table.
- Any additional information required to reanalyze the data reported in this paper is available from the lead contact upon request.

EXPERIMENTAL MODEL AND STUDY PARTICIPANT DETAILS

Postmortem human cohort

This study utilized postmortem human brain samples from 27 donors in the Grupo de Neurociencias de Antioquia brain bank. Brain donation followed informed consent and ethical approval from the Institutional Review Board (IRB) of the Medical Research institute, School of Medicine, Universidad de Antioquia (IORG0010323, FWA00028864). Written informed consent following the guidelines of the Code of Ethics of the World Medical Association, Helsinki declaration and Belmont Report were obtained from the donors legally authorized proxies.

We grouped the samples into three categories: individuals without neurodegenerative diseases or systemic diseases compromising the central nervous system, here referred as controls (n = 8); patients with autosomal dominant AD who were carriers of the presenilin-1 (*PSEN1*) NM_000021:c.839A>C, p.Glu280Ala mutation, here referred as *PSEN1*-E280A (n = 10); one patient with autosomal dominant AD who was a carrier of the presenilin-1 (*PSEN1*) and also homozygote for *APOE*3-Christchurch variant (see below), and patients with AD who didn't have first or second degree relatives affected by neurodegenerative illnesses, here referred as sporadic AD (n = 8). Five samples carried the minor *APOE*4 allele within the cohort and three of the *PSEN1*-E280A samples were heterozygotes for the *APOE*3-Christchurch variant. Specific characteristics of the individuals are displayed in Table S1.

METHOD DETAILS

Genetic sequencing

DNA from all donors was tested for APOE alleles rs429358 and rs7412 using next-generation sequencing and/or real-time PCR.

Neuropathological and immunohistochemical analysis

Brain donation was performed after informed consent signature and ethical approval as described above. We determined the presence of AD pathological hallmarks by microscopic examination of 17 brain areas including medial frontal gyrus, superior temporal gyrus, medial temporal gyrus, inferior temporal gyrus, hippocampus, amygdala, insula, gyrus cinguli, lenticular nucleus, caudate nucleus, thalamus, inferior parietal lobule, occipital lobule, cerebellum, mesencephalon, pons, and medulla oblongata. Tissue was cut in 5μm thick sections and stained with hematoxylin and eosin (H&E). Immunohistochemistry (IHC) for amyloid beta (Aβ, 1:200; mouse monoclonal BAM-10, Catalog # MA1-91209, ThermoFisher Scientific, USA), and hyperphosphorylated TAU Ser 202 and Thr 205 (TAU, 1:1200; mouse monoclonal AT8, MN1020; ThermoFisher Scientific, Dreieich, Germany) was performed with a Ventana Benchmark GX system (Roche AG, Basel, Switzerland) according to manufacturer instructions. Briefly, after dewaxing and inactivation of endogenous peroxidases (PBS/3% hydrogen peroxide), antibody specific antigen retrieval was performed, sections were blocked and afterward incubated with the primary antibody. For detection of specific binding, the Ultra View Universal 3,3′-Diaminobenzidine (DAB) Detection Kit (Ventana, Roche) was used which contains secondary antibodies, DAB stain and counter staining reagent. Sections were scanned using a Ventana DP200 (Roche, USA) to obtain images of whole stained sections at a resolution of at least 1 pixel per μm.

Single-nucleus RNA sequencing

A schematic of the nuclei isolation and sequencing workflow is shown in Figure S2A. In snRNA-seq, for each individual, we evaluated tissue from frontal cortex (FC).

Nuclei isolation

FC samples were dissociated, and nuclei isolation was performed separately for each sample using the Nuclei Isolation Kit: Nuclei EZ Prep (Sigma, #NUC101) as described in. 63 Briefly, tissue samples were dounce homogenized in 2 mL of ice-cold EZ PREP and incubated on ice for 5 min. Following dounce homogenization, an additional 2mL of EZ PREP was added and the samples were incubated for 5 min. Nuclei suspension was centrifuged ($500 \times g$, 5 min and 4° C) washed 1x in ice-cold EZ PREP buffer, and 1x in Nuclei Suspension Buffer (NSB; consisting of $1 \times$ PBS, 1 % (w/v) BSA and 0.2 U/µl RNase inhibitor (Clontech, #2313A), resuspended in 1 mL of NSB and filtered through a $40 \ \mu m$ cell strainer. Nuclei were stained with SYTOX green (1:1000) and counted twice. A final concentration of $1000 \ nuclei$ per μL was used for loading onto the $10 \times 100 \ nuclei$ per μL was used for loading onto the $10 \times 100 \ nuclei$ per μL was used for loading onto the $10 \times 100 \ nuclei$ per μL was used for loading onto the $10 \times 100 \ nuclei$ per μL was used for loading onto the $10 \times 100 \ nuclei$ per μL was used for loading onto the $10 \times 100 \ nuclei$ per μL was used for loading onto the $10 \times 100 \ nuclei$ per μL was used for loading onto the $10 \times 100 \ nuclei$ per μL was used for loading onto the $10 \times 100 \ nuclei$ per μL was used for loading onto the $10 \times 100 \ nuclei$ per $10 \times 100 \ nuclei$





Mapping single nuclei reads to the genome

Using the GRCh38 (1.2.0) reference from 10x Genomics, we made a pre-mRNA reference according to the steps detailed by 10X Genomics (https://support.10xgenomics.com/single-cell-gene512expression/software/pipelines/latest/advanced/references). Sequencing reads were aligned to the human pre-mRNA reference transcriptome using the 10x Genomics CellRanger pipeline (version 3.0.0; RRID: SCR_017344) with default parameters.

Quality control for expression matrix

Downstream analysis was performed using Seurat 4.0 in RStudio Version 4.1.0. An individual Seurat object was generated for each sample. Cells with fewer than 200 detected genes and with more than 5% of reads mapped to mitochondrial genes were filtered out. Doublets were identified using the DoubletFinder package⁵⁷ and removed assuming a doublet rate formation of 3%. In downstream analysis, the clusters that were highly scored with multiple cell type gene sets were further filtered from the dataset

Data processing, analyses, visualization, and differential expression testing

All samples were merged into a single Seurat object. Data were then normalized and scaled using the SCTransform function in Seurat using the default parameters. Anchor-based sample Integration was performed on the normalized counts, with the number of features in the anchor finding process set to 3000. Non-linear dimensionality reduction was performed by running UMAP on the first 30 PCs. Clustering was performed on the top 30 PCs as input in the FindNeighbors function, and a high resolution (res = 0.6) was set in the FindClusters function to obtain small clusters. By doing so, nuclei were separated into 89 pre-clusters. By choosing this high resolution, clusters with no clear identity can be further subsetted. Those clusters identified as doublets/multiplets scored high for multiple cell types and with the high resolution for clustering, these small clusters were separated from singlets. Next, we defined cell type specific gene sets for Neurons, Astrocytes, Oligodendrocytes, Oligodendrocyte precursor cells, Microglia, Endothelial cells and Pericytes (Table S1) using the top 100 cell type enriched genes from the literature 64-66 and from PanglaoDB Augmented database. For cell type annotation, DefaultAssay was set to "RNA" and data were normalized using NormalizeData function. Using AddModuleScore function, a cell type ModuleScore was set for each cluster, and the highest ModuleScore was used to annotate cell types. Clusters that scored for more than one cell type were further removed. By so doing, we obtained a dataset with 54,960 nuclei. The expression of known canonical marker genes for cell types found in human brain was further verified for each subcluster.

Identification of differentially expressed genes in cell-type subpopulations

After cell type annotation, differential gene expression (DGE) was performed for each cell typed cluster. To identify genes differentially expressed by a cell-type subpopulation across *PSEN1*-E280A and sporadic AD, we used a pseudo-bulk approach using the LIBRA package¹⁶ using the following arguments: de_method = edgeR and de_type = LRT. The pseudobulk analyses were confirmed with a generalized linear mixed model (GLMM). The glmer.nb function from the lme4 package⁶⁰ was used to run the negative binomial generalized linear mixed-effect models, which included a fixed effect for genotype and a random effect for patient to account for pseudo-replication bias and overdispersion in the data.^{30,68} An FDR-corrected p value of ≤0.05 was considered for both analysis (Table S2). The application of a GLMM produced a very high overlap (Table S2) in significant genes with the pseudobulk DGE method. Gene enrichment analysis for terms among DGEs was performed using EnrichR, Metascape,⁵⁹ and DA-VID.⁶⁹ The outcome found using all three tools were similar, and the reported results are from EnrichR. For heatmaps of relative gene expression across cell-type subpopulations, RNA normalized counts of each gene were *Z* score transformed across all cells and then averaged across cells in each cluster to enhance visualization of differences among clusters. Thus, genes with high relative expression had above-average expression (positive z-scores), and genes with low relative expression had below-average expression (negative z-scores).

Hd-WGCNA

High-dimensional weighted gene co-expression network analysis (hd-WGCNA) was performed using the package developed by Morabito et al.⁷⁰ Of glial cells, only oligodendrocytes (18,009 nuclei) and astrocytes (4,874 nuclei) had a large enough nuclei population to run hd-WGCNA. Of neuronal cells, only excitatory neurons (16,954 nuclei) had a large enough nuclei population to run hd-WGCNA. No modules were found in oligodendrocytes that distinguished the conditions (*PSEN1*-E280A vs. sporadic AD); thus the analysis was focused on astrocytes and excitatory neurons as follows.

Metacell formation

Nuclei were subset from the Seurat object and data were pre-processed by running the NormalizeData, VariableFeatures, ScaleData, RunHarmony, RunPCA, RunUMAP, and FindNeighbors functions. Similar cells were grouped by same cell type and biological sample into metacells using MetacellsByGroups with k = 15. Metacell expression matrix was normalized using NormalizeMetacells function.

Formation and identification of modules of interest

To perform a co-expression network analysis and construct a co-expression network we used ConstructNetwork function with a soft power threshold of eight as determined by TestSoftPowers. This step identified 10 modules in astrocytes, 7 modules in oligodendrocytes and 6 modules in excitatory neurons using TOM, as visualized in the dendrograms (Figures S4 and S6). The ModuleEigengenes function was used to calculate the module eigengene (hME) value for each module within each single nuclei and stored that value in the metadata of the Seurat object. Significant differences in the hME values between diagnosis were assessed by the Kruskal-Wallis test (one-way nonparametric ANOVA), and a p value threshold <0.01 was considered. Wilcoxon Rank Sum tests were performed to identify specific diagnosis comparisons in modules of genes that are significantly. Only comparisons

Neuron Article



that meet both a p value threshold <0.01 and Wilcoxon effect size >0.3 (moderate effect) were considered significantly different. The p value was adjusted due to the multiple comparisons using the Holm-Bonferroni method. To infer biological significance to the genes within each module, we ran GO/pathway analysis using Metascape. 59 To identify GO terms of interest, we looked at the particular genes from the module associated with a particular GO term and averaged their kME values. Terms with associated kME values that were higher than the average kME value of the overall module were considered, as it indicated that the genes that were associated with that term are highly connected and influential within the module network. To further identify significant GO terms, we also focused on GO terms which met a LogQ threshold of < -10.

Spatial transcriptomics

A schematic of the Visium spatial gene expression workflow is depicted in Figure 4A.

Slide preparation

Hippocampal and frontal cortical samples were cryosectioned at -20° C. The 10 μ m sections were placed on a Visium Tissue Optimization Slide (10x Genomics, #3000394) and Visium Spatial Gene Expression Slide (10x Genomics, #2000233). By following the Visium Spatial Tissue Optimization User Guide (10x Genomics, #CG000238 Rev E), the optimal permeabilization time was determined to be 6 min. The gene expression slides underwent methanol fixation, H&E staining, and brightfield imaging using a 10x objective on a Nikon Eclipse Ti2-E (10x Genomics, #CG000160 Rev C). Immediately after imaging, the tissues were permeabilized and the remaining steps for library construction were completed according to the user guide (10x Genomics, #CG000239 Rev F). Mapping spatial gene expression reads to the genome and microscope images. Using Loupe Brower (version 6.2.0) the fiducial frame was manually identified and only spots under tissue were selected for the 10x Genomics Space Ranger pipeline (version 1.3.1). Spot-level and gene-level filtering. Spots with more than 30% of reads mapped to mitochondrial genes were removed from the dataset. Genes expressed in less than 3 spots per sample and mitochondrial genes were excluded. Clustering, visualization, and integration. Using Seurat 4.1, data from each sample was individually normalized via SCTransform, followed by dimensionality reduction via RunPCA. The top 10 PCs were used for the FindNeighbors function, then FindClusters with resolution set to 0.1 and RunUMAP were run to produce a UMAP with 2-3 clusters per sample. Clusters were annotated based on the highest expression of known gray matter/neurons and white matter/oligodendrocytes marker genes, such as those visualized in Figures 4B and 4C.71 The normalized data from all samples was merged and then prepared for integration via PrepSCTIntegration, which used 5,000 features from the SelectIntegrationFeatures function. Anchors were identified by the FindIntegrationAnchors function and used as an input for the IntegrateData function. The same reduction and clustering steps as before were then performed on the integrated Seurat object. This produced a UMAP in which the gray/white matter assignments from the single-sample clustering corresponded with the two major integrated clusters (Figure 4F). Additionally, the identity of the two integrated clusters was further confirmed with additional neuron and oligodendrocyte markers (Figure S6).

Differential gene expression analysis

The data was stratified by white/gray matter assignments to identify genes differentially expressed between *PSEN1*-E280A and controls in the two strata. Differential gene expression was performed using a negative binominal GLMM with CDR as a fixed effect and individual as a random effect on the spatial data (*PSEN1*-E280A vs. Control).

Immunofluorescence

Immunofluorescence was performed on formalin-fixed paraffin-embedded (FFPE) brain tissue from the frontal cortex (superior frontal gyrus) of sporadic AD and *PSEN1*-E280A patients, at least 2 cases per group, 2 slices per case, and on FFPE brain tissue from the frontal cortex and occipital cortex of one *PSEN1*-E280A case that harbored the *APOE*3 Christchurch variant. 4μm thick sections were mounted on Superfrost plus slides and further processed for immunofluorescence staining for glial fibrillary acidic protein acidic protein (GFAP, 1:200; 173308, Synaptic- Systems), MAP2 (1:500; ab32454, Abcam), heat shock protein 90 (HSP90, 1:200; MA5- 33174, Invitrogen), cyclophilin A (CyPA, 1:100; PA1-025, ThermoFisher Scientific), total TAU protein (Tau-5, 1:200; AHB0042, ThermoFisher Scientific), Phospho-Tau Ser202, Thr205 (AT8, 1:500; MN1020, ThermoFisher Scientific), Low-density lipoprotein receptor-related protein 1 (LRP1 1:100; L2295, Sigma-Aldrich) and FKBP1B (1:200; 15114-1-AP, ThermoFisher Scientific). After deparaffinization, heat-induced epitope retrieval was performed using R-Universal buffer (AP0530-500; Aptum Biologics, Southampton, UK) in a pressure cooker for 20 min, sections were then blocked for 1 h with blocking medium (MAXblock, 15252; Active Motif GmbH) followed by incubation with primary antibodies at 4°C overnight. For detection of specific binding, secondary antibodies were incubated at room temperature for 1 h. After washing mounting was performed with 4′,6-Diamidino-2-phenylindole (DAPI) Fluroromount-G for nuclear counterstaining. High-resolution images were obtained with a Leica TCS SP8 confocal laser scanning microscope (Leica Microsystems, Mannheim, Germany) using a 63X immersion oil lens objective.

Multi dataset analyses

For the analysis of the *PSEN1*-E280A_*APOE3*-CC-hom, we used the data from snRNA-seq in the frontal cortex and occipital cortex previously published by our group (available at GEO under accession number GSE206744). We also integrated to this data, additional sequencing runs for the same brain regions (frontal cortex and occipital cortex) more recently performed at our laboratory.





QUANTIFICATION AND STATISTICAL ANALYSIS

Statistics

Throughout this manuscript, quantified nuclei outputs are displayed as the arithmetic mean (±s.d., if applicable), and plots were generated using the ggplot2 and ggpubr packages in R and/or using GraphPad Prism (v 6.01, Graphpad Software, Boston, MA, USA) unless otherwise noted.

Cell-specific co-localization analysis

For quantification of levels of HSP90 and PPIA expression in cells expressing GFAP or MAP2, image processing was done using Python 3.10.12. All image morphology and filtering operations were done using scikit-image 0.19.3 package. Immunohistochemistry images were uploaded using readlif 0.6.5 package. Maximum intensity projections of DAPI, MAP2 and/or GFAP z-stacks were summed and used for cell body segmentation. The summed image was filtered with Gaussian (s = 1) and cells were identified using triangle thresholding. Individual cells were identified using Euclidean distance transform followed by a local maxima search and a watershed segmentation. Objects with an area smaller than 500 pixels were removed. For cell-wise estimation of a protein of interest expression level a sum of the z stack was used, normalized by its maximum.

Immunofluorescence

Immunofluorescence colocalization analysis for TAU5 and AT8 were performed with FIJI ImageJ 1.53q Software, ⁷² following image automatic thresholding by the Costes method. Manders overlap coefficients and colocalization volumes for each channel were assessed. Results were analyzed with a two-way Student's t test, using Graphpad Prism.

Calculation of CMA activation score

CMA score was calculated according to Bourdenx et al. 17 Briefly, for each cell type, a CMA activation score was calculated for each individual. To do so, LAMP2 was attributed a weight of 2 (as it is the rate limiting component of CMA) and every other element was attributed a weight of 1. Every element received a direction score (+1 or -1) based on the known effect (activator or inhibitor) of a given element on CMA activity. The score was then calculated as the weighted/directed average of expression counts of every element of the CMA network for samples from *PSEN1*-E280A, sporadic AD and controls. The CMA score results for *PSEN1*-E280A and sporadic AD are normalized by control CMA score values.

Beta regression

The relative abundance of a given cell cluster or cell type (ranging from 0 to 1), was calculated for each sample. Statistical significance of changes in the relative abundance of a given cluster or cell type across diagnosis (control, PSEN1-E280A and sporadic AD), were determined using beta regression (betareg package, version 3.1–4), using the formula relative abundance \sim Diagnosis for the precision model, and the bias-corrected maximum likelihood estimator. p values obtained from beta regression were corrected for multiple hypotheses using Bonferroni correction.

Gene set HAM (human AD microglia) score

The HAM gene set scores were calculated using the function "AddModuleScore" from Seurat. The list of genes overexpressed and underpressed associated with the HAM profile used as the "feature" argument in the function were obtained from Olah and colleagues. 73

Overlap analysis

To evaluate the overlap between particular DGEs sets and modules found in the hd-WGCNA analysis, overlap analysis on the gene lists associated with positive markers for astrocytes and excitatory neurons and hd-WGCNA modules was performed. Essentially, the list of genes associated with each module, and the list of positive cluster markers for each of the population (*p_adjusted* < 0.05, Log2FC > 0.25) were retrieved. The R package GeneOverlap was used to perform a Fisher's Exact Test and to evaluate the overlap between the markers and module lists.

Negative binomial generalized linear mixed-effect model

The R package Ime4 was used to measure the fixed effect of the *APOE3*ch genotypes. Every gene expressed in more than 10% of nuclei for a given cell type was modeled. Microglia, OPCs, endothelial cells and pericytes could not be modeled due to the relatively small numbers of nuclei when only a subset of patients were included in these analyses. The glmer.nb function was used to run the negative binomial generalized linear mixed-effect models, all of which included a fixed effect for genotype and a random effect for patient to account for pseudo-replication bias and overdispersion in the data. 30,68

Randomization

No randomization was used in the analysis of snRNA-seq.

Neuron Article



Sample size estimation

No methods were used to predetermine the sample size used in this study. However, our donor cohort is similar in size to previously published works.

12. Abstract

Autosomal dominant Alzheimer's disease (ADAD) provides an invaluable framework for the study of Alzheimer's disease (AD) pathogenesis. Approximately 90% of all ADAD cases are due to mutations in the PSEN1 gene. In Antioquia (Colombia), a large kindred of individuals carrying the *PSEN1* E280A mutation (Paisa mutation) has been described. Affected individuals from this kindred have a very predictable clinical course, typically presenting with cognitive impairment by their mid-forties. Yet, inside this population, two carriers of rare genetic variants have shown a remarkable resilience and remained cognitively healthy for decades beyond the expected age of onset (AOO). This thesis recapitulates five publications describing the clinical course, neuropathological landscape, and molecular underpinnings of these protected cases. The first case was a female patient, homozygous for the rare APOEε3 Christchurch (APOE3ch) variant, while the second one was a male carrying the H3447R RELN variant (RELN-COLBOS). A more modest but still clinically significant delay in the AOO was observed in heterozygous carriers of APOE3ch. Aside from the cognitive preservation, the two protected subjects shared a high amyloid burden comparable to a typical PSEN1 E280A case but markedly limited or atypically distributed Tau pathology. 18F-Flortaucipir PET scan and postmortem assessment revealed that the APOE3ch homozygote had relative sparing in the frontal cortex and an unusually high Tau accumulation in the occipital cortex, while the RELN-COLBOS carrier showed a striking preservation of the entorhinal cortex, a highly susceptible structure in AD pathogenesis. A multimodal approach, including snRNA-seq and transcriptomics of human tissue, the generation of iPSC with the same genetic background and key mutation documented in the subjects, as well as organoids, mouse models, and in vitro assays, was used to elucidate the cellular and molecular pathways responsible for the protection. APOE3ch protection seems to be linked to a reduced affinity of APOE for heparan sulfate proteoglycans, potentially impairing tau uptake and spread and reducing Tau hyperphosphorylation via enhanced Wnt/βcatenin signaling. RELN-COLBOS protection, on the other hand, would be related to reduced Tau hyperphosphorylation through increased Dab1 activity. Overall, the findings indicate that clinical protection against ADAD is possible, even in the context of a high amyloid burden, through mechanisms that mitigate Tau-mediated neurodegeneration and underscore the value of studying extreme phenotypes.

13. Zusammenfassung

Die autosomal dominante Alzheimer-Krankheit (ADAD) bietet einen unschätzbaren Rahmen für die Untersuchung der Pathogenese der Alzheimer-Krankheit (AD). Ungefähr 90 % aller ADAD-Fälle sind auf Mutationen im *PSEN1*-Gen zurückzuführen. In Antioquia (Kolumbien) wurde eine große Verwandtschaft von Personen beschrieben, die die Mutation *PSEN1* E280A (Paisa-Mutation) tragen. Die Betroffenen dieser Verwandtschaft haben einen sehr vorhersehbaren klinischen Verlauf, der typischerweise mit kognitiven Beeinträchtigungen im Alter von Mitte vierzig beginnt. Innerhalb dieser Population haben jedoch zwei Träger seltener genetischer Varianten eine bemerkenswerte Widerstandsfähigkeit bewiesen und sind jahrzehntelang über das erwartete Erkrankungsalter (AOO) hinaus kognitiv gesund geblieben. In dieser Arbeit werden fünf Veröffentlichungen rekapituliert, in denen der klinische Verlauf, die neuropathologische Landschaft und die molekularen Grundlagen dieser geschützten Fälle beschrieben werden. Bei dem ersten Fall handelte es sich um eine weibliche Patientin, die homozygot für die seltene APOEε3-Christchurch-Variante (APOE3ch) war, während der zweite Fall ein Mann war, der die RELN-Variante H3447R (RELN-COLBOS) trug. Bei den heterozygoten Trägern der APOE3ch-Variante wurde eine geringere, aber dennoch klinisch signifikante Verzögerung der AOO beobachtet. Abgesehen von der kognitiven Erhaltung wiesen die beiden geschützten Probanden eine hohe Belastung durch Amyloid auf, die mit einem typischen PSEN1 E280A-Fall vergleichbar war, aber eine deutlich begrenzte oder atypisch verteilte Tau-Pathologie. Die 18F-Flortaucipir-PET-Untersuchung und die postmortale Beurteilung ergaben, dass der APOE3ch-Homozygote eine relative Schonung des frontalen Kortex und eine ungewöhnlich hohe Tau-Akkumulation im okzipitalen Kortex aufwies, während der RELN-COLBOS-Träger eine auffällige Erhaltung des entorhinalen Kortex zeigte, einer bei der AD-Pathogenese sehr anfälligen Struktur. Ein multimodaler Ansatz, der snRNA-seg und räumliche Transkriptomik von menschlichem Gewebe, die Erzeugung **iPSC** mit demselben genetischen Hintergrund und denselben von Schlüsselmutationen, die bei den Probanden dokumentiert wurden, sowie Organoide, Mausmodelle und In-vitro-Tests umfasst, wurde verwendet, um die für den Schutz verantwortlichen zellulären und molekularen Signalwege aufzuklären. Der APOE3ch-Schutz scheint mit einer verringerten Affinität von APOE für Heparansulfat-Proteoglykane zusammenzuhängen, was möglicherweise die Aufnahme und Ausbreitung von Tau beeinträchtigt und die Hyperphosphorylierung von Tau über eine verstärkte Wnt/β-Catenin-Signalisierung verringert. Der Schutz durch *RELN-COLBOS* hingegen würde mit einer verringerten Tau-Hyperphosphorylierung durch erhöhte Dab1-Aktivität zusammenhängen. Insgesamt deuten die Ergebnisse darauf hin, dass ein klinischer Schutz gegen ADAD möglich ist, selbst im Kontext einer hohen Belastung durch Amyloid , mit Hilfe von Mechanismen, die die Tau-vermittelte Neurodegeneration abschwächen, und unterstreichen den Wert der Untersuchung extremer Phänotypen.

14. List of abbreviations

AD Alzheimer's disease

ADAD Autosomal dominant Alzheimer's disease

AICD Amyloid precursor protein intracellular domain

AMY Amygdala

AOO Age of onset

APH1A Anterior pharynx-defective 1

APLP1 Amyloid precursor-like protein 1
APLP2 Amyloid precursor-like protein 2

APP Amyloid precursor protein

Aβ Amyloid beta

CAA Cerebral amyloid angiopathy

CAU Caudate

CB Cerebellum

CERAD Consortium to Establish a Registry for Alzheimer's Di

CMRgl Cerebral metabolic rate of glucose

CNG Cingulate cortex

CSF Cerebrospinal fluid

CTF Carboxy-terminal fragment

ERC Entorhinal cortex

FAD Familial Alzheimer's disease

FFPE Formalin-fixed paraffin-embedded

FTP 18F-Flortaucipir

FZD Frizzeld

GAG Glycosaminoglycans

GWAS Genome-wide association study

HIP Hippocampus

HSPG Heparan sulfate proteoglycans

IPC Inferior parietal cortex
ITC Inferior temporal cortex,

LDLR Low-density lipoprotein receptor

LTP Long-term potentiation

MCI Mild cognitive impairment

MED Medulla oblongata.

MES Mesencephalon

MFC Medial frontal cortex

MRI Magnetic resonance imaging
MTBR Microtubule-binding repeat

MTC Middle temporal cortex
NFTs Neurofibrillary tangles

NICD Notch intracellular domain

NTF Amino-terminal fragment

OL Occipital lobe

PEN2 Presenilin enhancer 2

PET Positron emission tomography

PiB Pittsburgh compound B

PON Pons

PSEN1 Presenilin 1
PSEN2 Presenilin 2
PUT Putamen

RORB Retinoid-related orphan receptor B

SAD Sporadic Alzheimer's disease

STC Superior temporal cortex

THA Thalamus

TM Transmembrane domain

VLDLR Very low-density lipoprotein receptor

WES Whole-exome sequencing

WT Wild-type

15. List of figures and tables

Figure 1 Longitudinal tau PET imaging measures in an <i>APOE3ch</i> homozygote	. 21
Figure 2 Neuropathological characterization of an ADAD <i>PSEN1</i> E280A mutation	
carrier with two copies of the APOE3ch variant	. 22
Figure 3 PET imaging of the RELN-COLBOS (H3447R) carrier	. 24
Figure 4 Neuropathological characterization of the case with PSEN1 E280A; RELI	٧-
H3447R	. 26
Figure 5 Cumulative incidence function for cognitive impairment and dementia	
among <i>PSEN1</i> E280A carriers	. 28
Figure 6 Decreased cerebral amyloid angiopathy in <i>APOE3Ch PSEN1</i> E280A	
carriers	. 28
Figure 7 Increased nuclear β-catenin signal in frontal cortex neurons	. 31
Figure 8 Protein immunoreactivity validates transcriptional alterations detected in t	he
frontal cortex by snRNA-seq	. 34

16. Declaration of own contribution to the publications

As a coauthor of the first publication, I contributed to every stage of the neuropathological characterization and conducted comprehensive image analyses of the immunohistochemical sections. As co–first author of the second paper, I was responsible for an in-depth neuropathological assessment, including detailed neuronal population analyses—an expertise I also applied to studies III, IV, and V. For papers IV and V, I played an active role in validating candidate markers in human tissue using immunofluorescence techniques. Additionally, for papers I, II, III, and V, I was involved in the critical review and final editing of the manuscripts, ensuring clarity, accuracy, and scientific rigor.

17. Curriculum Vitae

PERSONAL DETAILS

Full Name:	Nelson David Villalba Moreno
E-Mail:	chieco90@hotmail.com
	n.villalbamoreno@uke.de

ACADEMIC QUALIFICATIONS

2016	Magíster e	en cie	ncias biomédic	as, énfasis e	en Neurocieno	cias
	(Master	in	Biomedical	Science,	emphasis	in
	neuroscie	nce),	Universidad de	el Valle Title	: "Morpholog	ical
	Character	izatio	n of Layer VI in	nterneurons	in areas 10o a	and
	24 of the I	Huma	n Prefrontal Co	ortex"- Laur e	eate Thesis	
2012	Physician	and s	Surgeon (M.D.)), Universida	d del Valle.	

EMPLOYMENT HISTORY

January 2021 –					
April 2025	Doctoral	student, sklinikum H			1 9 /
August 2020 –	Onversion	okii iikai ii i	arriburg L	-ррспа	J11.
December 2020		Professor, D niversidad D	•	t of Mo	rphology, Health
July 2019 – August 2020	Emergenc	y Physician,	Clínica P	'alma R	eal, Palmira – Col.
January 2019 – April 2019	Praktikant, Universität	Instit		ür Eppende	Neuropathologie, orf.
November 2016 – January 2019	Emergenc	y Physician,	Clínica d	e Occid	dente, Cali – Col.

January 2016 –	
August 2019	Assistant Professor, Department of Morphology, Health
	Faculty, Universidad Del Valle.
January 2017 –	
December 2018	Assistant Professor, Department of Morphology, Medicine
	Faculty, Universidad ICESI
August 2015 –	
December 2015	Teaching Assistant, Department of Morphology, Health
	Faculty, Universidad Del Valle.
June 2014 –	
January 2016	Emergency Physician, Clínica de Occidente, Cali – Col.
Dec. 2012 –	
January 2013	Rural Physician, Hospital San Antonio, Roldanillo – Col.

TEACHING

January 2017 -

December 2018 Universidad ICESI

Teaching assistant in clinical and functional neuroanatomy courses for undergraduate medicine students, activities including lectures, and paperwork review.

August 2015 –	
August 2020	Universidad del Valle
	Teaching assistant in clinical and functional neuroanatomy
	courses, for undergraduate medicine students, dentistry, nursing,
	and psychology among other and postgraduate students from
	basic and clinical science. Activities include lectures, gross
	anatomy of nervous system laboratories orientation, seminars,
	and paperwork review.

18. Acknowledgements

I would like to thank my supervisor, Diego Sepulveda-Falla, for the position in his lab and Prof. Dr. Markus Glatzel for his training and for helping me to develop a keener eye to see the brain under a microscope. To Lisa for her support, confidence in me, and for helping me to be a better scientist. To all the kind colleagues of the Institute for Neuropathology for all the support, guidance, and help in the laboratory, particularly to Edda and Kyungeun.

19. Eidesstattliche Versicherung

Ich versichere ausdrücklich, dass ich die Arbeit selbständig und ohne fremde Hilfe,

insbesondere ohne entgeltliche Hilfe von Vermittlungs- und Beratungsdiensten,

verfasst, andere als die von mir angegebenen Quellen und Hilfsmittel nicht benutzt und

die aus den benutzten Werken wörtlich oder inhaltlich entnommenen Stellen einzeln

nach Ausgabe (Auflage und Jahr des Erscheinens), Band und Seite des benutzten

Werkes kenntlich gemacht habe. Das gilt insbesondere auch für alle Informationen aus

Internetquellen.

Soweit beim Verfassen der Dissertation KI-basierte Tools ("Chatbots") verwendet

wurden, versichere ich ausdrücklich, den daraus generierten Anteil deutlich kenntlich

gemacht zu haben. Die "Stellungnahme des Präsidiums der Deutschen

Forschungsgemeinschaft (DFG) zum Einfluss generativer Modelle für die Text- und

Bilderstellung auf die Wissenschaften und das Förderhandeln der DFG" aus

September 2023 wurde dabei beachtet.

Ferner versichere ich, dass ich die Dissertation bisher nicht einem Fachvertreter an

einer anderen Hochschule zur Überprüfung vorgelegt oder mich anderweitig um

Zulassung zur Promotion beworben habe.

Ich erkläre mich damit einverstanden, dass meine Dissertation vom Dekanat der

Medizinischen Fakultät mit einer gängigen Software zur Erkennung von Plagiaten

überprüft werden kann.

Datum

Unterschrift

158